ABSTRACT

MULTI-COMPONENT BORON COATINGS ON LOW CARBON STEEL AISI 1018

by
Naruemon Suwattananont

Boronizing and metalizing are thermo-chemical surface hardening treatments in which boron and metal atoms diffuse into the metal substrate forming metallic boride layers, providing complex properties of B-Me-Fe system.

To study multi-component boron coatings on low carbon steel AISI 1018, the simultaneous powder pack method of boronizing and metalizing was selected to perform the coatings. One B-Fe system and eight boron-metal (B-Me-Fe) systems from transition metals group IVB (Ti, Zr, Hf), group VB (Nb, Ta), and group VIB (Cr, Mo, W) were studied. The system specimens were thermo-chemically treated at 950°C for 4 hours in a crucible containing powder mixture of boron source, transition metal powder, and activator.

After the heat treatment process, the multi-component boron coatings were characterized by using optical microscope, microhardness tester, TGA, XRD, and Synchrotron microdiffraction. The coating morphology was observed and the coating thickness was measured as well as the microhardness across the depth of coating. The corrosion resistance of the coatings was evaluated by the continuous weighting method. The high temperature oxidation was also detected by isothermal method at a temperature range of 400–800°C for 24 hours. The Rietveld refinement method was used to examine the quantitative phase analysis, crystalline size, microstrain and lattice parameters of the multi-component boron coatings.

The results have shown that adding transition metals into the B-Fe system caused the formation of solid solution of transition-metal borides. The distortion of crystal lattice parameters generated microstrain in the boride phase. The Synchrotron microdiffraction confirmed the presence of about 5-10 microns of transition-metal boride phase at the surface. Moreover, the additional transition metal can provide better corrosion and high temperature oxidation resistance to the B-Fe system, preventing the deboronizing and stabilizing the boride phases.

MULTI-COMPONENT BORON COATINGS ON LOW CARBON STEEL AISI 1018

by
Naruemon Suwattananont

A Dissertation
Submitted to the Faculty of
New Jersey Institute of Technology
in Partial Fulfillment of the Requirements for the Degree of
Doctor of Philosophy in Materials Science and Engineering

Interdisciplinary Program in Materials Science and Engineering

May 2010

APPROVAL PAGE

MULTI-COMPONENT BORON COATINGS ON LOW CARBON STEEL AISI 1018

Naruemon Suwattananont

Dr. Roland A. Levy, Dissertation Co-Advisor — Date 5/10/2010
Distinguished Professor of Physics, NJIT

Dr. Roumiana S. Petrova, Dissertation Co-Advisor — Date 5/10/10
University Lecturer of Chemistry and Environmental Science, NJIT

Dr. Joseph W. Bozzelli, Committee Member — Date 5/10/2010
Distinguished Professor of Chemistry and Environmental Science, NJIT

Dr. Somenath Mitra, Committee Member — Date 5/10/10
Chair and Professor of Chemistry and Environmental Science, NJIT

Ms. Stacey C. Kerwien, Committee Member — Date
Deputy Division Chief of Material, Manufacturing and Prototyping Division
U.S. Army Armament Research, Development and Engineering Center (ARDEC),
Picatinny Arsenal, NJ

BIOGRAPHICAL SKETCH

Author: Naruemon Suwattananont

Degree: Doctor of Philosophy

Date: May 2010

Undergraduate and Graduate Education:

- Doctor of Philosophy in Materials Science and Engineering,
  New Jersey Institute of Technology, Newark, NJ, 2010
- Master of Science in Materials Science and Engineering,
  New Jersey Institute of Technology, Newark, NJ, 2004
- Master of Science in Materials Science (Ceramic Technology),
  Chulalongkorn University, Bangkok, Thailand, 1997
- Bachelor of Science in Chemistry,
  Chiang Mai University, Chiang Mai, Thailand, 1994

Major: Materials Science and Engineering

Presentations and Publications:

Naruemon Suwattananont and Roumiana S. Petrova,
"Oxidation Kinetics of Boronized Low Carbon Steel AISI 1018,"
Oxidation of Metals, Vol. 70, No. 5-6, pp. 307-315, December 2008.

Roumiana S. Petrova, Naruemon Suwattananont, and Veljko Samardzic,
"The Effect of Boronizing on Metallic Alloys for Automotive Applications,"
Journal of Materials Engineering and Performance, Vol. 17, No. 3, pp. 340-345, June 2008.

Roumiana S. Petrova, Naruemon Suwattananont, Kranthi K. Pallegar, and Raghasudha Vangaveti,
"Boron Coating to Combat Corrosion and Oxidation,"
Corrosion Reviews, Vol. 25, No. 5-6, pp. 555-569, 2008.

Roumiana S. Petrova, Naruemon Suwattananont, and Veljko Samardzic,
"The Effect of Boronizing on Metallic Alloys for Automotive Applications,"
Materials Science & Technology 2007 Conference and Exhibition, Session of Automotive: Automotive and Ground Vehicles: Materials and Processes for Vehicles, Detroit, MI, September 2007.

Naruemon Suwattananont and Roumiana S. Petrova,
"Boronization: Surface Treatment with Boron on Ferrous and Non-Ferrous Metals and Alloy,"
Materials Science &Technology 2006 Conference and Exhibition, Session of Surface Protection for Enhanced Materials Performances: Surface Modifications and Protection for Enhanced Performance II, Cincinnati, OH, October 2006.

Naruemon Suwattananont, Roumiana S. Petrova and B. Godenberg,
"Boronization of Ti-Alloy to Improve the Wear Resistance for Aerospace Applications,"
Materials Science &Technology 2006 Conference and Exhibition, Session of Materials Processing Challenges for the Aerospace Industry: Coatings, Cincinnati, OH, October 2006.

Roumiana S. Petrova and Naruemon Suwattananont,
"Surface Modification of Ferrous Alloys with Boron,"
Journal of Electronic Materials, Vol. 34, No. 5, pp. 575-582, May 2005.

Elias Jelis, Naruemon Suwattananont, and Roumiana S. Petrova,
"Boronizing of Ti-6Al-4V Eli by Powder Pack Method for Biomedical Application,"
Proceedings of the IEEE 31st Annual Northeast on Bioengineering Conference, Hoboken, NJ, pp. 193-194, April 2005.

Naruemon Suwattananont, Roumiana S. Petrova, James L. Zunino III, and Daniel P. Schmidt,
"Surface Treatment with Boron for Corrosion Protection,"
Proceedings of the 2005 Tri-Service Corrosion Conference, Session of Coatings and Surface Treatments, Orlando, FL, Paper No. 041, November 2005.

Roumiana S. Petrova, Naruemon Suwattananont, Kranthi K. Pallegar, and Raghasudha Vangaveti,
"Boron Coating to Combat Corrosion and Oxidation,"
Proceedings of the 2005 First World Congress on Corrosion in the Military, Session IX of Coatings and Finishes, Sorrento, Italy, June 2005.

Roumiana S. Petrova and Naruemon Suwattananont,
"Oxidation Kinetics of Boron Coating on Ferrous Alloys at High Temperature," Proceedings of the 2005 TMS Annual Meeting and Exhibition, Symposium of Frontiers in Thin Film Growth and Nanostructured Materials, San Francisco, CA, February 2005.

Roumiana S. Petrova and Naruemon Suwattananont,
"Corrosion Resistance of Boronized Steel",
Proceedings of the 2004 Materials Research Society, Session of Surface Engineering: Fundamentals and Applications, Boston, MA, November 2004.

Roumiana S. Petrova, Naruemon Suwattananont, and Elias Jelis,
"Microstructure and Properties of Boronized Metallic Alloys,"
Proceedings of the 2004 ASM Materials Solutions Conference and Show, Session of Processing of Metals and Composites, Columbus, OH, October 2004.

Roumiana S. Petrova and Naruemon Suwattananont,
"Surface Modification of Metals and Alloys with Boron,"
Proceedings of the 2004 TMS Annual Meeting and Exhibition, Session of Challenges in Advanced Thin Films: Microstructures, Interfaces, and Reactions: Modification, Characterization, and Modeling, Charlotte, NC, March 2004.

๏ วิชาเหมือนสินค้า.....อันมีค่าอยู่เมืองไกล
ต้องยากลำบากไป.....จึงจะได้สินค้ามา
๏ จงตั้งเอากายเจ้า.....เป็นสำเภาอันโสภา
ความเพียรเป็นโยธา.....แขนซ้ายขวาเป็นเสาใบ
๏ นิ้วเป็นสายระยาง.....สองเท้าต่างสมอใหญ่
ปากเป็นนายงานไป.....อัชฌาสัยเป็นเสบียง
๏ สติเป็นหางเสือ.....ถือท้ายเรือไว้ให้เที่ยง
ถือไว้อย่าให้เอียง.....ตัดแล่นเลี่ยงข้ามคงคา
๏ ปัญญาเป็นกล้องแก้ว.....ส่องดูแถวแนวหินผา
เจ้าจงเอาหูตา.....เป็นล้าต้าฟังดูลม
๏ ขี้เกียจคือปลาร้าย.....จะทำลายให้เรือจม
เอาใจเป็นปืนคม.....ยิงระดมให้จมไป
๏ จึงจะได้สินค้ามา.....คือวิชาอันพิสมัย
จงหมั่นมั่นหมายใจ.....อย่าได้คร้านการวิชา

เจษฎาจารย์ ฟ. ฮีแลร์

ACKNOWLEDGMENT

First and foremost, I would like to express my deepest appreciation to my advisors, Dr. Roland A. Levy and Dr. Roumiana S. Petrova, for providing me with most valuable and prodigious resources, guidance, opportunities, and heartfelt support all through my graduate education in both the master's and doctoral programs. Especially Dr. Roumiana S. Petrova, she has always been a source of encouragement and knowledge. Her perseverance, sincerity and hardworking qualities will always serve as an inspiration to me.

I would like to thank Dr. Somenath Mitra, Dr. Joseph W. Bozzelli and Ms. Stacey C. Kerwien, who are kind for actively participating in my dissertation committee, providing help, support, constructive criticism and valuable suggestions through this dissertation.

I also wish to thank the following people: Mr. Minh Tran for his help in characterizations, Dr. Zhonghou Cai for the great experiments at 2-ID-D beamline at Argonne National Laboratory, and Mr. Steve Zlatev for his help and financial support.

Appreciation is also extended to all professors, graduate students and staff from both Physics Department and Chemistry and Environmental Sciences Department, New Jersey Institute of Technology.

Finally, no words are enough to acknowledge the constant support, love and encouragement of my family. Thank you. Lastly, a special note of thanks goes to Dr. Pitipatana Sakarindr for his help during my entire study.

TABLE OF CONTENTS

TABLE OF CONTENTS
(Continued)

TABLE OF CONTENTS
(Continued)

Chapter **Page**

TABLE OF CONTENTS
(Continued)

TABLE OF CONTENTS
(Continued)

TABLE OF CONTENTS
(Continued)

Chapter **Page**

LIST OF TABLES

LIST OF FIGURES

LIST OF FIGURES
(Continued)

Figure **Page**

LIST OF FIGURES
(Continued)

LIST OF FIGURES
(Continued)

LIST OF FIGURES
(Continued)

Figure **Page**

LIST OF FIGURES
(Continued)

LIST OF FIGURES
(Continued)

Figure **Page**

CHAPTER 1

INTRODUCTION

1.1 Objectives

The purposes of this dissertation are to study a simultaneous thermo-diffusion process containing boron and transition metals Group IVB – VIB, and the characteristics and properties of multi-component boride coatings on low carbon steel AISI 1018. In this dissertation, AISI 1018 (a plain steel with low carbon content of 0.18%) is selected as a substrate for boronizing due to its cost-effectiveness and extensive use in many industrial applications. After boronizing, the boronized steel is expected to improve properties of the substrate in corrosion resistance, high temperature oxidation resistance and wear resistance, which can reduce the economic loss from the environmental deterioration. Even though boride coating can provide enough sufficient properties to many applications, the enhancement of boronized steel properties is in need. Adding a second element into the boride coating innovates a multi-component boride coating and delivers improved steel properties.

In this dissertation, eight second elements from 3 transition metal groups are investigated: Group IVB - Titanium (Ti), Zirconium (Zr), Hafnium (Hf), Group VB - Niobium (Nb), Tantalum (Ta) and Group VIB - Chromium (Cr), Molybdenum (Mo), Tungsten (W). The simultaneous thermo-diffusion process of boronizing and metallizing is used to perform the multi-component boride coating with reason to reduce the operating cost and time of two-step procedure. Powder pack cementation of boronizing and metallizing is selected because it is a simple and cost-effective method compared with other expensive advanced techniques such as CVD, PVD, etc. Finally, the

characteristics and properties of multi-component boron coatings are detected and compared for desiring the specific application of each multi-component boride coating.

1.2 Background Information

Boronizing and metallizing are a well-known thermo-chemical surface hardening for many decades. Boronizing is a process that boron atoms are diffused into a metal substrate and form a hard metallic boride layer on the metal surface. The treatment can be achieved on most ferrous materials (iron steels and alloys) and some nonferrous materials (nickel and nickel-based alloys, titanium and titanium alloys and refractory metals and alloys). On the other hand, metallizing involves the diffusion of metallic elements into the surface of components. One or several metallic elements such as aluminum, chromium, nickel, silicon and vanadium can be diffused into the metal substrate, then either substitutional solid solution layers or intermetallic layers are formed. In case the metal substrate has carbon content at least 0.45%, a carbide layer can be formed.

Boronizing provides high wear resistance, corrosion resistance, high temperature oxidation resistance and 3-10 times increasing service life [1]. One of boronizing advantages is to fill up the technology gap between conventional surface treatment and advanced surface treatment such as chemical/physical vapor deposition with low cost procedure, high quality products and similar service life improvement [2]. Diffusion metallizing is unlikely to provide a variety of properties as boronizing does. Metallizing gives an intentional surface treatment for a special case property; for example aluminizing improves oxidation and corrosion resistance, chromizing improves wear and corrosion resistance and siliconizing improves corrosion resistance in acid [3]. Therefore, the formation of multi-component boride coatings as borochromizing, borovadanizing or

borosiliconizing using boronizing and metalizing techniques will enhance the boride coating properties.

CHAPTER 2

BORONIZING

2.1 Objective

Boronizing is a thermo-chemical surface hardening process by which boron atoms diffuse into a base metal (steel) and form a hard metallic boride layer on the surface. The boronizing process can be applied to both ferrous and nonferrous materials by heating the materials at the temperature range of 700 to 1000°C (equivalently 1300 - 1830°F) for several hours. The process results in the metallic boride layer of about 20-300 μm thick.

2.2 Overview of Boronizing

Boronizing is a thermo-chemical surface hardening process by which boron atoms diffuse into a base metal (steel) and form a hard metallic boride layer on the surface. The boronizing process can be applied to both ferrous and nonferrous materials by heating the substrates at the temperature range of 700 to 1000°C (equivalently 1300 to 1830°F) for several hours. The process results in forming the metallic boride layer of about 20-300 μm thick, which yields the outstanding properties of high hardness, good wear and corrosion resistances, and moderate oxidation resistance at high temperatures. Unlike most metals and alloys, aluminium and magnesium alloys have not been successfully boronized by existing techniques because their melting temperatures are very low. In addition, copper alloy is unable to form the stable boride phase [4].

During boronizing, boron atoms diffuse and subsequently absorb into the metallic surface. As a result, since boron atom has a very small atomic radius (0.46 Å) an interstitial boron compound is formed with either a single-phase boride or a poly-phase boride layer. Several characteristics of the boride layer, including the morphology, the growth, and the phase composition, depend on the elements in the substrate materials, as depicted in Table 2.1.

Table 2.1 The Microhardness and Constitution of Boride Layers on Various Substrates Formed after Boronizing [4]

Substrate	Constituent phases in the boride layer	Microhardness of layer, HV or kg/mm^2
Fe	FeB Fe_2B	1900-2100 1800-2000
Co	CoB Co_2B	1850 1500-l600
Co-27.5 Cr	CoB Co_2B	2200 (100 g) ~l550 (100 g)
Ni	Ni_4B_3 Ni_2B Ni_3B	1600 1500 900
Inco 100	. . .	1700 (200 g)
Mo	Mo_2B Mo_2B_5	1660 2400-2700
W	W_2B WB W_2B_5	~2700 (overall hardness)
Ti	TiB TiB_2	2500 3370
Ti-6Al-4V	TiB TiB_2	3000 (100 g) (overall hardness)
Nb	Nb_2B_2 NbB_4	2600-3000 (overall hardness)
Ta	Ta_2B TaB_2	3200-3500 2500
Zr	ZrB_2 Zr_2B	2300-2600 (overall hardness)
Re	ReB	2700-2900

The following sections address the overview of boronizing processes that are applied to both ferrous and non-ferrous materials. Despite that, this dissertation will focus only on two-component boronizing processes of ferrous materials.

2.2.1 Boronizing of Ferrous Materials

The boride layer can be formed in either single phase or double phases on iron and steel, corresponding to a definite chemical composition from the Fe-B phase diagram, as illustrated in Appendix A. The single-phase boride layer consists of Fe_2B, while the double-phase boride layer consists of the exterior phase of FeB and the interior phase of Fe_2B. The morphology of the boride layer is a saw-tooth structure as depicted in Figure 2.1. The saw-tooth structure helps improving the mechanical adherence at the Fe_2B/substrate interfaces.

Figure 2.1 The saw-tooth structure of boride layers with the exterior phase of FeB and the interior phase of Fe_2B on AISI 1018.

During boronizing, Fe_2B phase is formed under high compressive stress, while FeB phase is formed under high tensile stress. At the end of boronizing when temperature is being reduced to an ambient temperature, if Fe_2B and FeB phases are formed in the boride layer, stresses from the two phases can lead to the crack formation at

the FeB/Fe_2B interface. Such crack formation can cause the spalling and, subsequently, the separation of the double-phase layer. To mitigate the crack formation, the annealing process can be applied at two different temperature ranges depending on two following objectives. Firstly, the annealing process applied at one temperature range can decrease the stresses between Fe_2B and FeB phases after boronizing [1]. That, in turn, reduces the crack formation. Secondly, the annealing process applied at the other temperature range can transform FeB phase into Fe_2B phase. That, in turn, decreases the occurrence of FeB phase and increases the occurrence of Fe_2B phase. Note that temperature ranges set in the annealing process are generally lower than those set in the boronizing process.

Even if the crack formation does not occur after boronizing, it can occur later to a boronized specimen especially under mechanical strain or thermal and mechanical shocks. Therefore, the annealing process is generally applied immediately following boronizing to reduce a chance that the crack formation may occur.

Besides the problem of crack formation, FeB phase is more brittle than Fe_2B phase; thus, the formation of Fe_2B phase is expectedly preferred than FeB phase. The annealing process may then be applied to decrease the occurrence of FeB phase. Furthermore, the occurrences of Fe_2B and FeB phases may be properly controlled by choosing appropriate temperature, time, and a chemical composition of powder mixtures. However, that is beyond the scope of the dissertation.

The characteristics of the Fe_2B phase include [3]:

- Composition with 8.83 wt. % boron
- Body-centered tetragonal crystal structure (a=5.078Å, c=4.249Å)
- Density of 7.43 g/cm^3

- Microhardness of about 18-20 GPa
- Young's modulus of 285-295 GPa
- Thermal expansion coefficient of 7.65×10^{-6} /°C in the range 200-600 °C, and 9.2×10^{-6} /°C in the range 100-800 °C

The characteristics of the FeB phase include [3]:

- Composition with 16.23 wt. % boron
- Orthorhombic crystal structure (a=4.053Å, b=5.495Å, c=2.946Å)
- Density of 6.75 g/cm^3
- Microhardness of about 19-21 GPa
- Young's modulus of 590 GPa
- Thermal expansion coefficient of 23×10^{-6} /°C in the range 200-600 °C

2.2.2 Boronizing of Nonferrous Materials

Refractory metals, titanium, nickel, cobalt and their alloys can be boronized by using special techniques such as gas and plasma boronizing, instead of conventional boronizing techniques. Since salt bath and conventional powder boronizing techniques are inapplicable for titanium and refractory metals because of the oxidation on the substrate and the corrosion from the activator that can cause the porosity in the boride layer [4]. Therefore, the heat treatment for refractory and titanium metals is operated under high vacuum and high purity argon atmosphere, or with gas (H_2-BCl_3) boronizing technique.

For the refractory metal and titanium, the process is prepared at the temperature above 1000 °C for approximately 10-15 hours [4]. The boride layer is formed with the thickness of about 50 μm, and has various high microhardness values as depicted in Table 2.1. However, the boride layers of tantalum, tungsten, niobium, molybdenum, and

nickel metal do not show the strong saw-tooth structure as seen in titanium and cobalt metals [3]. Furthermore, the saw-tooth structure in nonferrous materials is not manifest when compared to that in ferrous materials, e.g., low/medium carbon alloys.

2.3 Types of Boronizing Processes

The boronizing process consists of two stages:

1. The initial stage takes place between a boron medium and a component surface. Depending on boronizing temperature and time, the number of nuclei is formed at this stage and later the Fe_2B-phase boride layer is formed [3]. In case of ferrous materials as addressed in references [5] and [6], Fe_2B nuclei are first formed, which grow into a thin boride layer on the defect points of the metal surface. The defect points can be categorized into two types: macrodefects (e.g., surface roughness, scratches, etc.) and microdefects (e.g., grain boundaries, dislocation, etc.). If the active boron medium is excess, the boron-rich phase, such as FeB phase, will form and grow onto the Fe_2B phase.

2. The second stage is a diffusion-controlled process by which the thickness of boride layer is increased under a parabolic-time law:

$$x^2 = kt,$$

where x is the thickness of the boride layer; k as a constant corresponding to the temperature; and t as the boronizing time [4]. In case of ferrous materials, boron atoms are likely to diffuse in the [001]-crystallographic direction and form the body-centered tetragonal lattice of Fe_2B phase to achieve the maximum atomic density along this direction [5]-[6]. The growth of Fe_2B phase represents a columnar aggregation of crystals, which exhibits the saw-tooth morphology. For the double-phase boride layer,

the columnar growth of FeB phase likely follows into the [002]-crystallographic direction and the saw-tooth structure of FeB phase is underneath that of Fe_2B phase.

This dissertation will address several types of boronizing processes that are generally deployed and developed in commercial industries and academic institutions.

2.3.1 Pack Boronizing

The pack or solid state boronizing process is the most widely favored process due to its simplicity and cost-effectiveness. The process involves the embedding of the metals/alloys into the powder mixture that consists of three substance groups [4]:

- Boron source: Boron carbide (B_4C), ferroboron, and amorphous boron
- Activator: $NaBF_4$, KBF_4, $(NH_4)_3BF_4$, NH_4Cl, Na_2CO_3, BaF_2, and $Na_2B_4O_7$
- Diluent: SiC, Al_2O_3

The well-cleaned and smooth metals/alloys are packed with the boronizing powder mixture in the heat-resistant container sealed with a lid. The heat treatment is processed in the furnace by heating the furnace to the preset boronizing temperature and being preserved that temperature for a certain period of time. Boronizing temperature and time vary depending on the type of substrate. Thereafter, the temperature in the furnace is allowed cooling down to the ambient temperature, and the container is then removed from the furnace. To avoid the adverse effect of oxygen on boronizing, the boronizing process should be performed under the protective gas atmosphere, such as Ar, N_2, H_2, or a mixture of Ar-N_2-H_2. The protective gas atmosphere must be maintained immediately after boronizing until temperature is cooled down to 300 °C or equivalently 570 °F [1]. Using the above procedure, the powder mixture can be reused for about 5-6 times by blending in 20-50% with the new powder mixture [7].

2.3.2 Paste Boronizing

The paste boronizing process is a popular process to apply on the large substrate or a partial part of substrate because it is practically easy to select partial areas on the substrate material that is to be boronized. The boronizing paste consists of 55% B_4C, which has a grain size of 200-240μm, and 45% cryolite (Na_3AlF_6) [8], or the traditional boronizing powder mixture (B_4C-SiC-KBF_4) with the binder such as nitrocellulose/butyl acetate, methylcellulose, or hydrolyzed ethyl silicate [4]. The process applies the paste in several means such as dipping, brushing, or spraying until the paste has a thickness of about 1-2 mm, and the pasted material is heated under the protective gas atmosphere. After the treatment, the boronizing paste will be removed through blast cleaning, brushing or washing.

2.3.3 Liquid Boronizing

The liquid or salt bath boronizing process is performed by using the borax-based salt melts ($Na_2B_4O_7$) with or without electrolysis at temperatures above 900 °C [4]. The process is suitable for boronizing the complex body. The material specimen must resist to the thermal shock when being immersed and removed from the bath; otherwise, the deformation and cracking occurs. After the treatment, the excess melting salt must be removed from the material, but that incurs high labor cost and time-consuming. The maintenance cost is also high because the process requires the salt recharging for the appropriate viscosity to prolong the boronizing reaction. Another problem of the process is that the reaction creates the corrosive fume.

- Electroless liquid boronizing. The common salt bath is 30-70 % Borax-B_4C and the reaction is enhanced by replacing 20 % B_4C with ferroaluminium, which is an effective reductance. For the nickel alloy, the bath is composed of 74 wt. % KBF_4 -25 wt. % KF, operating at temperatures below 670 °C.

- Electrolytic liquid boronizing. The specimen material is attached to a cathode, while the graphite is acted as an anode. Both of them are immersed in the molten borax at 940 °C and the current ($0.15A/cm^2$) is passed to them. At the liquid state, Borax is decomposed to sodium ions (Na^+) and tetraborate ($B_4O_7^{2-}$). The reaction is as followed:

At anode; $B_4O_7^{2-} \rightarrow B_4O_7 + 2e^- \rightarrow 2B_2O_3 + O$

At Cathode; $6Na^+ + B_2O_3 \rightarrow 3Na_2O + 2B.$

2.3.4 Gas Boronizing

The gas boronizing process is a diffusion process of some gas media, such as diborane (B_2H_6) or boron chloride (BCl_3). This process is unpopular for the industry because these gas media are toxic and explosive. The BCl_3-H_2 gas mixture has previously been attempted to boronize steels, but a high concentration of BCl_3 caused the corrosion on the tested substrate and resulted the poor-adherence layers. To improve the process practicality, the diluted (1:15) BCl_3-H_2 gas mixture is commonly used at 700- 900 °C and under the pressure of about 67 kPa [9]. Moreover, the usage of a carrier-reductance gas of 75%N_2 and 25%H_2, rather than H_2, can reduce the BCl_3 concentration. As a result, it avoids $FeCl_3$ (corrosion) and diminishes the FeB formation. In addition, this process can be used with titanium and its alloys.

2.3.5 Plasma Boronizing

The plasma boronizing process is not yet available in the commercial industries because it encounters with the same problems as occurred in the gas boronizing process. The gas mixtures of B_2H_6–H_2 and BCl_3-H_2-Ar are commonly used in this process. Additionally, the usage of the BCl_3-H_2-Ar gas mixture enables a better control of an amount of BCl_3 concentration. That can reduce the discharged voltage and increase the microhardness of the boride layer [10]. Despite the porosity of the double-phase boride layer is observed, an increase the BCl_3 concentration can minimize it. The process is widely applied to the refractory metals because it yields the high-efficient deposition of the boride layer, which is higher than the deposition occurred by using the pack boronizing process. The process operates at the low temperature of approximately 600 °C (equivalently 1100 °F) and prolongs in a short period of time such that energy and gas consumptions are decreased. The conventional pack boronizing process, however, cannot operate at such low temperature.

2.3.6 Fluidized Bed Boronizing

The fluidized bed boronizing process is a recent innovation of boronizing technology. The bed materials, coarse-grained silicon carbide, and boronizing powder mixture, are served as a faster heat-transferring medium through which oxygen-free gases (N_2-H_2) flow. The high heating rate and high flowing rate make the boronizing process rapid, thereby shortening the boronizing time. Because of the temperature uniformity, the process can also produce the reproducibility, good tolerances, and uniform finishing mass-products. The process achieves the low operating cost for the mass production of boronized products. However, the major disadvantage is that the exhaust gases (e.g.,

fluorine compounds) must be completely eliminated by using the $CaCO_3$ absorber to avoid the environmental problems.

2.3.7 Multi-Component Boronizing

The multi-component boronizing process combines the diffusion of boron and one or more metallic element(s), including aluminum, chromium, vanadium, and silicon, into the substrate surface. Some multi-component boronizing systems are illustrated in Table 2.2. The multi-component boronizing can be classified into three types [4]:

- Type 1: simultaneous boronizing and metallizing
- Type 2: boronizing followed by metallizing
- Type 3: metallizing followed by boronizing

Table 2.2 The Multi-Component Boronizing [4]

Multi-component *boronizing* technique	Media type	Media composition, wt%	Process steps investigated*	Substrate(s) treated	Temperature, °C (°F)
Boroaluminizing	Electrolytic salt bath	3-20% Al_2O_3 in borax	S	Plain carbon steels	900 (1650)
Boroaluminizing	Pack	(A) 84% B_4C + 16%borax (B) 97%ferroaluminium + 3% NH_4Cl	S B-Al Al-B	Plain carbon steels	1050 (1920)
Borochromizing	Pack	(A) 5% B_4C + 5%KBF_4 + 90% SiC (Ekabor II) (B) 78% ferrochrome + 20% Al_2O_3 + 2% NH_4Cl	S B-Cr Cr-B	Plain carbon steels	Borided at 900 (1650) Chromized at 1000 (1830)
Borosiliconizing	Pack	(A) 5% B_4C + 5% KBF_4 + 90% SiC (Ekabor II) (B) 100% Si	B-Si Si-B	0.4% C steel	900-1000 (1650-1830)
Borovanadizing	Pack	(A) 5% B_4C + 5% KBF_4 + 90% SIC (Ekabor II) (B) 60% ferrovanadium + 37% Al_2O_3 + 3% NH_4Cl	B-V	1.0% C steel	Borided at 900 (1650) Vanadized at 1000 (1830)

* S = simultaneous boronizing and metallizing,
B-Al = boronized and then aluminized, Al-B= aluminized and then boronized.

The result shows the improvement of mechanical properties and oxidation resistance, as addressed in the followings:

- Boroaluminizing—the compact layer provides good wear and corrosion resistances, especially in humid environments.
- Borosiliconizing—the FeSi is formed on the boride-layer surface that increases the corrosion-fatigue strength of components.
- Borochromizing—this treatment provides the better oxidation resistance than boroaluminizing, forms the uniform layer, improves the wear resistance, and increases the corrosion-fatigue strength.
- Borovanadized and borochromvanadized—the layer will have ductility with a high microhardness of more than 3000 HV for a 15-grams load, which helps reducing the spalling under the impact loading condition.

2.4 Characteristics and Properties of Boride Layer

The prominent saw-tooth structure of the boride layer is well observed in pure iron, unalloyed low-carbon steel, and low alloy steels. When the alloying elements and/or carbon contents in the substrate steel are increased, the thickness of the boride layer is decreased. In addition, the smooth interface can also be observed instead of the saw-tooth structure, as illustrated in Figures 2.2 and 2.3. Alloying elements, except nickel, cobalt, and manganese, which delay the boron diffusion into the substrate, can increase the proportion of FeB constitution [4]. For example, in boronized stainless steel, alloying elements causes the thin smooth interface of almost 100% FeB phase of the boride layer.

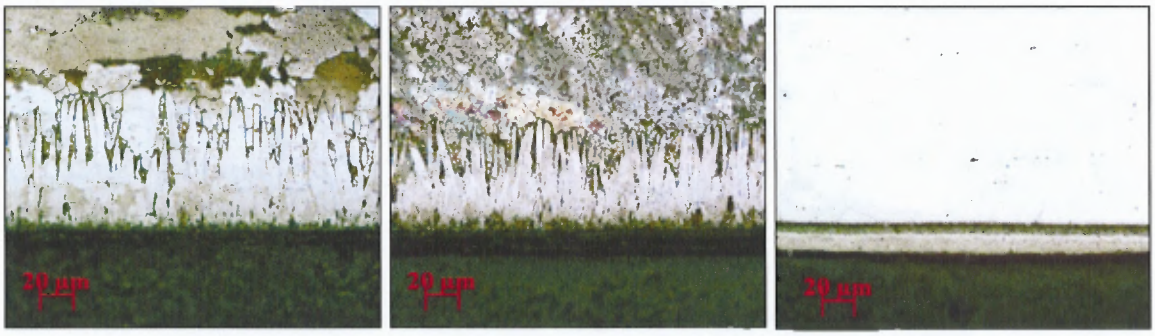

Figure 2.2 The effect of steel composition on the morphology and thickness of the boride layer.

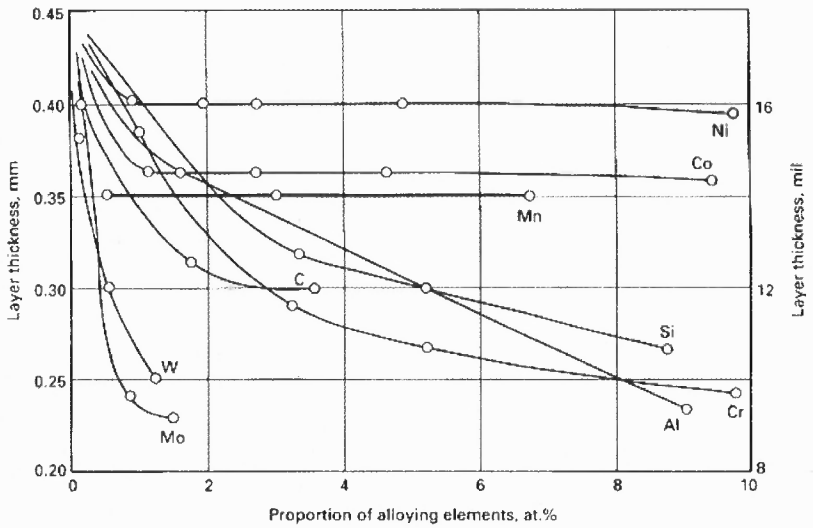

Figure 2.3 The effect of percent alloying elements on the boride layer thickness [7].

2.4.1 Effects of Alloying Elements in Boronizing Processes

Carbon, Silicon, and Aluminum is insoluble in the boride layer. During boronizing, the boride layer expels carbon and silicon from the surface into the substrate matrix, and forms the precipitation of iron silicoboride ($FeSi_{0.4}B_{0.6}$ or $FeSiB_2$) and iron carboboride ($Fe_{23}(B,C)_6$ and $Fe_3(B,C)$ beneath and/or between the boride saw-teeth structure. The contents of silicon and aluminum (larger than 0.8%) underneath the boride layer can form a soft ferrite phase, which has a low load-carrying capacity [11]. Under the high surface pressure, the failure can occur due to the hard boride layer penetrating into this soft ferrite region.

Nickel will restrict the solubility of boron atoms in iron because it diffuses into the boride layer and precipitates Ni_3B from the boride layer at the Fe_2B/substrate interface. The results are the reduction of boride-layer thickness and the saw-tooth structure. Although nickel may slightly reduce the microhardness value of the boride layer, nickel helps impeding the formation of FeB [11].

Chromium can modify the structure and the properties of boride layer. The solubility of chromium in the Fe_2B phase causes the replacement from iron to chromium and forms (Fe, Cr)B and $(Fe, Cr)_2B$ on the surface. The incorporation of chromium may increase the microhardness of boride layer but it also causes boron to diffuse along the grain boundaries. The diffusion leads to the decreasing of thickness of boride layer and the increasing of the smooth boride layer/substrate interface [11]. Chromium also promotes the formation of boron-rich phase, such as FeB phase, onto the boride layer.

Manganese, Tungsten, Molybdenum, and vanadium are typically used to reduce the boride thickness and to flatten out the saw-tooth morphology.

2.4.2 Characteristics and Properties of Boride Layer on Various Metals and Alloys

The characteristics and properties of both boronized ferrous and nonferrous metals and alloys are widely interested topics due to a need to increase the value of metals and alloys in terms of wear performance, corrosion and high temperature properties.

99.97 wt. % pure iron was investigated by Ozdemir *et al.* [12] and Asthana *et al.* [13]. The Fe_2B phase was formed with the hardness of 1700 HV and the fracture toughness of about 3 - 4 MPa $m^{1/2}$. The preferred crystallographic orientation was in the (002) direction.

The boronizing of AISI 1020 and AISI 5115 were investigated and compared to carburizing [14] and carbonitriding [15]. Friction coefficients obtained under the same conditions was at 0.45 - 0.62 for carburized, 0.36 - 0.57 for carbonitrided and 0.36 - 0.62 for boronized AISI 1020 steels, and 0.35 - 0.70 for carburized, 0.32 - 0.54 for carbonitrided and 0.12 - 0.24 for boronized AISI 5115. As well, the kinetics and fracture toughness of AISI 1040 and P20 were investigated. Fe_2B and FeB phases were formed

when boronizing AISI 1040, and the activation energy was 168 kJ/mol and the fracture toughness was 3.2 - 5.1 MPa $m^{1/2}$. Fe_2B, FeB, MnB and CrB phases were formed when boronizing AISI 5115, and the activation energy was 200 kJ/mol and the fracture toughness was 2.79 - 4.79 MPa $m^{1/2}$ [16].

Soydan *et al.* [17]-[18] investigated the slide friction and wear behaviors of AISI 1050, AISI 4140 and AISI 8620, which found that the wear rate (at 30N load) of AISI 1050 was 1.6×10^{-5} mm^3/Nm, 1.8×10^{-5} mm^3/Nm for AISI 4140, and 2×10^{-5} mm^3/Nm for AISI 8620. In addition, the friction coefficients of AISI 1050 and AISI 4140 were similarly 0.34 and about 0.35 for AISI 8642. Moreover, the activation energy of boronized AISI 4140 was observed at about 215 kJ/mol, and Fe_2B, FeB and CrB layers were formed.

Grey iron, cast iron and compacted graphite iron were investigated by Sahin *et al.* [19] and Meric *et al.* [20]. The coating thickness, hardness and abrasive wear were compared. Sen *et al.* [21] studied the boronized ductile iron and found that the coating composed of the boride layers of FeB and Fe_2B, and Si-rich ferrite and globular graphite appeared at the coating interface. The coating had the following properties: 114 – 185 μm in thickness, 1160 - 2140 HV in hardness and 2.19 - 4.47 MPa $m^{1/2}$ in fracture toughness [21]. In addition, when the concentration of copper increased, only Fe_2B was observed, the thickness was shorter and graphite did not appear at the coating interface [22]. Campos-Silva *et al.* [23] determined the kinetics of grey cast iron class 30 and found the activation energy at 175 kJ/mol. Cr12Mn2V2 high chromium cast iron was investigated and found the following properties: Fe_2B, FeB and CrB were formed; the thickness was 8

- 33 μm; the fracture toughness was 2.85 - 4.18 MPa $m^{1/2}$; and the relative wear resistance was 1.58 - 13.70 [24].

AISI W1 and W4 (water-hardening tool steel) were investigated by Genel *et al.* [25] and Ozbek *et al.* [26]. The coating layer composed of FeB and Fe_2B with the following properties: for AISI W1, the hardness of 1690 - 1800 HV and the activation energy of 171.2 ±16.6 kJ/mol; and for AISI W4, the hardness of 1407 - 2093 HV and the fracture toughness of 1.39 - 6.40 MPa $m^{1/2}$.

AISI H13 (hot work steel) was investigated and found that the FeB and Fe_2B phase composition on the coating with the following properties: the hardness in the range of 1650 - 2000 HV, the activation energy of about 186.2 kJ/mol for the boronizing process [27], the fracture toughness of about 3 - 4.5 MPa $m^{1/2}$ depending on the boronizng temperature and time [28]. The corrosion behaviors of boronized AISI H13 on the specific acid solutions (5 vol. % HCl, 5 vol. % H_2SO_4, 30 vol. % H_3PO_4) were later studied by Kariofillis *et al.* [29]. However, boronized AISI H13 was damaged from the increasing of expansion coefficient of the coating layer under the thermal fatigue testing [30].

Boronized AISI 304 was examined and found the smooth coating layers of FeB, Fe_2B, CrB and Ni_3B with the following properties: the hardness of 2150 HV and the activation energy of about 253.35 kJ/mol for the boronizing process [28]. In addition, boronized AISI 316 consisted of Fe_2B, CrB, and Ni_2B with the hardness of 1700 HV and the activation energy of 199 kJ/mol [31].

Brandstöter and Lengauer [32] studied the multiphase diffusion reactions between boron and transition metals of pure Titanium (Ti), Tantalum (Ta), and Molybdenum (Mo)

in the process of powder pack boronzing. The results showed that, at the heat treatment between 1200 - 1500°C for 4 hours, TiB_2 and TiB were formed on Ti-substrate on which TiB_2 was at the outer layer with the thickness of about 8 μm and TiB was at the inner layer with the thickness of about 20 μm; TaB_2 was the only phase to be formed on Ta-substrate, and MoB and Mo_2B were formed on Mo-substrate on which MoB was at the outer layer with the thickness of about 450 μm and Mo_2B was at the inner layer with the thickness of about 10 μm.

Yu, *et al.* observed the boronizing of tungsten [33] and molybdenum [34] by using the Spark Plasma Sintering (SPS) technology. They found the WB layer was formed on W-substrate with the thickness in the range of 35 - 112 μm at the preferred orientation in the (200) direction. In addition, the layer of MoB was formed on Mo-substrate with the thickness of 6 - 155 μm at the preferred orientation in the (002) direction.

Usta *et al.* studied the characteristics of niobium [35] and tungsten [36] using the pack cementation of Ekabor powders at 940°C for 2, 4, and 8 hours. The WB layer with the hardness of 2500 HV was formed on W-substrate, while the NbB_2 layer with the hardness of 2500 HV was formed on Nb-substrate.

Ingole *et al.* [37] studied the wear resistance of borided tungsten and reported that the friction value of the WB coating on W substrate was 0.75 comparing to 0.18 of the tungsten substrate itself.

Ribeiro *et al.* studied the boride coatings on niobium [38] and tantalum [39] substrates under dry- and wet-simulated body fluid conditions for biojoint applications.

The results showed the boride coatings were able to reduce the coefficient of friction but cracks could still occur under the wet condition.

The tribological comparison between pure chromium and boronized chromium was studied. Tested under three different conditions: dry sliding, with water, and with simulated body fluid SBF, the friction coefficients of pure Cr were measured at 0.19, 0.02 - 0.12, and 0.02, respectively, while these coefficients of boronized Cr were measured at 0.15 - 0.21, 0.06 - 0.09, and 0.035, respectively [40].

Ueda *et al.* [41] boronized 99.9% pure nickel by using the powder-pack method, and studied the properties at high temperatures. They chose the Ekabor Ni powder in boronizing, but noted that SiC was not contained in the powder components. The results showed that only the Ni_2B boride layer was formed and the high temperature hardness, friction coefficient and wear of borided Ni were higher than those of untreated Ni.

Özbeka *et al.* [42] boronized 99.5 % pure Ni by using the Ekabor powder. They found the exterior silicide layer of Ni_5Si_2 with the thickness of 280 μm and the interior layer of Ni_2B with the thickness of about 10 μm. However, Mu *et al.* [43] used the powder pack method with a powder mixture of 8% B_4C, 4% KBF_4 and 88% SiC, and they found silicide layers of Ni_5Si_2 and Ni_2Si instead of boride layers.

Anthymidis *et al.* [44] observed the boronizing of nickel in a fluidized bed reactor and found only Ni_3B layer on Ni substrate.

Lou *et al.* [45] studied the boronizing of pure nickel and Nimonic 90 superalloy by using paste boronizing. They found $Ni_2(B,Si)$, Ni_2B and Ni_3B layers on pure nickel with the hardness in a range of 100 - 1100 HV and (Cr, Ni, Co)B and $(Ni, Co)_2B$ layers on Nimonic 90 with the hardness in a range of 400 - 2500 HV.

Torun [46] studied the boronized nickel aluminide (Ni_3Al) using the Ekabor Ni powder. They found Ni_3B_4 and Ni_3B coating layers with the thickness of about 12 -70 μm and the activation energy of 188.8 ± 14.4 kJ/mol.

Pure titanium and Ti-6Al-4V alloy was produced by Pulsed-DC plasma boriding in an Ar - BCl_3 atmosphere at the temperature range of 700 to 900° C. TiB_2 was formed on the outer layer and TiB on the inner layer with the thickness of 4 - 10 μm and the hardness of 2800 HV [47]. Ti-6Al-4V alloy was also boronized by using the fluidized bed method at 1000 °C for 3 hours and the TiB_2 and TiB coating layers were formed with the thickness of 3 μm [48]. Laser Dispersion was another method for boronizing Ti-6Al-4V alloy that gave the coating layer with the thickness of 200 - 1000 μm and increased the hardness from 350 HV to 600 HV [49].

Pure titanium was performed by using dry B_4C powder at 1000°C for 20 hours and the compounds of TiC, TiB and TiB_2 was observed with the thickness of about 400 μm and the hardness of about 820 HV [50].

The electrochemical method was used to boronize Ti-alloy at a room temperature. An amorphous layer was formed and then tempered at 500°C in order to form subsequently the composition of TiB and TiB_2 layers [51].

The boronized Ti-6Al-4V was used to study the performance of wear under two conditions: dry and smear lubricated sliding. The results showed the excellent wear rate and the lower friction coefficient compared to untreated Ti-6Al-4V [52]. Furthermore, the tribological performance of the boronized Ti-6Al-4V balls was studied. The results showed that that the wear rate of boronized Ti-6Al-4V balls were forty times less than that of 97% dense alumina balls [53].

2.4.3 Properties of Boronized Steels

After boronizing, steels will have the desirable properties on the surface, including the increase of wear resistance, corrosion resistance, and enhance the service life in 3-10 times.

1. Toughness

The boride layer provides the good bonding with the base metal, which can ensure that under load, the flaking or the peeling will not happen. However, the toughness of the boronized steel relies on its boride layer thickness, cross-section area, and mechanical properties. In the bending test, the boronized specimen with the boride-layer thickness of 150-200 μm has 4% elongation without cracking [1].

2. Adhesion Resistance

The boronized surfaces show neither accretion nor wear of material as well as having hardly any tendency to cold-weld [11]. Consequently, this property is used in the cold-metal working (chipless shaping) as a tool to form the metals. Without the non-lubricant, the boronized layers do not have an appreciable change at 300 °C in order to protect the environment by reducing the lubricant.

3. Abrasive Wear Resistance

High microhardness provides a high wear resistance. Some properties of boronized steels are depicted in Figures 2.4 and 2.5.

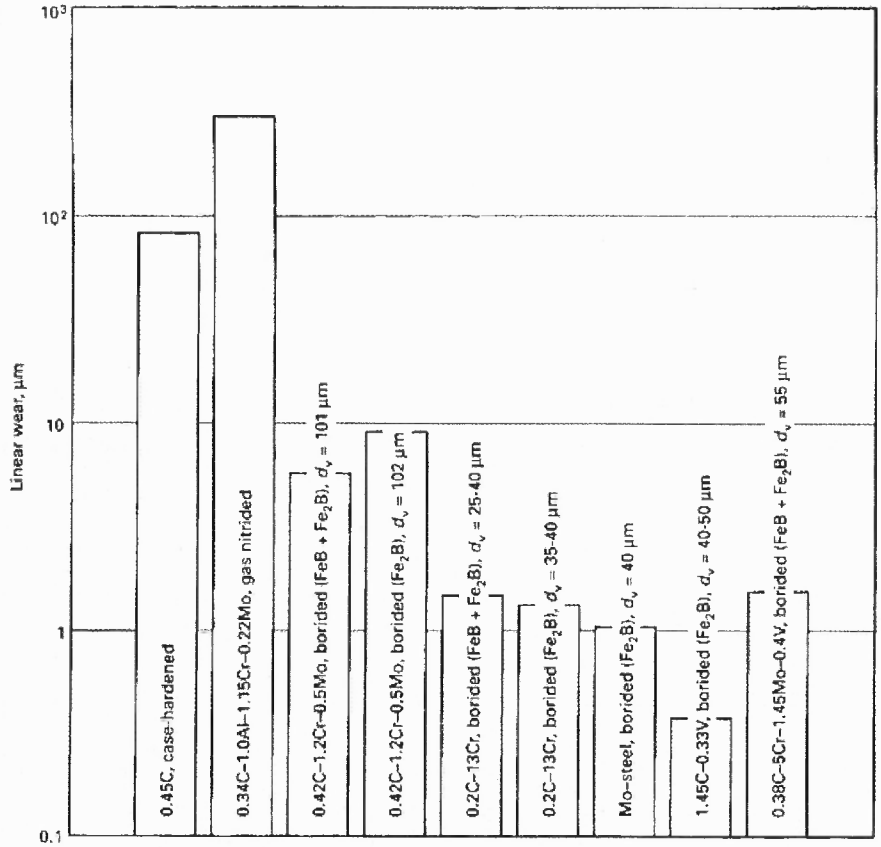

Figure 2.4 The effect of steel compositions (nominal values in wt. %) on wear resistance under abrasive wear (d_v = thickness of the boride layer);
test conditions: DP-U grinding tester, SiC paper 220, testing time 6 minutes [7].

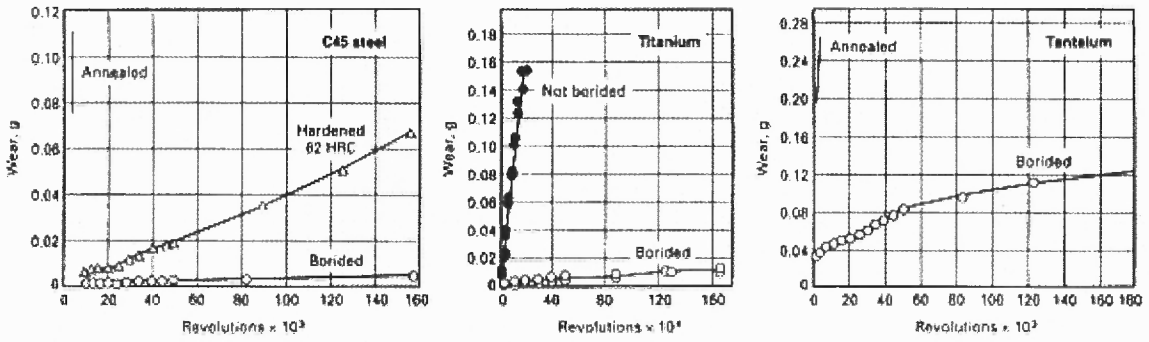

Figure 2.5 The comparison of wear resistance between boronized steels and non-boronized steel [7].

4. Corrosion Resistance in Acids

Boronized carbon and alloy steel have increased the corrosion resistance in HCl, H_2SO_4, and H_3PO_4. Boronizing austenitic stainless steel improves the corrosion resistance in HCl as depicted in Figure 2.6.

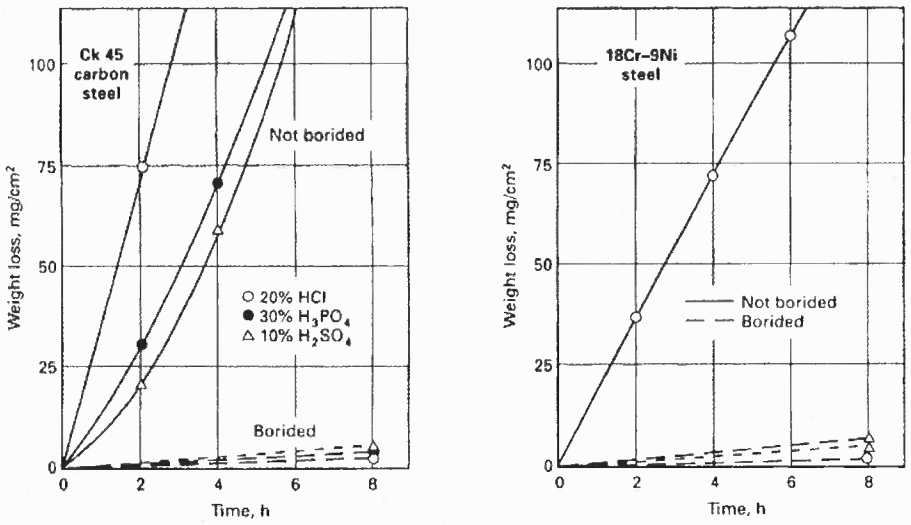

Figure 2.6 The comparison of corrosion resistance between boronized steels and non-boronized steels [7].

2.5 Advantages and Disadvantages of Boronizing

The advantages of boronizing include the followings:

- In cases of boronized steels, the boronizing process provides extremely high hardness to steels, compared to other thermo-chemical treatments that are applied onto any other hard materials, as depicted in Table 2.3 and Figure 2.7.
- The combination of high surface hardness and low surface coefficient of friction in boronized steels provides outstanding wear properties in terms of adhesion, tribooxidation, abrasion, and surface fatigue.

- The surface hardness of boronized steels can still retain at high temperatures.
- The process can be applied to a variety of metals and alloys.
- Boronized surfaces of ferrous materials have high corrosion-erosion resistance in dilute acid and alkali media and are widely deployed in various industrial applications.
- Boronized surfaces have moderate oxidation resistance at up to 850 °C, equivalently 1550 °F.
- Boronized surfaces provide corrosion resistance in applications with molten metals.
- The boronized steels can prolong the fatigue life and enhance the service performance under normal usages and in oxidative or corrosive environments.

The disadvantages of boronizing include the followings:

- The process is inflexible and labor-intensive. Therefore, the process is less cost-effective than other thermo-chemical treatments.
- The boride thickness cannot be well controlled because the thickness growth depends on the substrate composition and the consistency of boronized powder composition.
- Boronizing generally causes the rough surface of the boride layer. In some applications, the roughness of the boride layer may fail the tolerance requirements. To satisfy the tolerance requirements, the removal of a part of boride layer is required. It can be practically performed by using the diamond

lapping, which is expensive. Note that the conventional grinding cannot be utilized because it can cause the fracture of the layer.

Table 2.3 The Surface Hardness of Boronized Steels Compares to Other Treatments and Hard Materials [7]

Material	**Microhardness kg/mm^2 or HV**
Boride mild steel	1600
Borided AISI H13 die steel	1800
Borided AISI A2 steel	1900
Quenched steel	900
Hardened and tempered H13 die steel	540-600
Hardened and tempered A2 die steel	630-700
High-speed steel BM42	900-910
Nitrided steels	650-1700
Carburized low-alloy steels	650-950
Hard chromium plating	1000-1200
Cemented carbides, WC + Co	1160-1820 (30 kg)
$Al_2O_3 + ZrO_2$ ceramic	1483(30 kg)
$Al_2O_3 + TiC + ZrO_2$ ceramic	1738 (30 kg)
Sialon ceramic	1569 (30 kg)
TiN	2000
TiC	3500
SiC	4000
B_4C	5000
Diamond	>10,000

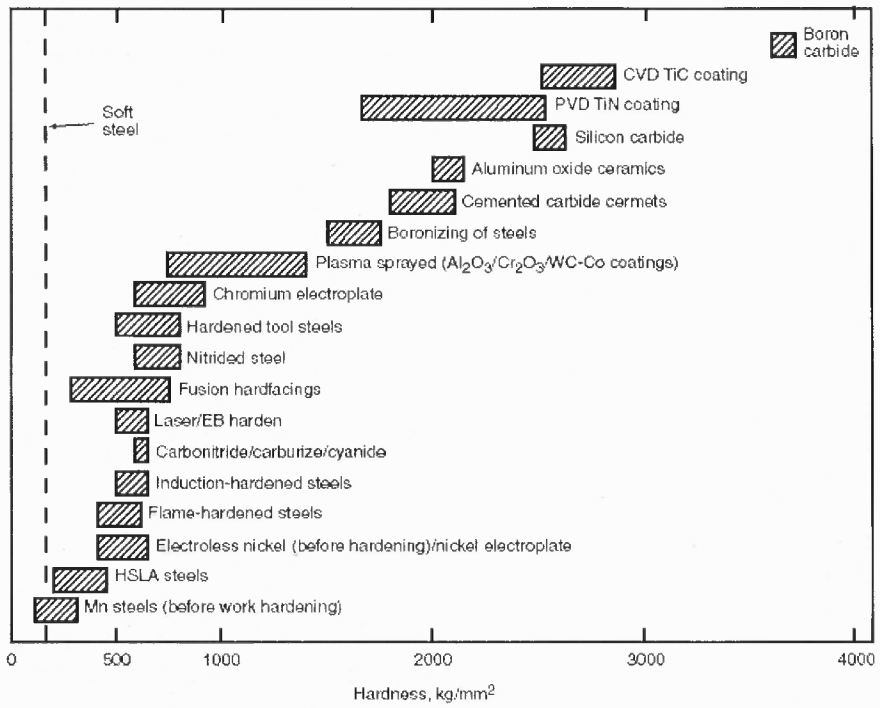

Figure 2.7 The hardness value for various materials and surface treatments [54].

2.6 Applications of Boronized Products

The conclusive boronized parts have been widely used in a variety of industrial applications as depicted in Table 2.4.

Table 2.4 The Applications of Boronized Ferrous Materials [7]

Substrate material			Application
AISI	BSI	DIN	
		St37	Bushes, bolts, nozzles, conveyer tubes, base plates, runners, blades, thread guides
1020	...	C15 (Ck15)	Gear drives, pump shafts
1043	...	C45	Pins, guide rings, grinding disks, bolts
		St50-1	Casting inserts, nozzles, handles
1138	...	45S20	Shaft protection sleeves, mandrels
1042	...	Ck45	Swirl elements, nozzles (for oil bumpers), rollers, bolts, gate plates
		C45W3	Gate plates
W1	...	C60W3	Clamping chucks, guide bars
D3	...	X210Cr12	Bushes, press tools, plates, mandrels, punches, dies
C2	...	115CrV3	Drawing dies, ejectors, guides, insert pins
		40CrMnMo7	Gate plates. bending dies
H11	BH11	X38CrMoV51	Plungers, injection cylinders, spruce
H13	...	X40CrMoV51	Orifices, ingot molds. upper and lower dies and matrices for hot forming, disks
H10	...	X32CrMoV33	Injection molding dies, fillers, upper and lower dies and matrices for hot forming
D2	...	X155CrVMo121	Threaded rollers, shaping and pressing rollers, pressing dies and matrices
		105WCr6	Engraving rollers
D6	...	X210CrW12	Straightening rollers
S1	~BS1	60WCrV7	Press and drawing matrices, mandrels, liners, dies, necking rings
D2		X165CrVMo12	Drawing dies, rollers for cold mills
L6	BS224	56NiCrMoV7	Extrusion dies, bolts, casting inserts, forging dies, drop forges
		X45NiCrMo4	Embossing dies, pressure pad and dies
02	~BO2	90MnCrV8	Molds, bending dies, press tools, engraving rollers, bushes, drawing dies, guide bars, disks, piercing punches
E52100	...	100Cr6	Balls, rollers, guide bars, guides
		Ni36	Parts for nonferrous metal casting equipment
		X50CrMnNiV229	Parts for unmagnetizable tools (heat treatable)
4140	708A42 (En19C)	42CrMo4	Press tools and dies, extruder screws, rollers, extruder barrels, non-return valves
4150	~708A42 (CDS-l5)	50CrMo4	Nozzle base plates
4317	...	17CrNiMo6	Bevel gears, screw and wheel gears, shafts, chain components
5115	...	16MnCr5	Helical gear wheels, guide bars, guiding columns
6152	...	50CrV4	Thrust plates, clamping devices, valve springs, spring contacts
302	302S25 (EN58A)	XI2CrNi188	Screw cases, bushes
316	~316S16 (EN58J)	X5CrNiMo1810	Perforated or slotted hole screens, parts for the textile and rubber industries
		G-X10CrNiMo189	Valve plugs, parts for the textile and chemical industries
410	410S21 (En56A)	X10Cr13	Valve components, fittings
420	~420S45 (EN56D)	X40Cr13	Valve components, plunger rods, fittings, guides, parts for chemical plants
		X35CrMo17	Shafts, spindles, valves
Gray and ductile cast iron			Parts for textile machinery, mandrels, molds, sleeves

2.7 Research and Development on Boronizing Processes

There are many previous researches that develop new surface treatments using boron, apply new techniques to existing boronizing processes, and determine new chemical compositions and boronizing conditions (e.g., temperature and time). This subsection provides literature reviews on some outstanding researches and developments on boronizing processes.

2.7.1 Research and Development on Advanced Boronizing Processes

Pack and paste boronizing processes are mainly deployed by commercial industries because they are simple, safe, and cost effective. However, the processes are limited to only small-size products. In addition, they require a high labor cost in packing or pasting powder with metal samples during preparation process and in removing powder off samples after boronizing process.

Gas boronizing provides a better control of boron potentials in the chemical composition of the substrate and the depth of the boride layer. In addition, it is applicable for large-size products, reduces the labor cost of packing and cleaning the powder, and operates at low temperature. However, this process is barely deployed in commercial industries because it uses some highly toxic and explosive gases in the process, including diborane (B_2H_6), boron chloride (BCl_3), and boron trifluoride (BF_3). Thus, many researchers have been developing new boronizing processes or improving existing processes that can be economically and safely deployed by industries.

Pierson *et al.* [55] determined the formation of boron-coatings from the dissociation of borane at low temperature by using chemical vapor deposition (CVD) technique.

Unlike gas boronizing, the new process reduces a concentration of toxic and explosive boron-source gas, lowers boronizing temperature, and shortens boronizing time.

Wierzchoń *et al.* [56] introduced the glow-discharge plasma boronizing of 10 vol. % BCl_3 - H_2 by processing at 4-13 kPa and 1053 - 1123 °K for less than 6 hours, which produces the boride layer with a thickness of 200 μm and a microhardness of 2500 HV.

Dearnley *et al.* [57] reported that plasma boronizing with a gas mixture of BCl_3-H_2 - Ar requires a small quantity of BCl_3 below 0.5 vol. % to form the boride layer. However, the porosity was also observed on the coating layer.

Filep *et al.* [58] studied the kinetics of boron diffusion under a glow discharge in the BCl_3 - H_2 mixture and reported that the glow-discharge plasma boronizing was more efficient than chemical vapor deposition and other thermochemical processes.

Hunger *et al.* [59] found that plasma-assisted gas boronizing using boron trifluoride (BF_3) gave the same boride layer quality and less acute corrosion than using boron trichloride (BCl_3).

Industrial equipments such as automotive oil pump gears was successfully coated by using the pulsed DC glow-discharge plasma boronizing process with the gas mixture of BCl_3 - H_2 - Ar [60].

Instead of toxic borane and boron halide gases, some harmless boron-source precursors such as trimethyl borate $B(OCH_3)_3$, triethyl borane $B(C_2H_5)_3$, and borane triethyl amine BH_3-$N(C_2H_5)_3$ weretested in plasma and gas boronizing processes [61].

The two-step temperature in the glow-discharge plasma boronizing process was reportedly succeeded in eliminating the occurrence of porosities on boride layers [62].

During the development of plasma boronizing with gas precursors, plasma technique were also applied to solid, paste, and liquid boronizing processes. Lyakhovich *et al.* [63] studied paste boronizing in a glow discharge of H_2, and denoted that the formation thickness of boride layers was 2 - 3 times higher than the process without the glow discharge.

Yoon *et al.* [64] reported that the formation of boride layers occurred in a shorter time in the process of plasma paste boronizing on AISI 304 with a gas mixture of Ar/H_2.

Plasma electrolysis boronizing was used to boronize different steels in borax aqueous solution for 15 minutes, forming the boride layer with a thickness of 1 - 5 mm. [65].

Spark plasma sintering (SPS) technique uses a high current discharge to activate the powder pack boronizing media (SiC-B_4C) and to accelerate the diffusion of boron atoms into a substrate, which reduces boronizing temperature and time [66].

Besides plasma-assisted CVD process, some physical vapor depositions (PVD) techniques were also used. Ion implantation boronizing was done by implanting boron ions into iron at 600 °C and steel at 700 °C for 15min, and boron was found to diffuse about 0.5 – 0.8 μm under the ballistic implantation depth, which is 0.05 μm [67]. Moreover, Yan *et al.* [68] used ion implantation technique as a post boronizing treatment

method to mitigate the problem of embrittlement in boride layers. Sputtering deposition is another PVC technique used to form boride coating on glass and steel substrates. The hard compound targets (e.g., FeB [69], CrB_2 [70], ZrB_2 [71]) were used and deposited at low temperatures. The deposited thin films had the thickness at a range of 1 - 6 μm with a preferred crystal orientation.

Plasma transfer arc (PTA) welding process was developed to form boride coating on AISI 1018. The steel specimen was covered with B_4C powder paste and then scanned with the transferred arc plasma beam. The process provided the hypoeutectic and hypereutectic compositions of Fe_2B and the eutectic components of α-Fe and Fe_2B, which was about 1 - 1.5 mm in thickness and 400 - 1600 HV in hardness [72].

Similar to PTA, direct diode laser boronizing was used to form thermal-diffusion boron coating on carbon steel (S56C) by scanning the laser light on a paved substrate with powder mixture of B_2O_3 – FeB [73]. The method provided the coating thickness up to 200 - 300 μm.

Laser induced surface improvement (LISI™) process was used to form molybdenum and chromium coatings on AISI 4130 steel by using CrB_2 and MoB_2 as precursors [74]. The deposited coatings were composed of the eutectic component of Cr-CrB_2 and the eutectic component of Mo-MoB_2 above the Cr layer.

Anthymidis *et al.* [75] studied boride coatings obtained from pack cementation and fluidized bed methods. The results showed that the pack cementation method gave the boride coating with residual stress and a preferred orientation, while the fluidized bed method provided the boride coating with no residual stress and random orientations.

Tsipas *et al.* [76] utilized the fluidized bed method to deposit hard boride coatings on steels, as well as titanium alloys and multi-component coatings of Cr, Al, Hf and Y on steel alloys. Balandin utilized the fluidized bed method to form simultaneously boronitriding [77], borocoppering and borochromizing [78] on die steels.

Vacuum plasma spray (VPS) technique was able to produce thick boride coatings in a short period of time and at lower substrate temperature by feeding the target compounds (e.g., FeB and Fe_2B) and spraying to the substrate, which provided coating of at thick about 200 μm [79].

2.7.2 Research and Development on Multi-component Boronizing Processes

In boronizing processes, boron atoms diffuse into a substrate and boride layers are formed on the substrate. The boride layers and the substrate may have different properties that cause some problems such as the problem of large microhardness gradient between a substrate and boride layers. Furthermore, new problems may be inherently caused by the coating boride layers such as the problem of the brittleness on boride layers. These problems can cause the weak adhesion, deterioration, or even cracks to boronized specimens under circumstances such as a compressive load and a high thermal shock.

The multi-component boronizing process has been initially developed to resolve these problems by using boron and other metal elements. During the multi-component boronizing process, boron and other transition metals or refractory metals diffuse into a substrate such that boronized specimens have increased high temperature oxidation and corrosion properties. Note that the names of multi-component boronizing processes and corresponding coating layers are dependent to metal elements used in the processes. For

instances, the multi-component boronizing process of boron and carbon is called borocarbonizing, and that of boron, carbon, and nitrogen is called borocarbonitriding.

Kulka *et al.* studied the multi-component coatings of boron (B) and carbon (C) on Armco iron [80], low carbon steel (AISI 5120) [81], medium carbon steel (AISI 5140) [82]. They had also studied boronizing chromium and nickel-based low carbon steel by using boron and carbon [83], and by using boron, carbon, and nitrogen [84]. Using boron and carbon, these experiments were first performed carburizing at 930 °C and then gas boronizing at 950 °C to form the borocarburized layers. On the other hand, using boron, carbon, and nitrogen, the borocarbonitriding was performed in which the carbonitriding was performed at 840 °C, followed by boronizing at 950 °C. From these experiments, carbon atoms (from carbon-based substrate and carburizing process) decreased the layer thickness, and the microhardness gradient between the substrate and iron boride layers. Moreover, multi-component boronizing processes were able to decrease the brittleness of iron boride which led to the increase of wear resistance. For Armco iron, the carbon content changed the crystallographic orientation of iron boride which caused to the lower texture and lower porosity of borided layer [80]. In addition, the microhardnesses of borocarbonitriding, boronizing, borocarburizing, carburizing, and carbonitriding were 1850, 1800, 1500, and 950 HV, respectively. The wear resistances were ranked in an increasing order of the following processes: boronizing (highest), carburizing, carbonitriding, borocarburizing, and borocarbonitriding (lowest).

Buijnsters *et al.* [85] investigated the deposition of diamond film on boronized AISI 316 and H11 steels. The pack boronizing process was performed at 950 °C to form the FeB layer on the substrate. Then, the CVD process was performed at the temperature range of 520 to 650 °C to form the diamond film on top of the FeB-coated substrate. The results showed that high thermal expansion coefficient of FeB layer caused the reduction of adhesion at the interfaces of three layers under high thermal stress.

Boronitriding of US 37-1 steel was studied by performing two stage processes of pack boronizing and gas nitriding [86]. The Fe_2B layer was first formed as the inner layer on the substrate, followed by the second layer of Fe_4N and $B_{25}N$, and the final outer layer of Fe_4N.

The simultaneous process for B-C-nitriding in a two-temperature stage was studied by Yan and Su [87]. The process was treated by powder pack method, which composed of a mixture of boron carbide, activated charcoal, carbamide, iron potassium cyanide, potassium boron fluorite, and silicon carbide at 570 °C for 5 hours to induce carbon-nitriding and then at 920 °C for 3 hours for boronizing. The B-C-nitriding specimens showed the improvement of microhardness, wear resistance and corrosion resistance in acid when compared to those properties from pure boronizing specimens.

The simultaneously-boroaluminizing process on C3, C5XHM, X12, 3X2B8 and X18H9T steels was tested by using varieties of mixtures composed of the commercial Borozar paste and various amounts of alumina (Al_2O_3) contents. For boroaluminizing these specified steels, the tests found that the suitable formula was a mixture of 55 wt. % B_4C, 45 wt. % Na_3AlF_6, 30 wt. % Al_2O_3, and 10 wt. % NaF [88]. The gas phase reaction during the boroaluminizing was also described in forms of thermodynamics based on the

reactions from B_4C, Al, and NaF [89]. Moreover, different types of the activators were studied, and $(NH_4)_2O{\cdot}4BF_3$ was found to be the suitable activator for low carbon steels and alloys [90]. Furthermore, three different formulas were tested in the powdery simultaneous boroaluminizing process on C45 steels, yielding different morphologies and thickness and microhardness properties [91].

The simultaneous boroaluminizing process on 2.25 Cr-Mo steel was performed by using the powder pack method with a mixture of 33 wt. % B-Al, 65 wt. % Al_2O_3 and 2 wt. % NH_4Cl at 950 °C for 6 hours [92]. The process formed three coating layers on the substrate: Al-rich phase on the outer, Al- and Fe-rich phase on the middle, and Fe_2B phase on the inner.

Recently, Thermocalc software was used to calculate the optimal temperature of the boroaluminizing process based on gas precursors from a powder mixture of Al, B, $AlCl_3/NH_4Cl$, KBF_4, and Al_2O_3 [93]. The thermodynamic calculation gave 2 different mixture formulas to be used in boroaluminizing at 715 °C for 6 hours. The first mixture was composed of 4 wt. % Al, 2 wt. % NH_4Cl, 3 wt. % KBF_4, 15 - 20 wt. % B, and balance Al_2O_3, which FeAl, Fe_2B and Fe_2AlB_2 layers were formed with the coating thickness of 15 μm. The second mixture was composed of 5 wt. % Al, 1.5 wt. % Al_3Cl, 4.5 wt. % KBF_4, 20 wt. % B, and balance Al_2O_3, which only FeAl and Fe_2B layers were formed with the coating thickness of 20 μm.

Chernega *et al.* [94] studied chromium contents in a saturated borochromizing powder mixture by observing changes in the lattice parameter (in terms of size and atomic volume) and the microhardness. The study found that 3.5 - 6 wt. % chromium, 1 - 1.5 wt. % activator, and balance B_4C powder mixtures resulted in the highest properties

in terms of thickness and microhardness. The study also found that if the amount of chromium concentration was increased to more than 10 wt. %, it could reduce the lattice parameter of FeB. The smaller lattice parameter and atomic volume of FeB increases the microhardness property due to a strengthened chemical bond of the covalent component.

Lee *et al.* [95] studied mechanical properties of the borochromized layer on AISI 403 steel. The specimen was first chromized at 1100 °C for 2 hours with a powder mixture composed of 25 wt. % Cr, 69 wt. % Al_2O_3 and 6 wt. % NH_4Cl. It was subsequently boronized at 950 °C for 9 hours with Ekabor III. The results showed that the wear rate of the borochromized layer decreased 1.5 times compared to the wear rate of the boronized layer. Furthermore, the high-temperature oxidation at 700 °C of the borochromized layer was four times slower than the oxidation of the boronized layer.

The borochromizing process was performed in the vibrofluidized bed at a temperature range of 900 - 950°C for a period of 30 to 90 minutes by using a fluidized powder mixture composed of 10 wt. % Cr, 89.9 wt. % Al_2O_3, and 0.1 wt. % of NH_4Cl and $NaBF_4$ [96]. The results showed the improvement of the corrosion and wear resistances on borochromized specimens.

Moreover, the borochromizing process was studied in the fluidized bed with a mixture composed of 10 wt. % B_4C, 1 wt. % $CrCl_2$, 1 wt. % $CuCl_2$, 0.5 wt. % AlF_3, and 87.5 wt. % Al_2O_3 [97]. The study found that the content of chromium in the boride (FeB and Fe_2B) layers decreased the microbrittleness of the boride layers and increased the wear resistance when compared to those layers formed in the conventional boronizing process.

Furthermore, the plasma-transformed arc (PTA) process produced the borochromized layers. In the process, boron and chromium diboride powder were used to cover the sample steel and the covered specimen were scanned with the plasma arc. The borochromized layers were formed of the eutectic components between ferrite and CrB_2. The borochromized layer provided the microhardness of 900 HV compared to 1000 – 1300 HV of the boronized layer [98]. Additionally, the friction coefficient of borochromizing was lower than 0.15 compared to a range of 0.2 - 0.8 of boronizing.

Ivanov *et al.* [99] studied the borocopperizing process with the mixture compositions of B_4C, Na_3AlF_6, and CuO. The study showed that copper diminished the boride coating thickness and the content of copper could be used to control the phase composition of the formed boride layers.

The borocopperizing process was also tested using the fluidized bed with the powder mixture composed of 10 wt. % B_4C, 0.5 wt. % Cu_2O, 0.2 wt. % NH_4Cl, and 89.3 wt. % Al_2O_3 [97]. As a result, the borocopperized layers had the microhardness of about 1500 HV compared to 1800 HV of the boronized layers. However, the wear resistance of the borocopperized layers was higher than that of the boronized layers.

The multi-component coating of Ni-Fe-B on AISI 1045 steel was investigated by Sikorski *et al.* [100]. The coating process was performed by using the Ni-P chemical electroless method at 87°C, followed by the plasma boronizing process at 650 °C and 850 °C. During boronizing, phosphorus from the Ni-P plate diffused inside the substrate and left nickel and iron to form the boride layers. The study found $(Ni_xFe_{(1-x)})_4B_3$, $(Ni_xFe_{(1-x)})_2B$, and $(Ni_xFe_{(1-x)})B$ boride phases formed at 650 °C, and only $(Ni_xFe_{(1-x)})_2B$, and $(Ni_xFe_{(1-x)})B$ boride phases formed at 850 °C. Moreover, the content of nickel in

these boride layers reduced the residual stress between the coating and substrate, thus improving coating properties [101]. Finally, it was concluded that the higher Ni-concentration in boride layers, the better corrosion and wear resistance.

Boron-nickel layers were formed by using the fluidized bed technology with a powder mixture composed of 10 wt. % B_4C, 0.1 wt. % NiO, 0.2 wt. % NH_4Cl, and 89.7 wt. % Al_2O_3 at 950 °C [102]. The study reported the decrease of microbrittleness and the increase of wear resistance on boron-nickel layers with a small change of microhardness compared to those properties of boronized layers.

Niobium boride coating on AISI M2 steel was found after performing the two-step process of salt bath boronizing at 1000 °C for 2 hours and pack niobizing at 900 °C for a period of 1 to 4 hours [103]. The study found the coating was composed of the outer smooth layers of NbB and Nb_3B_2 and the inner needle layers of FeB and Fe_2B.

Carbucicchio *et al.* [104] studied the reaction effect of silicon compounds (e.g., SiC, SiO_2, and Si_3N_4) to a boronizing powder mixture. The study presented the following findings: SiC was as a suitable diluent in the mixture; SiO_2 reduced the boron diffusion; and Si_3N_4 reacted with KBF_4 and produced SiF_4 to react with the deposited iron boride, which finally formed a boron-containing iron silicide.

The simultaneous borosiliciding process with a powder mixture composed of KBF_4, B_4C and Si_3N_4 at 850 °C for 8 hours was performed on Armco iron and Fe-Ni alloy [105]. The study addressed that after the borosiliciding treatment, the coating phases on Armco iron were Fe_2B, FeB, and Fe_3Si, and $Fe_3Si_{1-x}B_x$, while the coating phases on Fe-Ni alloy were $Ni_{74}Si_{26}$, Ni_3Si, possibly Ni_2Si and $NiSi_2$ (in small amounts), Fe_3Si, Fe_2Ni_2B, and α-$FeSi_2$.

The paste borosiliciding method was used to form the multilayer coatings on Nimonic 90 superalloy [106]. The coatings were consisted of the outer layer of $(Ni,Co)_2Si$, the intermediate layer of $(Cr,Co)_2B$, and the inner layer of Ti-rich nickel silicide with the total thickness of 40 - 90 μm. The microhardness of coated Nimonic 90 superalloy increased about 3 times and the abrasive wear increased 2.5 to 5 times when compared to those of uncoated Nimonic 90 superalloy.

The two-step process of borovandizing was prepared by treating with vanadium—in a powder mixture of Fe-V, Al_2O_3, and NH_4Cl—at a temperature range of 950 to 1250 °C for a period of 3 to 16 hours, then treating with boron—in a powder mixture of B_4C, $Na_2B_4O_7$, NaCl, and NH_4Cl—at a temperature range of 950 to 1000°C for 5 and 9 hours [107]. As results, the VC and VB_2 layers were observed and the coating hardness of the coated specimen was 23600 MPa.

Sen [108] studied the boro-vanadizing process on AISI 8620 steel. The slurry salt bath boronizing with a composition of borax, boric acid, and ferro-silicon was performed at 900 °C for 4 hours and followed by vanadizing with a powder mixture composed of Fe-V, Al_2O_3, and NH_4Cl at a temperature of 950 - 1000 °C for a period of 1 to 6 hours. The FeB, VB and V_2B_3 layers were form, in which the coating thicknesses of these layers were measured in the range of 3 - 24 μm and the hardnesses of up to 2080 HV.

The V-B-N coatings were formed in the magnetron sputtering process with the gas mixture of Ar and N_2 [109]. The study found that with the gas mixture of 98 wt. % Ar and 2 wt. % N_2, only amorphous film of VB_2 was formed. If the weighted concentration of N_2 was changed to 5 %, the crystalline $VN_{0.35}$ was formed instead. If the weighted concentration of N_2 was changed to 20 %, both VN and $VN_{0.35}$ were formed.

The decorative boride coatings of LaB_6, ZrB_2, and ZrB_{12} were formed in the magnetron sputtering process, and the coating composition, morphology, color, and corrosion tests were characterized, studied, and performed in [110]. The study found that the flow rate of Ar and N_2 has the effects on the phase compositions, characteristics and properties of the coatings. LaB_6 coating was colored in reddish purple, ZrB_2 in silver grey, and ZrB_{12} in rosy-red. The simulated perspiration corrosions of these coatings were tested and showed that ZrB_2 was the attractive choice rather than LaB_6. However, an improvement of both mechanical and optical properties of the boride coatings was not successful. The decorative color coating of LaB_6 - ZrB_2 gave a silver-grey color with the hardness at a range of 1100 - 2100 HV [111]. The corrosion resistances of Zr-B and Zr-B-N coatings were also studied and shown that the Zr-B-N coating gave less coating porosity and better corrosion resistance when compared to these properties of the Zr-B coating [112].

The boro-lanthanum layer was formed in the simultaneous powder pack method using a powder mixture composed of B_4C, V_2O_5, and La_2O_3 [113]. The study found that the wear resistance of the boro-lanthanum boride layer was about 1.5 times higher than that of the conventional boride layer.

HfB_2 and Hf-B-N coatings were formed in CVD process by using $Hf(BH_4)_4$ as a precursor and mixing with Ar and N_2, at a temperature less than 350 °C [114]. During the test, the nitrogen content in the coating was controlled by the flow rate of N_2. As results, HfB_2 films were observed in two forms: a form ofamorphous film with the hardness of 20 GPa, and a form of nanocrystalline with the hardness of 40 GPa. In addition, Hf-B-N film composed of HfB_2, HfN, and BN was formed with the hardness of 16 GPa.

The borotitanizing process was studied by using a paste boronizing mixture composed of 55 wt. % B_4C, 5 wt. % NaF, 30 wt. % iron oxide, and 10 wt. % Ti-metal [115]. The study showed that the iron borides coating had the thickness of about 120 – 150 μm and contained 0.4 – 0.7 wt. % Ti.

Kholin [116] also studied the borotitanizing process and addressed that the Ti additive in the iron boride layers increased the microhardness to 2400 HV when compared to the microhardness of about 1700HV of the iron boride layers formed in the boronizing process.

CHAPTER 3

MULTI-COMPONENT BORONIZING EXPERIMENTS

3.1 Introduction of Boronizing Experiments

The low carbon steel samples (AISI 1018) wee chosen to be simultaneously boronized and metalized at 950 °C for 4 hours under the Argon atmosphere. The multi-component boride layer of steel samples was characterized in terms of phase identification, thickness, morphology, and microhardness. The corrosion and oxidation resistances of multi-component boronized steel samples were tested. The samples were investigated by five corresponding experiments as depicted in Figure 3.1.

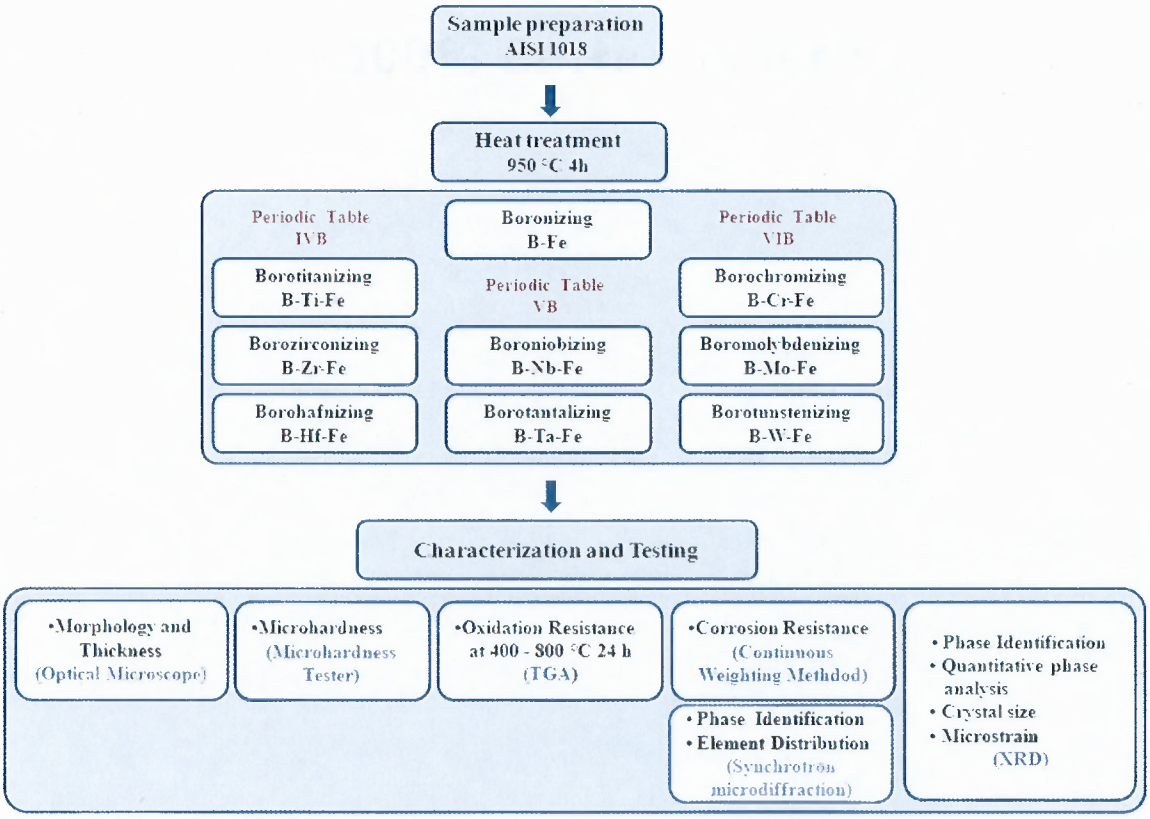

Figure 3.1 The experimental flow chart.

3.2 Experimental Procedures

The experimental procedures are described as follows.

3.2.1 Sample Characteristics and Preparation

The low carbon steel AISI 1018 samples were cut into two sizes and categorized into two groups, respectively, as follows.

- Group-1 sample had the dimensions of 10 mm (width) ×10 mm (length) ×3 mm (height). The group-1 samples were used for four experiments: morphology, microhardness, corrosion resistance, and phase identification.
- Group-2 sample had the dimensions of 4 mm (width) ×4 mm (length) ×3 mm (height). The group-2 samples were only used in the oxidation resistance testing.

The chemical compositions of the AISI 1018 sample are depicted in Table 3.1.

Table 3.1 The Chemical Composition of the AISI 1018 Steel Sample

	Chemical Composition, %												
Steel	C	Mn	P	S	Si	Cu	Ni	Cr	Mo	Al	V	Co	N
1018	0.200	0.720	0.008	0.008	0.016	-	-	-	-	0.065	-	-	-

The samples were ground with 180-, 320-, and 600-grit sand papers. Then, the samples were cleaned with acetone in the ultrasonic bath for approximately 2-3 minutes to remove dirt and oils on the sample surface and the samples are dried in the air.

3.2.2 Procedures of Boronizing Heat Treatment

There were three procedures in boronizing heat treatment processes. First, nine boronizing powder mixtures were prepared with different chemical compositions. Secondly, the steel samples were packed with these powder mixtures. Thirdly, the specimens were processed with the heat treatment method. All procedures were illustrated in Figure 3.2.

1. Preparation of Boronizing Powder Mixtures

Nine types of boronizing powder mixtures were prepared for test specimens as follows.

- **Type 1**: the powder mixture was prepared by mixing 1 w/w % KBF_4 (potassium tetrafluoroborate of which an assay is 99.5%) with 99 w/w % B_4C (technical-graded boron carbide with the grit size of 240).
- **Type 2**: the powder mixture was prepared by mixing 1 w/w % KBF_4, 79 w/w % B_4C, and 20 w/w % metal powder of Chromium (Cr) (-325 mesh).
- **Type 3**: the powder mixture was prepared by mixing 1 w/w % KBF_4, 79 w/w % B_4C, and 20 w/w % metal powder of Molybdenum (Mo) (-325 mesh).
- **Type 4**: the powder mixture was prepared by mixing 1 w/w % KBF_4, 79 w/w % B_4C, and 20 w/w % metal powder of Tungsten (W) (-325 mesh).
- **Type 5**: the powder mixture was prepared by mixing 1 w/w % KBF_4, 79 w/w % B_4C, and 20 w/w % metal powder of Niobium (Nb) (-325 mesh).
- **Type 6**: the powder mixture was prepared by mixing 1 w/w % KBF_4, 79 w/w % B_4C, and 20 w/w % metal powder of Tantalum (Ta) (-325 mesh).
- **Type 7**: the powder mixture was prepared by mixing 1 w/w % KBF_4, 79 w/w % B_4C, and 20 w/w % metal powder of Titanium (Ti) (-325 mesh).

- **Type 8**: the powder mixture was prepared by mixing 1 w/w % KBF_4, 79 w/w % B_4C, and 20 w/w % metal powder of Zirconium (Zr) (-325 mesh).
- **Type 9**: the powder mixture was prepared by mixing 1 w/w % KBF_4, 79 w/w % B_4C, and 20 w/w % metal powder of Hafnium (Hf) (-325 mesh).

For each powder mixture type, the chemical substances are mixed together in the mortar until the mixture becomes homogeneous.

2. Packing of Boronizing Powder

The well-cleaned sample steels were packed in an inconel crucible that contained the boronizing power mixture. After the boronizing powder mixture was fully filled in the crucible, the crucible was lightly tapped to remove the air trapped in the crucible until the powder mixture was densely packed. The crucible was sealed with a lid, and then placed in a vacuum dessicator. It was degassed overnight for approximately 12 hours at room temperature.

3. Boronizing Heat Treatment

The packed crucible was dried under vacuum for two hours at 250 °C inside a retort box furnace. Then, the furnace was heated up under the Argon atmosphere until the temperature in the furnace reached 950 °C and held for 4 hours. Note that the Argon gas was flown into the furnace at the rate of 5 cubic feet per hour (ft^3/h). After being heated for 4 hours, the furnace was cooled down to 250 °C under the Argon atmosphere. Then, the furnace was turned off to allow the temperature to cool down to the ambient temperature. Finally, the coated specimens were removed from the crucible and cleaned with methanol in the ultrasonic bath.

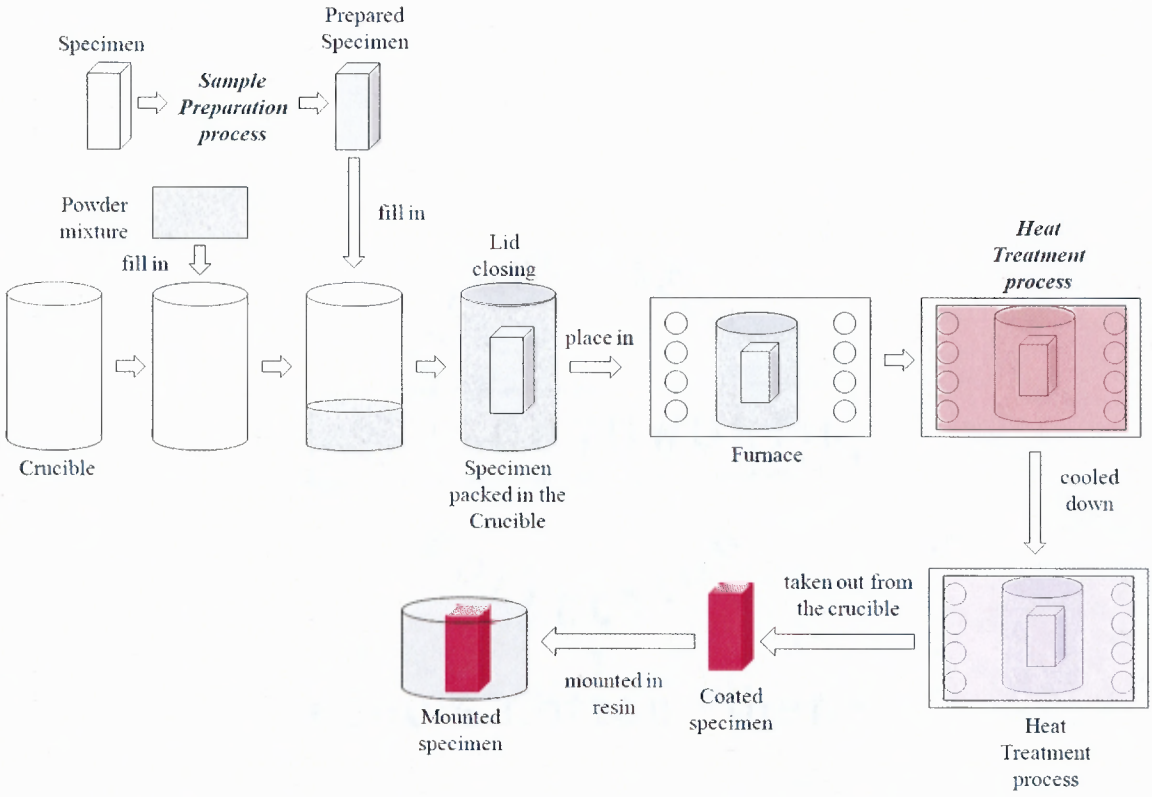

Figure 3.2 The illustration of all procedures taken in the borozning heat treatment.

3.3 Characterization and Testing of Boronized Specimens

Boronized specimens were analyzed in five experiments: structure (in forms of morphology and thickness), microhardness, oxidation resistance, corrosion resistance, and phase identification (in forms of phase identification, quantitative phase analysis, crystal size, and microstrain) as follows.

3.3.1 Structure (Morphology and Thickness) Characterization

A cross-sectional specimen was used to examine the thickness and morphology of the multi-component boron coating coated on the sample steel. The coated specimens were mounted by using a mounting press machine (in this dissertation, TechPress2^{TM} machine from Allied High Tech Products, Inc. was used) with the phenolic mounting powder at 140 °C and 4.5 bar.

The grinding and polishing machine (in this dissertation, MetPrep3 machine from Allied High Tech Products, Inc. was used) was used to grind and polish the samples. The grinding and polishing procedures are summarized in Table 3.2. The illustration of the grinding and polishing procedures is depicted in Figure 3.3

Table 3.2 The Grinding and Polishing Procedures for the Steel Substrates

Step	1	2	3	4	5	6	7
Abrasive size	180 grit	320 grit	600 grit	6 micron	3 micron	1 micron	0.05 micron
Abrasive type	SiC	SiC	SiC	Diamond Lapping Film Type B	Diamond Compound	Diamond Compound	Colloidal Silica Suspension
Carrier	Grinding Disc	Grinding Disc	Grinding Disc	Grinding Disc	Grinding Disc	Grinding Disc	Grinding Disc
Polishing cloth	N/A	N/A	N/A	N/A	Gold Label	Imperial	Chem-Pol
Extender	H_2O	H_2O	H_2O	BlueLube	Red Lube	Red Lube	N/A
Plated speed	150 RPM (CCW)	150 RPM (CCW)	150 RPM (CCW)	150 RPM (CCW)	150 RPM (CCW)	150 RPM (CCW)	150 RPM (CCW)
Head Pressure	8 LB	8 LB	8 LB	8 LB	8 LB	8 LB	8 LB
Time	3 min	3 min	3 min	3 min	3 min	3 min	3 min

Note: The consumer products are supplied by Allied High Tech Products, Inc.

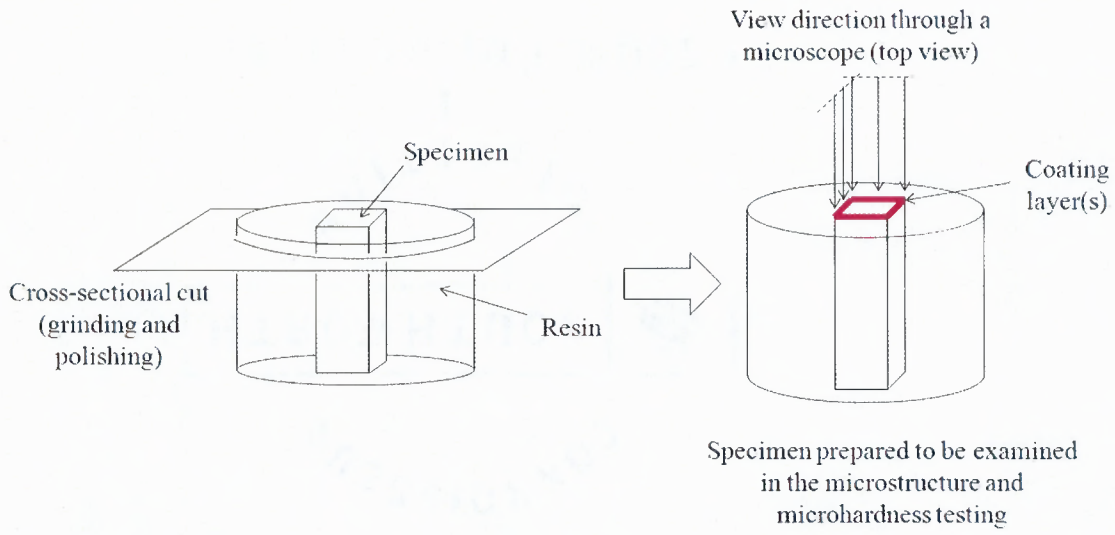

Figure 3.3 The illustration of the grinding and polishing procedures to prepare a specimen to be tested for microstructure and microhardness.

After grinding and polishing, the cross-sectional specimens were cleaned with a micro soap solution. The solution is prepared by mixing one part of micro soap (in this dissertation, the micro soap from Allied High Tech Products, Inc. was used) with ten parts of water. The specimens were cleaned in the ultrasonic bath until the polishing substances were completely eliminated from the surface of the specimens. Then, the specimens were dried with high pressure air.

The specimens were etched in 3 v/v % nitric acid to observe the morphology and thickness of coating layers. After etching, the specimens were washed with running water and then dried with high pressure air. It is important that the etching solution must be completely washed off the specimens and no acid residual is left on the specimen surface.

To observe the morphology and thickness of the multi-component boron coatings, the optical microscope (in this dissertation, the AxioTech microscope along with optic lens from Carl Zeiss, Inc was used) equipped with 10x eyepiece lens and 20x, 50x, 100x objective lens was utilized. The microscope can function in three different modes: Differential Interference Contrast (DIC), Darkfield, and Brightfield. The images of coating microstructures were taken by a digital camera (in this research, Pixelink PL-A662) attached to the AxioTech microscope. In this dissertation, eight images were taken per specimen, and each image was taken from a randomly selected area on the specimen where the coating layer was formed and observed. The illustration of observed coating on an unspecified specimen is depicted in Figure 3.4.

1. Morphology

The morphology of coating microstructures was observed and categorized into two types: saw-tooth (or needle) and smooth. The following chapter will address the characteristics and effects of these two structures in more details.

2. Thickness

The coating thicknesses in every image were measured by using AxioVision Software Version 4.5 from Carl Zeiss, Inc. For each specimen, at least 100 measurements of the length of saw-tooth or smooth microstructures were randomly chosen on the selected coating area. (Note here, before the measurement, the microscope was calibrated with a reticle to get an accurate measurement value). Of all eight images, the distribution and average values of these thicknesses were evaluated and calculated by using a statistical analysis method. For each specimen, the distribution of coating

thicknesses was shown as a histogram, and values of mean, mode and median were calculated.

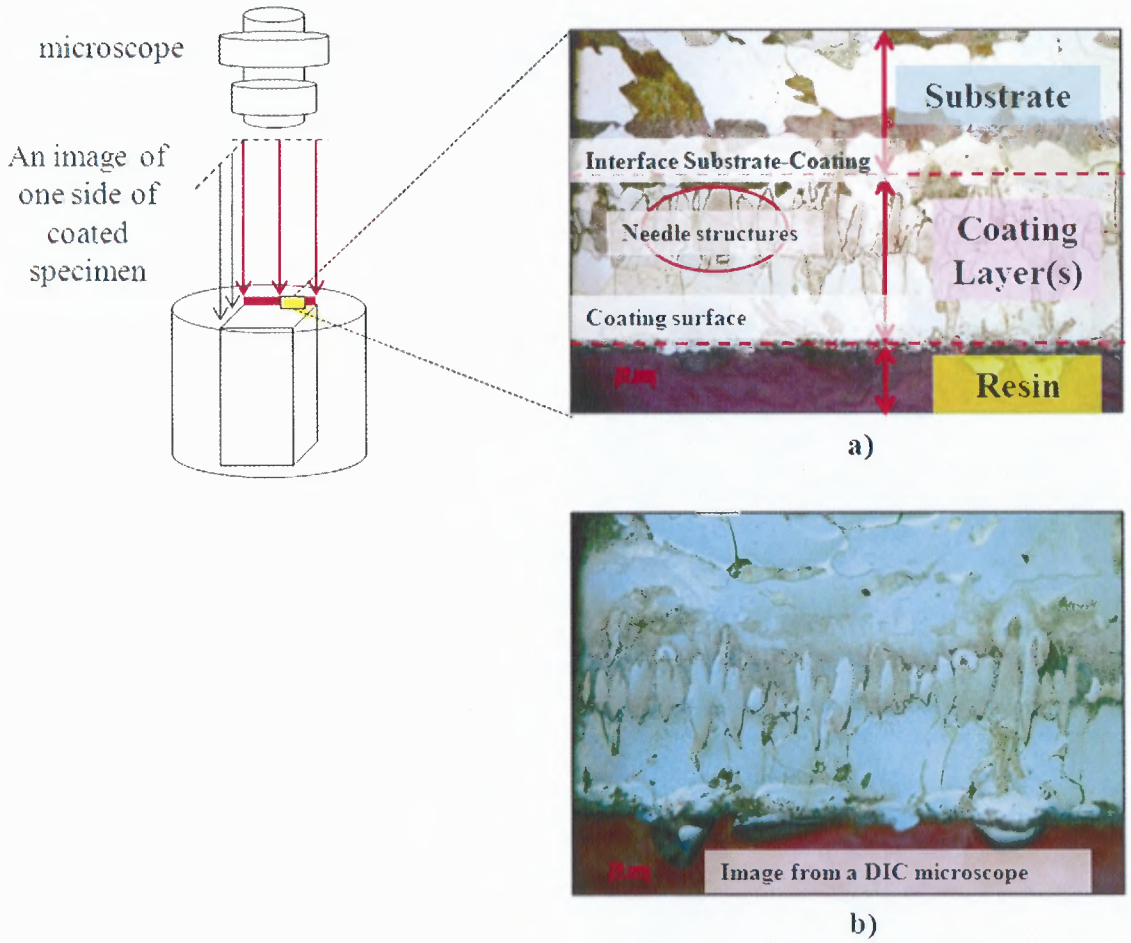

Figure 3.4 The illustration of observations, a) the illustration of observing images taken on one side of the coated specimen and b) the 3-D image taken by using the Differential Interference Contrast (DIC).

As illustrated in Figure 3.4 a), there are three areas observed through the microscope: resin at the bottom, coating layer(s) at the middle, and the substrate at the top of the image. Boron and other elements atoms diffuse into the substrate and form the needle structures toward the substrate. The same position of the same specimen in Figure 3.4 a) was observed through the same microscope by using the differential

interference contrast (DIC) mode, and the image was shown in a three dimensional (3D) view in Figure 3.4 b). More details will be discussed intensively in the following chapters.

3.3.2 Microhardness Testing

The microhardness of coated specimens was determined by using the LM-700 Digital microidentation tester (from Leco Corp.) with the Knoop indenter under the test force of 10 gf (Gravity force) for 10 seconds. The tester conforms to the ASTM E-384, which is the standard test method for microindentation hardness of materials [117].

Similar to the preparation processes for measuring the morphology and thickness, the cross-sectional specimen was mounted, ground, and polished. The microhardness of the cross-sectional specimen was then measured across the coating thickness through the substrate. As a result, a graph of microhardness versus depth from the surface was plotted.

Knoop indenter is a rhombic-based pyramidal-shaped diamond indenter with the longitudinal edge angle of 172° 30' and the transverse edge angle of 130° 0'. After indenting, the long diagonal length of the indentation on the tested area of a specimen is measured. The Knoop hardness number is calculated by the formulae as follows:

$$HK = 1.000 \times 10^3 \times \left(\frac{P}{A_p} \right) = 1.000 \times 10^3 \times \frac{P}{c_p \times d^2}$$

or

$$HK = 14229 \times \frac{P}{d^2}$$

$$c_p = \frac{\tan\left(\frac{\angle B}{2}\right)}{2\tan\left(\frac{\angle A}{2}\right)}$$

,

where P = the test force, gf

d = the length of the long diagonal, μm

A_p = the projected area of indentation, μm^2

$\angle A$ = the included longitudinal edge angle, 172° 30' for the Knoop

$\angle B$ = the included transverse edge angle, 130° 0' for the Knoop

c_p = the indenter constant relating the projected area of the indentation to the square of the length of the long diagonal, ideally 0.07028.

3.3.3 High Temperature Oxidation Resistance Testing

The high temperature oxidation resistance of coated specimens was tested by using the Pyris 1 Thermal Gravimetric Analyzer (TGA), from PerkinElmer Co. [118], at a temperature range of 400 to 800°C.

As addressed in Section 3.2.1, each specimen that was used in the oxidation resistance testing had the dimensions of 4 mm×4 mm×3 mm and the total mass of not over 1300 mg. (Milligrams). Specimens packed and processed with nine powder mixtures were tested at two different sets of test temperatures as follows. Specimens packed and

processed with seven powder mixture types 1- 6 were tested at a set of four test temperatures, which were 500 °C, 600 °C, 700 °C, and 800 °C. Specimens packed and processed with three powder mixture types 7- 9 were tested at another set of four test temperatures, which were 400 °C, 500 °C, 600 °C, and 700 °C.

The test specimens were well cleaned and dried before testing. The oxidation resistance testing had the following steps.

Step 1. The TGA alumina pan was weighted and tared to zero.

Step 2. The test specimen was placed in the alumina pan and weighted for an initial mass.

Step 3. The test specimen was heated to the desired temperature with the heating rate of 50 °C per minute.

Step 4. Once the desired temperature was reached, and the test specimen was then isothermally held for 24 hours under the atmosphere control with an air purse rate of 10 milliliters per minute.

The mass of the test specimen was continuously detected and recorded over a time period of 24 hours by using the Pyris software. Based on these recorded data, the weight change per area of the test specimen was plotted against time. The high temperature oxidation resistance of each multi-component boron coating was compared at different test temperatures.

3.3.4 Corrosion Resistance Testing

The corrosion resistance of coated specimens was investigated by a continuous weighting method. The weight loss of the specimen was continuously detected as a function of time. The 0.5M sulfuric acid (H_2SO_4) was used as a corrosive media. The setting equipment for this experiment is illustrated in the following Figure 3.5.

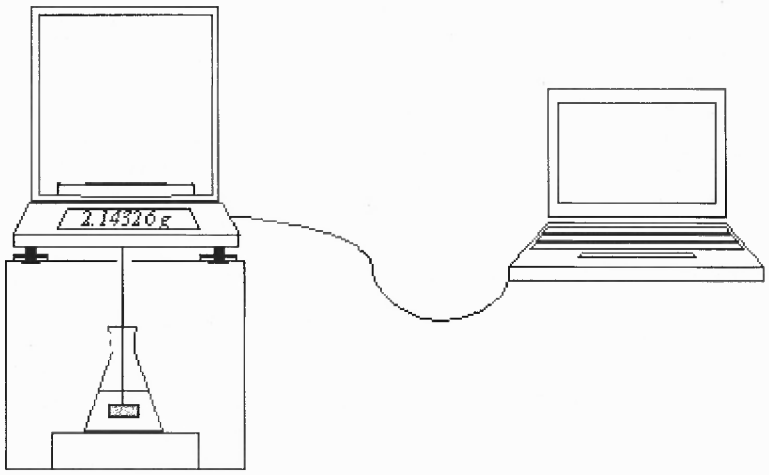

Figure 3.5 The equipment setting for corrosion testing (using the continuous weighting method).

From Figure 3.5, the test specimen was hung down from the balance (Analytical Balance GR-202 of A&D) with platinum wire and immersed in sulfuric acid solution for 12 hours. The test specimen weight was detected every 1 second and automatically stored in computer. The weight change per area of the test specimen was plotted versus time.

3.3.5 Phase Identification (Phase Identification, Quantitative Phase Analysis and Crystal Size and Microstrain by X-ray Diffraction (XRD)) Testing

X-ray diffraction (XRD) was used to characterize phase presences and compositions, lattice parameters, crystal size, and microstrain of multi-component boron coatings.

In this dissertation, the XRD Philips (PW3040 MPD DY715) with the X'Pert Data Collector was used to perform and record the experimental data. The measurement used Copper (Cu) K_α –X-radiation with $K_{\alpha1}$ of 1.54060 Å, $K_{\alpha2}$ of 1.5443 Å, K_β of 1.39225 Å, and the ratio of $K_{\alpha2}$/ $K_{\alpha1}$ equal to 0.50000; the generator setting was 45 kV and 40 mA; the Goniometer radius was 200 mm; the Distance Focus-Divergence Slit was 100 mm; the Divergence slit was 0.8709°; the Receiving slit was 0.1000°; and the specimen length was 10 mm. The XRD spectrum was detected in the 2θ scan range of 10 - 140° with the step size of 0.02°, and the time period per step was 20 seconds.

1. Phase Identification

Phase identification was analyzed by using the Search and Match function available in X'Pert HighScore Plus (PANalytical B.V.). This function searched the reference databases—2009 PDF-4+ database files of ICDD- International Center for Diffraction Data—for patterns that matched the XRD test spectrum profile. The matching patterns were closely examined in details and were ranked according to their scores shown in a candidate list. The well-fitting patterns based on the score and scale factors were accepted as acceptable candidates.

2. Quantitative Phase Analysis

Quantitative phase analysis was performed by using the Rietveld refinement method which is a full-pattern fit method. The measured profile (e.g., XRD test specimen spectrum) was then compared with the calculated profile.

To perform the Rietveld refinement, the crystal structure data, presented in the crystallographic information file (CIF) of all phases that were presented on the XRD test specimen spectrum, must be input, and then peak positions and intensities were simulated from these crystal structure data (similar to the atomic coordinates in a unit cell) and presented as a calculated profile.

Scale factors, cell and profile parameters, and other parameters were varied to minimize the differences between the measured profile and the calculated profile. After the Rietveld refinement, the percentages of all phases were calculated.

Quantitative phase analysis on multi-phase samples with the Rietveld refinement relies on the following relationship:

$$W_p = \frac{(SZMV)_p}{\sum_{i=1}^{n}(SZMV)_i},$$

where W_p is the weight fraction of phase p in a mixture of n phases; S is the scale factor; Z is the number of formula units per unit cell; M is the molecular mass of the formula unit; and V is the unit cell volume (in $Å^3$).

3. Crystal Size and Microstrain

The analysis of crystallite size and microstrain by the Rietveld refinement is based on a change(s) of the profile parameters, compared to a standard sample. The profile parameters depend on the instrument settings used for data collection as well as the

profile function used for the Rietveld refinement. The peak broadening is used to calculate the crystallite size and strain.

To evaluate the XRD test specimen spectrum, the size-strain standard or instrument line position and profile shape standard was firstly obtained by using the NIST SRM 660 LaB_6. Then, the Rietveld refinement was used to evaluate the size-strain standard and to compare with the XRD test specimen spectrum under the same parameters.

The diffraction peak profile is the result of the convolution of a number of independent contributing shapes, some symmetric and some asymmetric, which comes from both instrument and specimen and are shown as peak broadening. Both microstrain broadening and crystallite size broadening of specimen are varied as a function of 2θ, but in different ways. Microstrain broadening is dependent of the order of reflection, while crystallite size broadening is independent of the order of reflection.

The crystallite size and microstrain are calculated from the extra peak broadening of a specimen with respect to a standard sample. The Pseudo-Voigt profile function is used to evaluate both the crystallite size and microstrain of the specimen.

There are four functions used in the crystallite size and strain analysis as follows.

A. Crystallite size, D_i, is depicted as:

$$D_i = \left(\frac{180}{\pi}\right)\frac{\lambda}{\left(W_i - W_{std}\right)^{1/2}}.$$

B. The variance of the crystallite size is depicted as:

$$\sigma^2(D_i) = \frac{A_D^2}{4(W_i - W_{std})^3}\left[\sigma^2(W_i) + \sigma^2(W_{std})\right]$$

with $A_D = 180 \times \lambda/\pi$. The mean error of the crystallite size is equal to the square root of the variance.

C. Microstrain, ε_i, is depicted as:

$$\varepsilon_i = \frac{\left[(U_i - U_{std}) - (W_i - W_{std})\right]^{1/2}}{\frac{1}{100}\left(\frac{180}{\pi}\right)4(2\ln 2)^{1/2}}.$$

The U parameter contains information about the strain broadening, and the W parameter corrects for a possible size broadening.

D. Variance of the micro strain is depicted as:

$$\sigma^2(\varepsilon_i) = \frac{A_\varepsilon^2}{4\left[(U_i - U_{std}) - (W_i - W_{std})\right]} \times\left[\sigma^2(U_i) + \sigma^2(U_{std}) + \sigma^2(W_i) + \sigma^2(W_{std}) - 2\,\mathrm{cov}(U_i, W_i) - 2\,\mathrm{cov}(U_{std}, W_{std})\right]$$

with $A_\varepsilon = \dfrac{1}{\frac{1}{100}\left(\frac{180}{\pi}\right)4(2\ln 2)^{1/2}}$.

The approximate mean error of the micro strain is equal to the square root of the variance, and the software ignores the covariance.

If only strain broadening occurs (W_i - W_{std} = 0), the variance formula reduces to:

$$\sigma^2(\varepsilon_i) = \frac{A_\varepsilon^2}{4\left[(U_i - U_{std})\right]} \times\left[\sigma^2(U_i) + \sigma^2(U_{std})\right].$$

3.3.6 Synchrotron X-Ray Microdiffraction and Microfluorescence

The synchrotron x-ray microdiffraction and microfluorescence experiments were performed at the 2-ID-D beamline at Advanced Photon Source (APS), Argonne National Laboratory. A Si (111) double-crystal monochromator was used to select the beam energy 10 keV (λ = 1.2398 Å) and 10.5 keV (λ = 1.1808 Å). The microfocusing optics of the phase zone plate produced a beam size of 200 nm. A Ge energy dispersive detector was used for the fluorescence measurement and a CCD detector mounted on the 2-theta arm was used for diffraction measurement.

The 5mm×5mm×3mm cross-sectional specimen was mounted to the sample holder on the submicron XYZ motorized stage for focusing and positioning. Before the experiments, the CCD detector was calibrated to determine the center of beam on the detector which was presented as zero Nu-angle (Nu_0). Noted here, Nu is used to present instead of 2θ. The calibration gave the x-y position of zero Nu-angle (Nu_0) at x-position of 606 and at y-position of 600 with the image size of CCD to sample of 3896 pixels.

After the calibration, the sample on the XYZ motorized stage was aligned to Nu_0 before the sample was moved to the detected area. At the detected area, the sample was checked for the microdiffraction and microfluorescence peaks. The experiment conditions were 1 μm step size for the coarse measurement and 0.3 μm step size for the fine measurement, 10° sample rotation, 60 seconds for CCD exposure time, and 10 seconds for fluorescence exposure time. The sample was measured in a range of 100-200 μm depending on the coating thickness of the sample.

SDI Application software was used to view the result images of microdiffraction and converse the images to the diffraction data plots between intensity and two-theta. The data of fluorescence intensity of the elements on the coating respected to the depth of the coating was detected and plotted as an element distribution profile.

3.4 Rietveld Refinement Method

This section specifically addresses the Rietveld method used to determine phase identification, quantitative phase analysis, and crystallite size and microstrain analysis. More information is referred to [119] - [120].

The Rietveld refinement method is a least-square refinement model which determines a calculated profile pattern from 4 data types—crystal structures, instrument factors, diffraction optic factors, and specimen characteristics—and analytically compares to an observed XRD profile pattern. The method can accurately identify one or more phases that appear on the coatings. As a result, it confirms or denies phases that have been preliminarily observed in the XRD profile pattern.

The Rietveld refinement method calculates, S_y:

$$S_y = \sum_i w_i (Y_i - Y_{ic})^2 ,$$

where $w_i = 1/Y_i$; Y_i is the observed intensity at point i in the pattern; Y_{ic} is the calculated intensity at point i in the pattern; and the residual S_y is the sum of overall data points. The Rietveld refinement method determines the minimized quantity of the residual, and in case of the best fit, $S_y = 0$.

There are eight profile parameters attributed in the Rietveld refinement method as follows.

A. The calculated intensities, Y_{ic}, are determined from the structural model and the background intensity as the equation:

$$Y_{ic} = Y_{ib} + \sum_{p} \sum_{k=k_1^p}^{k_2^p} G_{ik}^p I_k ,$$

where Y_{ib} is the background intensity; G_{ik} is the reflection peak profile function; I_k is the intensity of the k^{th} Bragg reflection; k represents the Miller indices, contributing intensity to point i; and p is the possible phase(s) appeared on the sample.

B. The Pseudo-Voigt profile function, G_{jk}, is used and expressed as:

$$G_{jk} = \gamma \frac{C_0^{1/2}}{H_k \pi} \left[1 + C_0 X_{jk}^2\right]^{-1} + (1-\gamma) \frac{C_1^{1/2}}{H_k \pi^{1/2}} \exp\left[-C_1 X_{jk}^2\right] ,$$

where $C_0 = 4$, $C_1 = 4ln2$; H_k is the full-width at half-maximum (FWHM) of the k^{th} Bragg reflection, $X_{jk} = (2\theta_i - 2\theta_k)/H_k$; and γ is a refinable mixing parameter ($0 > \gamma > 1$).

The variation of peak shape across the pattern can be refined from the function: $\gamma = \gamma_1 + \gamma_2 2\theta + \gamma_3 (2\theta)^2$, where γ_1, γ_2 and γ_3 are refinable parameters, as well as the variation of the peak FWHM is defined by the function $H_k = \left(U \tan^2 \theta + V \tan\theta + W\right)^2$ where U, V and W are refinable parameters.

C. The intensity, I_k, is given by the expression:

$$I_k = S M_k L_k |F_k|^2 P_k A_k E_k ,$$

where S is the scale factor; M_k is the multiplicity; L_k is the Lorentz polarization factor; P_k is the preferred orientation function; A_k is the absorption correction; E_k is the extinction correction; and F_k is the structure factor.

The Intensity I_k can be refined by these functions below:

D. The structure factor, F_k, is the details of crystal structure of a material (e.g. coordinates, types of atoms, distribution among different lattice site, thermal motion) which is expressed as:

$$F_k = \sum_{j=1}^{n} f_j \exp\left[2\pi i\left(h_r^t r_j - h_k^t B_j h_k\right)\right]$$

where f_j is the scattering factor or scattering length of atom j; and h_k, r_j, and B_j are matrices representing the Miller indices, atomic coordinates and anisotropic thermal vibration parameters, respectively; and t indicates matrix transposition.

E. The preferred orientation function, P_k, presents the tendency of crystalline orientation in a specimen. If no preferred orientation, $P_k = 1$. The preferred orientation is the equation:

$$P_k = \left[P_1^2 \cos^2 \alpha_k + P_1^{-1} \sin^2 \alpha_k\right]^{-3/2}$$

where P_1 is a refinable parameter; and α_k is the angle between the scattering vector and the reciprocal lattice vector (corresponding to a Bragg peak, hkl).

F. The absorption correction, A_k, is used to correct the effects from the geometry and properties of the sample and both incident and diffracted beam absorption. For flat plate geometry (Bragg-Brentano), the absorption correction is shown as the function:

$$A_k = \left(1 - P_0 - P_s(\theta)\right) = 1 - P_0\left(1 + \alpha_0\left(\tau / \sin(\theta)(1 - \tau / \sin(\theta)) - 1\right)\right),$$

where P_0 is the bulk term; P_s is the θ dependent term as a function of packing density; α_o, and degree of roughness; and τ. P_0, α_o and τ are refinable parameters.

G. The extinction correction, E_k, is used to correct the radiation reflections (back-reflection and/or re-reflection) and to be maintained at constant wavelength. The extinction correction is expressed as:

$$E_k = E_B \cos^2 \theta_k + E_L \sin^2 \theta_k$$

where k is the reflection and E_B, E_L are the extinction at the Bragg ($2\theta = \pi$) and the Laue ($2\theta = 0$) components. These are given by:

$$E_B = \frac{1}{\sqrt{1+x}} \quad \text{and} \quad E_L = \begin{cases} 1 - \frac{x}{2} + \frac{x^2}{4} - \frac{5x^3}{48} + \ldots & x < 1 \\ \sqrt{\frac{2}{\pi x}} \left[1 - \frac{1}{8x} - \frac{3}{128x^2} - \frac{15}{1024x^3} + \ldots \right] & x > 1 \end{cases}$$

where $x = D \times \left(\lambda \times F_k / V \right)^2$; D = mosaic block size; λ = wavelength; F_k = structure factor of reflection k; and V = volume of the unit cell.

H. The Lorentz-Polarization factor, LP, is the correction of the diffraction geometry and partial polarization of scattered electromagnetic wave, which is used as:

$$LP = \frac{1 + POL \times \cos^2 2\theta}{\sin^2 \theta \times \cos \theta}$$

POL is an additional polarization factor when a monochromator is used. $POL = \cos^2 2\theta$, where $2\theta_m$ is the monochromator diffraction angle.

To evaluate the best fit of the entire calculated pattern to the entire observed pattern, agreement indices are used and the goodness of fit value is estimated. Agreement indices are shown as the equations below:

The profile value: $R_p = \frac{\Sigma \left| Y_{io} - Y_{ic} \right|}{\Sigma Y_{io}}$.

The weighted value: $R_{wp} = \left[\frac{\Sigma w_i \left(Y_{io} - Y_{ic} \right)^2}{\Sigma w_i Y_{io}^2} \right]^{1/2}$.

The Bragg value: $R_B = \frac{\Sigma \left| I_{ko} - I_{kc} \right|}{\Sigma I_{ko}}$.

The expected value: $R_{\exp} = \left[\frac{N - P}{\Sigma w_i Y_{io}^2} \right]^{1/2}$.

The goodness of fit value: $\chi^2 = \frac{\Sigma w_i \left(Y_{io} - Y_{ic} \right)^2}{N - P} = \left[\frac{R_{wp}}{R_{\exp}} \right]^2$.

CHAPTER 4

EXPERIMENTAL RESULTS AND DISCUSSION

4.1 Boron – Iron (B-Fe) Experiments

The results of boron-iron coating experiments are discussed as follows.

4.1.1 Microstructure

In the boron-iron system, the needle-like or saw tooth structure was observed by using the optical microscope on the cross-sectional specimen and depicted in Figure 4.1. The thickness of boride coating was about 84.24 ± 1.14 μm. The morphology images of boronized low carbon steel and the coating thickness distribution are also shown in Figure 4.1.

In this experiment, the deboronizing process was also found during heat treatment, which caused the boron atoms that had previously been diffused into the substrate in the boronizing process to diffuse outward the substrate. The deboronizing diminished the content of boride phases which led to the decrease of microhardness and thickness of the coating.

In Figure 4.1 a), the deboronizing was depicted in the optical microstructure images as white areas (as referred to the spot A), which were located next to the outer surface. The boride layer was depicted as the brown needle structure (as referred to the spot B) above the deboronizing areas.

In Figure 4.1 b), the coating image was taken under the differential interface contrast (DIC) mode of the optical microscope. Using the DIC mode, the image is shown in three-dimensional (3D) under very oblique illumination. The DIC image gives the information of surface textures including pores and cracks. Under the DIC image, the hard surfaces of coating were seen as a convex surface and the soft surfaces of substrate and deboronizing area were seen as a concave surface.

In Figure 4.1 c), the lengths of a number of needle structures were randomly measured. The coating thickness distribution was then plotted in histogram by using Origin Pro 8 software, in which the Y-axis is the number of needle structures (referred to as counts) and the X-axis is the coating thickness in microns. Observed from Figure 4.1 c), most needle lengths were in the range of 80 - 85 μm as 60 counts and the lowest counts (about 5 counts) were in the range of 60 - 65 μm. The statistical data, such as mean, standard derivative (SD), and standard error (SE), were calculated as 84.24 μm, 9.79, and 0.58, respectively. Details and analysis of the microstructure are further addressed in Chapter 5, Section 5.1.

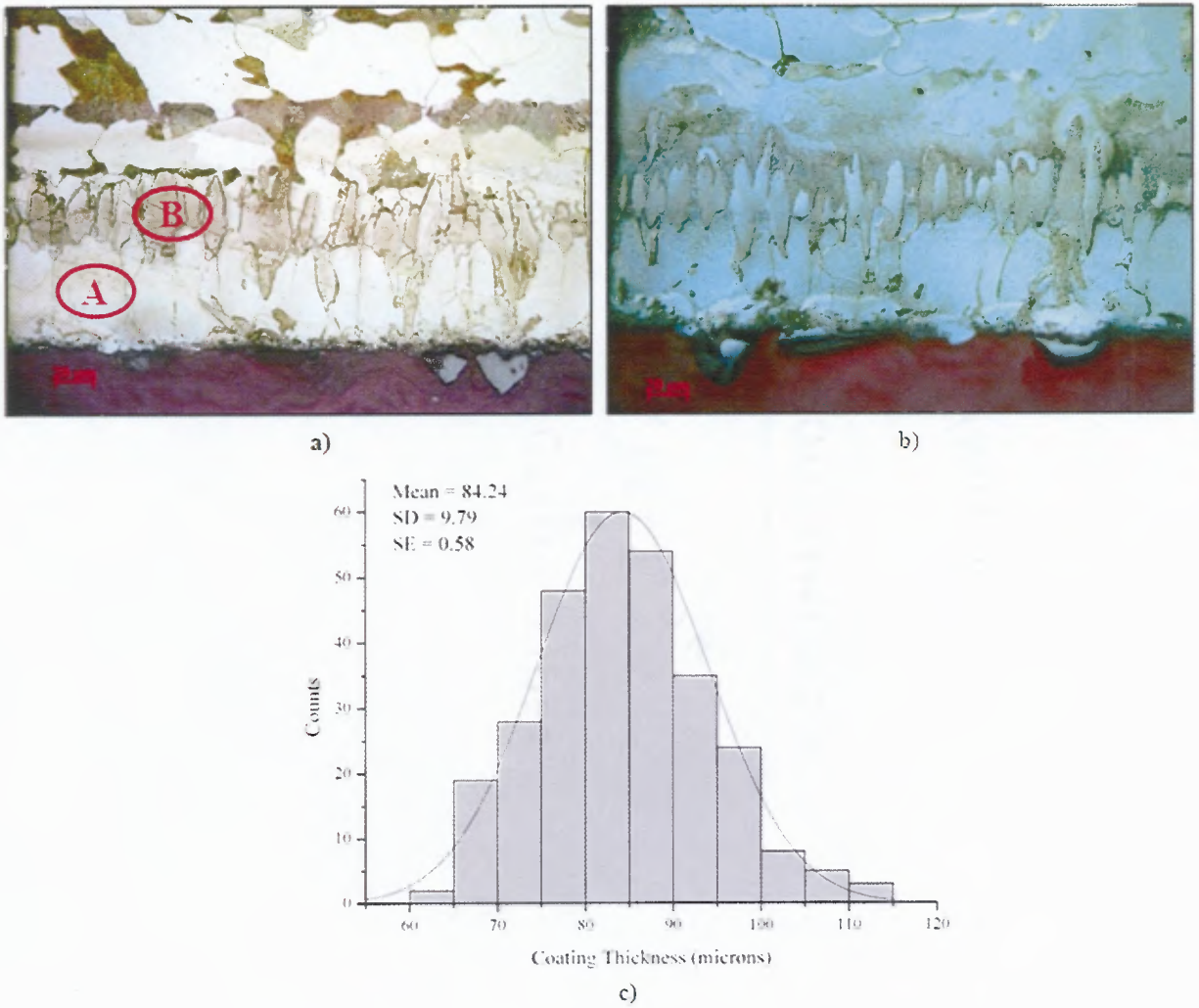

Figure 4.1 The morphology images of boride coating (in the B-Fe system) on low carbon steel AISI 1018 a) under bright field, b) under differential interface contrast (DIC), and c) the distribution of coating thickness.

4.1.2 Phase Identification

The XRD pattern of boronized specimen in boron-iron system was refined by the Rietveld method as illustrated in Figure 4.2. As addressed earlier in Chapter 3, the calculated intensities (I_{calc}) were retrieved from the simulated XRD pattern by adding the crystallographical data into the HighScore Plus Software while the observed intensities (I_{obs}) were from the XRD measurements. The simulated XRD pattern was refined and fitted to the observed XRD pattern by minimizing the residues between them in terms of the difference intensities (I_{diff}). The appearing peaks at 2 theta (in X-axis) based on the reflection of x-ray light at a certain reciprocal plane of crystal were used to identified the phase presences of coating, which each phase has its own pattern.

With the Rietveld refinement method, the quantitative phase analysis was shown that the boron-iron coating was composed of 90.1 wt. % Fe_2B and 9.9 wt. % FeB. The Rietveld standard agreement indices were the residual profile (R_p) = 10.61 %, the weighted residual profile (R_{wp}) = 14.54 % and the good of fitness (GOF) = 6.32.

Furthermore, the Rietveld refinement method also provides the information of microstrain and crystal size by calculating from the peak broadening. The microstrain occurs from the distortion of crystal lattice parameters or the crystal imperfection. The refinement of lattice parameters, microstrain and crystal size of Fe_2B and FeB phases of coating in boron-iron system were calculated and summarized in Table 4.1.

Details of the phase identification and analysis are further addressed in Chapter 5 Section 5.2, sub-section 5.2.1.

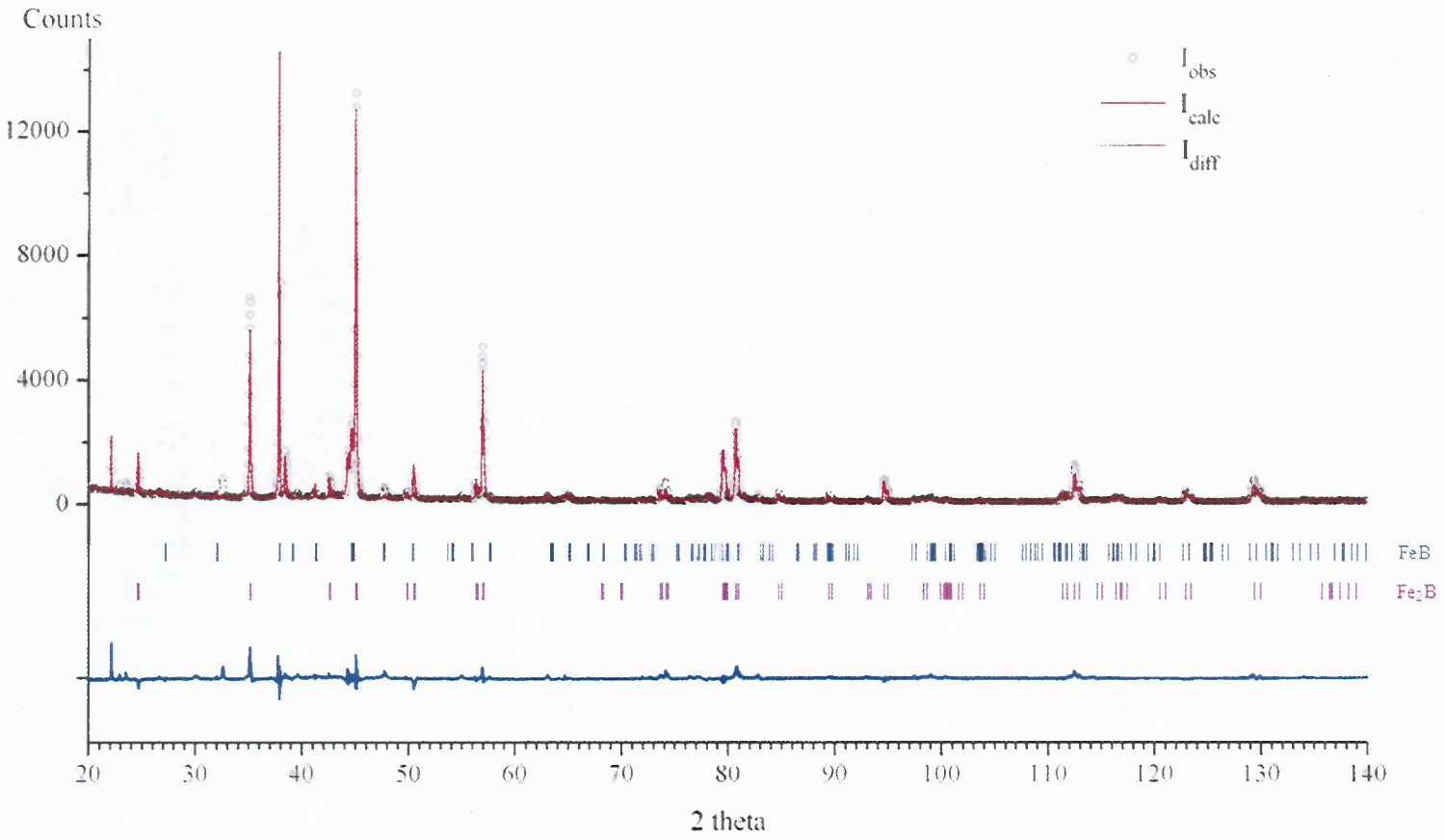

Figure 4.2 The XRD pattern (refined with the Rietveld Refinement) of the boride coating in the boron-iron (B-Fe) system.

Table 4.1 The Lattice Parameters, Microstrain and Crystal Size of Boride Coating in the Boron-Iron (B-Fe) System

Phase presence	**% Phase composition**	**Lattice parameters**	**Microstrain (%)**	**Crystal size (Å)**
Fe_2B	90.1%	a = b = 5.11436 Å c = 4.24674 Å vol.= 111.08050 $Å^3$ (Tetrahedral)	0.058	478.47
FeB	9.9%	a = 5.60305 Å b = 2.93551 Å c = 4.05556 Å vol.= 66.70497 $Å^3$ (Orthorhombic)	0.13	282.50
R_p = 10.61 % R_{wp} = 14.54 % GOF = 6.32				

4.1.3 Microhardness

The microhardness of coating depends on the types of boride phases. In B-Fe system, 2 types of boride phases (e.g., Fe_2B and FeB) were formed. The inner layer of Fe_2B phase had the microhardness of about 1800 - 2100 HV and the outer layer of FeB phase had the microhardness of about 1900 - 2200 HV. The microhardness measurement of boride layers were detected across the coating through the substrate as depicted in Figure 4.3. The smaller the indentation is, the higher the hardness is.

As seen in Figure 4.3 the boron coating showed the maximum microhardness at 2240 HK and the average microhardness at below 2000 HK, while the microhardness of substrate was roughly 160 HK. However, in this B-Fe system, the deboronizing occurred and the existing boron atoms in the substrate moved out from the substrate. The decreasing of boron contents led to the lessening of boride phases, and subsequently reduced the microhardness of coating at the depth near the surface. The microhardness of deboronizing area was measured at about 300 - 900 HK at the coating depth of 5 - 23 microns from the surface.

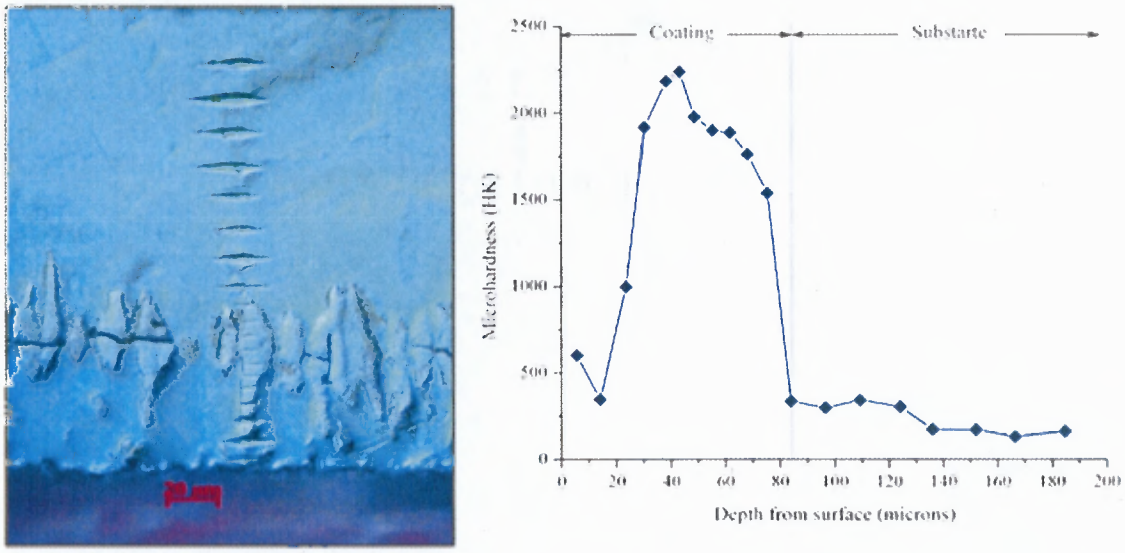

Figure 4.3 The plot between the microhardness and the depth from the surface of boride coating in the boron-iron (B-Fe) system

4.1.4 Corrosion Resistance

The corrosion resistance of coating in B-Fe system was tested in 0.5 M H_2SO_4 for 12 hours. The weight change per area (mg/mm^2) of the specimen was plotted against time (mins) as shown in Figure 4.4. The graph spikes can be interpreted as a formation of passive film to protect the specimen from the corrosive media; however, the passive film was unstable and remained for certain time before disappeared. The dissolve of passive film caused the decreasing of specimen weight, and when the passive film was reformed, the specimen weight was increase. Moreover, the result was shown that during the 12-hour period, the average weight change per area of specimen was almost constant at about 0.05 mg/mm^2.

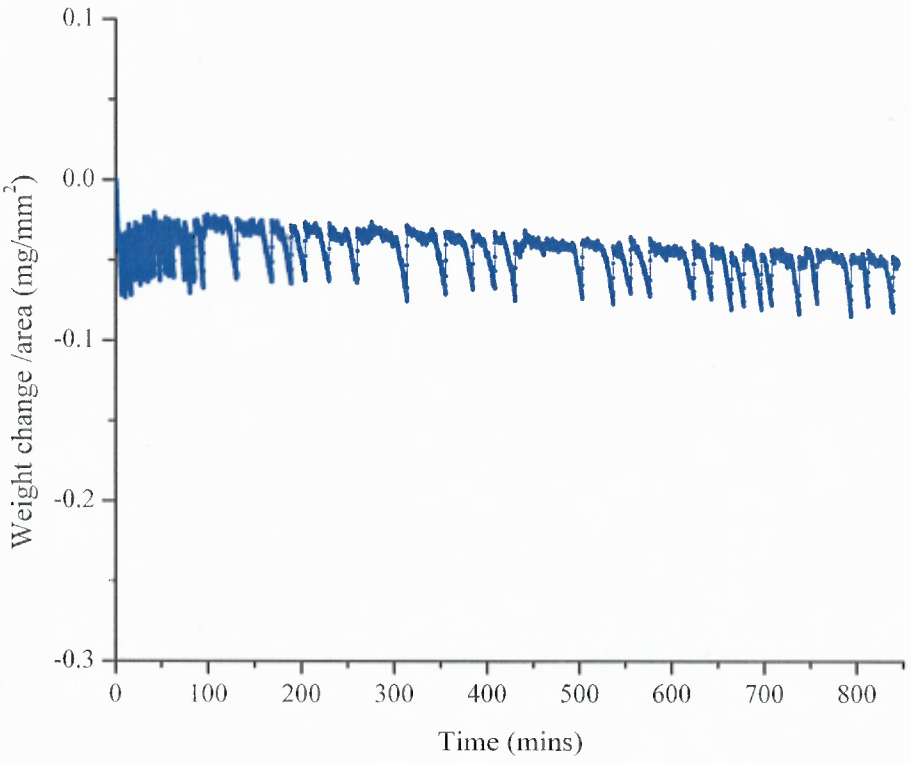

Figure 4.4 The corrosion resistance of boride coating in the boron-iron (B-Fe) system (in 0.5 M H_2SO_4).

4.1.5 Oxidation Resistance

The high temperature oxidation resistance of coating in B-Fe system was tested under the air for 24 hours. The plot of weight change per area (mg/mm^2) against time (mins) at different temperature in the range of 500 - 800 °C was evaluated as shown in Figure 4.5. As higher temperature, the oxygen can penetrate deeply through the coating and form more amount of oxide content in the coating and causes the specimen to gain more weight. The less weight gain is, the higher oxidation resistance of the specimen is.

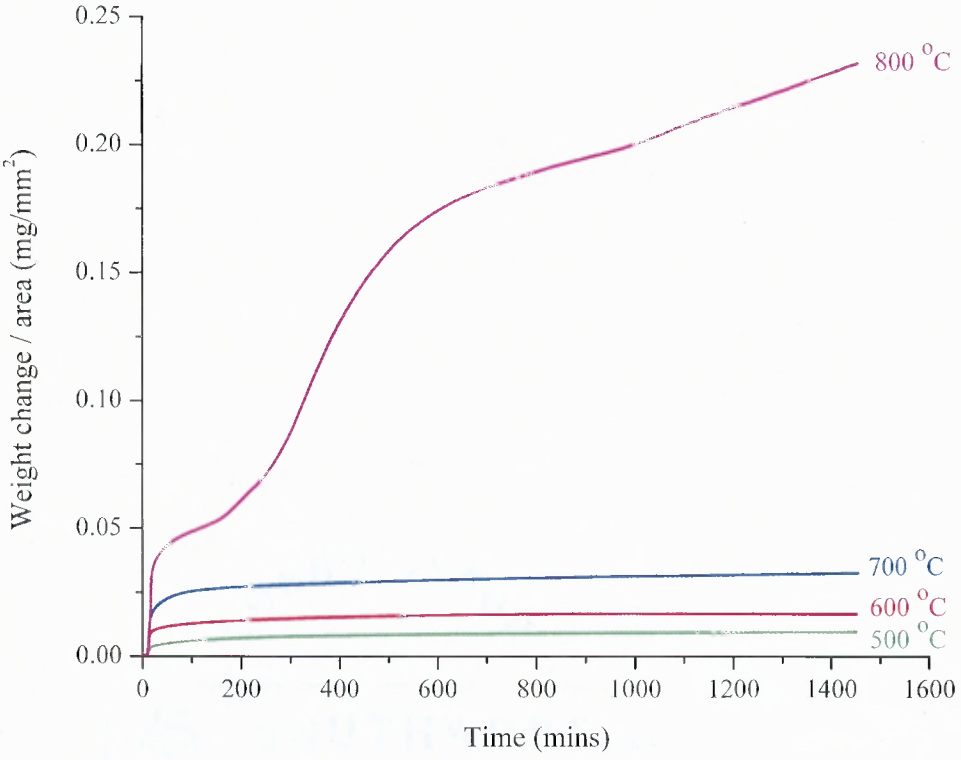

Figure 4.5 The high temperature oxidation resistance of boride coating in the boron-iron (B-Fe) system which coated on low carbon steel AISI 1018 substrate at a temperature range of 500 to 800 °C for 24 hours.

4.2 Boron- Chromium - Iron (B - Cr- Fe) Experiments

The results of boron-chromium-iron coating experiments are discussed as follows.

4.2.1 Microstructure

In the boron-chromium-iron system, Similar to the coating in B-Fe system, the needle-like was observed from the cross-sectional specimen. The thickness of boride coating was about 105.78 ± 2.63 μm. The morphology images of coating and the coating thickness distribution are shown in Figure 4.6.

Observed from Figure 4.6 a), some fractures were observed near the surface of coating. Details and analysis of these cracks are specifically addressed in Chapter 5 Section 5.3.

Observed from Figure 4.6 c), the distribution of coating thickness was in the wide range which most of the needle lengths were in the range of 80 - 90 μm and 110 - 120 μm (with the counts from the histogram reaches approximately 47 counts) and the lowest counts were in the range of 50 - 60 μm. The statistical data, including mean, standard derivative (SD), and standard error (SE) were calculated as 105.78 μm, 21.88, and 1.33, respectively. Details and analysis of the microstructure are further addressed in Chapter 5 Section 5.1.

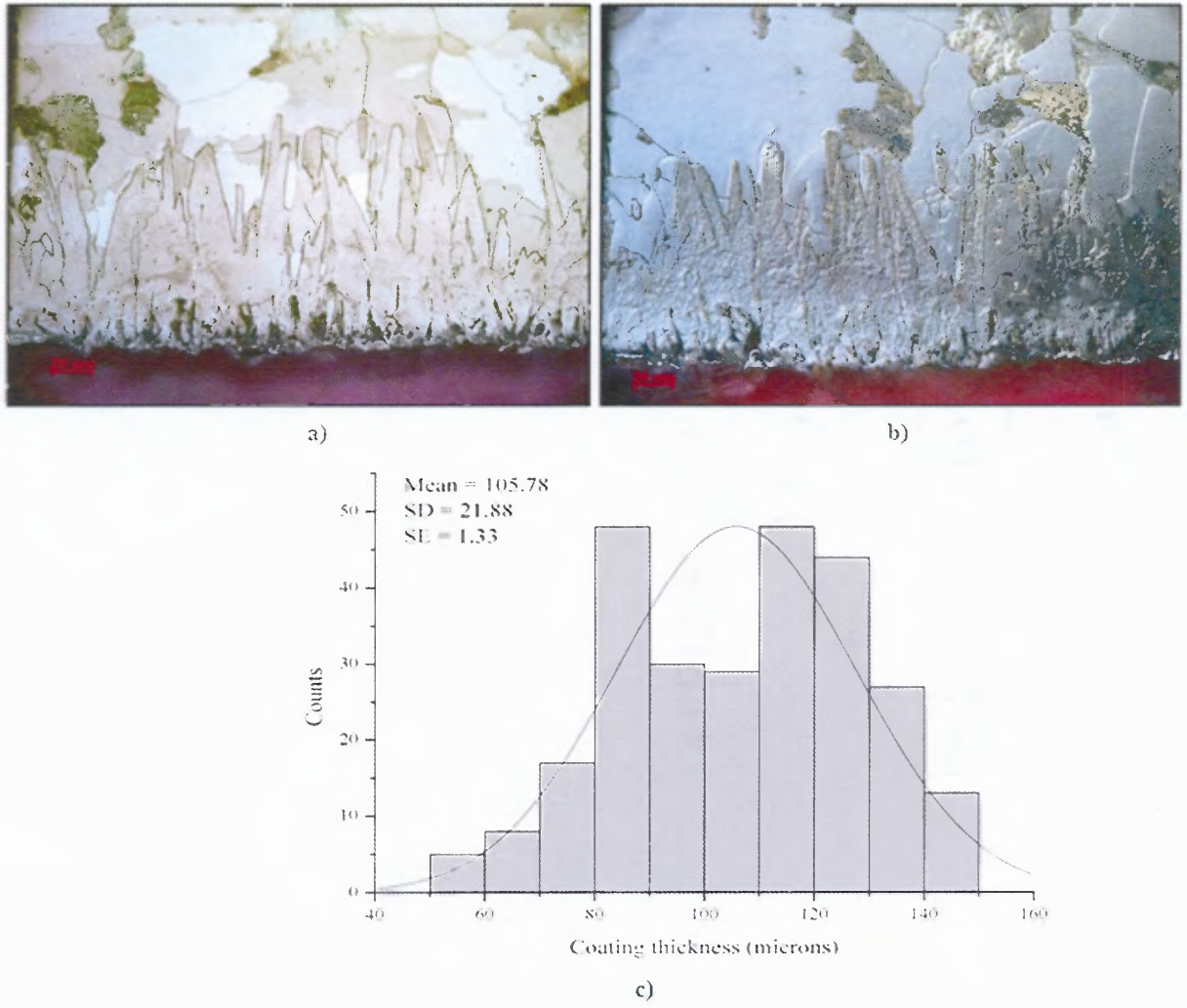

Figure 4.6 The morphology images of boride coating (in the B-Cr-Fe system) on low carbon steel AISI 1018 a) under bright field, b) under differential interface contrast (DIC), and c) the distribution of coating thickness.

4.2.2 Phase Identification

The XRD pattern of boronized specimen of boron-chromium-iron system was refined by the Rietveld refinement method as illustrated in Figure 4.7. The quantitative phase analysis from the Rietveld refinement method was shown that the boron-chromium-iron coating was composed of 81.4 % weight of Fe_2B, 5.4 % weight of Cr_2B and 13.2 % weight of CrB. The Rietveld standard agreement indices were the residual profile (R_p) = 10.58 %, the weighted residual profile (R_{wp}) = 13.63 % and the good of fitness (GOF) = 4.83. The refinements of lattice parameters, microstrain and crystal size of Fe_2B, Cr_2B, and CrB phases of boron-iron coating were shown in Table 4.2. Details and analysis of the phase identification and analysis are further addressed in Chapter 5 Section 5.2, sub-section 5.2.1.

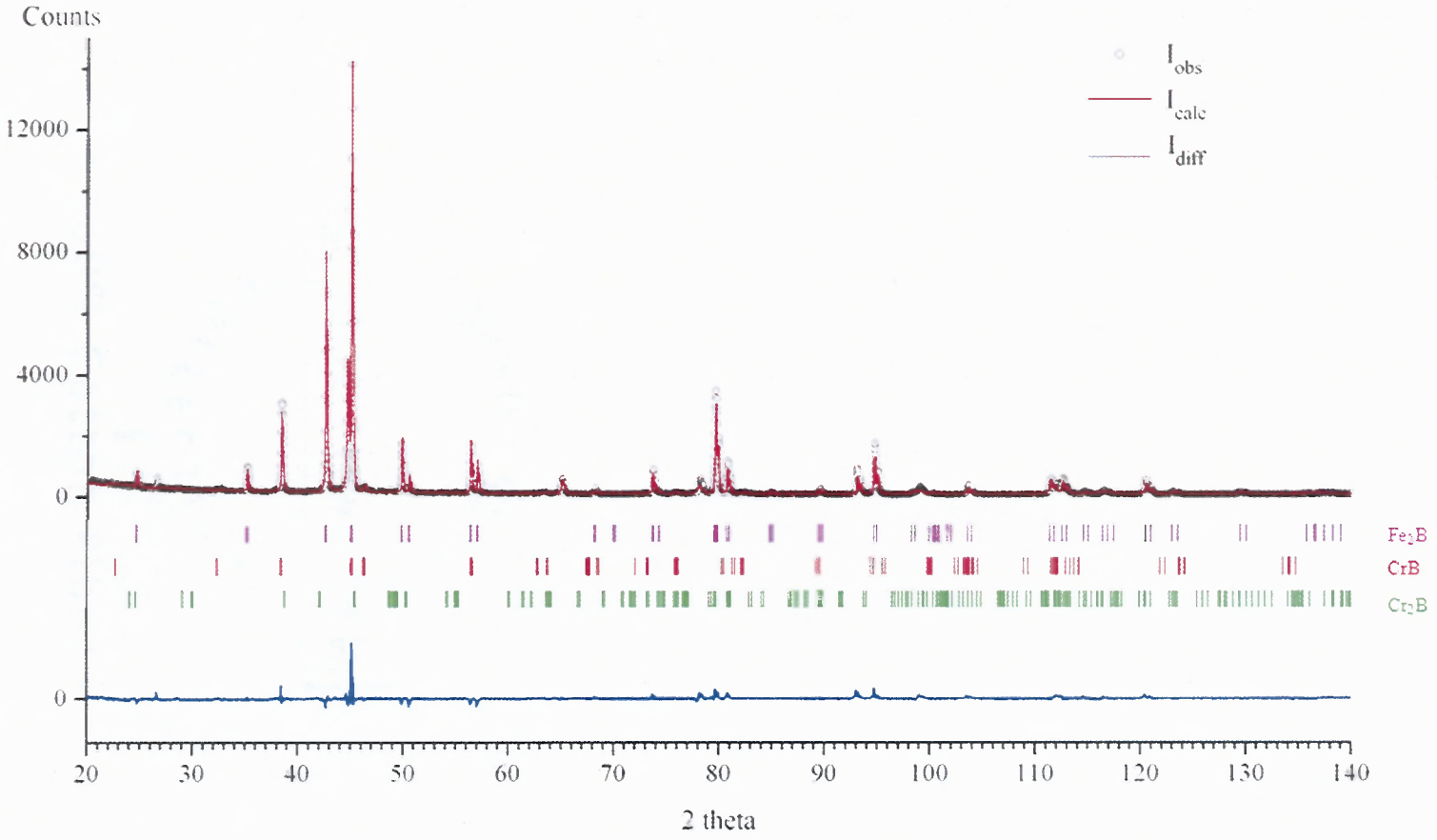

Figure 4.7 The XRD (refined with the Rietveld Refinement) of the boride coating in the boron-chromium-iron (B-Cr-Fe) system.

Table 4.2 The Lattice Parameters, Microstrain and Crystal Size of Boride Coating in the Boron-Chromium-Iron (B-Cr-Fe) System

Phase presence	% Phase composition	Lattice parameters	Microstrain (%)	Crystal size (Å)
Fe_2B	81.4	a = b = 5.11220 Å c = 4.24847 Å vol.= 111.03190 $Å^3$ (Tetrahedral)	0.051	548.10
Cr_2B	5.4	a = 4.25689 Å b = 7.34201 Å c = 13.84783 Å vol.= 432.80200 $Å^3$ (Orthorhombic)	0.21	153.30
CrB	13.2	a = 2.96595 Å b = 7.86375 Å c = 2.96113 Å vol.= 69.06407 $Å^3$ (Orthorhombic)	0.12	273.47
R_p = 10.58 % R_{wp} = 13.63% GOF = 4.58				

4.2.3 Synchrotron Microdiffraction and Microfluorescence

The results of B-Cr-Fe system from microdiffraction and microfluorescence were shown in Figures 4.8 and 4.9, respectively. In Figure 4.8, the 3-dimensional graph of intensity, 2-theta and distance was plotted and analyzed. CrB phase was detected at the distance between 10 - 45 μm at 2θ = 25.8, 30.5, and 35.4. In Figure 4.9, the element profile which measured by microfluorescence also confirmed the presence of chromium atoms in the substrate.

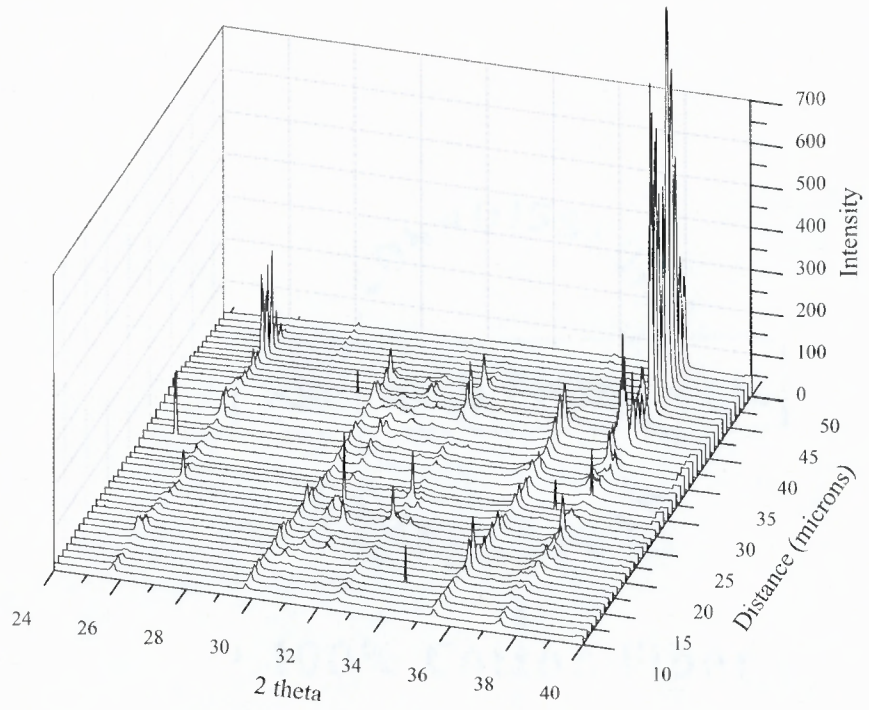

Figure 4.8 The microdiffraction of B-Cr-Fe system.

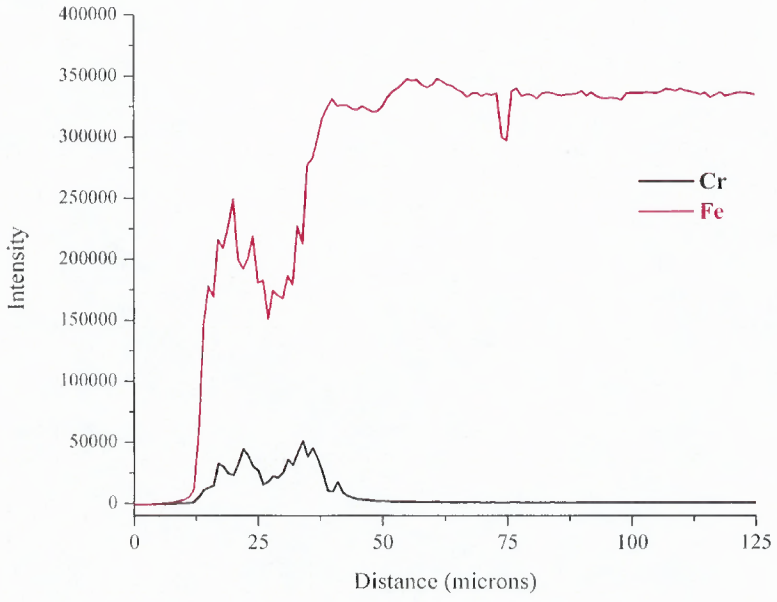

Figure 4.9 The microfluorescence of B-Cr-Fe system.

4.2.4 Microhardness

In B-Cr-Fe system, 3 types of borides phases (e.g., Fe_2B, Cr_2B, and CrB) were formed. Generally, Fe_2B phase has the microhardness of about 1800 – 2000 HV and CrB phase has the microhardness of about 2280 HV. The microhardness measurement of boride layers were detected across the coating through the substrate as depicted in Figure 4.10.

As seen in Figure 4.10 the boride coating had the maximum microhardness about 2100 HK while that of the substrate was roughly 140 HK. The microhardness was measured at about 1700 HK at the coating depth of 10 microns from the surface, which was the effect from the fracture at the surface.

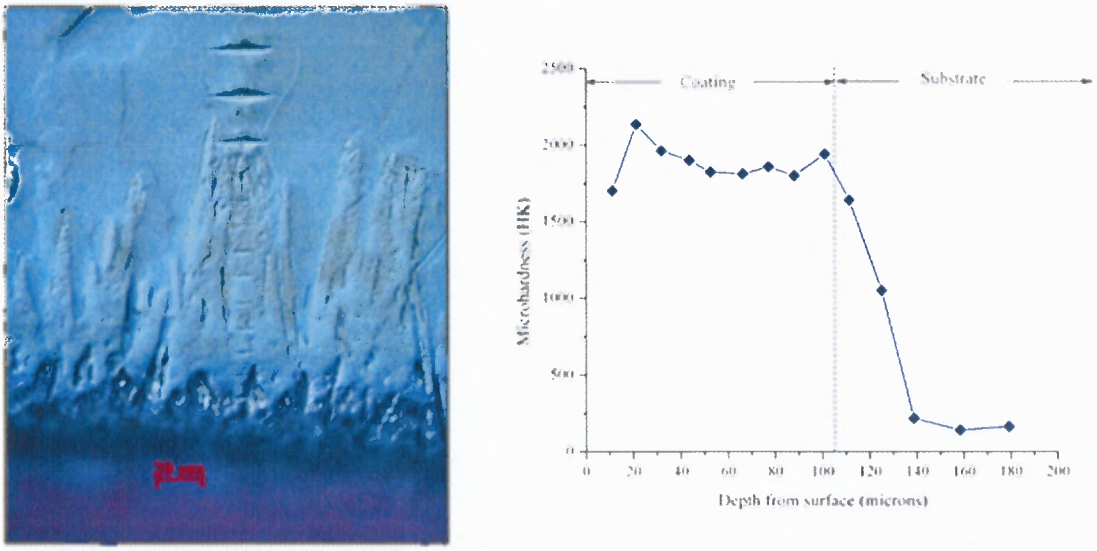

Figure 4.10 The plot between the microhardness and the depth from the surface of boride coating in the boron-chromium-iron (B-Cr-Fe) system.

4.2.5 Corrosion Resistance

The corrosion resistance of coating in B-Cr-Fe system was tested in 0.5 M H_2SO_4 for 12 hours. The weight change per area (mg/mm^2) of the specimen was plotted against time (mins) as shown in Figure 4.11. For 12 hour exposure time in the corrosive media, the weight loss per area of the borochromized coating was constant at about 0.04 mg/mm^2.

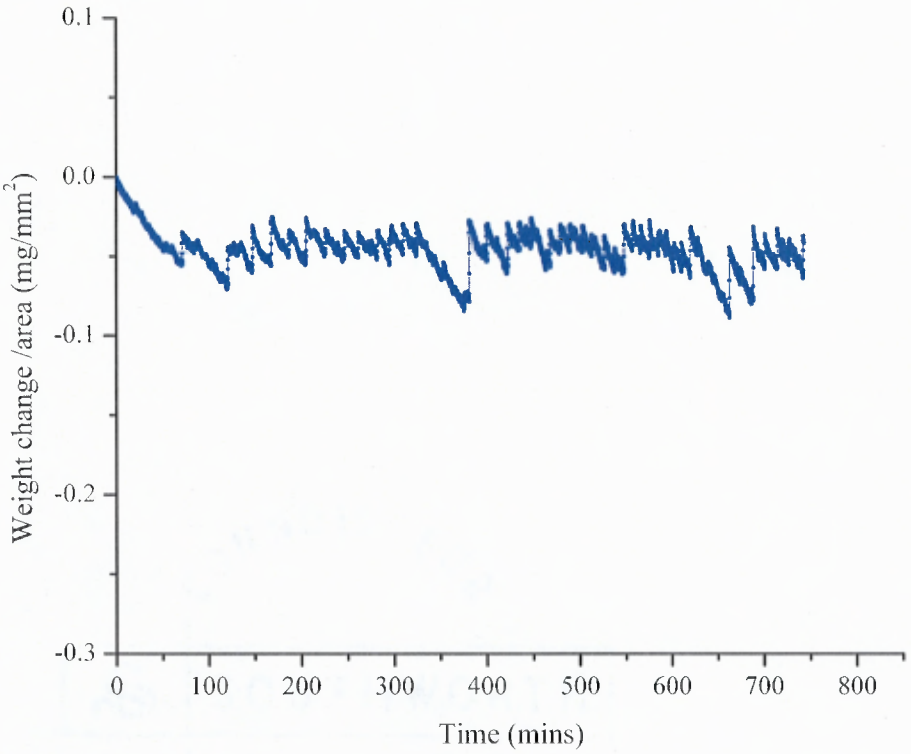

Figure 4.11 The corrosion resistance of boride coating in the boron-chromium-iron (B-Cr-Fe) system (in 0.5 M H_2SO_4).

4.2.6 Oxidation Resistance

The high temperature oxidation resistance of coating in B-Cr-Fe system was detected as a plot of weight change per area (mg/mm^2) against time (mins) as shown in Figure 4.12.

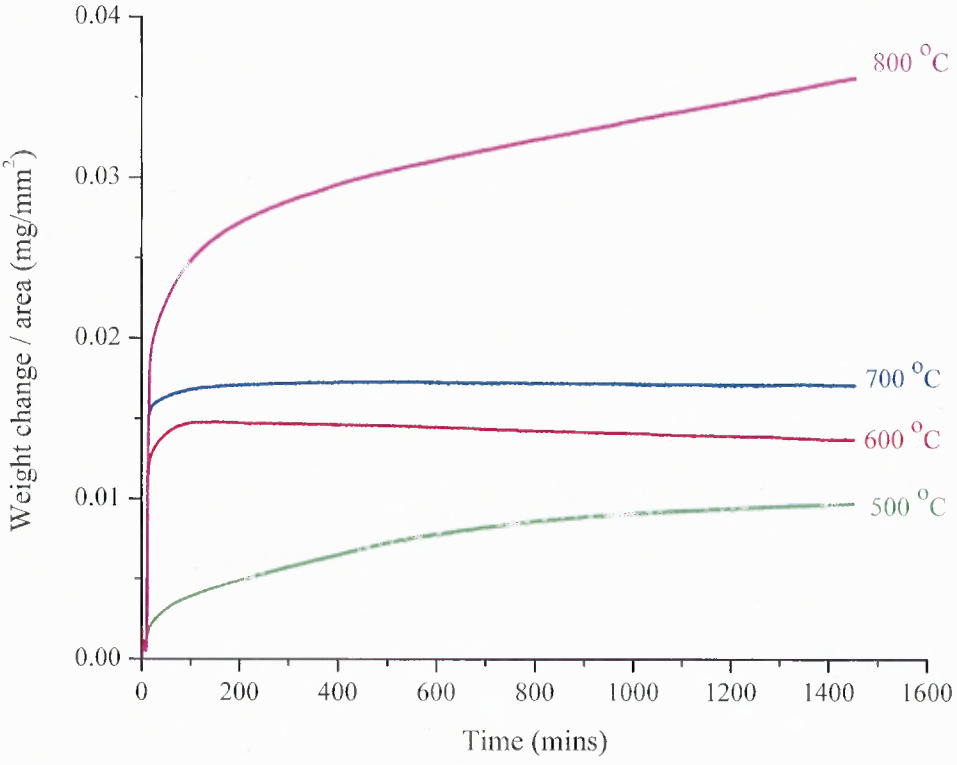

Figure 4.12 The high temperature oxidation resistance of boride coating in the boron-chromium-iron (B-Cr-Fe) system which coated on low carbon steel AISI 1018 substrate at a temperature range of 500 to800 °C for 24 hours.

4.3 Boron – Molybdenum - Iron (B - Mo - Fe) Experiments

The results of boron-molybdenum-iron coating experiments are discussed as follows.

4.3.1 Microstructure

In the boron-molybdenum-iron system, the needle-like structure with the coating thickness about 116.91 ± 2.37 was observed from the cross-sectional specimen. The morphology images of boromolybdenized specimen and the coating thickness distribution were shown in Figure 4.13.

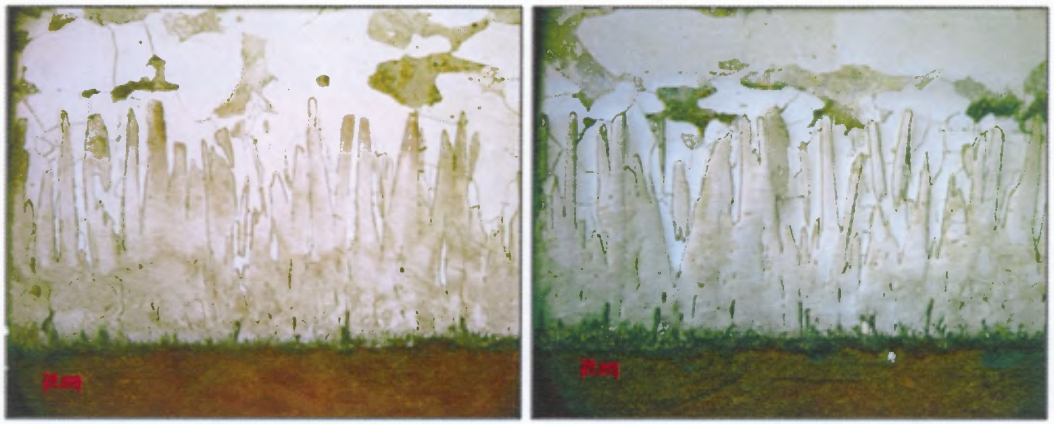

a) b)

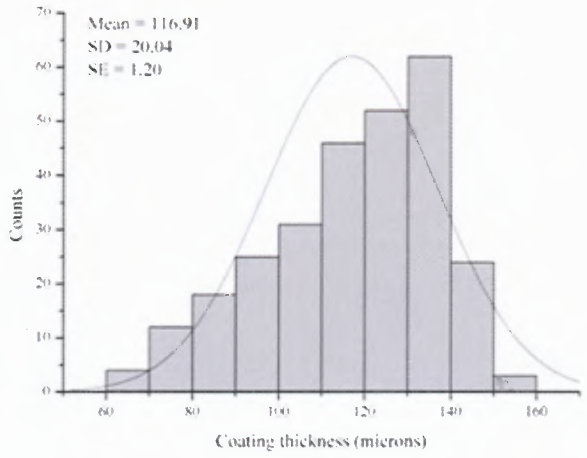

c)

Figure 4.13 The morphology images of boride coating (in the B-Mo-Fe system) on low carbon steel AISI 1018 a) under bright field, b) under differential interface contrast (DIC), and c) the distribution of coating thickness.

4.3.2 Phase Identification

The XRD pattern of boronmolybdenized specimen in boron-molybdenum-iron system was refined by Rietveld method as illustrated in Figure 4.14. The quantitative phase analysis from Rietveld refinement method was shown that the boron-molybdenum-iron coating was composed of 88.1 % weight of Fe_2B and 11.9 % weight of MoB. The Rietveld standard agreement indices were the residual profile (R_p) = 8.16 %, the weighted residual profile (R_{wp}) = 11.75 % and the good of fitness (GOF) = 4.58. The refinements of lattice parameters, microstrain and crystal size of Fe_2B and MoB phases of boron-molybdenum-iron coating are shown in Table 4.3. Details and analysis of the phase identification and analysis are further addressed in Chapter 5 Section 5.2, sub-section 5.2.1.

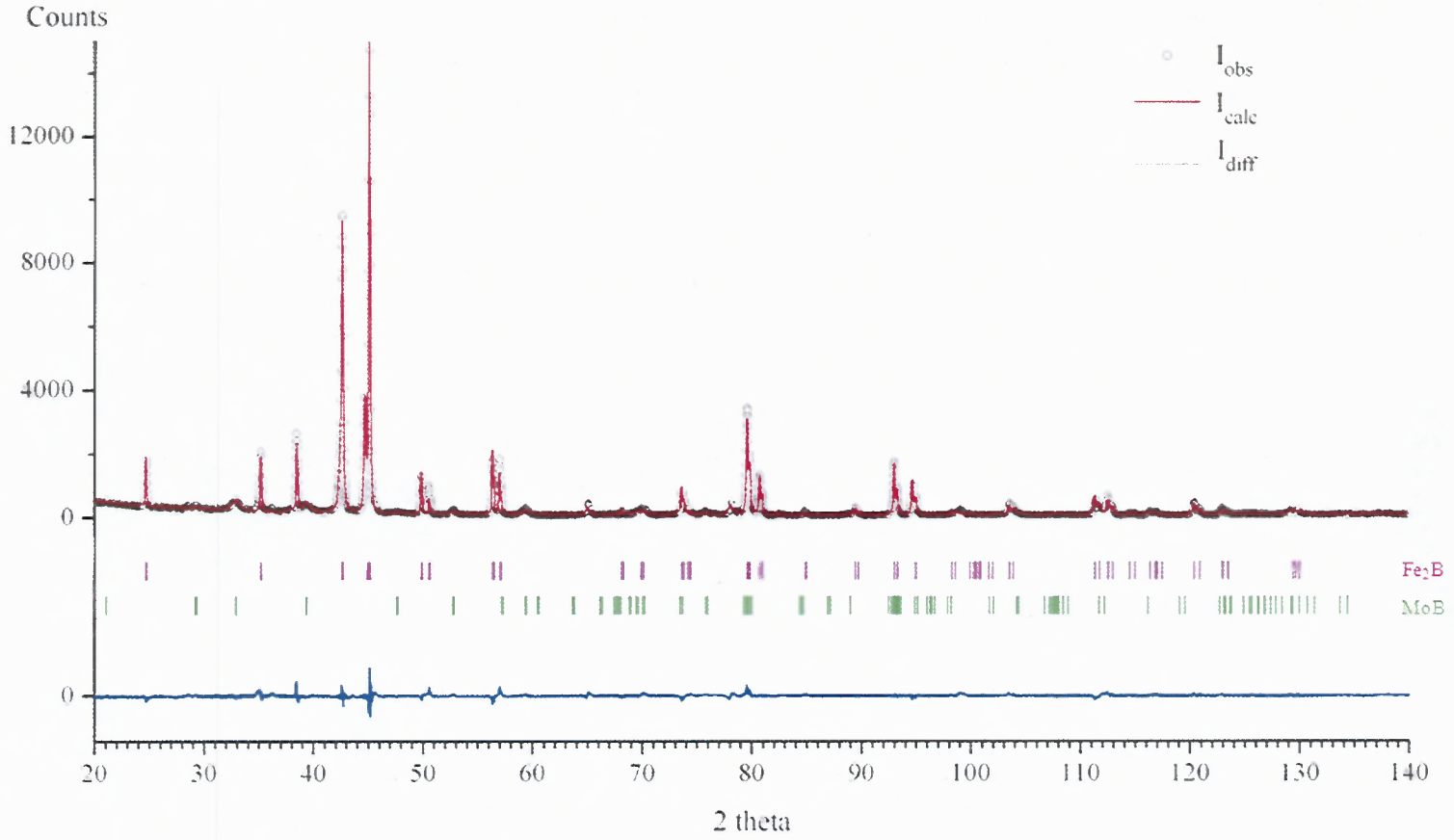

Figure 4.14 The XRD pattern (refined with the Rietveld Refinement) of the boride coating in the boron-molybdenum-iron (B-Mo-Fe) system.

Table 4.3 The Lattice Parameters, Microstrain and Crystal Size of Boride Coating in the Boron-Molybdenum-Iron (B-Mo-Fe) System

Phase presence	% Phase composition	Lattice parameters	Microstrain (%)	Crystal size (Å)
Fe_2B	88.1	a = b = 5.11357 Å c = 4.25066 Å vol.= 111.14860 $Å^3$ (Tetrahedral)	0.062	441.74
MoB	11.9	a = b = 3.11845 Å c = 16.95622 Å vol.= 164.89430 $Å^3$ (Orthorhombic)	0.22	82.96
R_p = 8.16 % R_{wp} = 11.75 % GOF = 4.58				

4.3.3 Synchrotron Microdiffraction and Microfluorescence

The results of B-Mo-Fe system from microdiffraction and microfluorescence were shown in Figures 4.15 and 4.16, respectively. In Figure 4.15, the 3-dimensional graph of intensity, 2-theta and distance was plotted and observed. MoB phase was detected at the distance between 5 - 20 μm at 2θ = 26.0, 31.2, 33.6, and 33.7. In Figure 4.16, the element profile which measured by microfluorescence also confirmed the presence of molybdenum atoms in the substrate.

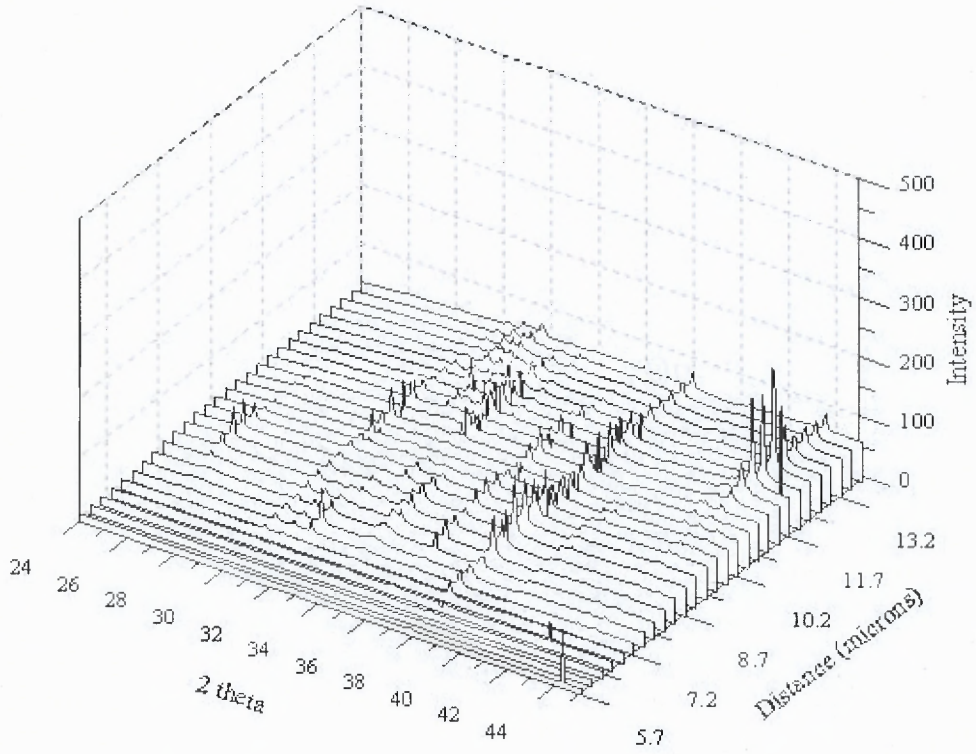

Figure 4.15 The microdiffraction of B-Mo-Fe system.

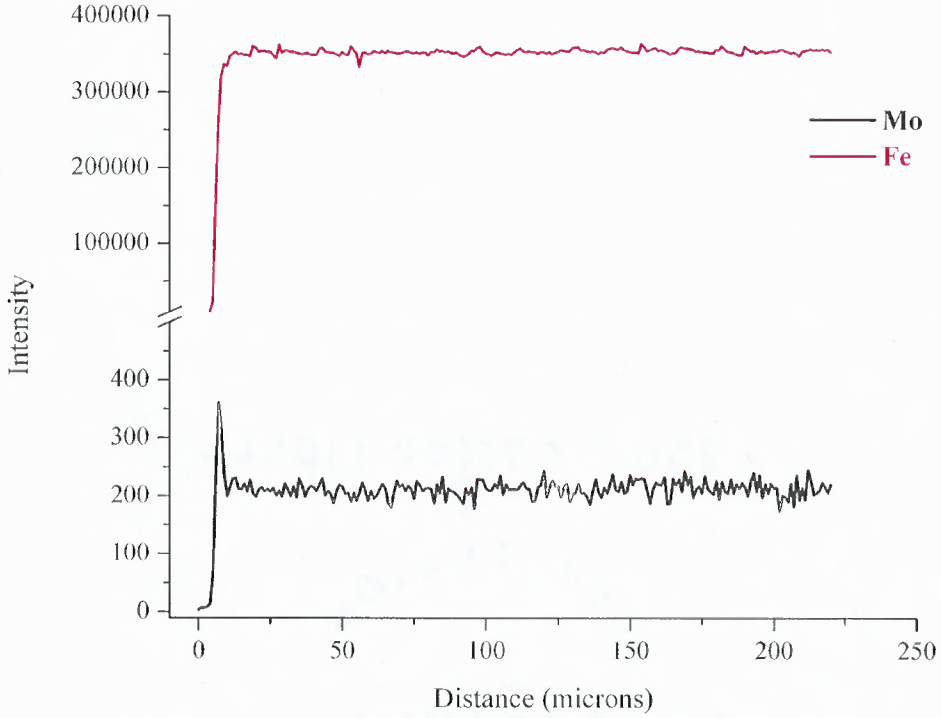

Figure 4.16 The microfluorescence of B-Mo-Fe system.

4.3.4 Microhardness

In B-Mo-Fe system, 2 types of borides phases (e.g., Fe_2B and MoB) were found as the coating. Genarally, Fe_2B phase has the microhardness of about 1800 - 2000 HV and MoB phase has the microhardness of about 2260 HV. The microhardness measurement of boride layers were detected across the coating through the substrate as depicted in Figure 4.17.

As seen in Figure 4.17, the coating had the maximum microhardness at 2142 HK while the microhardness of the substrate was roughly 140 HK. The microhardness was measured at about 1250 HK at the coating depth about 5 μm from the surface, which was from the fracture near the surface.

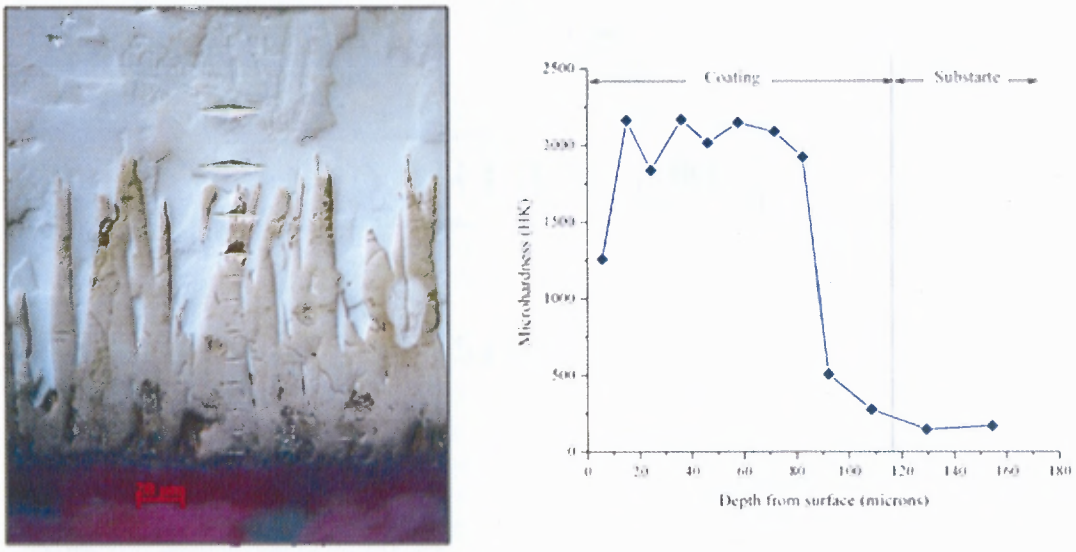

Figure 4.17 The plot between the microhardness and the depth from the surface of boride coating in the boron-molybdenum-iron (B-Mo-Fe) system.

4.3.5 Corrosion Resistance

The corrosion resistance of coating in B-Mo-Fe system was tested in 0.5 M H_2SO_4 for 12 hours. The weight change per area (mg/mm^2) of the specimen was plotted against time (mins) as shown in Figure 4.18. The weight loss of boromolybdenized specimen was constant at about 0.05 mg/mm^2.

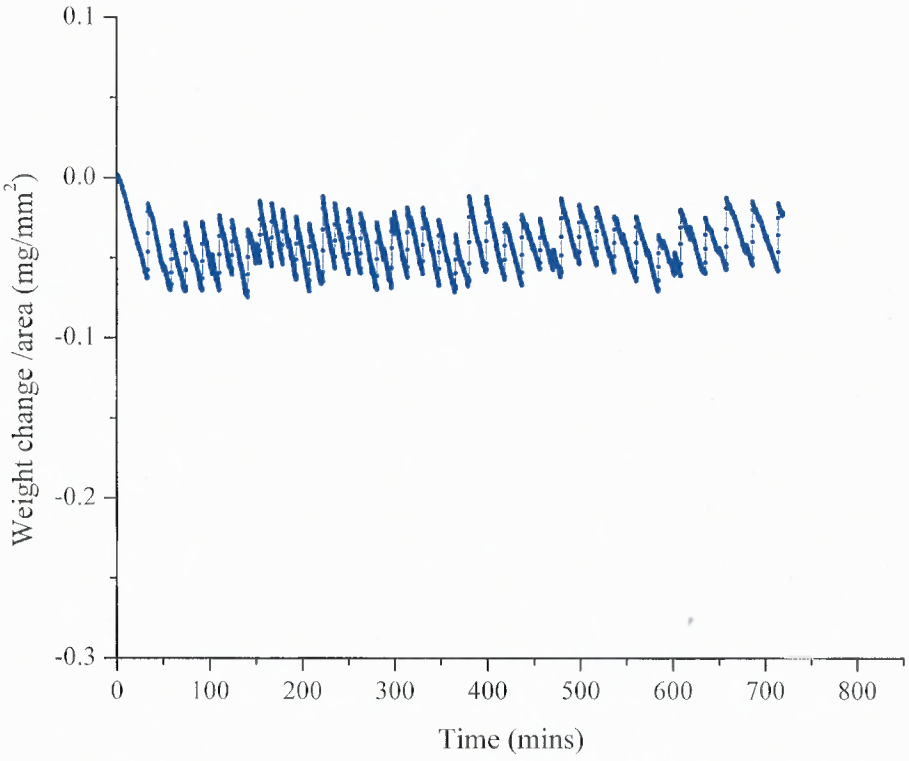

Figure 4.18 The corrosion resistance of boride coating in the boron-molybdenum-iron (B-Mo-Fe) system (in 0.5 M H_2SO_4).

4.3.6 Oxidation Resistance

The high temperature oxidation resistance of coating in B-Mo-Fe system was detected as a plot of weight change per area (mg/mm^2) against time (mins) at temperature between 500 to 800 °C as shown in Figure 4.19.

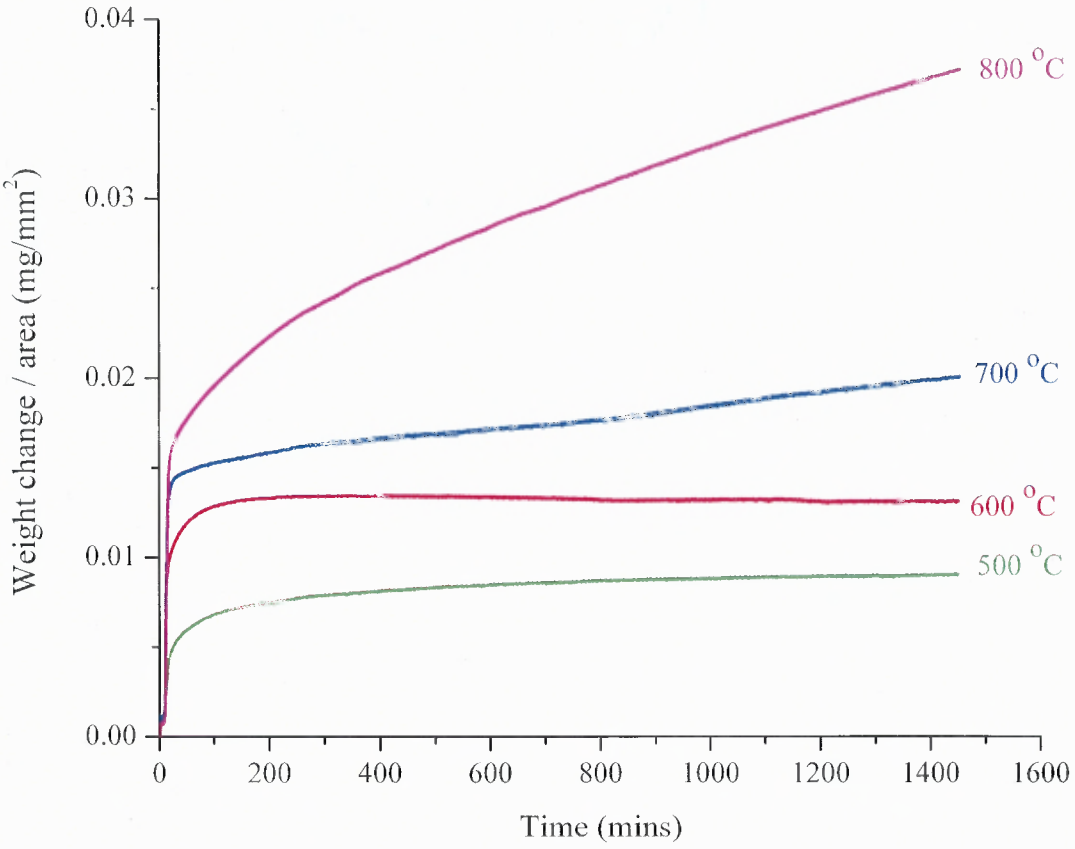

Figure 4.19 The high temperature oxidation resistance of boride coating in the boron-molybdenum-iron (B-Mo-Fe) system which coated on low carbon steel AISI 1018 substrate at a temperature range of 500 to 800 °C for 24 hours.

4.4 Boron – Tungsten - Iron (B-W-Fe) Experiments

The results of boron-tungsten-iron coating experiments are discussed as follows.

4.4.1 Microstructure

In the boron-iron system, the needle-like or saw tooth structure was observed from the cross-sectional specimen. The thickness of boride coating was about 144.39 ± 2.25 μm. The morphology images of coated specimen and the coating thickness distribution were shown in Figure 4.20.

Moreover, the microstructure images in Figure 4.20 revealed the parallel cracks formed inside the coating.

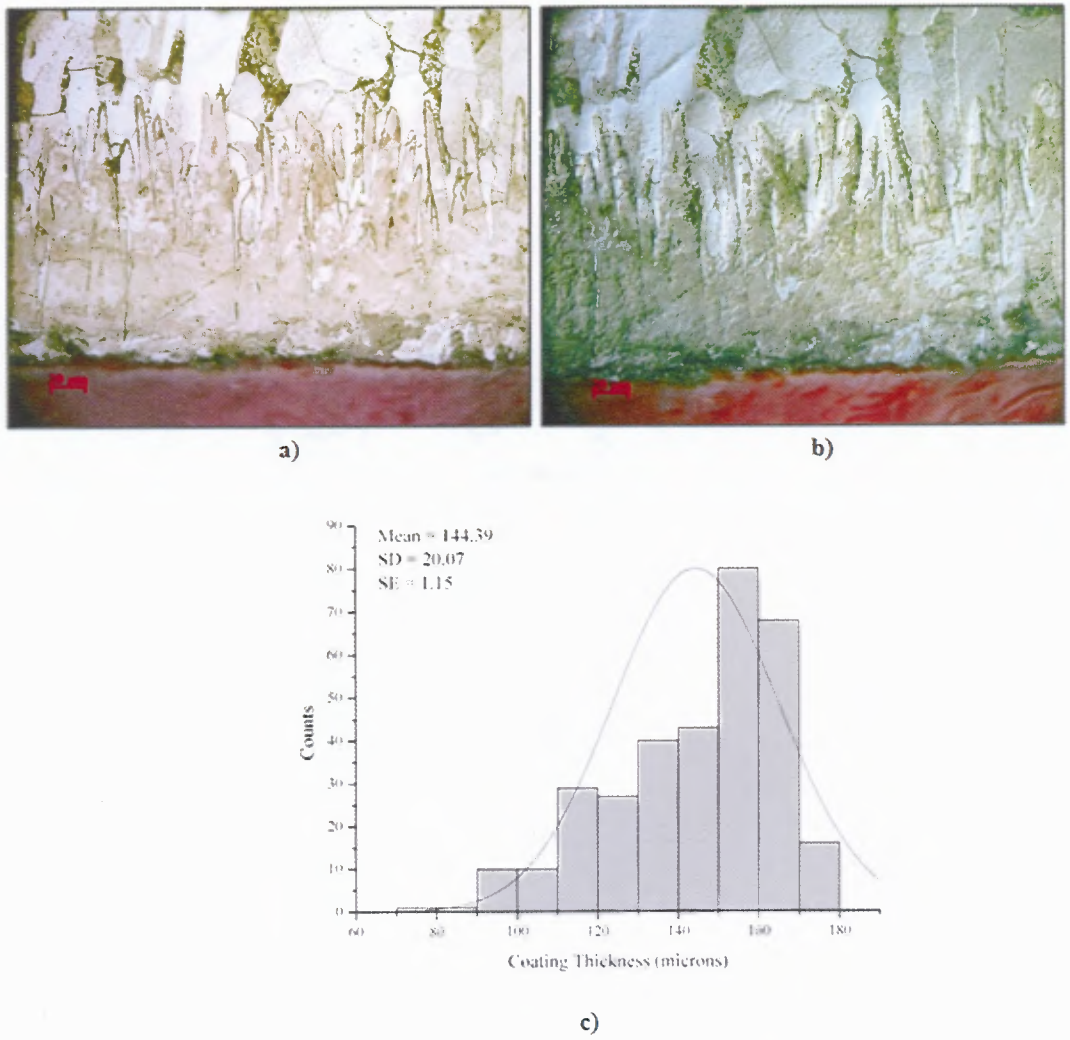

Figure 4.20 The morphology images of boride coating (in the B-W-Fe system) on low carbon steel AISI 1018 a) under bright field, b) under differential interface contrast (DIC), and c) the distribution of coating thickness.

4.4.2 Phase Identification

The XRD pattern of borotunstenized specimen in boron-tungsten-iron system was refined by the Rietveld refinement method as illustrated in Figure 4.21. The quantitative phase analysis from the Rietveld refinement method was shown that the boron-tungsten-iron coating was composed of 7.2 % weight of Fe_2B, 75.3 % weight of FeB, 7.4 % weight of W_2B, and 10.1 % weight of Fe_7W_6. The Rietveld standard agreement indices were the residual profile (R_p) = 11.13 %, the weighted residual profile (R_{wp}) = 14.41 % and the good of fitness (GOF) = 5.60. The refinements of lattice parameters, microstrain and crystal size of Fe_2B, FeB, W_2B, and Fe_7W_6 phases of boron-tungsten-iron coating were shown in Table 4.4. Details and analysis of the phase identification and analysis are further addressed in Chapter 5 Section 5.2, sub-section 5.2.1.

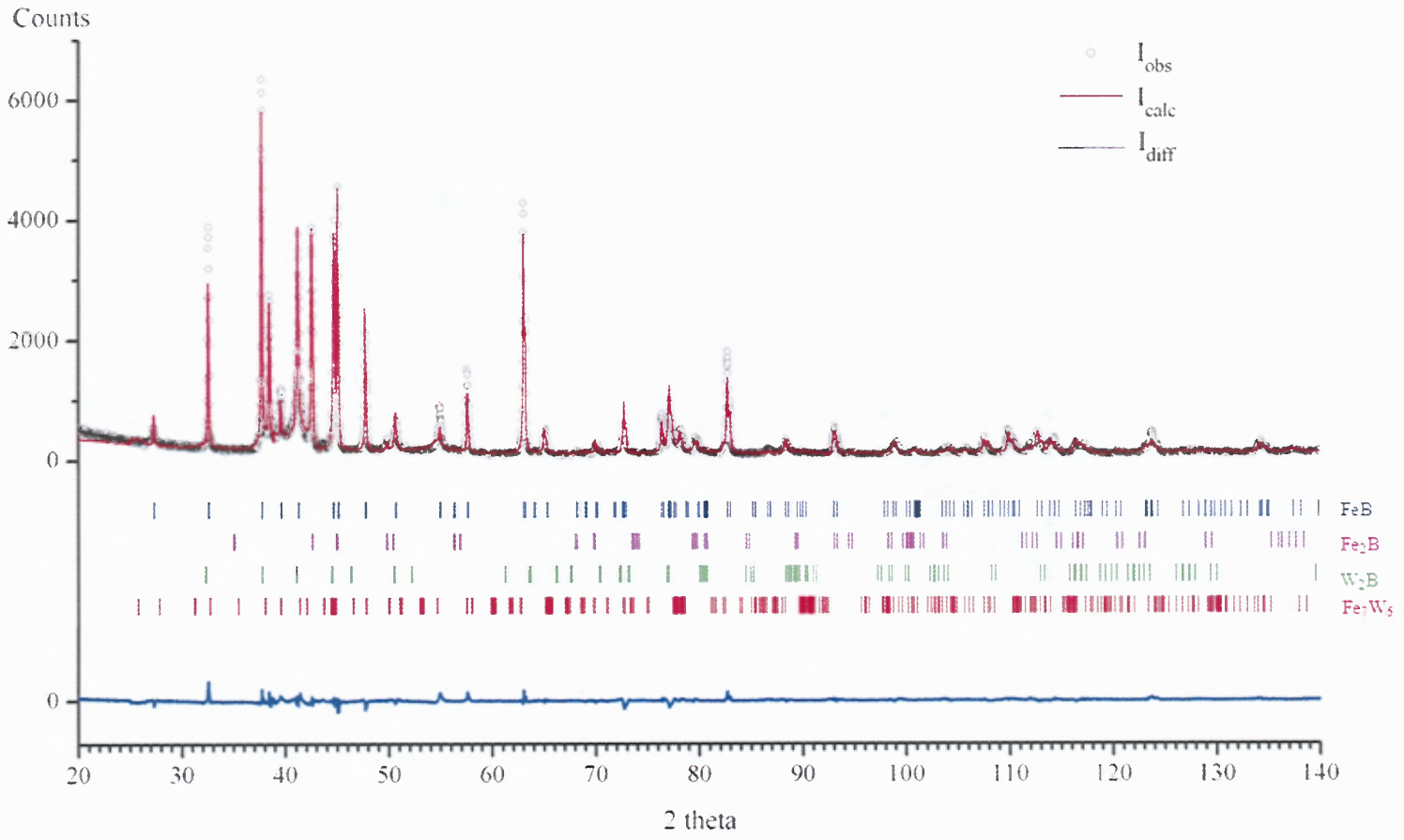

Figure 4.21 The XRD pattern (refined with the Rietveld Refinement) of the boride coating in the (B-W-Fe) system.

Table 4.4 The Lattice Parameters, Microstrain and Crystal Size of Boride Coating in the Boron-Tungsten-Iron (B-W-Fe) System

Phase presence	**% Phase composition**	**Lattice parameters**	**Microstrain (%)**	**Crystal size (Å)**
Fe_2B	7.2	a = b = 5.12832 Å c = 4.24797 Å vol.= 111.72030 $Å^3$ (Tetrahedral)	0.097	337.76
FeB	75.3	a = 5.50276 Å b = 2.94912 Å c = 4.06264 Å vol.= 65.92980 $Å^3$ (Orthorhombic)	0.067	494.05
W_2B	7.4	a = b = 5.54624 Å c = 4.76965 Å vol.= 146.17190 $Å^3$ (Tetrahedral)	0.30	113.60
Fe_7W_6	10.1	a = b = 4.63293 Å c = 25.81903 Å vol.= 479.74970 $Å^3$ (Trigonal)	0.60	43.95
R_p = 11.13 % R_{wp} = 14.41 % GOF = 5.60				

4.4.3 Synchrotron Microdiffraction and Microfluorescence

The results of B-W-Fe system from microdiffraction and microfluorescence were shown in Figures 4.22 and 4.23, respectively. In Figure 4.22, the 3-dimensional graph of intensity, 2-theta and distance was plotted and observed. W_2B phase was detected at the distance between 7 - 15 μm at 2θ = 24.4, 31.1, and 33.8. In Figure 4.23, the element profile which measured by microfluorescence also confirmed the presence of tungsten atoms in the substrate.

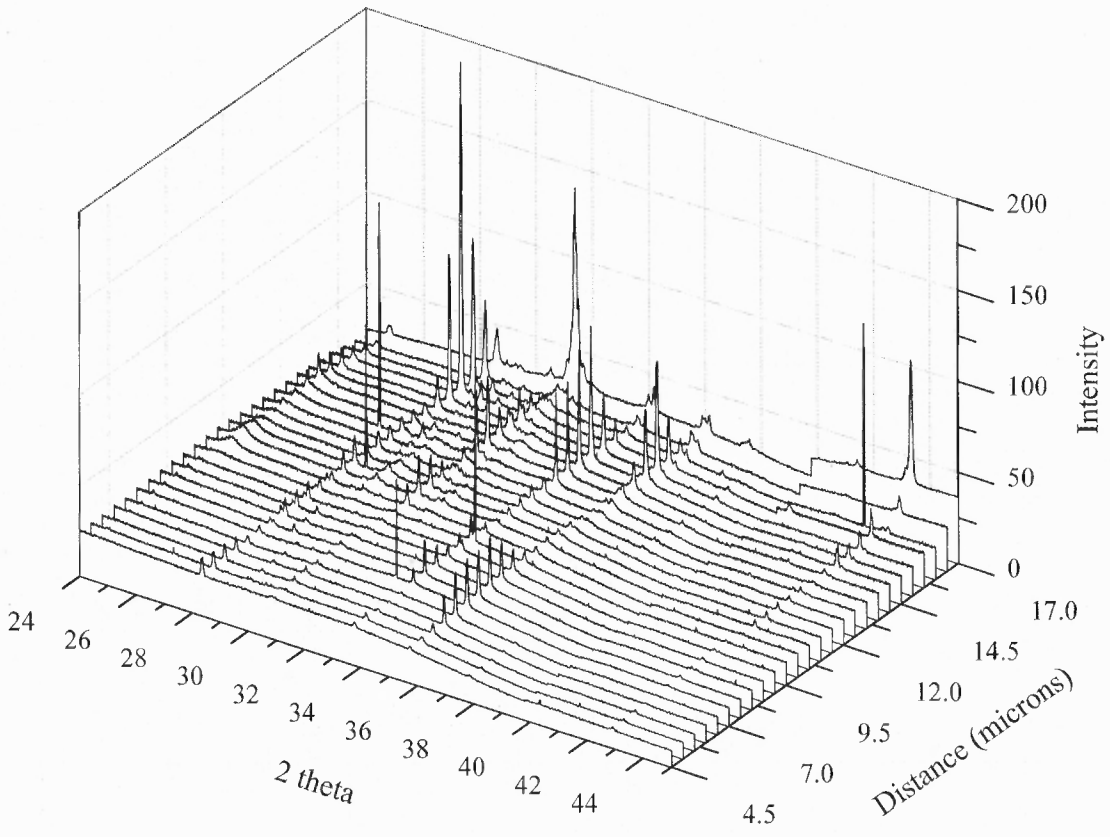

Figure 4.22 The microdiffraction of B-W-Fe system.

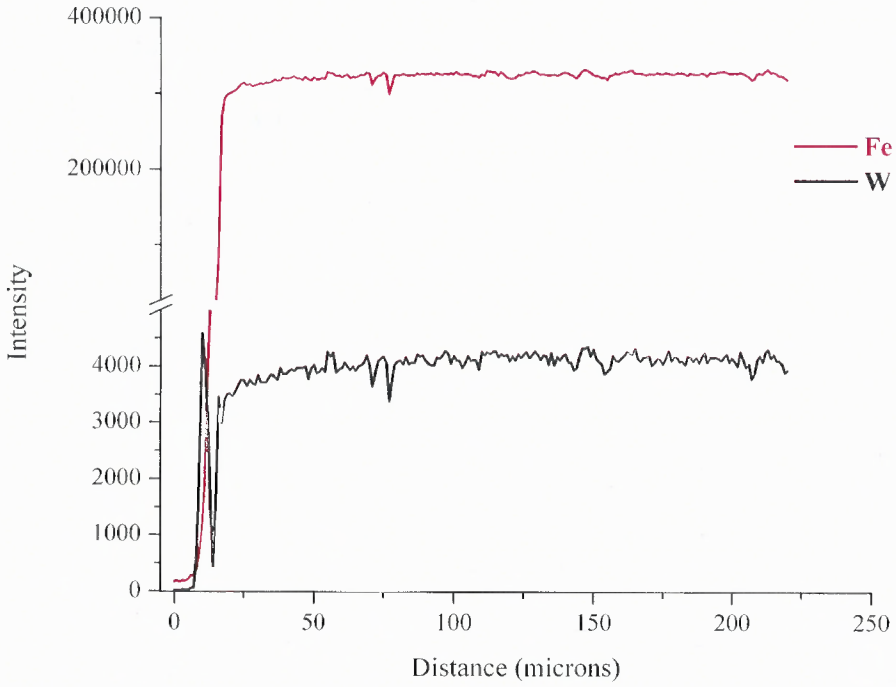

Figure 4.23 The microfluorescence of B-W-Fe system.

4.4.4 Microhardness

In B-W-Fe system, 4 types of borides phases (e.g., Fe_2B, FeB, W_2B, and Fe_7W_6) were formed. Generally, the inner layer of Fe_2B phase has the microhardness of about 1800 - 2000 HV. The layer of FeB phase has the microhardness of about 1900 – 2200 HV. The layer of W_2B phase has the microhardness of about 2400 - 2500 HV. The microhardness measurement of boride layers were detected across the coating through the substrate as depicted in Figure 4.24.

As seen in Figure 4.24, the coating had the maximum microhardness at 2640 HK and average microhardness at 2500 HK while that of the substrate was roughly 140 HK. At the coating depth of 30 - 40 μm, the measured microhardnesses were reduced because of the parallel cracks forming on the interior coating.

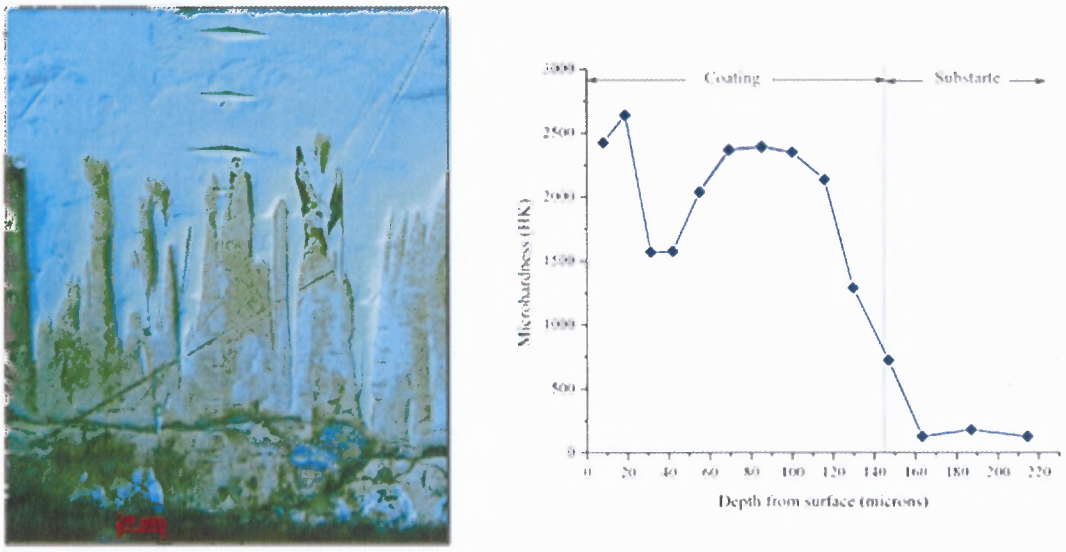

Figure 4.24 The plot between the microhardness and the depth from the surface of boride coating in the boron-tungsten-iron (B-W-Fe) system.

4.4.5 Corrosion Resistance

The corrosion resistance of the B-W-Fe specimen was tested in 0.5 M H_2SO_4 for 12 hours, which gave the constant weight loss per area at about 0.04 mg/mm^2. The weight change per area (mg/mm^2) of the borotunstenized specimen was plotted against time (mins) as shown in Figure 4.25.

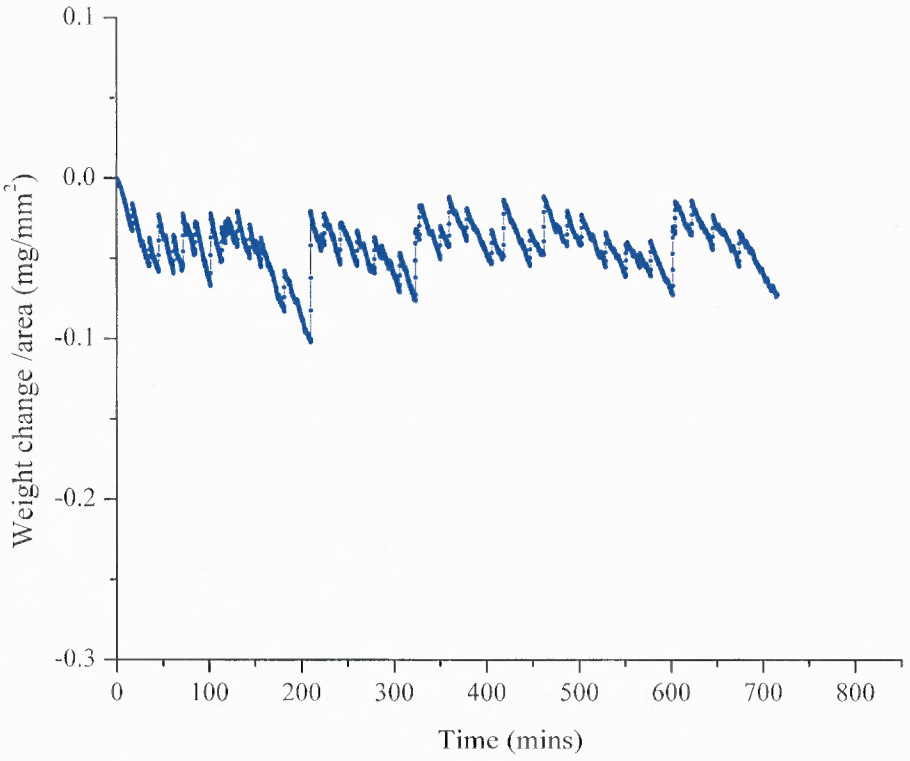

Figure 4.25 The corrosion resistance of boride coating in the boron-tungsten-iron (B-W-Fe) system (in 0.5 M H_2SO_4).

4.4.6 Oxidation Resistance

The high temperature oxidation resistance of coating in B-W-Fe specimen was detected as a plot of weight change per area (mg/mm^2) against time (mins) as shown in Figure 4.26.

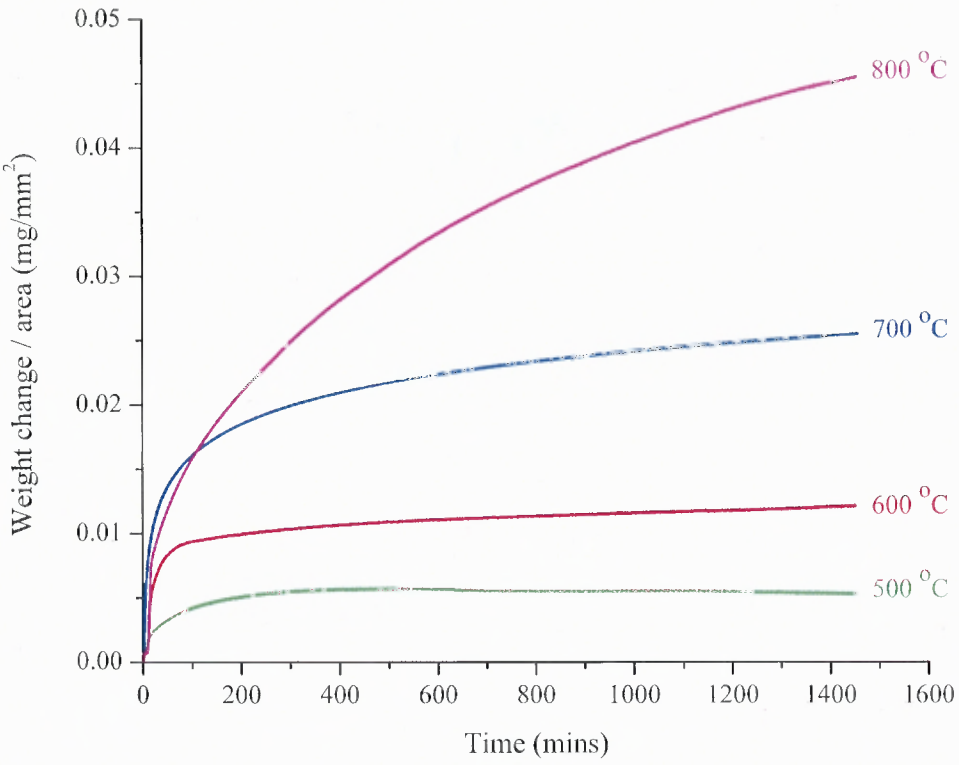

Figure 4.26 The high temperature oxidation resistance of boride coating in the boron-tungsten-iron (B-W-Fe) system which coated on low carbon steel AISI 1018 substrate at a temperature range of 500 to 800 °C for 24 hours.

4.5 Boron – Niobium - Iron (B-Nb-Fe) Experiments

The results of boron-niobium-iron coating experiments are discussed as follows.

4.5.1 Microstructure

In the boron-niobium-iron system, the needle-like or saw tooth structure was observed from the cross-sectional specimen. The thickness of boride coating was about 92.65 ± 2.77 μm. The morphology images of boroniobized and the coating thickness distribution were shown in Figure 4.27.

In Figure 4.27 b) the pores were observed on the coating; however, the parallel cracks and fracture at the surface were not observed. Moreover, the needle structures were wider than boron coatings in Group VIB.

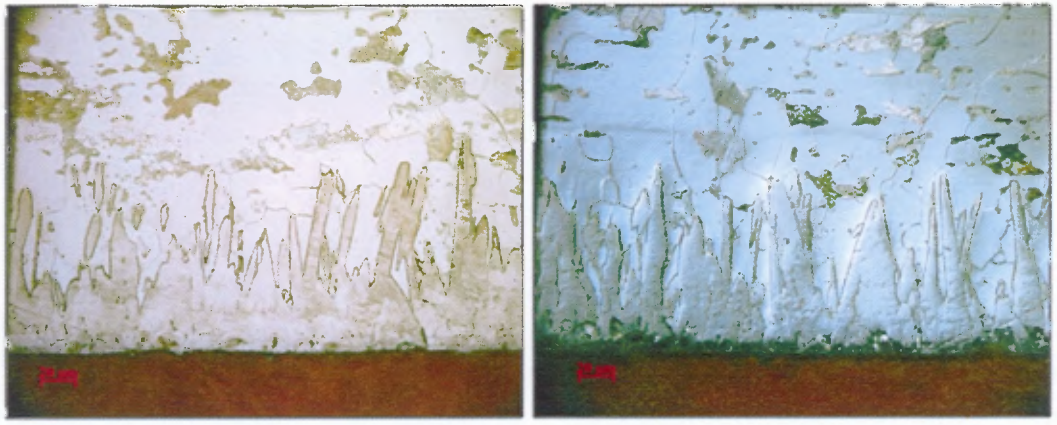

a) b)

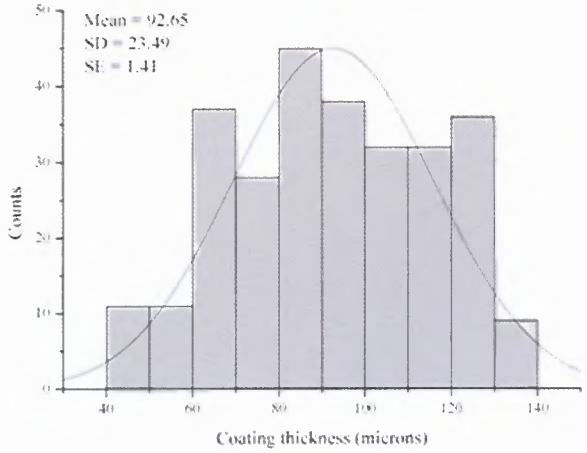

c)

Figure 4.27 The morphology images of boride coating (in the B-Nb-Fe system) on low carbon steel AISI 1018 a) under bright field, b) under differential interface contrast (DIC), and c) the distribution of coating thickness.

4.5.2 Phase Identification

The XRD pattern of coated specimen in boron-niobium-iron system was refined by the Rietveld refinement method as illustrated in Figure 4.28. The quantitative phase analysis from the Rietveld refinement method was shown that the boron-niobium-iron coating was composed of 89.0 % weight of Fe_2B and 11.0 % weight of NbC. The Rietveld standard agreement indices were the residual profile (R_p) = 8.94 %, the weighted residual profile (R_{wp}) = 12.56 % and the good of fitness (GOF) = 5.32. The refinements of lattice parameters, microstrain and crystal size of Fe_2B and NbC phases of boron-niobium-iron coating were shown in Table 4.5. Details and analysis of phase identification and analysis are further addressed in Chapter 5 Section 5.2, sub-section 5.2.1.

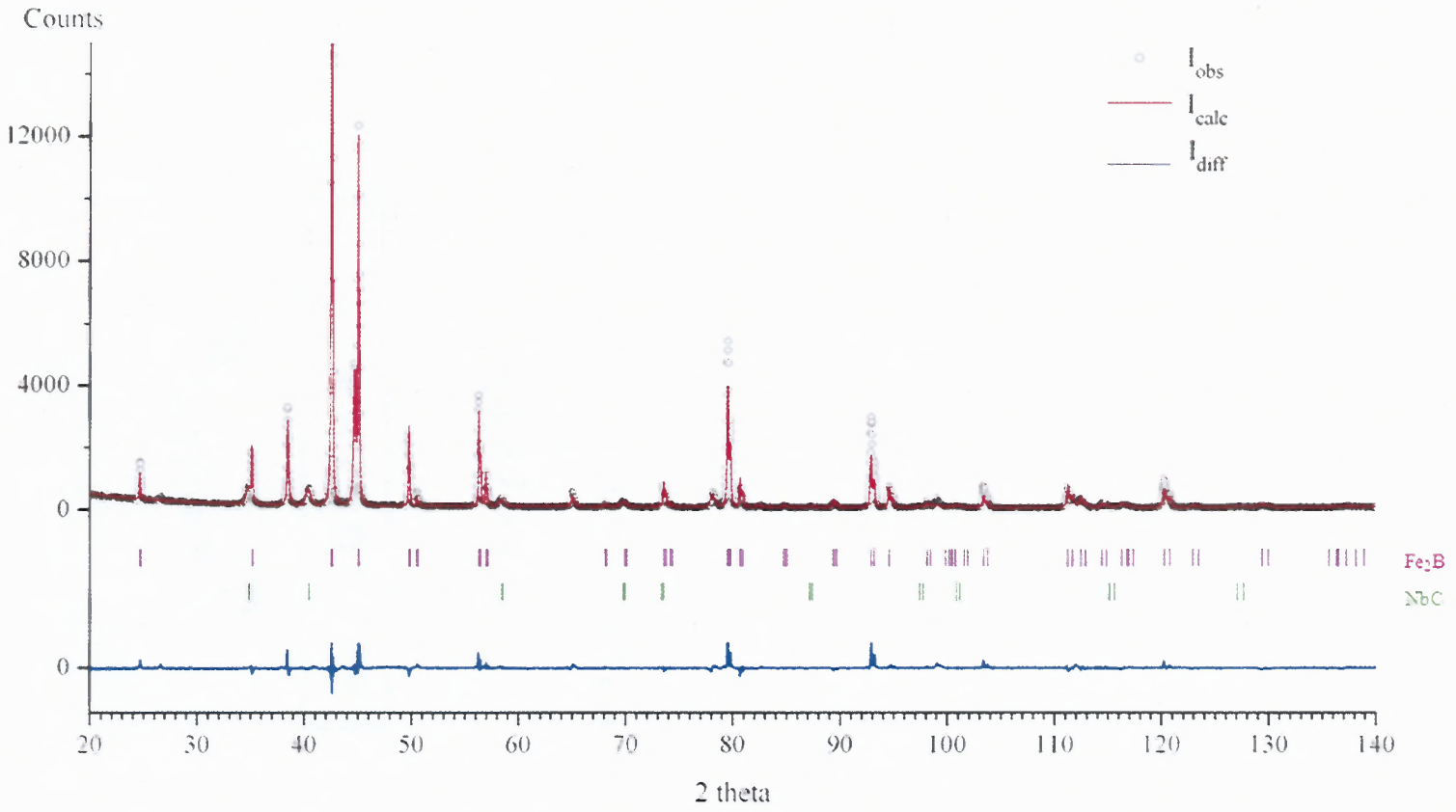

Figure 4.28 The XRD pattern (refined with the Rietveld Refinement) of the boride coating in the boron-niobium-iron (B-Nb-Fe) system.

Table 4.5 The Lattice Parameters, Microstrain and Crystal Size of Boride Coating in the Boron-Niobium-Iron (B-Nb-Fe) System

Phase presence	**% Phase composition**	**Lattice parameters**	**Microstrain (%)**	**Crystal size (Å)**
Fe_2B	89.0	a = b = 5.11474 Å c = 4.25376 Å vol.= 111.28080 $Å^3$ (Tetrahedral)	0.069	451.45
NbC	11.0	a = b = c = 4.47253 Å vol.= 89.46633 $Å^3$ (Cubic)	0.15	150.75
R_p = 8.94 % R_{wp} = 12.65 % GOF = 5.32				

4.5.3 Synchrotron Microdiffraction and Microfluorescence

The results of B-Nb-Fe system from microdiffraction and microfluorescence were shown in Figures 4.29 and 4.30, respectively. In Figure 4.29, the 3-dimensional graph of intensity, 2-theta and distance was plotted and observed. NbC phase was detected at the distance between 17-27 μm at 2θ = 27.80 and 32.22. In Figure 4.30, the element profile which measured by microfluorescence also confirmed the presence of niobium atoms in the substrate.

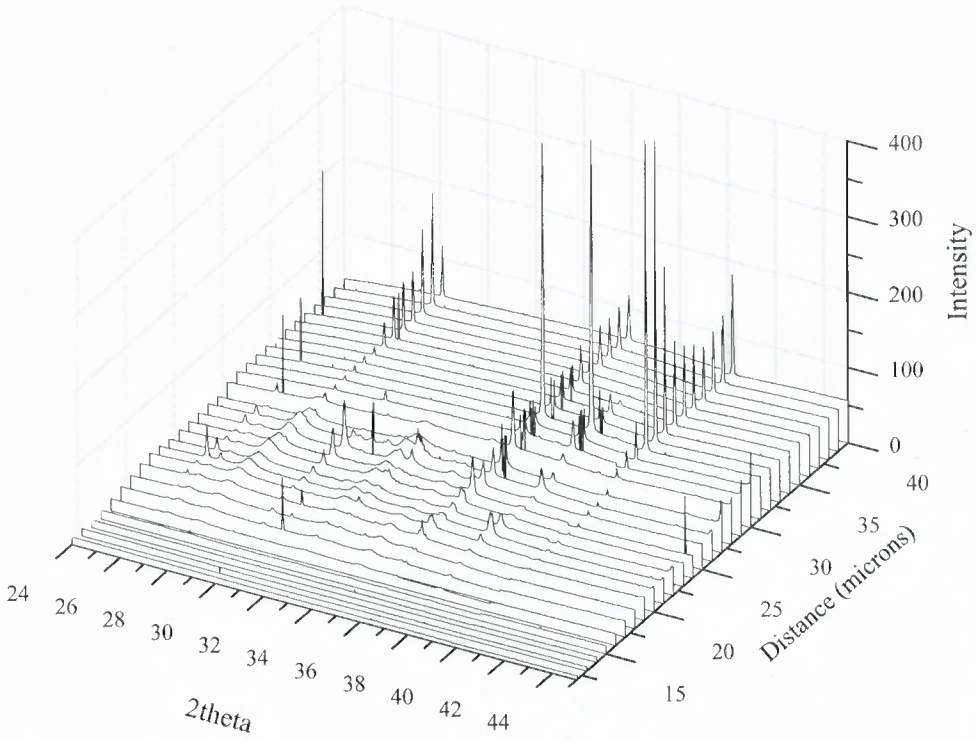

Figure 4.29 The microdiffraction of B-Nb-Fe system.

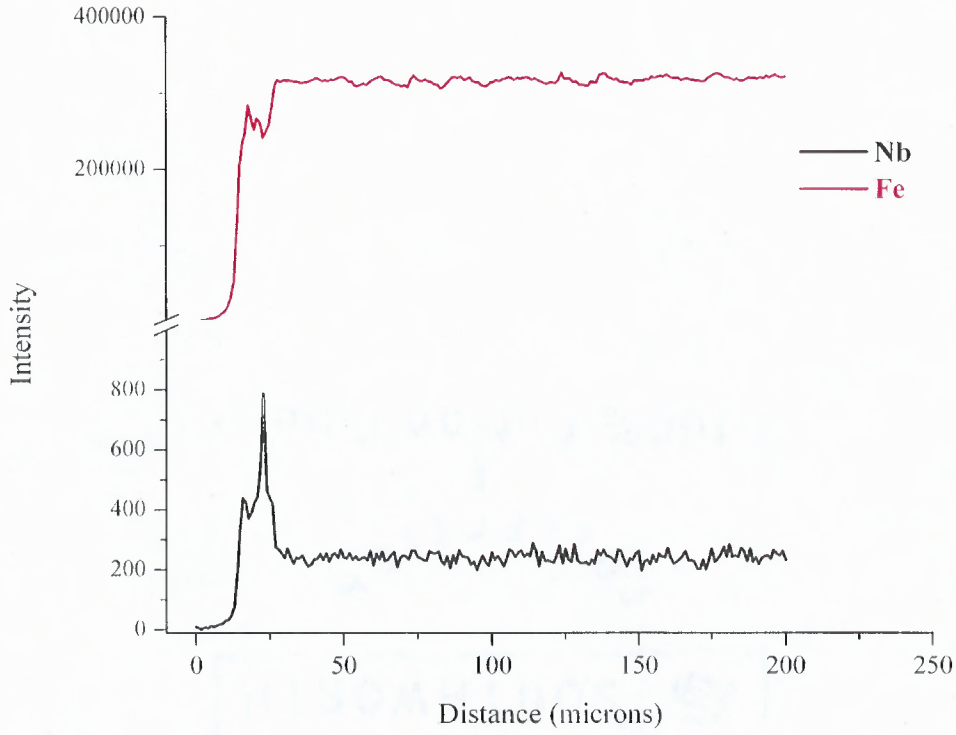

Figure 4.30 The microfluorescence of B-Nb-Fe system.

4.5.4 Microhardness

In B-Nb-Fe system, 2 types of borides phases (e.g., Fe_2B and NbC) were formed. The inner layer of Fe_2B phase has the microhardness of about 1800 – 2000 HV. The outer layer of NbC phase has the microhardness of about 2300 - 2700 HV. The microhardness measurement of boride layers were detected across the coating through the substrate as depicted in Figure 4.31.

As seen in Figure 4.31, the boride coating had the maximum microhardness about 2722 HK at the edge and average microhardness about 2100 HK while that of the substrate was roughly 140 HK.

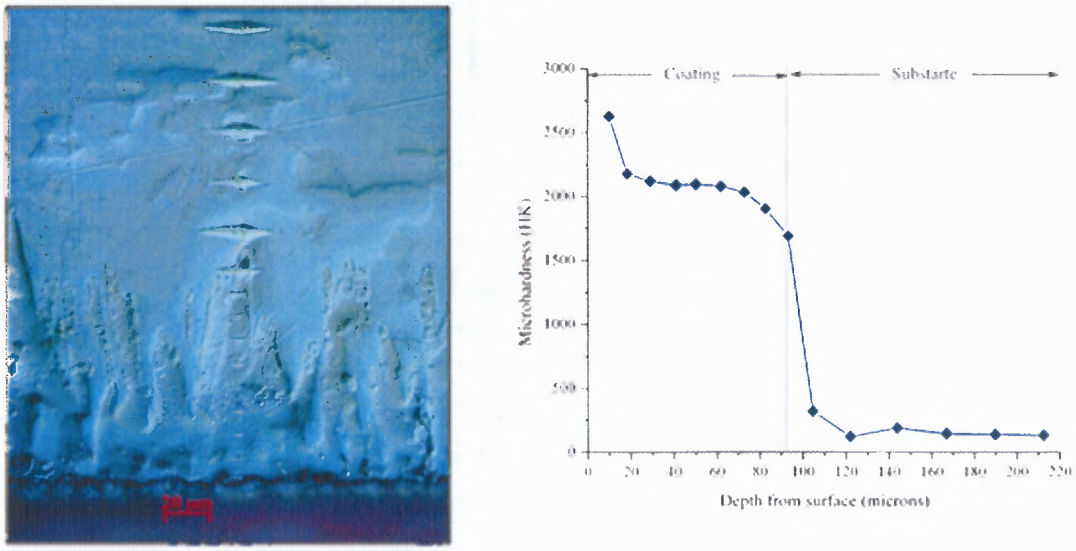

Figure 4.31 The plot between the microhardness and the depth from the surface of boride coating in the boron-niobium-iron (B-Nb-Fe) system.

4.5.5 Corrosion Resistance

The corrosion resistance of coating in B-Nb-Fe system was tested in 0.5 M H_2SO_4 for 12 hours and found that the weight loss per area of boroniobized specimen was constant at 0.07 mg/mm^2. The weight change per area (mg/mm^2) of the specimen was plotted against time (mins) as shown in Figure 4.32.

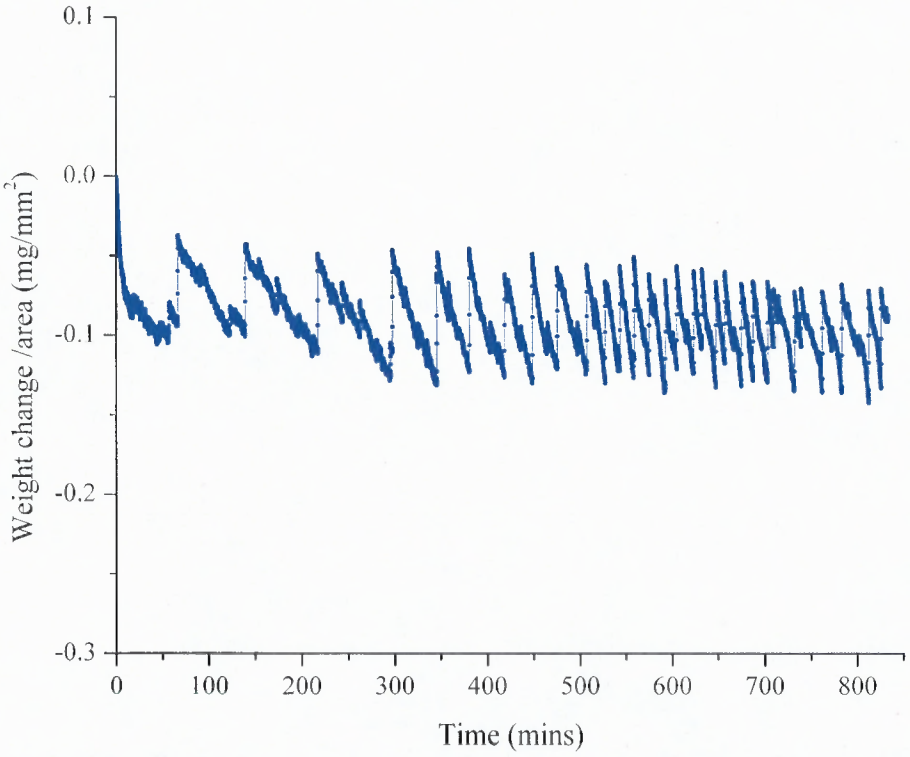

Figure 4.32 The corrosion resistance of boride coating in the boron-niobium-iron (B-Nb-Fe) system (in 0.5 M H_2SO_4).

4.5.6 Oxidation Resistance

The high temperature oxidation resistance of the B-Nb-Fe specimen was detected as a plot of weight change per area (mg/mm^2) against time (mins) as shown in Figure 4.33.

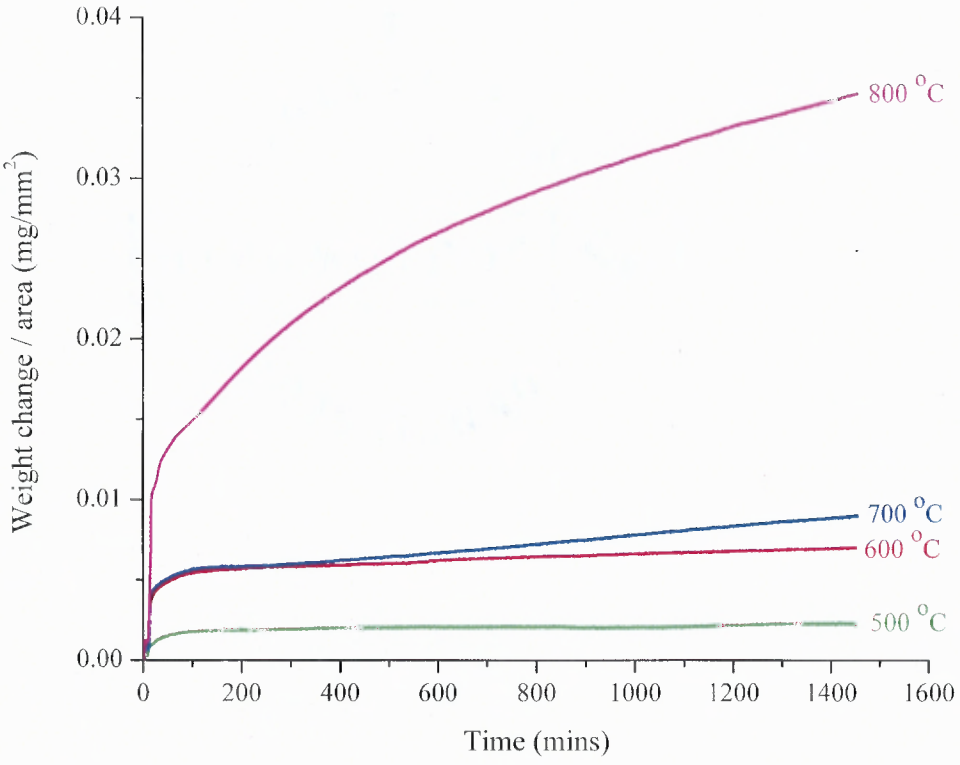

Figure 4.33 The high temperature oxidation resistance of boride coating in the boron-niobium-iron (B-Nb-Fe) system which coated on low carbon steel AISI 1018 substrate at a temperature range of 500 to 800 °C for 24 hours.

4.6 Boron – Tantalum - Iron (B-Ta-Fe) Experiments

The results of boron-tantalum-iron coating experiments are discussed as follows.

4.6.1 Microstructure

In the boron-tantalum-iron system, the needle-like or saw tooth structure was observed from the cross-sectional specimen. The thickness of boride coating was about 127.16 ± 2.13 μm. The morphology images of boronized low carbon steel and the coating thickness distribution were shown in Figure 4.34.

Similar to the coating microstructure of boron-tungsten-iron system, the parallel cracks was observed on the coating in boron-tantalum-iron system.

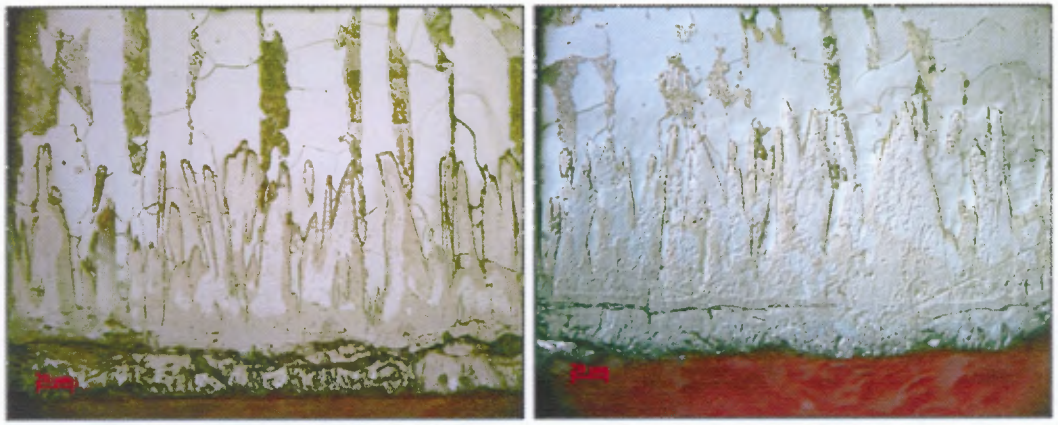

a) b)

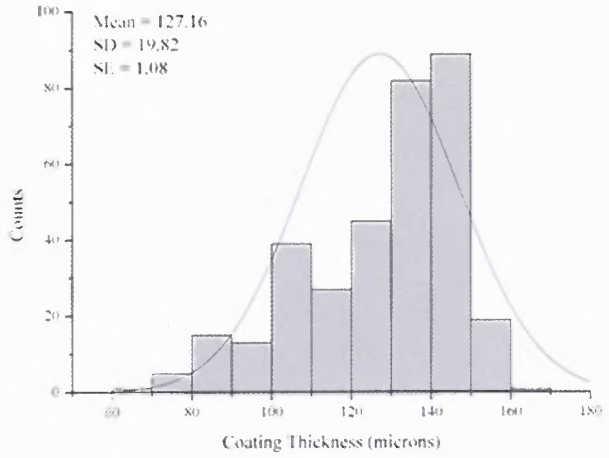

c)

Figure 4.34 The morphology images of boride coating (in the B-Ta-Fe system) on low carbon steel AISI 1018 a) under bright field, b) under differential interface contrast (DIC), and c) the distribution of coating thickness.

4.6.2 Phase Identification

The XRD pattern of borotantalized specimen in boron-tantalum-iron system was refined by the Rietveld refinement method as illustrated in Figure 4.35. The quantitative phase analysis from the Rietveld refinement method was shown that the boron-tantalum-iron coating was composed of 3.9 % weight of Fe_2B, 93.9 % weight of FeB, and 2.2 % weight of Ta_3B_2. The Rietveld standard agreement indices were the residual profile (R_p) = 11.14 %, the weighted residual profile (R_{wp}) = 15.05 % and the good of fitness (GOF) = 6.83. The refinements of lattice parameters, microstrain and crystal size of Fe_2B, FeB, and Ta_3B_2 phases of boron-tantalum-iron coating were shown in Table 4.6. Details and analysis of the phase identification and analysis are further addressed in Chapter 5 Section 5.2, sub-section 5.2.1.

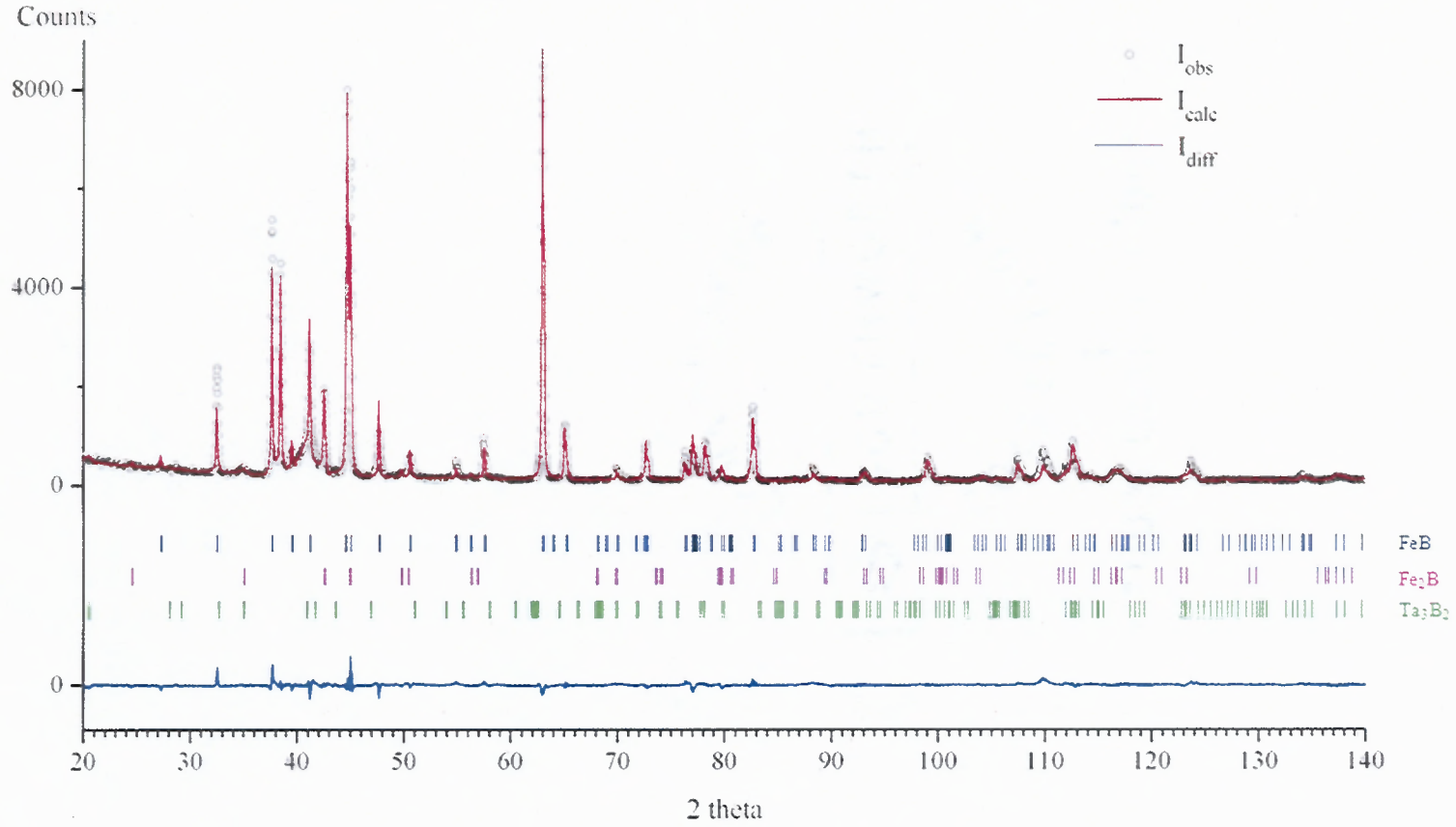

Figure 4.35 The XRD pattern (refined with the Rietveld Refinement) of the boride coating in the boron-tantalum-iron (B-Ta-Fe) system.

Table 4.6 The Lattice Parameters, Microstrain and Crystal Size of Boride Coating in the Boron-Tantalum-Iron (B-Ta-Fe) System

Phase presence	% Phase composition	Lattice parameters	Microstrain (%)	Crystal size (Å)
Fe_2B	3.9	a = b = 5.11758 Å c = 4.24555 Å vol.= 111.19980 $Å^3$ (Tetrahedral)	0.18	186.55
FeB	93.9	a = 5.50452 Å b = 2.94915 Å c = 4.06495 Å vol.= 65.98890 $Å^3$ (Orthorhombic)	0.090	300.23
Ta_3B_2	2.2	a = b = 6.12671 Å c = 3.17790 Å vol.= 119.28760 $Å^3$ (Tetrahedral)	0.76	41.25
R_p = 11.14 % R_{wp} = 15.05 % GOF = 6.83				

4.6.3 Synchrotron Microdiffraction and Microfluorescence

The results of B-Ta-Fe system from microdiffraction and microfluorescence are shown in Figures 4.36 and 4.37, respectively. In Figure 4.36, the 3-dimensional graph of intensity, 2-theta and distance were plotted and observed. Ta_3B_2 phase was detected at the distance between 2 - 26 μm at 2θ = 25.9, 27.3, and 31.9. In Figure 4.37, the element profile which measured by microfluorescence also confirmed the presence of tantalum atoms in the substrate.

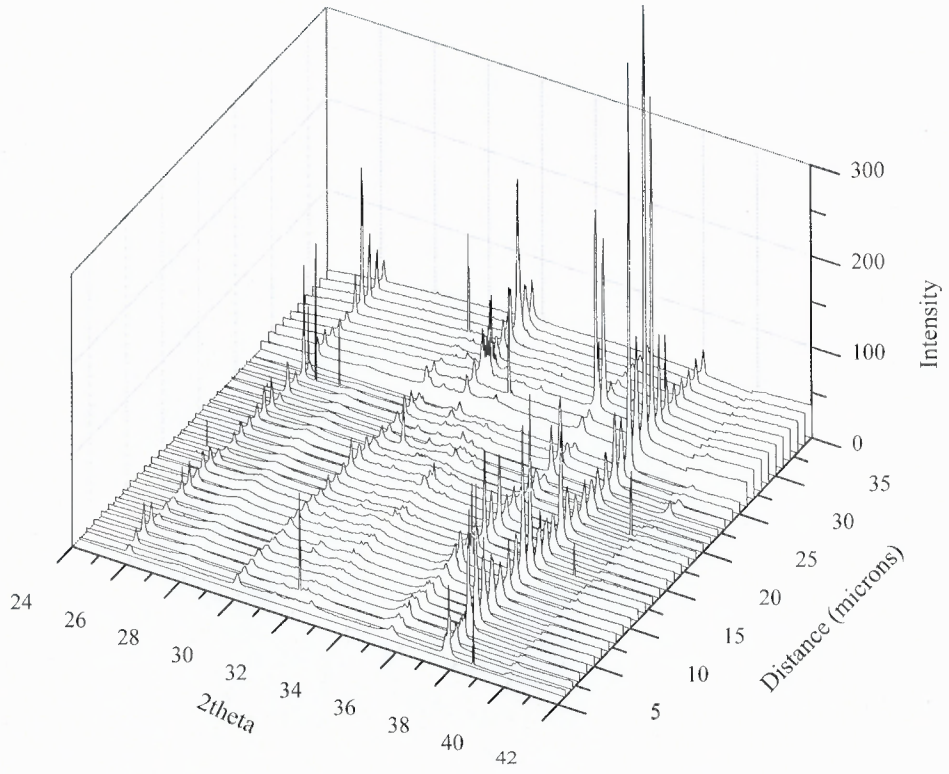

Figure 4.36 The microdiffraction of B-Ta-Fe system.

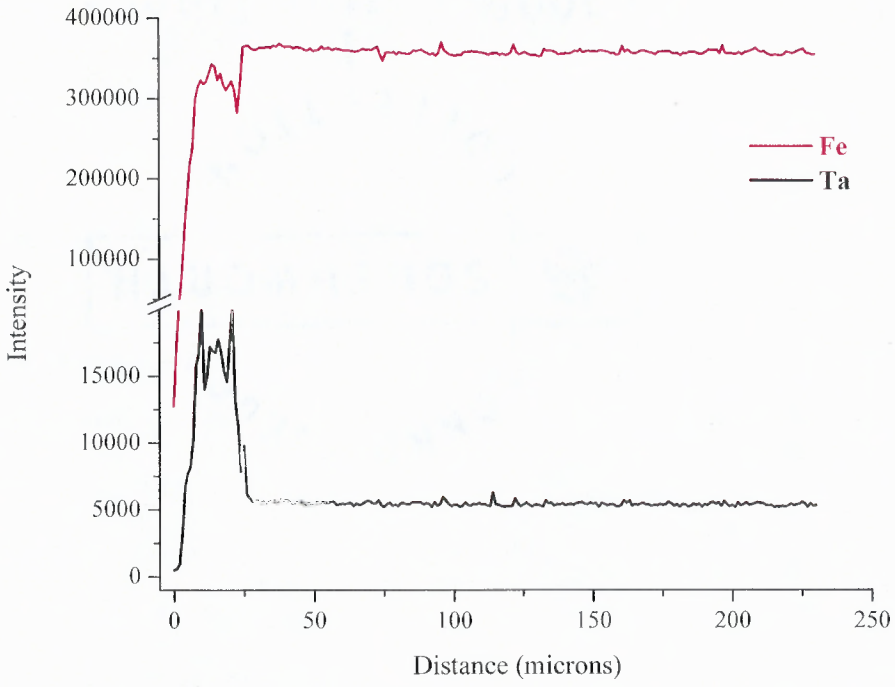

Figure 4.37 The microfluorescence of B-Ta-Fe system.

4.6.4 Microhardness

In B-Ta-Fe system, 3 types of borides phases (e.g., Fe_2B, FeB, and Ta_3B_2) were formed. The inner layer of Fe_2B phase has the microhardness of about 1800 – 2000 HV. The layer of FeB phase has the microhardness of about 1900 – 2200 HV. The layer of Ta_3B_2 phase has the microhardness of 2770 HV. The microhardness measurement of boride layers were detected across the coating through the substrate as depicted in Figure 4.38.

As seen in Figure 4.38, the boride coating had the maximum microhardness about 2879 HK and overall microhardness of the coating was between 2000 - 2500 HK, while that of the substrate has roughly 140 HK. The decrease of microhardness (about 1700 - 2100 HK) at the coating depth of 20 - 60 μm from the surface was an effect from the parallel cracks on the coating.

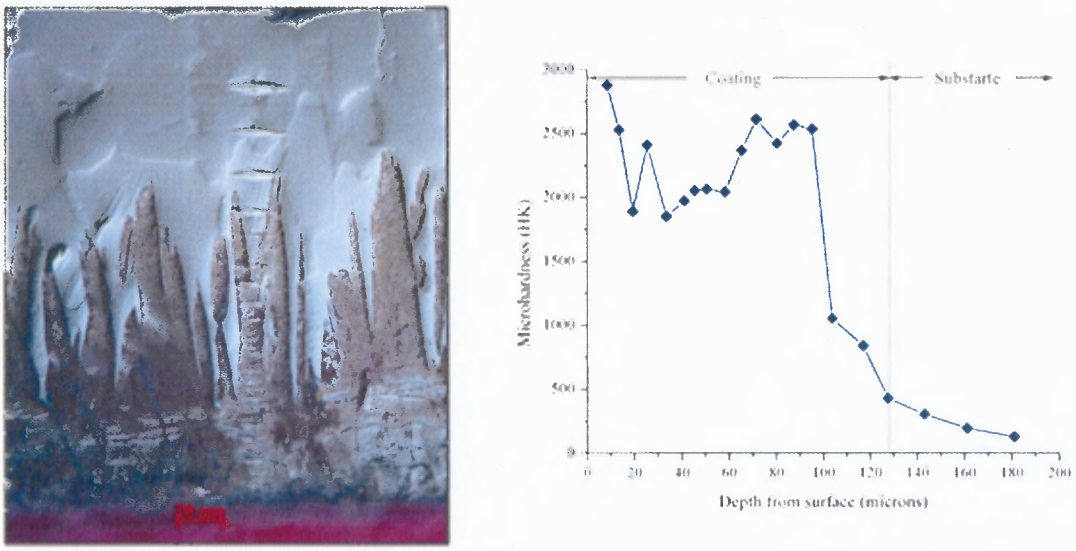

Figure 4.38 The plot between the microhardness and the depth from the surface of boride coating in the boron-tantalum-iron (B-Ta-Fe) system.

4.6.5 Corrosion Resistance

The corrosion resistance of coating in B-Ta-Fe system was tested in 0.5 M H_2SO_4 for 12 hours and shown that the weight loss per area of the borotantalized specimen was constant at 0.04 mg/mm^2. The weight change per area (mg/mm^2) of the specimen was plotted against time (mins) as shown in Figure 4.39.

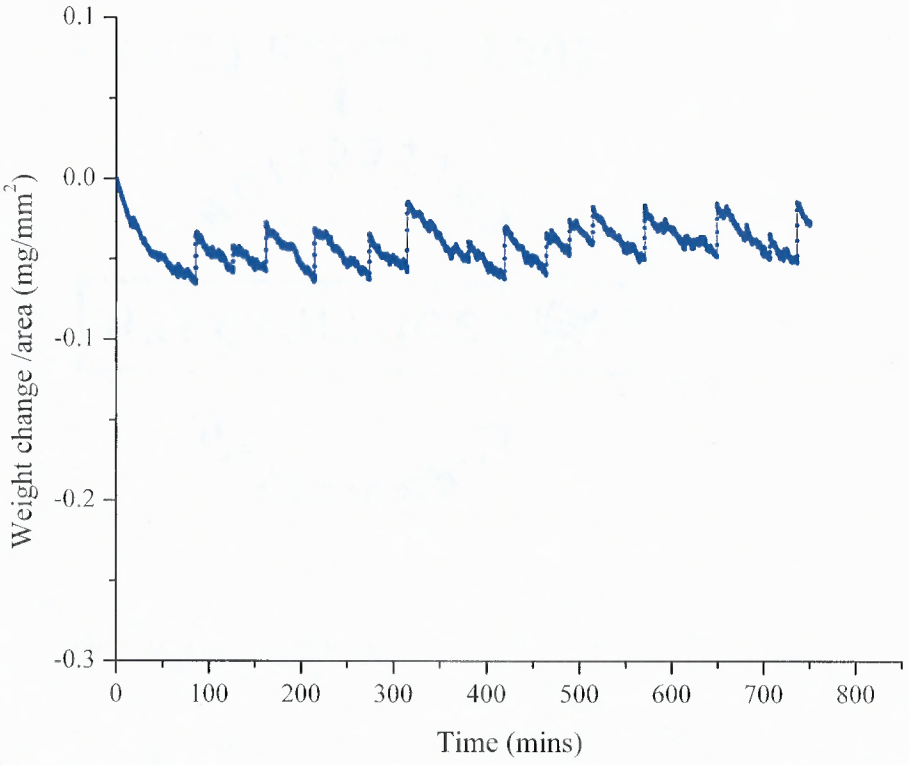

Figure 4.39 The corrosion resistance of boride coating in the boron-tantalum-iron (B-Ta-Fe) system (in 0.5 M H_2SO_4).

4.6.6 Oxidation Resistance

The high temperature oxidation resistance of the B-Ta-Fe specimen was detected as a plot of weight change per area (mg/mm^2) against time (mins) as shown in Figure 4.40.

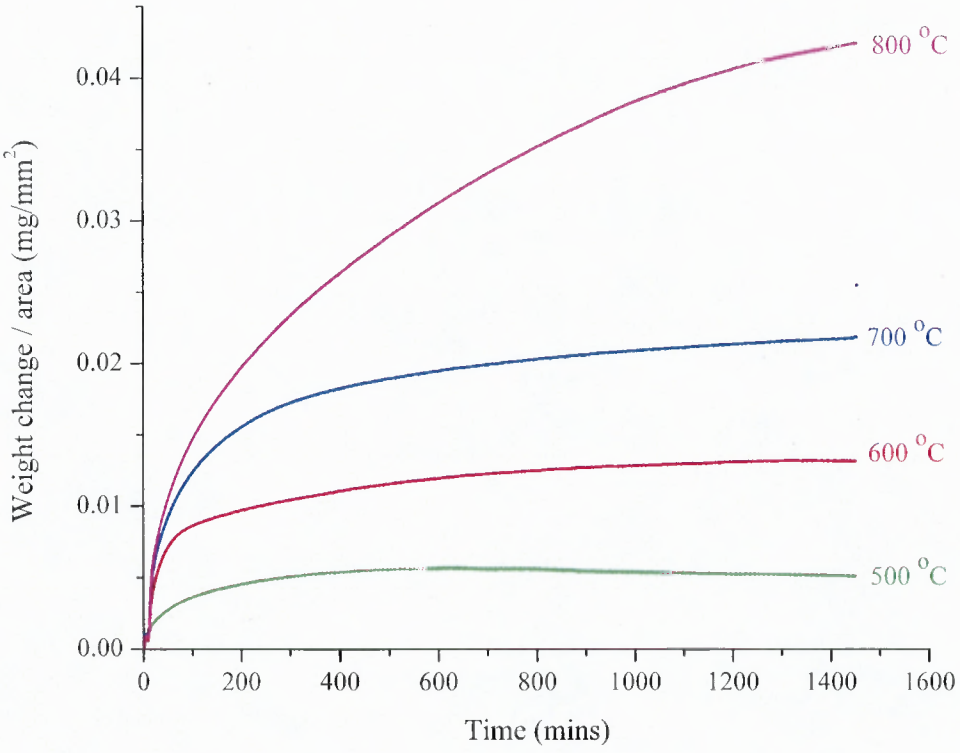

Figure 4.40 The high temperature oxidation resistance of boride coating in the boron-tantalum-iron (B-Ta-Fe) system which coated on low carbon steel AISI 1018 substrate at a temperature range of 500 to 800 °C for 24 hours.

4.7 Boron – Titanium - Iron (B-Ti-Fe) Experiments

The results of boron-titanium-iron coating experiments are discussed as follows.

4.7.1 Microstructure

In the boron-titanium-iron system, the smooth or flat structure was observed from the cross-sectional specimen. The coating thickness was about 3.02 ± 0.07 μm. The morphology images of boronized low carbon steel and the coating thickness distribution were shown in Figure 4.41.

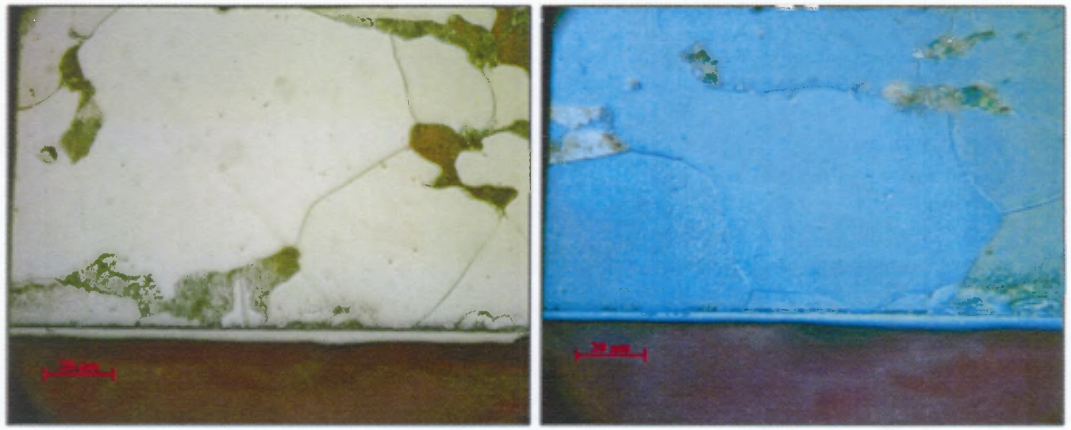

a) b)

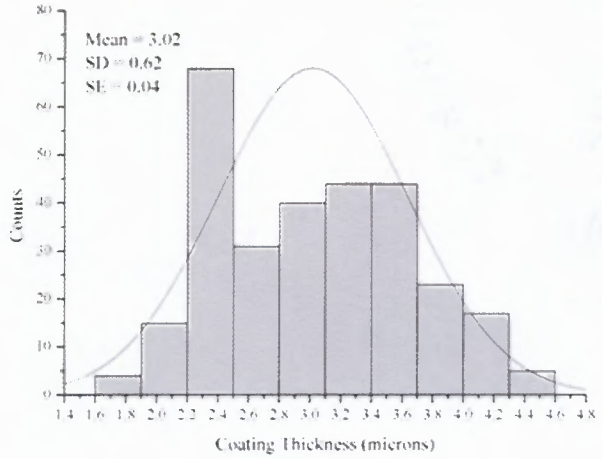

c)

Figure 4.41 The morphology images of boride coating (in the B-Ti-Fe system) on low carbon steel AISI 1018 a) under bright field, b) under differential interface contrast (DIC), and c) the distribution of coating thickness.

4.7.2 Phase Identification

The XRD pattern of borotitanized specimen in boron-titanium-iron system was refined by the Rietveld refinement method as illustrated in Figure 4.42. The quantitative phase analysis from the Rietveld refinement method was shown that the coating in boron-titanium-iron system was composed of 6.3 % weight of Fe_2B, 4.2 % weight of FeB, 77.1 % weight of TiC, 3.4 % weight of TiB, 3.7 % weight of Ti_3B_4, and 5.3 % weight of TiB_2. The Rietveld standard agreement indices were the residual profile (R_p) = 7.45 %, the weighted residual profile (R_{wp}) = 10.28 % and the good of fitness (GOF) = 3.79. The refinements of lattice parameters, microstrain and crystal size of Fe_2B, FeB, TiC, TiB, Ti_3B_4, and TiB_2 phases of boron-titanium-iron coating were shown in Table 4.7. Details and analysis of the phase identification and analysis are further addressed in Chapter 5 Section 5.2, sub-section 5.2.2.

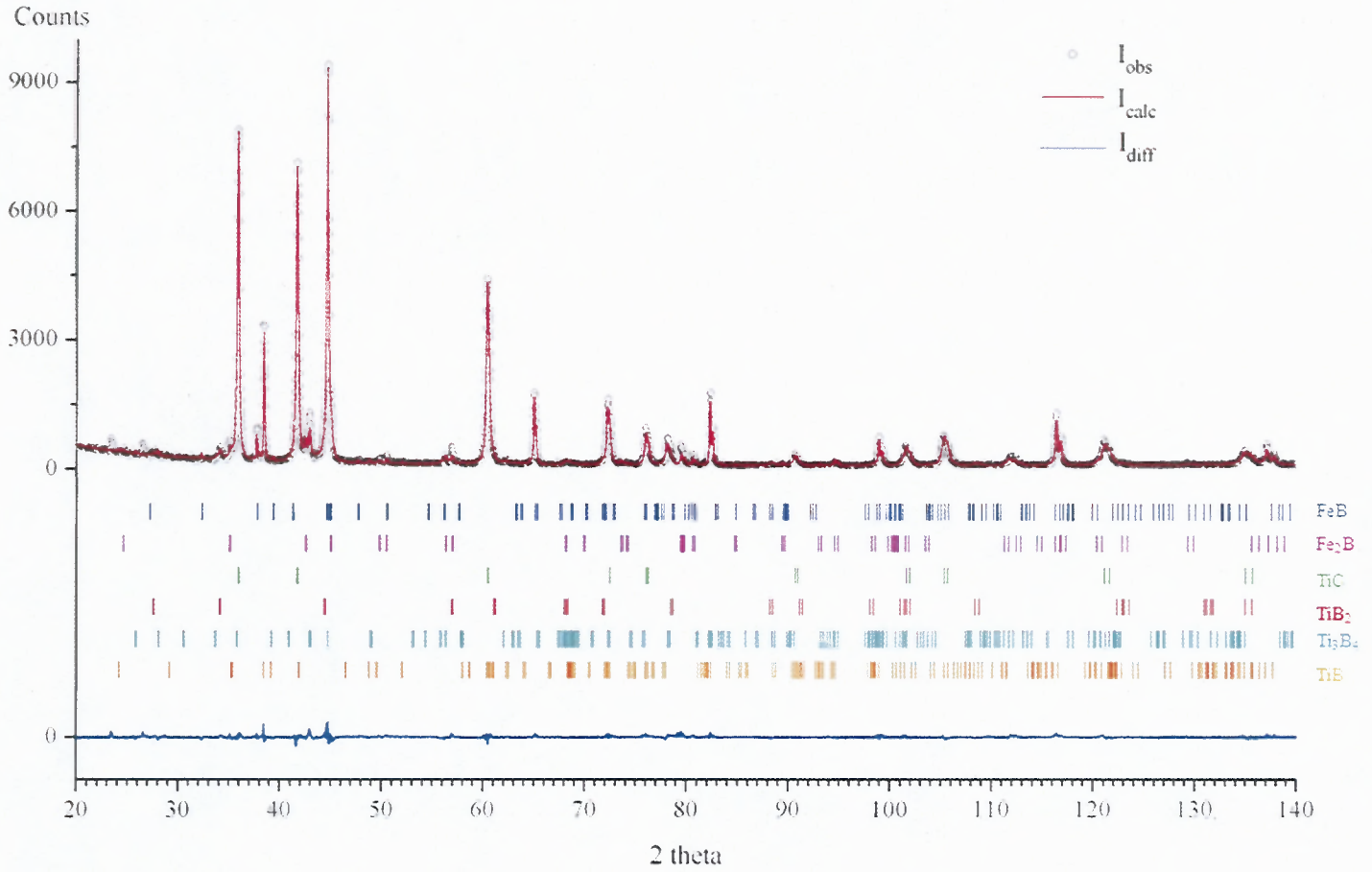

Figure 4.42 The XRD pattern (refined with the Rietveld Refinement) of the boride coating in the boron-titanium-iron (B-Ti-Fe) system.

Table 4.7 The Lattice Parameters, Microstrain and Crystal Size of Boride Coating in the Boron-Titanium-Iron (B-Ti-Fe) System

Phase presence	% Phase composition	Lattice parameters	Microstrain (%)	Crystal size (Å)
Fe_2B	6.3	a = b = 5.11517 Å c = 4.24907 Å vol.= 111.17650 $Å^3$ (Tetrahedral)	0.12	266.57
FeB	4.2	a = 5.54219 Å b = 2.94130 Å c = 4.06302 Å vol.= 60.23230 $Å^3$ (Orthorhombic)	0.18	182.69
TiC	77.1	a = b = c = 4.43330 Å vol.= 81.36831 $Å^3$ (Cubic)	0.13	234.80
TiB	3.4	a = 6.13287 Å b = 3.04175Å c = 4.60681 Å vol.= 85.93863 $Å^3$ (Orthorhombic)	0.21	164.14
Ti_3B_4	3.7	a = 2.99863Å b = 3.27012Å c = 13.80988 Å vol.= 135.41770 $Å^3$ (Orthorhombic)	0.08	367.43
TiB_2	5.3	a = b = 3.03507 Å c = 3.23443 Å vol.= 25.80280 $Å^3$ (Hexagonal)	0.33	90.91

R_p = 7.45 %
R_{wp} = 10.28 %
GOF = 3.79

4.7.3 Microhardness

In B-Ti-Fe system, 6 types of borides phases (e.g., Fe_2B, FeB, TiC, TiB, TiB_2, and Ti_3B_4) were formed. Fe_2B phase has the microhardness of about 1800 - 2000 HV. FeB phase has the microhardness of about 1900 - 2200 HV. TiC phase has the microhardness of about 2600 – 3100 HV. TiB phase has the microhardness of about 2700 - 2800 HV. TiB_2 phase has the microhardness of 3370 HV. The microhardness measurement of boride layers were detected across the coating through the substrate as depicted in Figure 4.43.

As seen in Figure 4.43, the boride coating has the microhardness up to 3327 HK while that of the substrate is roughly 140 HK. Because the coating is very thin, the microhardness of the coating was measured at the depth from surface about 2 μm.

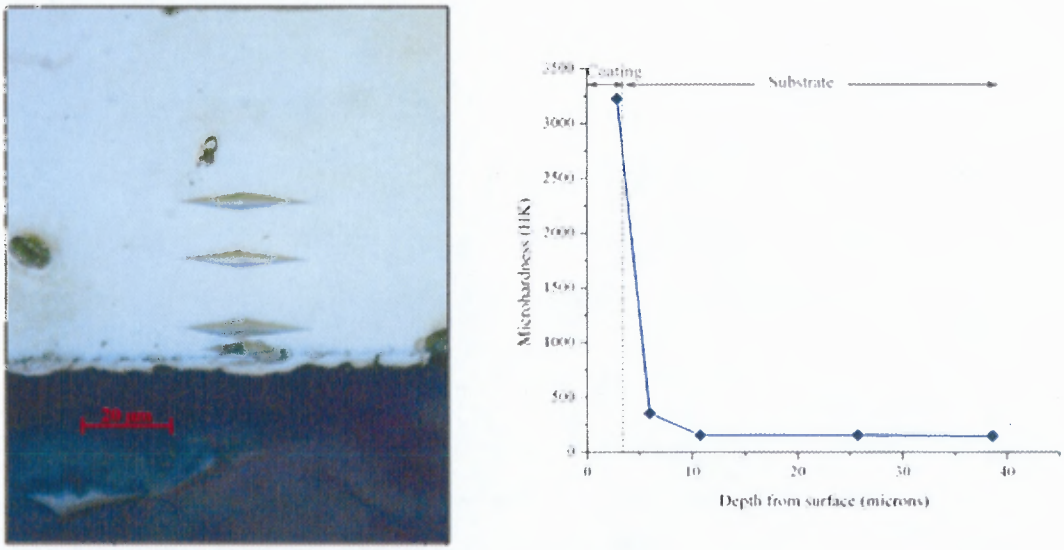

Figure 4.43 The plot between the microhardness and the depth from the surface of boride coating in the boron-titanium-iron (B-Ti-Fe) system.

4.7.4 Corrosion Resistance

The corrosion resistance of coating in B-Ti-Fe system was tested in 0.5 M H_2SO_4 for 12 hours and shown the constant weight loss per area at 0.05 mg/mm^2. The weight change per area (mg/mm^2) of the specimen was plotted against time (mins) as shown in Figure 4.44.

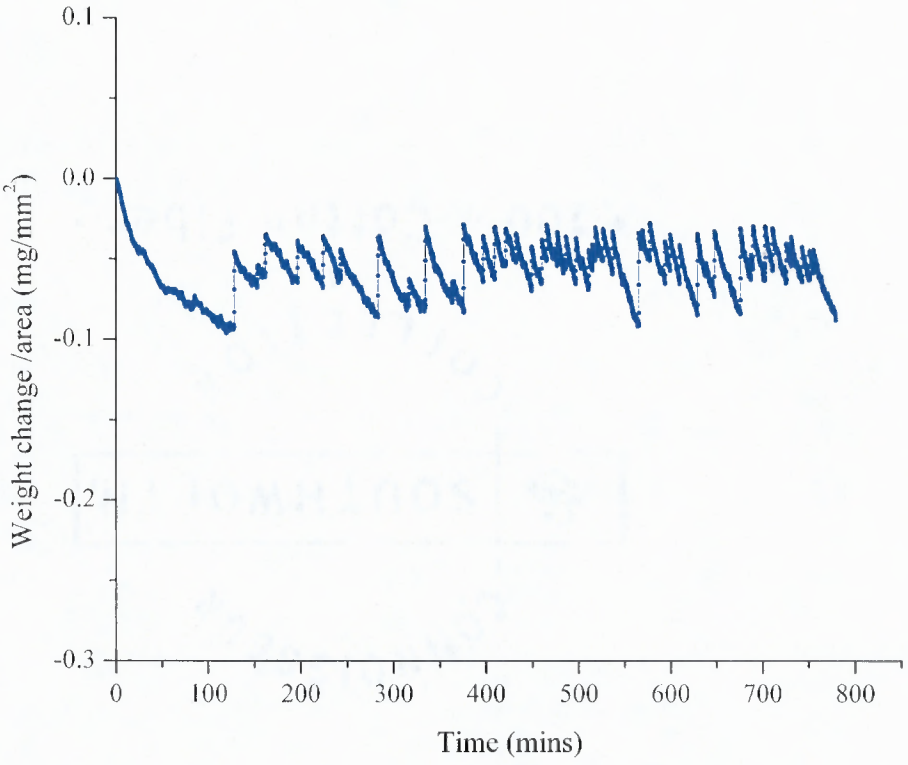

Figure 4.44 The corrosion resistance of boride coating in the boron-titanium-iron (B-Ti-Fe) system (in 0.5 M H_2SO_4).

4.7.5 Oxidation Resistance

The high temperature oxidation resistance of the B-Ti-Fe specimen was detected as a plot of weight change per area (mg/mm^2) against time (mins) as shown in Figure 4.45

Since the coating thickness was very thin.about 3.02 μm, the coating was able to endure at the temperature as low as 600 °C. At 700°C the weight gain of coating was dramatically increased due to the coating rupture.

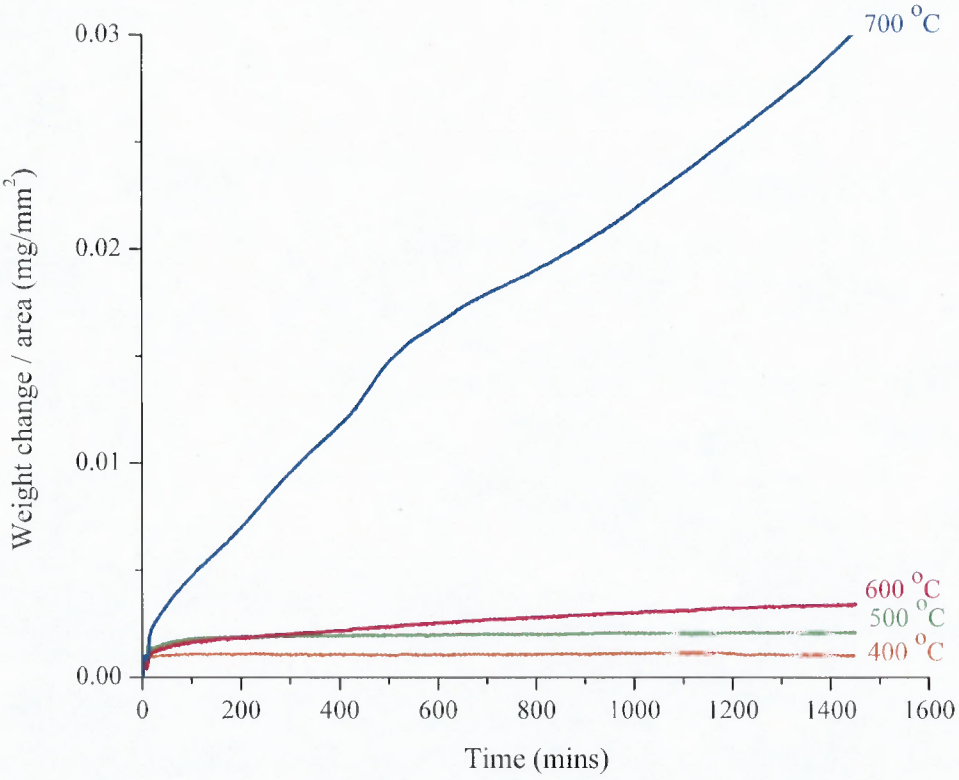

Figure 4.45 The high temperature oxidation resistance of boride coating in the boron-titanium-iron (B-Ti-Fe) system which coated on low carbon steel AISI 1018 substrate at a temperature range of 400 to 700 °C for 24 hours.

4.8 Boron – Zirconium - Iron (B-Zr-Fe) Experiments

The results of boron-zirconium-iron coating experiments are discussed as follows.

4.8.1 Microstructure

In the boron-zirconium-iron system, the smooth or flat structure was observed from the cross-sectional specimen. The coating thickness was about 3.01 ± 0.05 μm. The morphology images of coating and the coating thickness distribution in B-Zr-Fe system were shown in Figure 4.46.

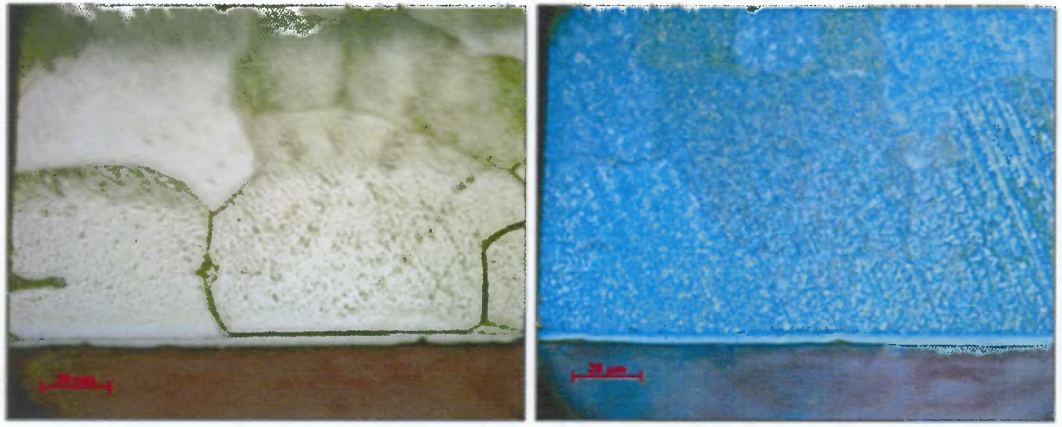

a) b)

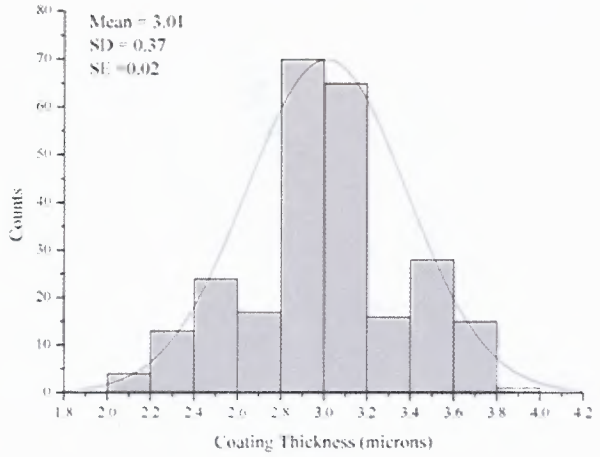

c)

Figure 4.46 The morphology images of boride coating (in the B-Zr-Fe system) on low carbon steel AISI 1018 a) under bright field, b) under differential interface contrast (DIC), and c) the distribution of coating thickness.

4.8.2 Phase Identification

The XRD pattern of borozirconized specimen in boron-zirconium-iron system was refined by the Rietveld refinement method as illustrated in Figure 4.47. The quantitative phase analysis from the Rietveld refinement method was shown that the boron-zirconium-iron coating was composed of 7.5 % weight of Fe_2B, 91.4 % weight of ZrC, and 1.1 % weight of ZrB_2. The Rietveld standard agreement indices were the residual profile (R_p) = 9.28 %, the weighted residual profile (R_{wp}) = 12.63 % and the good of fitness (GOF) = 7.43. The refinements of lattice parameters, microstrain and crystal size of Fe_2B, ZrC, and ZrB_2 phases of boron-zirconium-iron coating were shown in Table 4.8. Details and analysis of the phase identification and analysis are further addressed in Chapter 5 Section 5.2, sub-section 5.2.2.

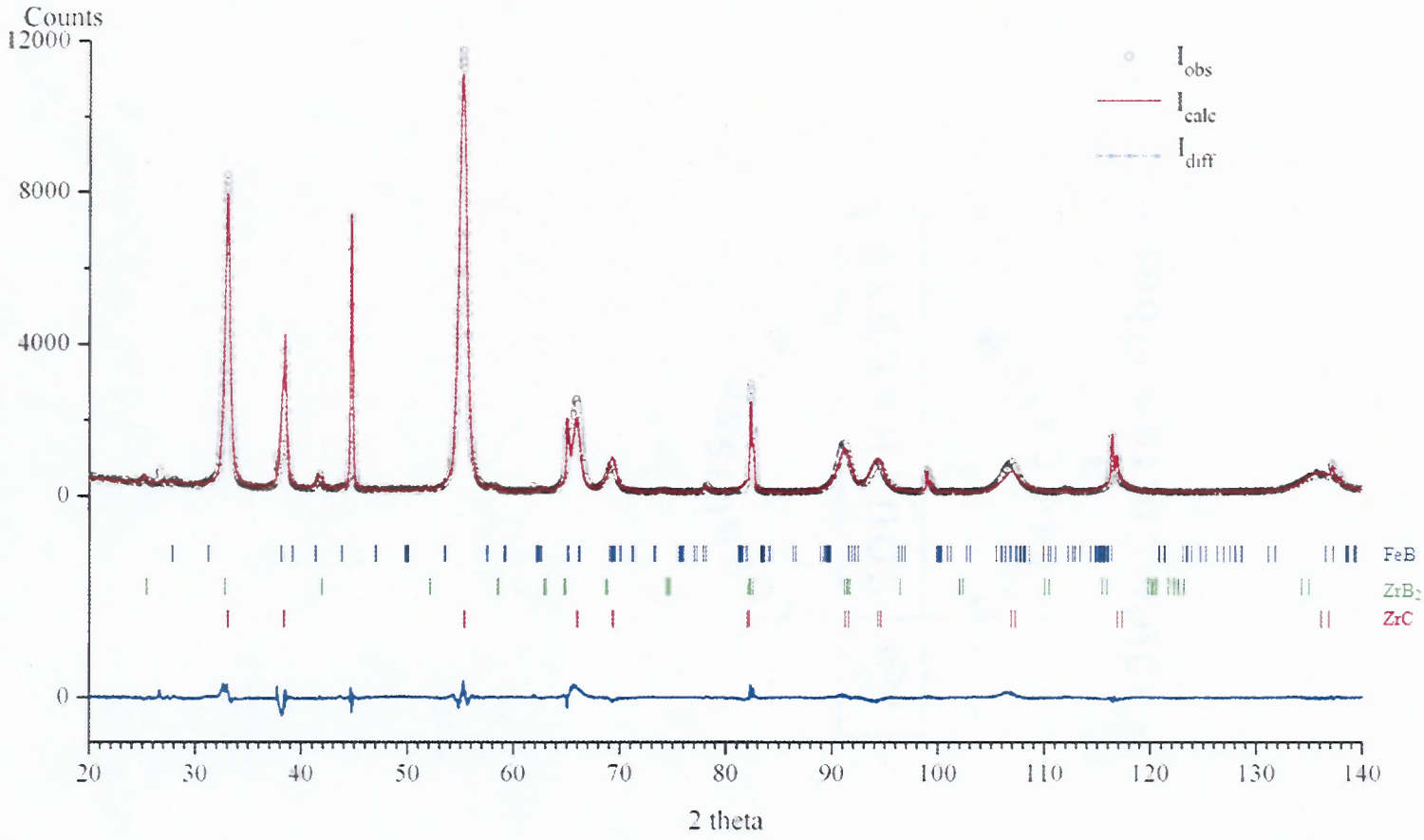

Figure 4.47 The XRD pattern (refined with the Rietveld Refinement) of the boride coating in the boron-zirconium-iron (B-Zr-Fe) system.

Table 4.8 The Lattice Parameters, Microstrain and Crystal Size of Boride Coating in the Boron-Zirconium-Iron (B-Zr-Fe) System

Phase presence	**% Phase composition**	**Lattice parameters**	**Microstrain (%)**	**Crystal size (Å)**
FeB	7.5	a = 5.42175 Å b = 2.88933 Å c = 4.07268 Å vol.= 63.79950 $Å^3$ (Orthorhombic)	0.70	46.18
ZrC	91.4	a = b = c = 4.69890 Å vol.= 103.47990 $Å^3$ (Cubic)	0.47	67.62
ZrB_2	1.1	a = b = 3.16232 Å c = 3.57168 Å vol.= 30.46484 $Å^3$ (Hexagonal)	0.42	64.82
R_p = 9.28 % R_{wp} = 12.63 % GOF = 7.43				

4.8.3 Microhardness

In B-Zr-Fe system, 3 types of borides phases (e.g., FeB, ZrC, and ZrB_2) were formed. The layer of FeB phase has the microhardness of about 1900 – 2200 HV. The layer of ZrC phase has the microhardness of about 2000 -2700 HV. The layer of ZrB_2 phase has the microhardness of about 2700 – 2900 HV. The microhardness measurement of boride layers were detected across the coating through the substrate as depicted in Figure 4.48.

As seen in Figure 4.48, the boride coating had the microhardness up to 2206 HK while that of the substrate is roughly 140 HK. Because the coating thickness was very thin about 3.01 μm, the microhardness of the coating was detected at 2 μm from the surface.

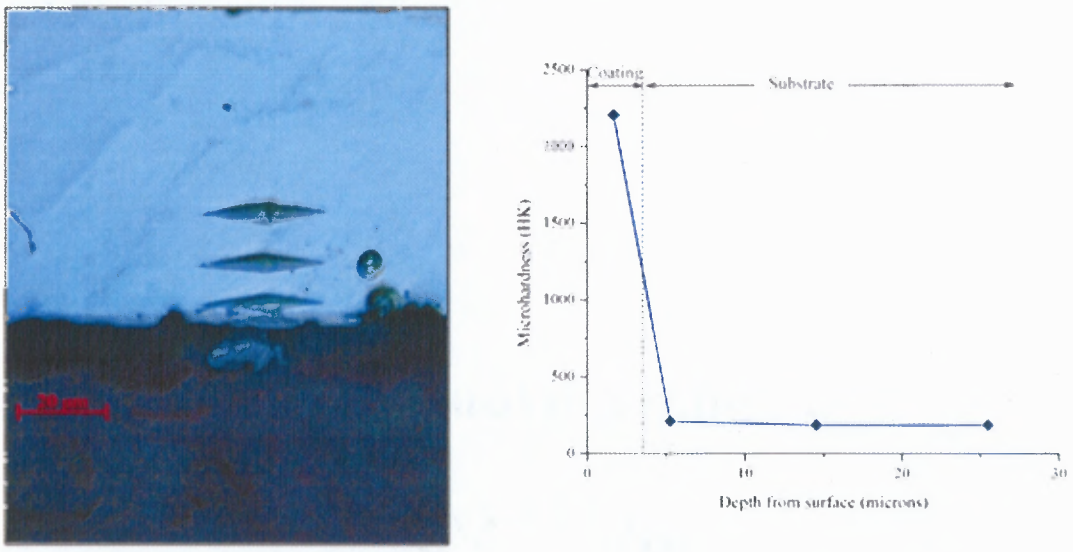

Figure 4.48 The plot between the microhardness and the depth from the surface of boride coating in the boron-zirconium-iron (B-Zr-Fe) system.

4.8.4 Corrosion Resistance

The corrosion resistance of coating in B-Zr-Fe specimen was tested in 0.5 M H_2SO_4 for 12 hours. The weight loss of coated specimen was constant at about 0.05 mg/mm^2. The weight change per area (mg/mm^2) of the specimen was plotted against time (mins) as shown in Figure 4.49.

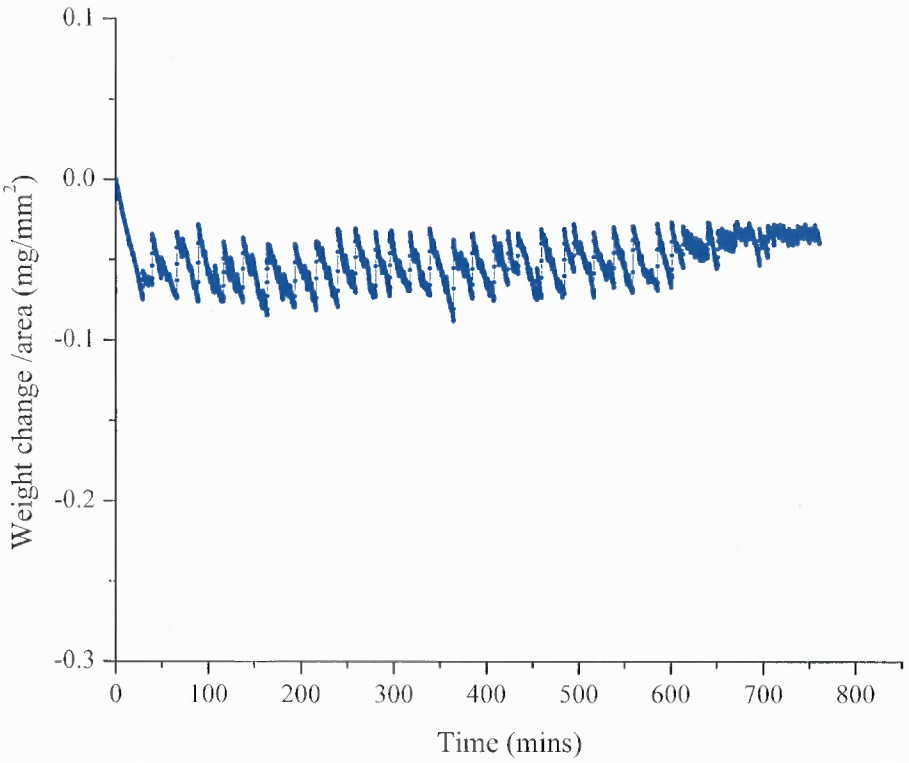

Figure 4.49 The corrosion resistance of boride coating in the boron-zirconium-iron (B-Zr-Fe) system (in 0.5 M H_2SO_4).

4.8.5 Oxidation Resistance

The high temperature oxidation resistance of the B-Zr-Fe specimen was detected as a plot of weight change per area (mg/mm^2) against time (mins) as shown in Figure 4.50.

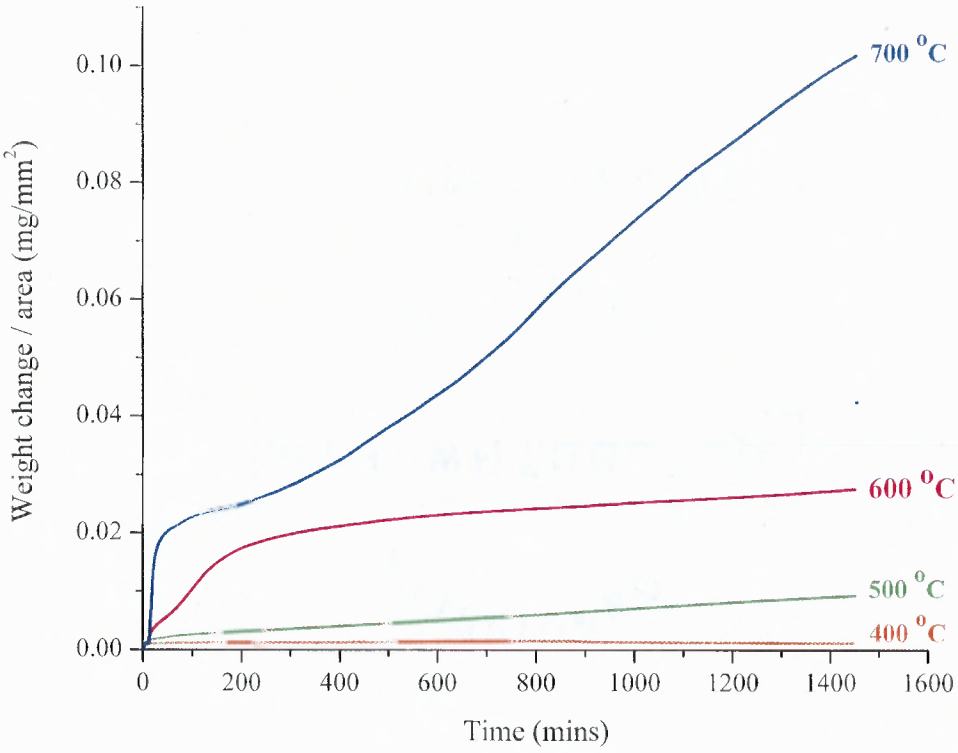

Figure 4.50 The high temperature oxidation resistance of boride coating in the boron-zirconium-iron (B-Zr-Fe) system which coated on low carbon steel AISI 1018 substrate at a temperature range of 400 to 700 °C for 24 hours.

4.9 Boron – Hafnium - Iron (B-Hf-Fe) Experiments

The results of boron-hafnium-iron coating experiments are discussed as follows.

4.9.1 Microstructure

In the boron-hafnium-iron system, the smooth structure was observed from the cross-sectional specimen. The thickness of boride coating was about 1.56 ± 0.05 μm. The morphology images of coating and the coating thickness distribution were shown in Figure 4.51.

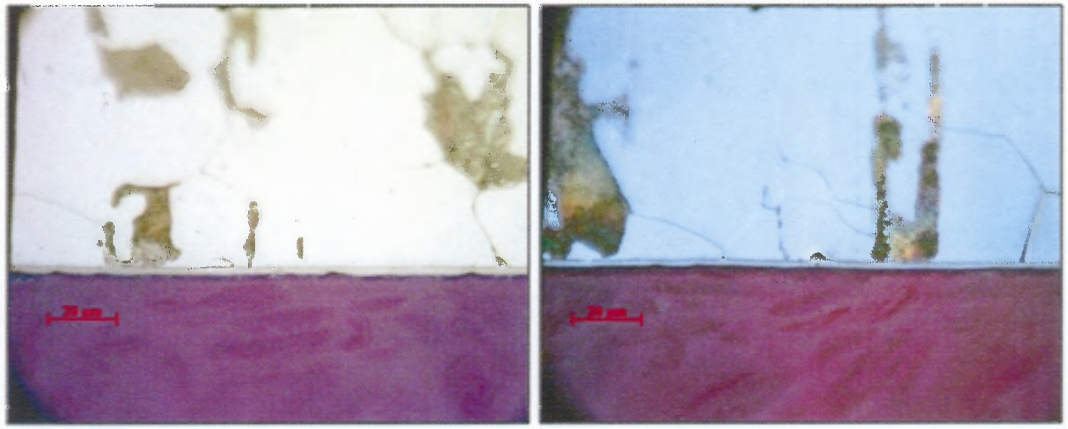

a) b)

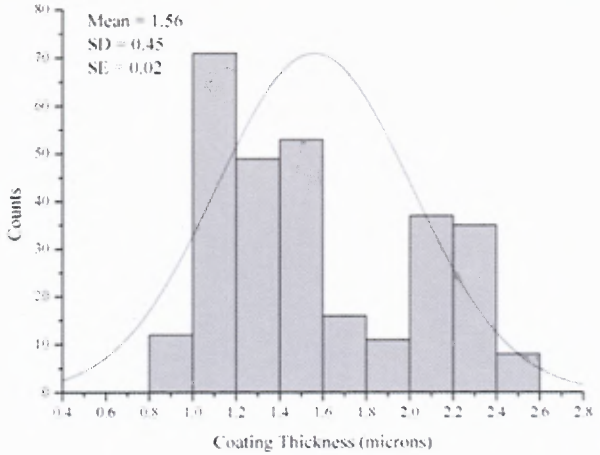

c)

Figure 4.51 The morphology images of boride coating (in the B-Hf-Fe system) on low carbon steel AISI 1018 a) under bright field, b) under differential interface contrast (DIC), and c) the distribution of coating thickness.

4.9.2 Phase Identification

The XRD pattern of coated specimen in boron-hafnium-iron system was refined by the Rietveld refinement method as illustrated in Figure 4.52. The quantitative phase analysis from the Rietveld refinement method was shown that the boron-hafnium-iron coating was composed of 29.9 % weight of Fe_2B, 68.5 % weight of HfC, and 1.6 % weight of HfB_2. The Rietveld standard agreement indices were the residual profile (R_p) = 6.45 %, the weighted residual profile (R_{wp}) = 9.03 % and the good of fitness (GOF) = 5.43. The refinements of lattice parameters, microstrain and crystal size of Fe_2B, HfC, and HfB_2 phases of boron-hafnium-iron coating were shown in Table 4.9. Details and analysis of the phase identification and analysis are further addressed in Chapter 5 Section 5.2, sub-section 5.2.2.

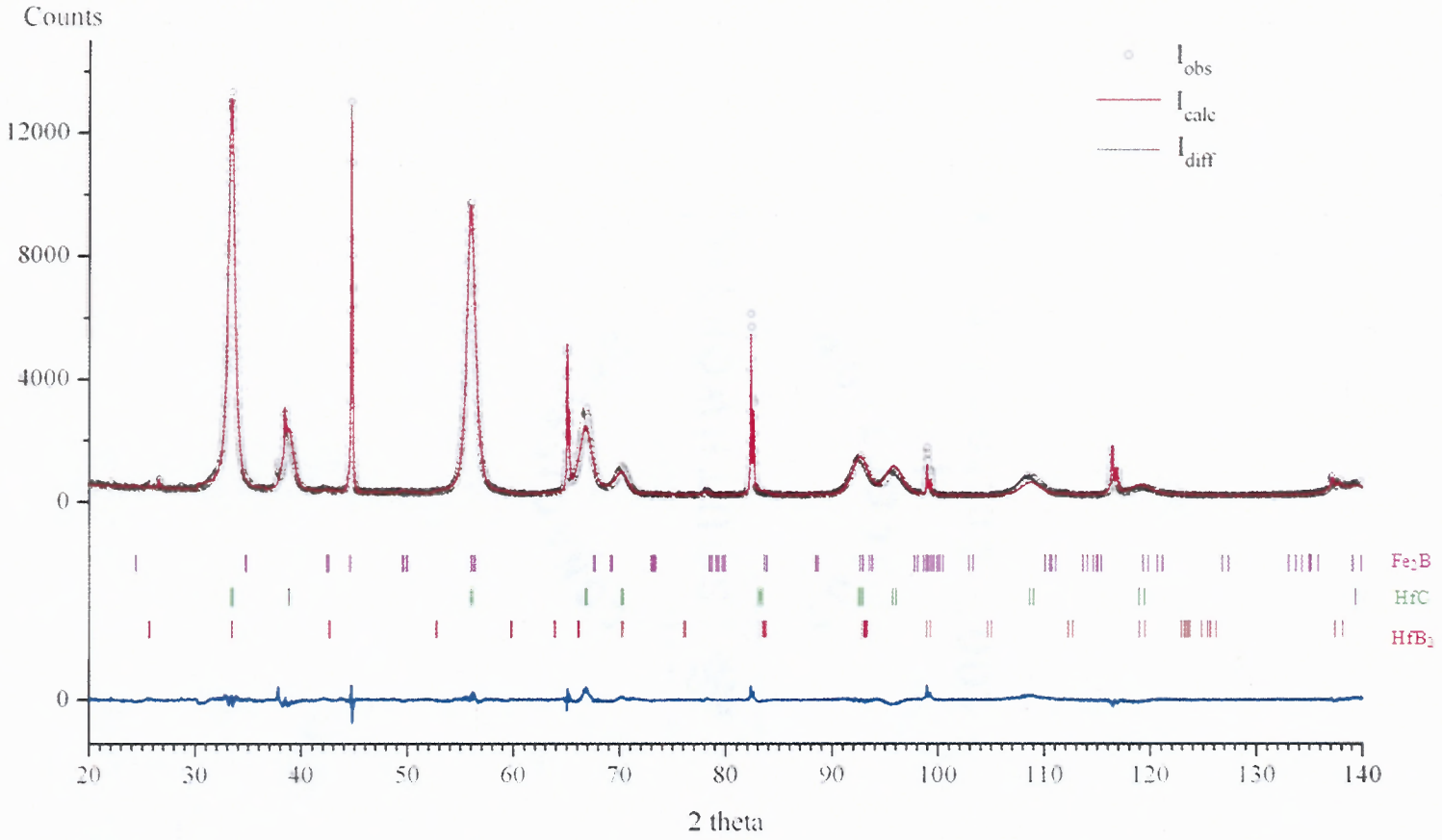

Figure 4.52 The XRD pattern (refined with the Rietveld Refinement) of the boride coating in the boron-hafnium-iron (B-Hf-Fe) system.

Table 4.9 The Lattice Parameters, Microstrain and Crystal Size of Boride Coating in the Boron-Hafnium-Iron (B-Hf-Fe) System

Phase presence	% Phase composition	Lattice parameters	Microstrain (%)	Crystal size (Å)
Fe_2B	29.9	a = b = 5.16995 Å c = 4.26415 Å vol.= 113.97380 $Å^3$ (Tetrahedral)	0.44	73.89
HfC	68.5	a = b = c = 4.64814 Å vol.= 100.42410 $Å^3$ (Cubic)	0.61	53.63
HfB_2	1.6	a = b = 3.09825 Å c = 3.50062 Å vol.= 29.10095 $Å^3$ (Hexagonal)	0.89	36.50
R_p = 6.45 % R_{wp} = 9.03 % GOF = 5.43				

4.9.3 Microhardness

In B-Hf-Fe system, 3 types of borides phases (e.g., Fe_2B, HfC, and HfB_2) were formed. The layer of Fe_2B phase has the microhardness of about 1800 - 2100 HV. The layer of HfC phase has the microhardness of about 2100 -2600 HV. The layer of HfB_2 phase has the microhardness of about 2800 – 3000 HV. In this dissertation, the microhardness measurement of boride layers could not be detected across the coating through the substrate because the coating is very thin, about 1.56 μm.

However, the microhardness of the whole specimen, including coating and substrate, could be measured at about 1000 - 1100 HK while that of the substrate was roughly 250 HK.

4.9.4 Corrosion Resistance

The corrosion resistance of the B-Hf-Fe specimen was tested in 0.5 M H_2SO_4 for 12 hours and shown the constant weight loss about 0.05 mg/mm^2. The weight change per area (mg/mm^2) of the specimen was plotted against time (mins) as shown in Figure 4.53.

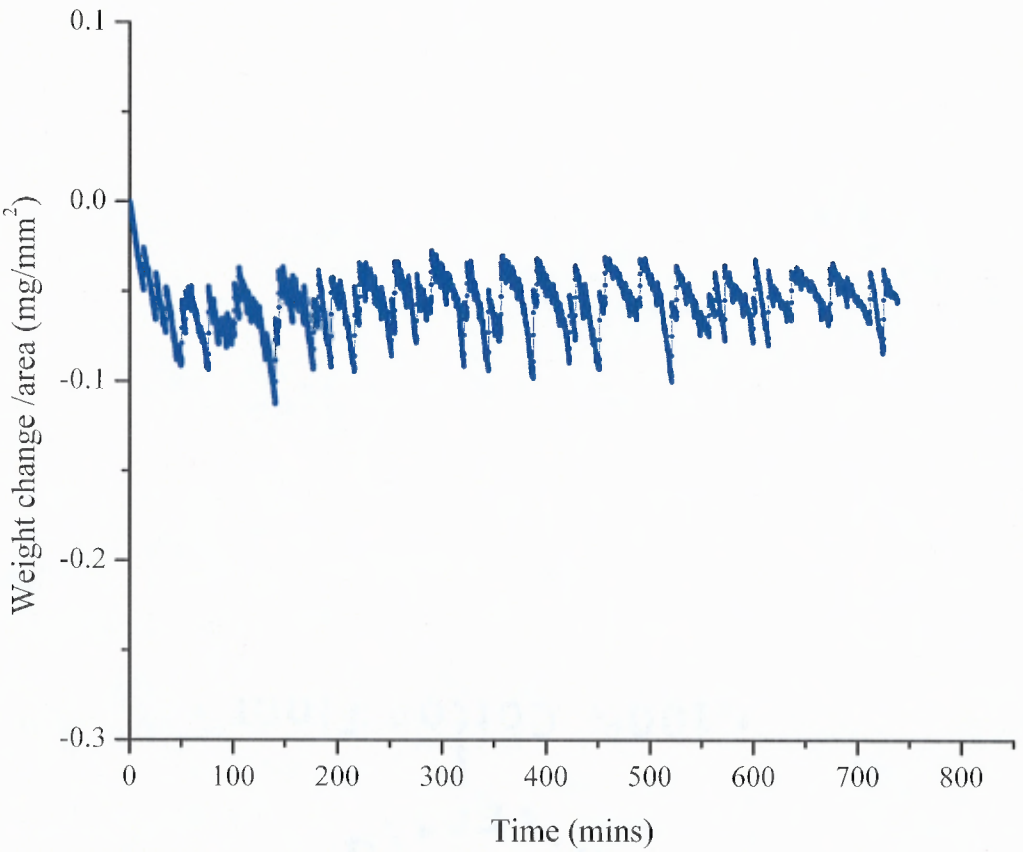

Figure 4.53 The corrosion resistance of boride coating in the boron-hafnium-iron (B-Hf-Fe) system (in 0.5 M H_2SO_4).

4.9.5 Oxidation Resistance

The high temperature oxidation resistance of the B-Hf-Fe specimen was detected as a plot of weight change per area (mg/mm^2) against time (mins) as shown in Figure 4.54.

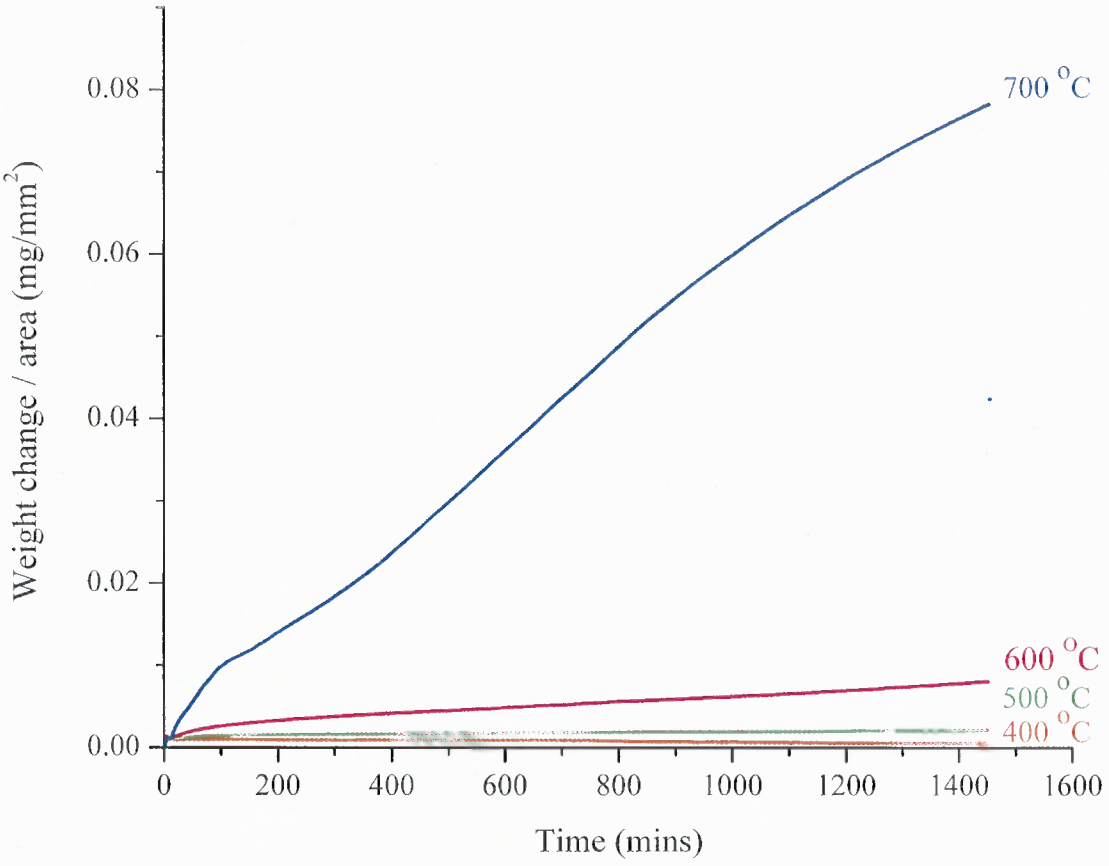

Figure 4.54 The high temperature oxidation resistance of boride coating in the boron-hafnium-iron (B-Hf-Fe) system which coated on low carbon steel AISI 1018 substrate at a temperature range of 400 to 700 °C for 24 hours.

CHAPTER 5

RESULTS COMPARISON AND DISCUSSION

The dissertation focuses on the study and characterization of the multi-component boron coating by adding eight transition metals as second elements in the conventional boronizing process. These eight elements include three elements from the periodic table group VIB: chromium (Cr), molybdenum, and tungsten (W), two elements from the periodic table group VB: niobium (Nb) and tantalum (Ta), and three elements from the period table group IVB: titanium (Ti), zirconium (Zr), and hafnium (Hf). For all eight additional second elements in multi-component boronizing, five experimental tests have been completed in studying microstructure, microhardness, phase identification and analysis, oxidation resistance, and corrosion resistance. All experiment results are given in the earlier chapter 4.

In accordance with five experimental tests, this chapter provides detailed information and explanations on some observations of taken images, collected data, and analyzed graphs that are previously depicted in the chapter 4.

5.1 Microstructure

To understand and analyze the experimental results, some important information regarding to characteristics of second elements are reminded, as depicted in Figures 5.1 and 5.2.

5.1.1 Microstructure of B-Cr-Fe, B-Mo-Fe, B-W-Fe, B-Nb-Fe, and B-Ta-Fe Coatings

The relationships between atomic radii, diffusion coefficient, and coating thickness of the chosen second elements from the periodic table groups VB and VIB are similar, which is "diffusion coefficient varies dependent on atomic size". An element atom in the SAME periodic group, either VB or VIB, with a bigger atomic size has less diffusion coefficient. For instances, chromium atom with a smaller atomic size—1.249 Å—has the higher diffusion coefficient of 1.47×10^{-14} m^2/s while a tungsten atom with a larger atomic size—1.376 Å—has the less diffusion coefficient of 0.61×10^{-14} m^2/s. That means when these atoms diffuse into a substrate, the atom with the higher diffusion coefficient can diffuse faster into the substrate. In this example, chromium atoms can diffuse into the iron substrate faster than tungsten atoms.

In multi-component boronizing, boron and second element atoms independently diffuse into the substrate. Since boron atoms have the smaller atomic size of 0.46 Å and the higher diffusion coefficient of 0.225 m^2/s, they can diffuse faster and further than the second elements into the substrate. As a result, boron atoms form boride phases with iron atoms of the substrate before the second element atoms can diffuse into the substrate.

As discussed above, the boride phases (e.g., Fe_2B and FeB) which formed by iron and boron atoms were shown in the needle structures. Hence, needle structures are always shown in the coating layer, as depicted in a comparison Figure 5.3, for all five second elements of the periodic table groups VB and VIB.

Because of the small atomic size of boron, boron is placed in the space between the host atoms, and becomes an interstitial solid solution before the boride phases are formed. When the second element atoms diffuse into the iron substrate, they replace iron atoms and form a substitutional solid solution instead of interstitial solid solution as depicted in Figure 5.2. In the interstitial solid solution, smaller solute atoms locate in the spaces between larger solvent atoms. In the substitutional solid solution, solute atoms substitute with solvent atoms. The formation of substitutional solid solution, which is caused by the second element, acts as an "alloying element" in the steel substrate. As known, the alloying elements in the steel substrate retard the diffusion of boron and subsequently decrease the coating thickness in boronizing process. In multi-component boronizing, the substitutional solid solution between iron and the second element means the increase of alloying element contents to the substrate which will affect the diffusion of boron atoms and finally reduce the coating thickness.

In case of chromium and tungsten, chromium atoms are smaller than tungsten atoms; they diffuse faster into the iron substrate, compared to tungsten atoms. Therefore, the number of chromium atoms diffused into iron in B-Cr-Fe system is higher than the number of tungsten atoms diffused into iron in B-W-Fe system, which leads to the substitutional solid solution quantity of Cr and Fe is formed more than that of W and Fe.

The higher number of chromium atoms acting as alloying elements in the substrate can effectively retard the number of boron atoms diffusing into the substrate. On the other hand, the lower number of tungsten atoms means the lower alloying elements in the substrate which causes to less effectively retard the diffusion of boron atoms into the substrate.

As mention above, the coating thickness is dependent on the number of boron atoms that can diffuse into the substrate and the quantity of alloying elements. Therefore, the coating thickness of B-Cr-Fe system with high quantity of alloying elements is thinner (105.78 μm) than that of 144.31 μm in the B-W-Fe system.

Although the second element atoms limit the number of diffused boron atoms and the coating thickness is limited, the second element improves other properties, such as oxidation and corrosion resistance, and provides stability in boride phase structures.

5.1.2 Microstructure of B-Ti-Fe, B-Zr-Fe, and B-Hf-Fe Coatings

The relationships between atomic radii, diffusion coefficient, and coating thickness of the chosen second elements of the periodic table group IVB are dependent on chemical affinity and the diffusion mechanism is different from the second elements of the periodic table group VB and VIB. Alternatively, the relationships may be predicted and discussed from the perspective of thermodynamics.

As known, transition metals in the periodic table group IVB have high chemical affinity. From the perspective of thermodynamics, the Gibbs free energy of formation at 950 °C of Fe_2B is -18.10 KJ/mole, and -66.41 KJ/mole of FeB, while the Gibbs free energy of formation at 950 °C of TiC is -195.89 KJ/mole, and -304.47 KJ/mole of TiB_2, the Gibbs free energy of formation at 950 °C of ZrC is -184.24 KJ/mole, and -307.34 KJ/mole of ZrB_2, and the Gibbs free energy of formation at 950 °C of HfC is -201.97 KJ/mole, and -312.89 KJ/mole of HfB_2. During the heat treatment, boron carbide (as the boron source) is preferred to have a reaction with the transition metal which added as the second element, rather than to diffuse into the substrate.

Thus, the solid state reaction of transition metal and boron carbide is

$$3M + B_4C \rightarrow 2MB_2 + MC$$

when M is the transition, which is Ti, Zr, or Hf in this dissertation. The solid state reaction for titanium, zirconium, and hafnium can be respectively expressed as

$$3Ti + B_4C \rightarrow 2TiB_2 + TiC$$

$$3Zr + B_4C \rightarrow 2ZrB_2 + HfC$$

$$3Hf + B_4C \rightarrow 2HfB_2 + HfC$$

As metalizing is a dominant process, carbon in the substrate diffuse outward to the surface and then form metal carbide with the excessive transition metal at the surface as well as the excessive carbon from boron carbide can diffuse into substrate and form carbide phases. These results can be seen from the high percentage of metal carbide in the substrate. In B-Ti-Fe system, TiC occurs 77.1 % weight of the total composition of the coating. Similarly, ZrC occurs 91.4 wt. % in B-Zr-Fe system, and HfC occurs 68.5 wt. % in B-Hf-Fe system.

After metal carbide (e.g TiC, ZrB, HfC) is formed on the substrate, the carbide phase is much more effectively to retard the diffusion of boron atoms into the substrate to form Fe_2B and/or FeB. The diffusion of boron is strictly limited and the number of boron atoms in the substrate is dramatically decreased, compared to the number of boron atoms diffusing with the second element in the periodic table group VB and VIB. Therefore, the needle structure is not observed in B-Ti-Fe, B-Zr-Fe, and B-Hf-Fe systems. With high limitation of boron diffusion, the smooth or flat structure is formed in B-Ti-Fe, B-Zr-Fe, and B-Hf-Fe systems and the thin coating thickness in the range of 1-3 μm are observed.

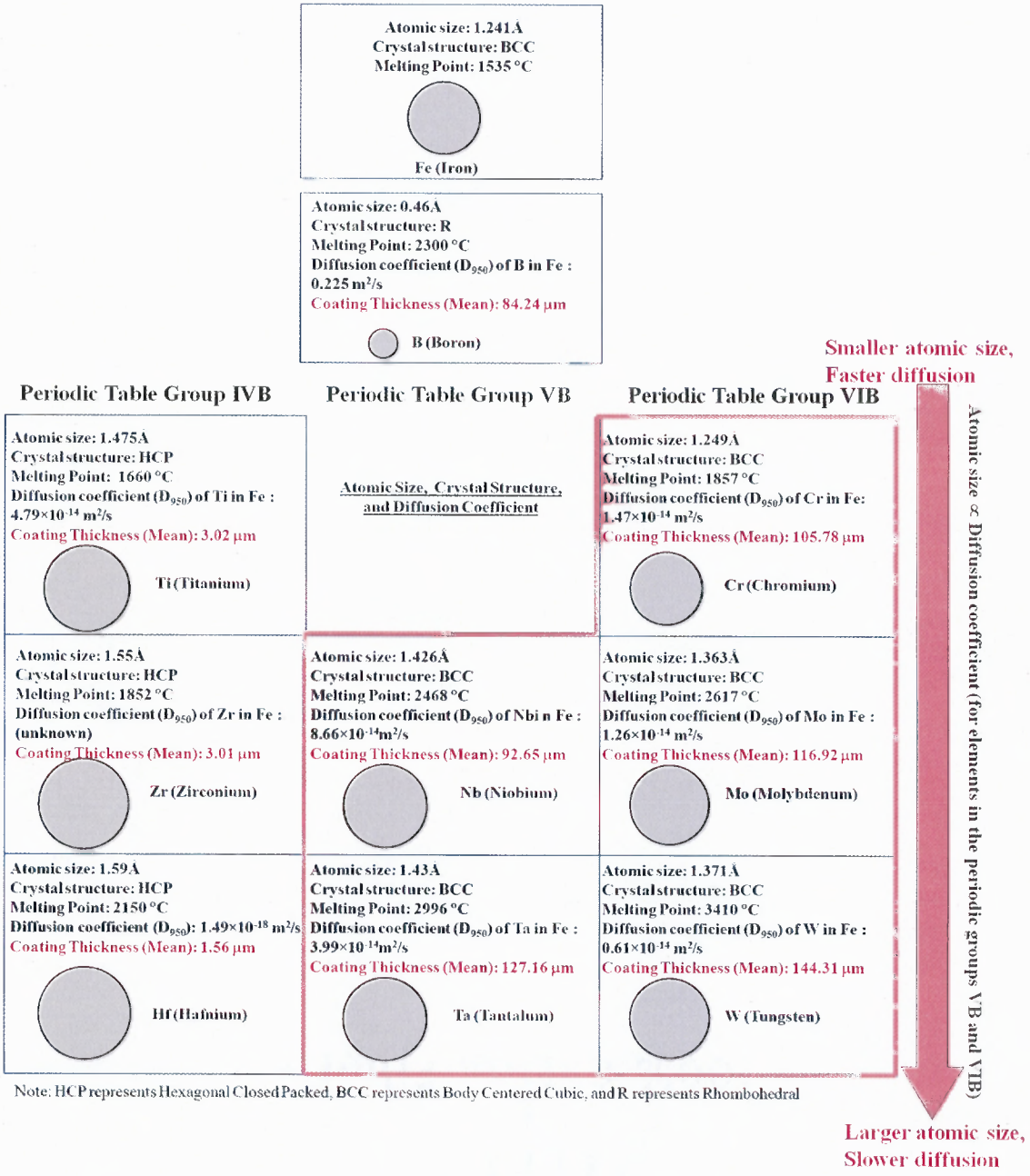

Figure 5.1 Atomic size, crystal structure, and diffusion coefficient of elements used in the boronizing process with respect to the periodic table.

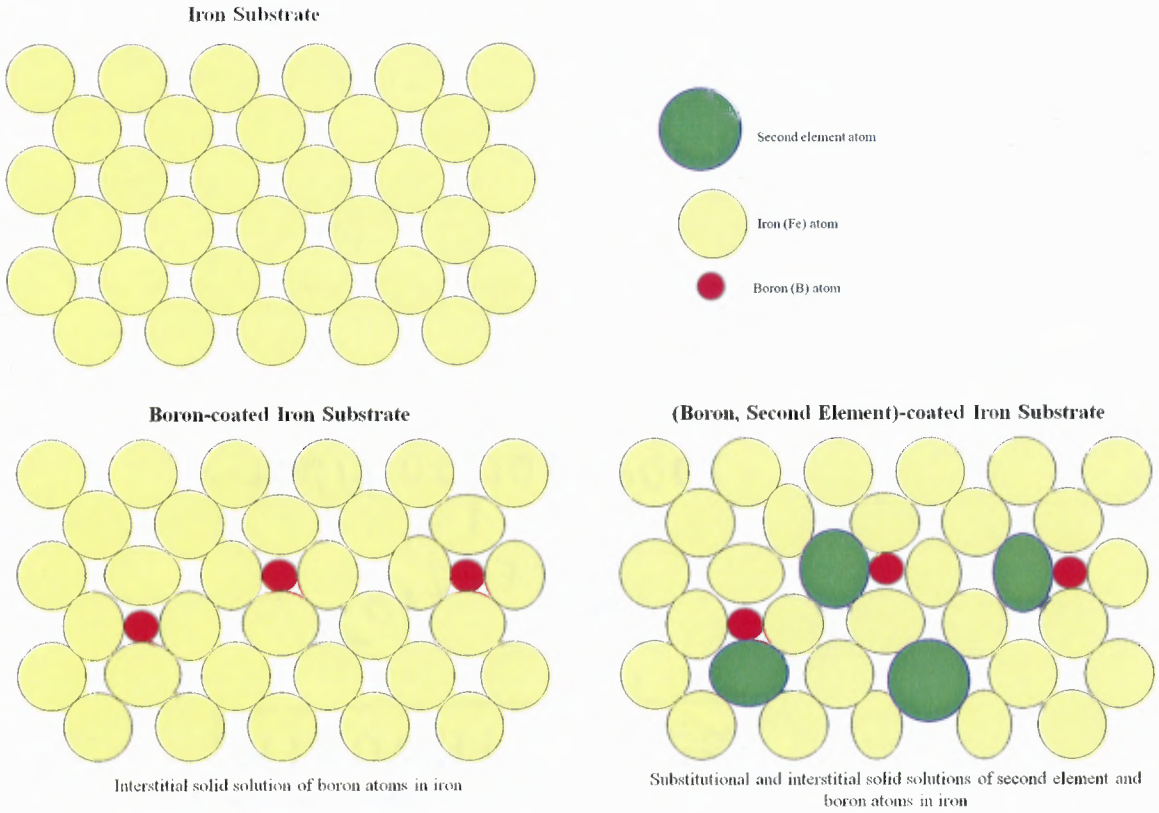

Figure 5.2 Solid solutions in multi-component boronizing.

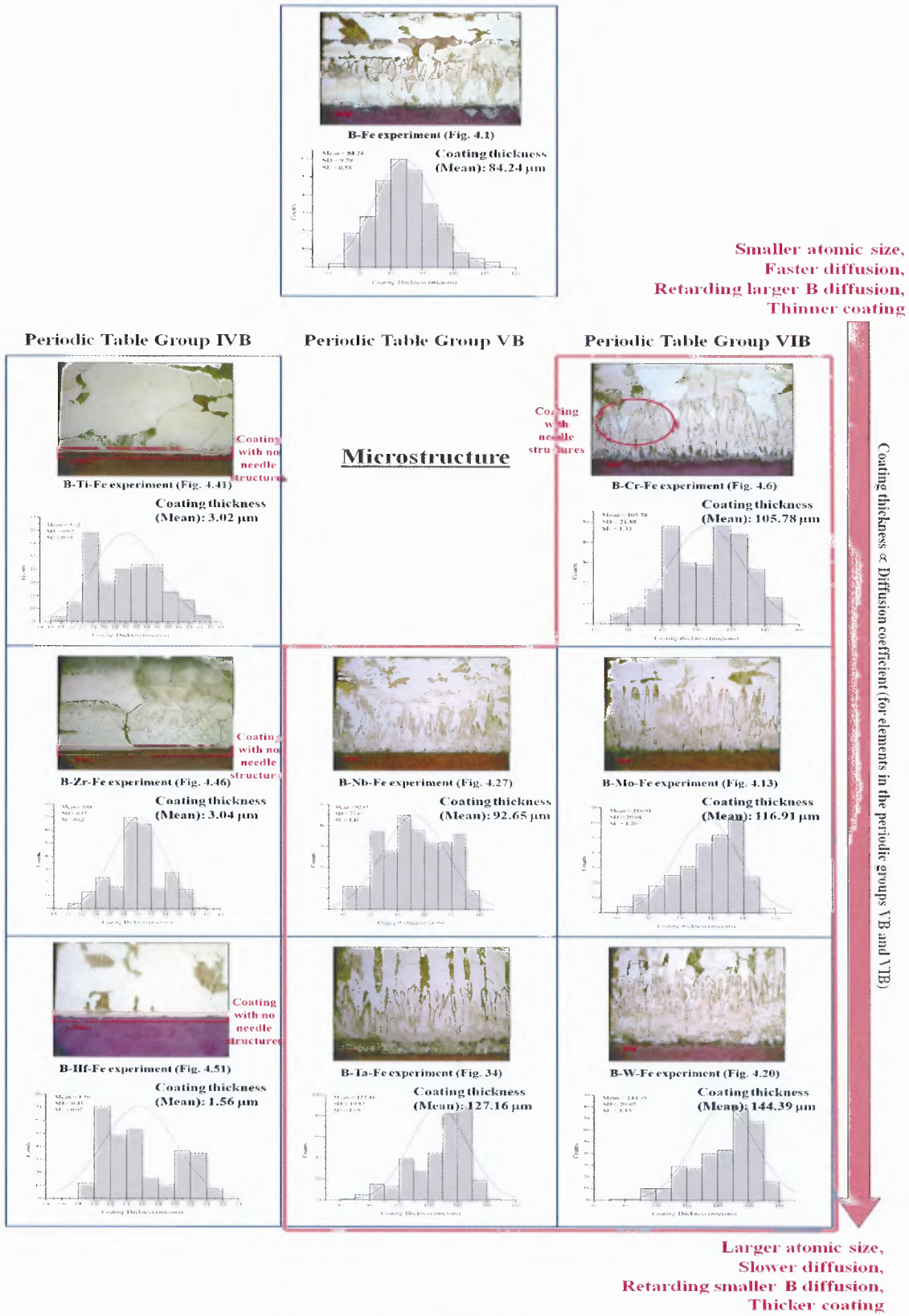

Figure 5.3 The comparison of microstructures of all nine experimental systems.

5.2 Phase Identification and Analysis

This section discusses and analyzes phase identification properties in forms of lattice parameters, microstrain, and crystal size as follows. The following Figure 5.4 depicts the comparison of all phased formed in all nine systems, along with other phase properties.

The presence of second elements in the multi-component boronizing can be confirmed by the occurring formation of metal borides of second elements. Forming other metal borides (besides Fe_2B and FeB) in the iron substrate is involved in the substituitional solid solution of second element and iron atoms. The second element substitution at iron causes the distortion of crystal structure and leads to the microstrain in the crystal.

To calculate the microstrain, the crystallographical data, such as lattice parameters, of all phases observed in the dissertation are referenced from the corresponding PDF cards as depicted in Figures B.1 - B.17 in Appendix B.

5.2.1 Lattice Parameters, Microstrain, and Crystal Size Properties of B-Cr-Fe, B-Mo-Fe, B-W-Fe, B-Nb-Fe, and B-Ta-Fe Coatings

The lattice parameters in three dimensions are represented with three lattice constants: a, b, and c. When either interstitial or substitutional solid solution is formed, the crystal structure is distorted, and then the microstrain is detected. The crystal distortion can be observed as the change of lattice constants and microstrain is calculated as the percentage of the distortion of crystal structure.

Due to the atomic size, substitutional solid solutions—occurring by second element atoms—can distort the crystal structure of boride phases more substantial than the distortion by interstitial solid solutions—occurring by boron atoms. Therefore, it can be seen in Tables 4.1 – 4.9, if the substitutional solid solution occurs in any boride phase, it will raise the microstrain.

For instance, in B-Mo-Fe system, the microstrain of Fe_2B phase is about 0.062%, which microstrain can come from the imperfect crystal while microstrain of MoB phase are 0.22%, which can result from the iron substitution at molybdenum in MoB phase.

Moreover, it is observed that the microstrain increases with respect to the atomic size of second elements for both period and group of period table.

5.2.2 Lattice Parameters, Microstrain, and Crystal Size Properties of B-Ti-Fe, B-Zr-Fe, and B-Hf-Fe Coatings

As addressed in Section 5.1.2, the coating thickness is very thin for these three systems. The substitutional solid solution occurs among boride /carbide phases which can form as the iron substitution at second element — $(Me,Fe)_xB_y$ / (Me,Fe)C — and the second element substitution at iron — $(Fe,Me)_xB_y$. It is apparent that the distortions of structure of phases are severe, thus resulting in high microstrain in all phases.

For instance, in B-Ti-Fe system, the microstrains of Fe_2B and FeB phases formed by boron atoms in iron are 0.12% and 0.18%, respectively. On the other hand, the microstrains of TiC, TiB, Ti_3B_4, and TiB_2 phases formed by titanium atoms in iron are 0.13, 0.21, 0.08, and 0.33, respectively

Crystal structure: BCC

Fe (Iron)

Crystal structure: R

Phase presence	% Chemical composition	Lattice parameters	Microstrain (%)	Crystal size (Å)
Fe_2B	90.1%	Tetrahedral	0.058	478.47
FeB	9.9%	Orthorhombic	0.13	282.50

B (Boron)

Periodic Table Group IVB

Phase presence	% Chemical composition	Lattice parameters	Microstrain (%)	Crystal size (Å)
Fe_2B	6.3	Tetrahedral	0.12	266.57
FeB	4.2	Orthorhombic	0.18	182.69
TiC	77.1	Cubic	0.13	234.80
TiB	3.4	Orthorhombic	0.21	164.14
Ti_3B_4	3.7	Orthorhombic	0.08	367.43
TiB_2	5.3	Hexagonal	0.33	90.91

Crystal structure: HCP

Ti (Titanium)

Periodic Table Group VB

Phase Identification and Analysis

Periodic Table Group VIB

Phase presence	% Chemical composition	Lattice parameters	Microstrain (%)	Crystal size (Å)
Fe_2B	81.4	Tetrahedral	0.051	548.10
Cr_2B	5.4	Orthorhombic	0.21	153.30
CrB	13.2	Orthorhombic	0.12	273.47

Crystal structure: BCC

Cr (Chromium)

Phase presence	% Chemical composition	Lattice parameters	Microstrain (%)	Crystal size (Å)
FeB	7.5	Orthorhombic	0.70	46.18
ZrC	91.4	Cubic	0.47	67.62
ZrB_2	1.1	Hexagonal	0.42	64.82

Crystal structure: HCP

Zr (Zirconium)

Phase presence	% Chemical composition	Lattice parameters	Microstrain (%)	Crystal size (Å)
Fe_2B	89.0	Tetrahedral	0.069	451.45
NbC	11.0	Cubic	0.15	150.75

Crystal structure: BCC

Nb (Niobium)

Phase presence	% Chemical composition	Lattice parameters	Microstrain (%)	Crystal size (Å)
Fe_2B	88.1	Tetrahedral	0.062	441.74
MoB	11.9	Orthorhombic	0.22	82.96

Crystal structure: BCC

Mo (Molybdenum)

Phase presence	% Chemical composition	Lattice parameters	Microstrain (%)	Crystal size (Å)
Fe_2B	29.9	Tetrahedral	0.44	73.89
HfC	68.5	Cubic	0.61	53.63
HfB_2	1.6	Hexagonal	0.89	36.50

Crystal structure: HCP

Hf (Hafnium)

Phase presence	% Chemical composition	Lattice parameters	Microstrain (%)	Crystal size (Å)
Fe_2B	3.9	Tetrahedral	0.18	186.55
FeB	93.9	Orthorhombic	0.090	300.23
Ta_3B_2	2.2	Tetrahedral	0.76	41.25

Crystal structure: BCC

Ta (Tantalum)

Phase presence	% Chemical composition	Lattice parameters	Microstrain (%)	Crystal size (Å)
Fe_2B	7.2	Tetrahedral	0.097	337.76
FeB	75.3	Orthorhombic	0.067	494.05
W_2B	7.4	Tetrahedral	0.30	113.60
Fe_7W_6	10.1	Trigonal	0.60	43.95

Crystal structure: BCC

W (Tungsten)

Note: HCP represents Hexagonal Closed Packed, BCC represents Body Centered Cubic, and R represents Rhombohedral

Figure 5.4 The comparison of phase identification properties for all nine experimental systems.

5.3 Microhardness

In boronizing process, the rich-boron phase will provide more stable and stronger boride phase. In B-Fe system, the low-stable iron-boride phases are formed, in which possess only metal-metal bonds, resulted in lower microhardness. Furthermore, in B-Fe system, deboronizing is found because the weak bond (metal-metal bond) of the boride compounds is destroyed during the heat treatment at high temperature and causes boron atoms diffusing outward the substrate.

The electronic configuration is used to explain the microhardness of the boride phases. Adding the second element to the boronizing process will increase the microhardness of coating, because second element atom and iron atom combine and share outer shell electrons and result in a new electronic configuration in the solid solution [121]. The new configuration of second element and iron atoms gives up some of their electrons to boron atoms, and that allows boron atoms to form more-stable boride structures, in which possess stronger boron-boron bonds and boron-metal bonds, thereby increasing microhardness.

In B-W-Fe, and B-Ta-Fe systems, the parallel cracks were observed on the coating, which is the result of large different amount of thermal expansion coefficient between two different boride phases during the cooling process. For instance, in B-W-Fe boronizing, the thermal expansion coefficient of W_2B phase is 6.7×10^{-6} K^{-1} and 12×10^{-6} K^{-1} of FeB phase.

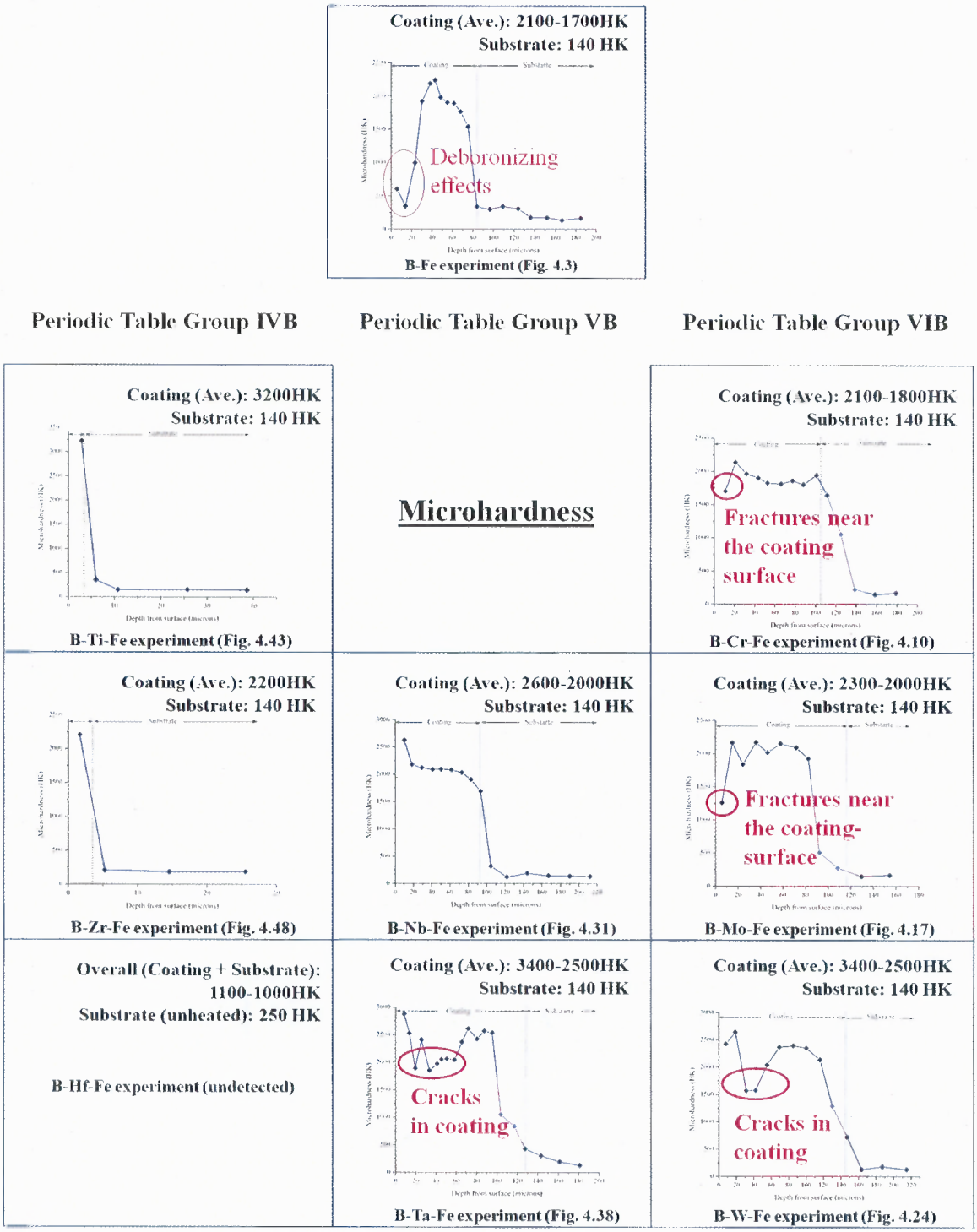

Figure 5.5 The comparison of microhardness of all nine experimental systems.

5.4 Corrosion Resistance

In this experiment, adding the second element into the boron coating is expected to improve the corrosion resistance. The corrosion resistance is measured by detecting the weight change of specimen per area. The coated specimen with higher corrosive resistance has a smaller change in specimen weight. From the percentage of phase composition, as depicted in Tables 4.1 to 4.6, phases formed by the second elements of the periodic table groups VB and VIB occur in a small percentage. For overall in these corrosion experiments, the results are not clear to conclude the effect of corrosion resistance by the second elements due to the small amount of second element in the coating and high corrosion resistance of iron boride phases as a main coating. The experiments were tested for the testing period of 12 hours and found that the weight loss of specimens was constant at 0.05 mg/mm^2. However, before the corrosion mechanism of iron boride is dominant, the effect of second elements can observed by the weight loss of coated specimens in the early testing time when the passive films are not formed yet as depicted in Figure 5.6.

The results showed that adding the second elements to the boronizing process can improve the corrosion resistance. However, after immersing the specimens in the acid media solution for 24 hours, it found the peeling of coating from B-Fe and B-Nb-Fe systems, corresponding to the results in Figure 5.6 which the weight losses of coating in B-Fe and B-Nb-Fe systems at the early testing time are below other systems The peeling of coating in B-Nb-Fe system could be from the pores occurring in the coating, and the peeling of coating in B-Fe system could be the effect of deboronizing.

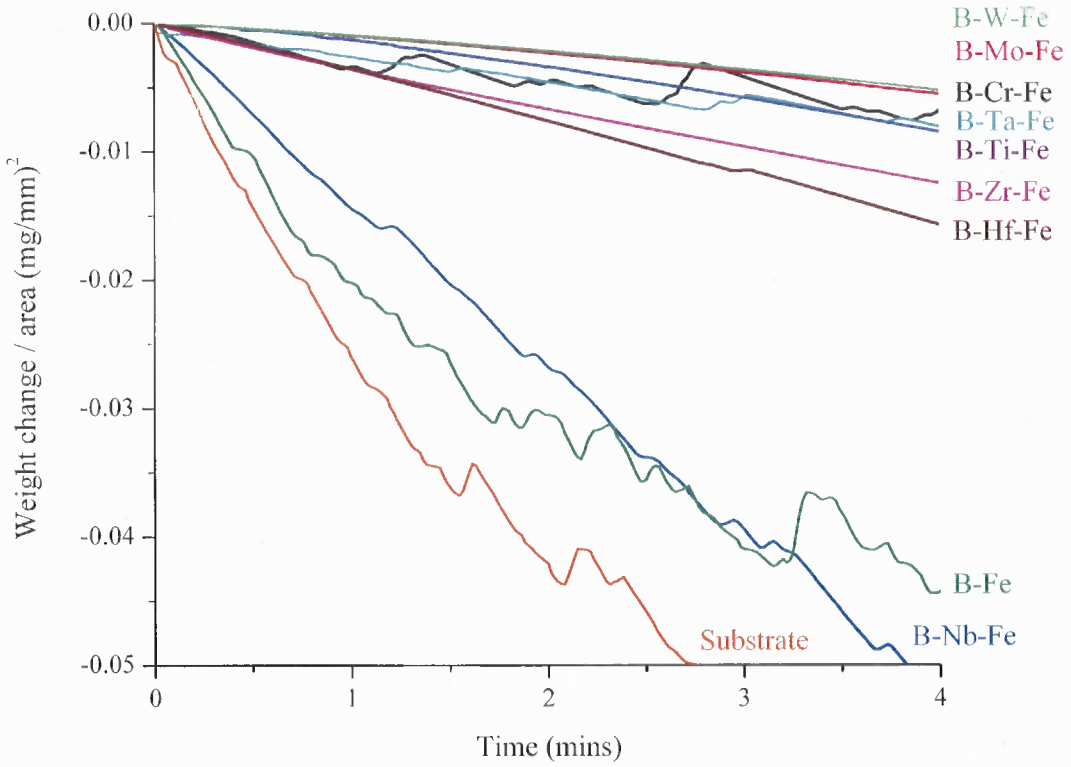

Figure 5.6 The comparison of weight change per area (mg/mm^2) against time (mins) of all testing systems due to corrosion.

5.5 Oxidation Resistance

In one-component boronizing, when oxygen atoms diffuse into boron coating, it forms the boron-oxide film covering the surface, thus reducing the oxidation. However, at higher temperature or at longer exposure time, the boron-oxide film will be mostly disappeared, and oxygen atoms can diffuse into iron substrate, causing the oxidation [122].

To increase oxidation resistance at high temperature, the second element is added into the boronizing powder mixture in multi-component boronizing. All eight second elements chosen in the experiments have a refractory property, which allows the multi-component boron coating to stand at higher temperature than the one-component boron coating. After boron-oxide film disappears at high temperature, oxygen atoms diffuse further into the coating. Because of the refractory property, the second element-oxide compound less occurs, thus, increasing the oxidation resistance.

The experiments of high temperature oxidation resistance have been conducted at different temperatures, between 400 and 800 °C. The results showed that the additional second element can provide the better high temperature oxidation resistance to the boron-coating as shown in Figure. 5.7. For B-Ti-Fe, B-Zr-Fe, and B-Hf-Fe system, the thin coating thickness limits the usage application at higher temperature above 700 °C. However, Zr is not the candidate of the second element to add into multi-component boron coating for the purpose of high temperature oxidation resistance due to the high chemical reaction between zirconium and oxygen. The best second element for the wide range of temperatures for oxidation resistance is niobium. For B-Fe system, the coating can endure high temperature up to 800 °C, and the coating starts losing oxidation

resistance property after temperature above 800 °C. Then, oxygen atoms have increasingly penetrated through the weakening coating into the substrate, which in turn, loosed more resistance until the coating has completely lose the temperature oxidation resistance. Up to that point, oxygen atoms would freely diffuse into the unprotected substrate and the substrate would finally break down.

At temperature of 800 °C, other second elements from the periodic table groups VB and VIB still showed the excellent high temperature oxidation resistance. This dissertation determines that by adding the second element, the multi-component-boron-coated applications can be used at high temperatures of up to 800 °C.

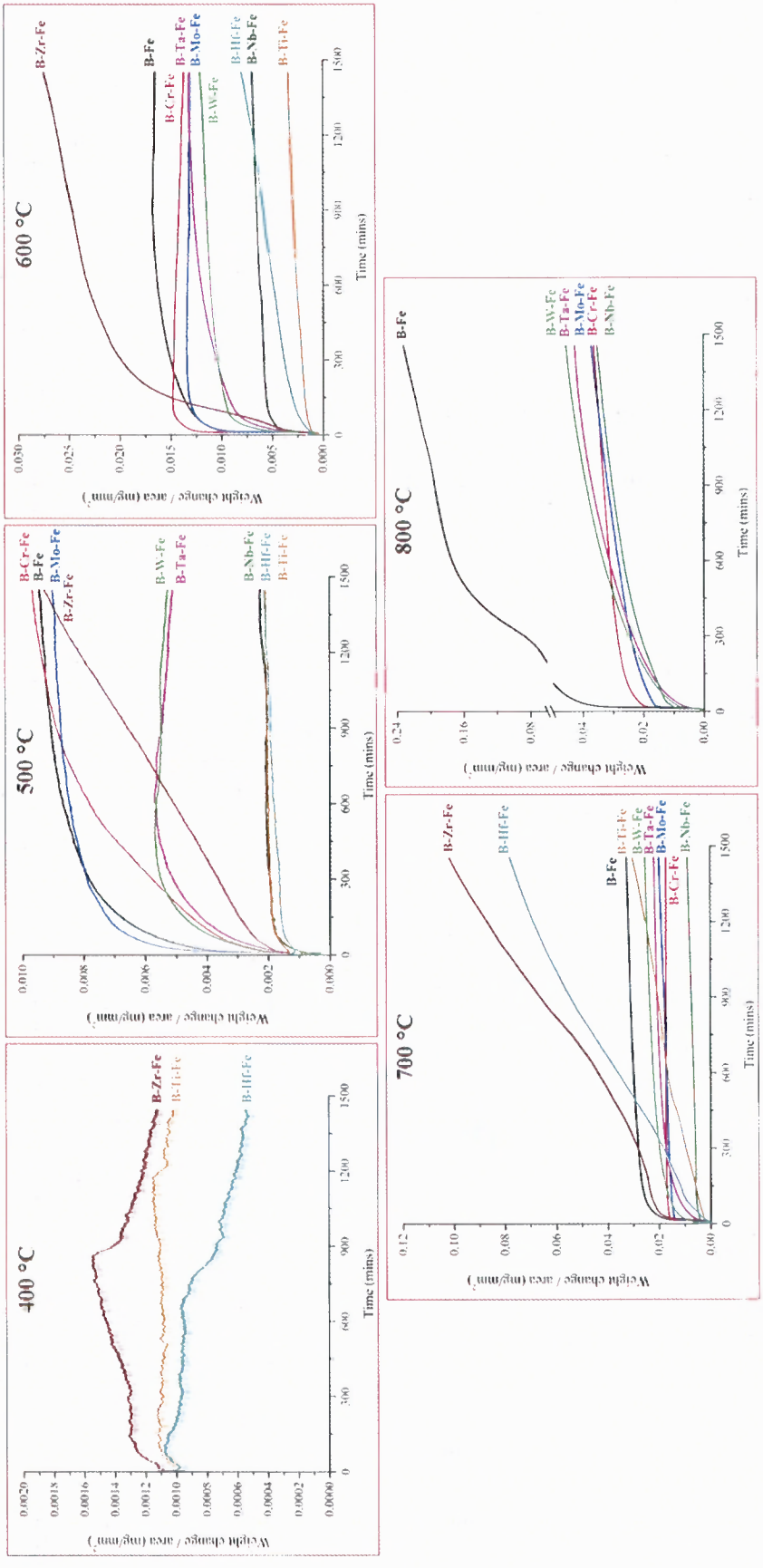

Figure 5.7 The comparison of oxidation resistance of multi-component boronizing at various temperatures between 400 to 800 °C.

CHAPTER 6

CONCLUSIONS AND FUTURE WORK

Boronizing process has been originally deployed to improve several properties of steel substrate, such as wear resistance, oxidation resistance, and corrosion resistance, by forming boronized coating on steel substrate. However, in some environments that endure extreme wear, high temperature oxidation, and high corrosion, those properties of boronized coating may not be sufficient. Many researchers and industries have been developing and studying to add other elements, as referred to the multi-component boronizing process, to increase those properties.

This dissertation focuses on developing the multi-component boronizing process to improve the properties of boronized coating using own original powder mixtures. Eight additional elements, which include chromium, molybdenum, tungsten, niobium, tantalum, titanium, zirconium, and hafnium, have been individually added into the boron powder mixtures that are used in conventional boronizing process. The dissertation addressed major developments as follows.

1. The simultaneous multi-component boronizing process is successfully achieved to perform the multi-component boron coating on low carbon steel AISI 1018 by using our own originally developed powder mixture.

2. Two diffusion mechanisms are proposed for the multi-component boronizing based on the periodic table groups of the additional second elements. For transition metals Group VB and VIB, boron diffusion is dominant at the initial stage and the coating thickness is controlled by the diffusion rate of the additional second elements.

For transition metals Group IVB, chemical affinity is dominant at the initial stage. The metal carbide is formed, and retards the diffusion of boron.

3. Adding the second elements to the boronizing process causes the distortion of crystal structure. However, this effect bases on the atomic size for both group and period on the periodic table.

4. The second element is found to provide the stable phases of Fe_2B and FeB in the coating. If second element is not added to the powder mixture, there is a possibility of deboronizing to occur during the boronizing process at high temperature. Deboronizing is known to cause boron atoms to diffuse outward from the substrate and decrease the microhardness of the coating. By adding any one of eight second elements into the boronizing powder mixture, the formation of substitutional solid solution of the additional second element atoms in iron can prevent the deboronizing.

5. The multi-component boronizing in the experiments improves the corrosion resistance, compared to conventional boronized coating. From the experiments, Tungsten and Molybdenum can be the candidates of second elements to add in multi-component boronizing for high corrosion resistance applications.

6. The multi-component boronizing in the experiments also improves the oxidation resistance. It is apparent that Niobium is the best candidate of second elements to add in the multi-component boronizing for oxidation resistant applications for a wide range temperature, up to 800 °C. Hafnium and titanium can be added for high oxidation resistance at temperature below 600 °C.

7. The multi-component boronizing is found to improve microhardness of coated specimens. The formation of new phases of the second element at the surface gives higher microhardness than Fe_2B and FeB phases alone. Specifically, the boronizing processes with tantalum and tungsten forms new phases that yield microhardness of more than 3,000 HK, compared to 2,100 HK from the Fe_2B and FeB phases.

The future work will involve in studying the chemical composition of powder mixtures among boron, second elements and activators, as well as heat treatment times and temperatures. The study is to control phase compositions in coating and to eliminate cracks. With controlled phase compositions, the properties, in terms of wear resistance, oxidation resistance, corrosion resistance, and microhardness, can be controllably improved.

The oxidation kinetics and mechanisms of each second element in multi-component boronizing will be further studied to investigate behaviors of oxidation process as well.

APPENDIX A

PHASE DIAGRAMS

The binary diagrams of nine experimental systems are depicted as follows.

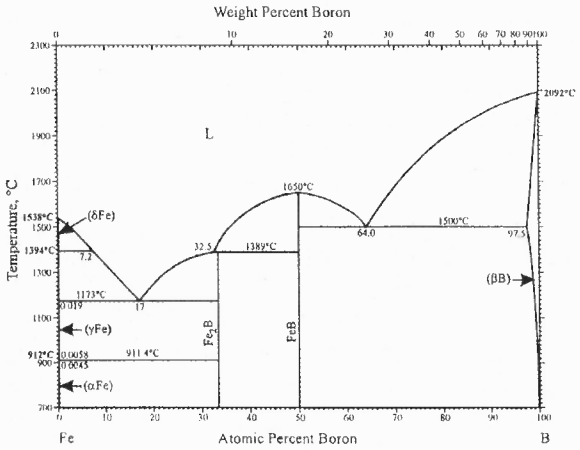

B-Fe

Fe-B

Phase	Composition, at.% B	Pearson symbol	Space group	Strukturbericht designation	Prototype
(δFe)	0	*cI*2	$Im\bar{3}m$	*A*2	W
(γFe)	0 to 0.019	*cF*4	$Fm\bar{3}m$	*A*1	Cu
(αFe)	0 to 0.0045	*cI*2	$Im\bar{3}m$	*A*2	W
Fe_2B	33.3	*tI*2	*I*4/*mcm*	*C*16	Al_2Cu
FeB	50	*oP*8	*Pbmn*	*B*27	FeB
(βB)	97.5 to 100	*hR*108	$R\bar{3}m$	...	...

P.K. Liao and K.E. Spear, *Phase Diagrams of Binary Iron Alloys*, H. Okamoto, ed., ASM International, Materials Park, OH, 41-47 (1993)

H. Okamoto, *J. Phase Equilibria*, *16*(4), 364-365 (1995)

Figure A.1 Phase diagram in B-Fe (Boron-Iron) system [123].

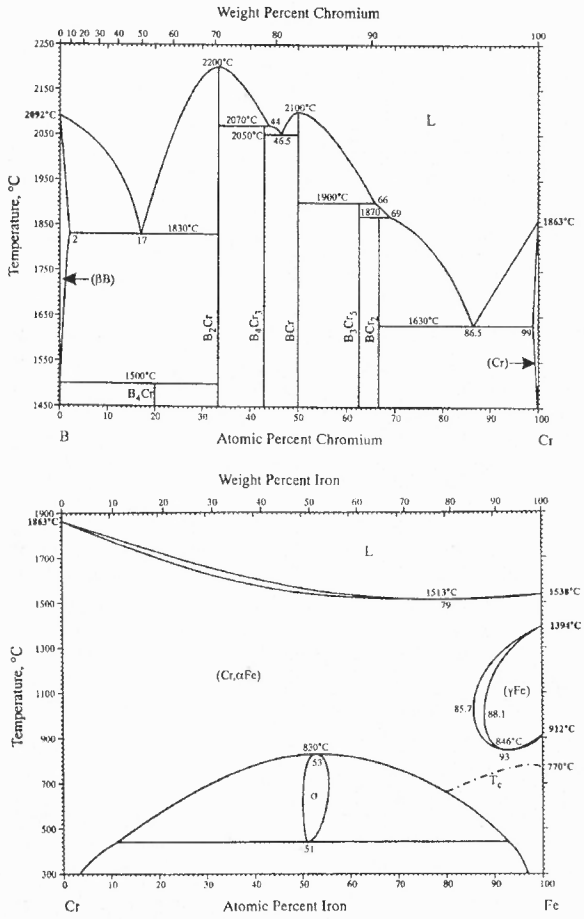

B-Cr

B-Cr

Phase	Composition, at.% Cr	Pearson symbol	Space group	Strukturbericht designation	Prototype
(ββ)	0 to 2	*hR*108	$R\bar{3}m$	...	...
B_4Cr	20	*o***	...	...	...
B_2Cr	33.3	*hP*3	*P6/mmm*	*C*32	AlB_2
B_4Cr_3	42.9	*oI*14	*Immm*	$D7_b$	Ta_3B_4
BCr	50	*oC*8	*Cmcm*	B_f	CrB
B_3Cr_5	62.5	*tI*32	*I4/mcm*	$D8_l$	Cr_3B_5
BCr_2	66.7	*oF*40	*Fddd*	$D1_f$	Mn_4B
(Cr)	99 to 100	*cI*2	$Im\bar{3}m$	*A*2	W

P.K. Liao and K.E. Spear, *Bull. Alloy Phase Diagrams*, 7(3), 232-237 (1986)

Cr-Fe

Cr-Fe

Phase	Composition, at.% Fe	Pearson symbol	Space group	Strukturbericht designation	Prototype
(Cr,αFe)	0 to 100	*cI*2	$Im\bar{3}m$	*A*2	W
σ	50 to 55.5	*tP*30	$P4_2/mnm$	$D8_b$	σCrFe
(γFe)	88.1 to 100	*cF*4	$Fm\bar{3}m$	*A*1	Cu

O. Kubaschewski, *Iron – Binary Alloy Phase Diagrams*, Springer-Verlag, Berlin (1982)

See also
V.P. Itkin, *Phase Diagrams of Binary Iron Alloy*, H. Okamoto, ed., ASM International, Materials Park, OH, 102-129 (1993)

Figure A.2 Phase diagrams in B-Cr-Fe (Boron-Chromium-Iron) system [123].

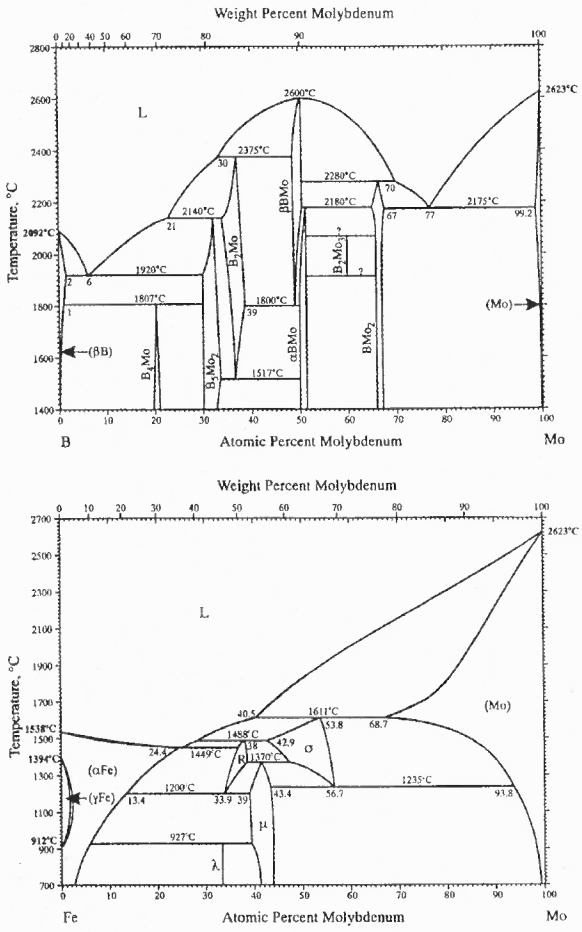

B-Mo

B-Mo

Phase	Composition, at.% Mo	Pearson symbol	Space group	Strukturbericht designation	Prototype
(βB)	0 to 2	*hR*108	$R\bar{3}m$	…	…
B_4Mo	19 to 21	*hP*20	$P6_3/mmc$	…	B_4W
B_5Mo_2	30 to 34	*hR*7	$R\bar{3}m$	$D8_l$	Mo_2B_5
B_2Mo	34 to 39	*hP*3	*P6/mmm*	*C*32	AlB_2
βBMo	48.5 to 50.5	*oC*8	*Cmcm*	B_f	CrB
αBMo	50 to 51.5	*tI*16	$I4_1/amd$	B_g	MoB
B_2Mo_3	60	…	…	…	…
BMo_2	65 to 67	*tI*12	*I4/mcm*	*C*16	Al_2Cu
(Mo)	99.2 to 100	*cI*2	$Im\bar{3}m$	*A*2	W

K.E. Spear and P.K. Liao, *Bull. Alloy Phase Diagrams*, *9*(4), 457-466 (1988)

Fe-Mo

Fe-Mo

Phase	Composition, at.% Mo	Pearson symbol	Space group	Strukturbericht designation	Prototype
(αFe)	0 to 24.4	*cI*2	$Im\bar{3}m$	*A*2	W
(γFe)	0 to 1.7	*cF*4	$Fm\bar{3}m$	*A*1	Cu
λ	33.3	*hP*12	$P6_3/mmc$	*C*14	$MgZn_2$
R	33.9 to 38.5	*hR*53	…	…	…
μ	39.0 to 44.0	*hR*13	$R\bar{3}m$	$D8_5$	Fe_7W_6
σ	42.9 to 56.7	*tP*30	$P4_2/mnm$	$D8_b$	σCrFe
(Mo)	68.7 to 100	*cI*2	*Im*3*m*	*A*2	W

A. Fernandez-Guillermet, *Bull. Alloy Phase Diagrams*, *3*(3), 359-367 (1982)

Figure A.3 Phase diagrams in B-Mo-Fe (Boron-Molybdenum-Iron) system [123].

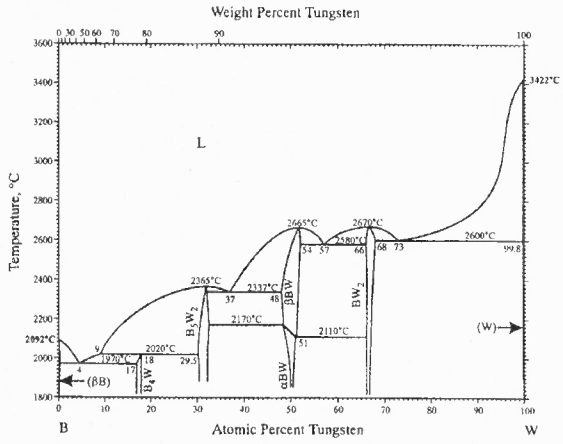

B-W

B-W

Phase	Composition, at.% W	Pearson symbol	Space group	Strukturbericht designation	Prototype
(βB)	0	*hR*108	$R\bar{3}m$	...	...
B_4W	17 to 18	*hP*20	$P6_3/mmc$	...	MoB_4
B_5W_2	29.5 to 32.5	*hP*14	$P6_3/mmc$	$D8_h$	W_2B_5
βBW	48 to 54	*oC*8	*Cmcm*	B_f	CrB
αBW	48 to 51	*tI*16	$I4_1/amd$	B_g	MoB
BW_2	66 to 68	*tI*12	*I*4/*mcm*	*C*16	Al_2Cu
(W)	99.8 to 100	*cI*2	$Im\bar{3}m$	*A*2	W

S.V. Nagender Naidu and P. Rama Rao, *Phase Diagrams of Binary Tungsten Alloys*, S.V. Nagender Naidu and P. Rama Rao, ed., Indian Institute of Metals, Calcutta, India, 21-28 (1991)

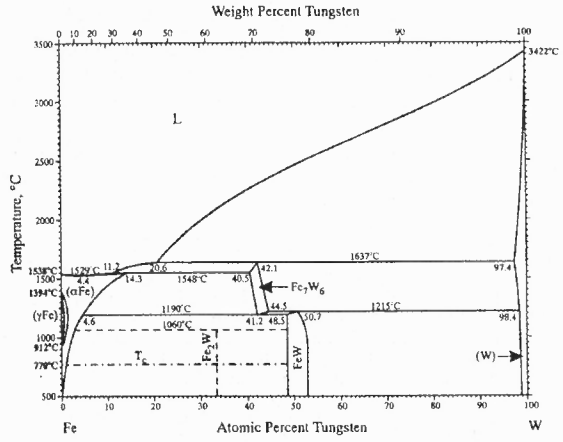

Fe-W

Fe-W

Phase	Composition, at.% W	Pearson symbol	Space group	Strukturbericht designation	Prototype
(αFe)	0 to 14.3	*cI*2	$Im\bar{3}m$	*A*2	W
(γFe)	0 to 1.5	*cF*4	$Fm\bar{3}m$	*A*1	Cu
Fe_2W*	33.3	*hP*12	$P6_3/mmc$	*C*14	$MgZn_2$
Fe_7W_6	40.5 to 44.5	*hR*13	$R\bar{3}m$	$D8_5$	Fe_7W_6
FeW	48.5 to 53	*oP*112	$P2_12_12_1$	...	MoNi
(W)	97.4 to 100	*cI*2	$Im\bar{3}m$	*A*2	W

* Metastable

S.V. Nagender Naidu, A.M. Sriramamurthy, and P. Rama Rao, *Phase Diagrams of Binary Iron Alloys*, H. Okamoto, ed., ASM International, Materials Park, OH, 444-453 (1993)

Figure A.4 Phase diagrams in B-W-Fe (Boron-Tungsten-Iron) system [123].

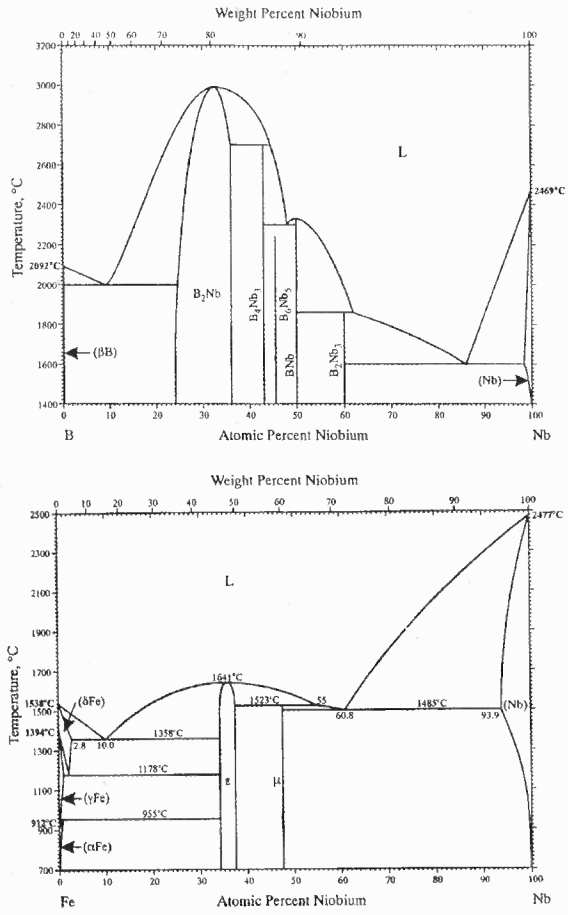

B-Nb

B-Nb

Phase	Composition, at.% Nb	Pearson symbol	Space group	Strukturbericht designation	Prototype
(βB)	0	*hR*108	$R\bar{3}m$	...	...
B_2Nb	24 to 36	*hP*3	*P6/mmm*	*C*32	AlB_2
B_4Nb_3	42.9	*oI*14	*Immm*	$D7_b$	Ta_3B_4
B_6Nb_5	45.5	*oC**	*Cmmm*	...	...
BNb	50	*oC*8	*Cmcm*	B_f	CrB
B_2Nb_3	60	*tP*10	*P4/mbm*	$D5_a$	Si_2U_3
(Nb)	? to 100	*cI*2	$Im\bar{3}m$	*A*2	W

Binary Alloy Phase Diagrams, 2nd ed., T.B. Massalski, H. Okamoto, P.R. Subramanian, and L. Kacprzak, ed., ASM International, Materials Park, OH, 505-506 (1990)

Fe-Nb

Fe-Nb

Phase	Composition, at.% Nb	Pearson symbol	Space group	Strukturbericht designation	Prototype
(δFe)	0 to 2.8	*cI*2	$Im\bar{3}m$	*A*2	W
(γFe)	0 to 1	*cF*4	$Fm\bar{3}m$	*A*1	Cu
(αFe)	0 to 0.8	*cI*2	$Im\bar{3}m$	*A*2	W
ε	34.1 to 37.3	*hP*12	$P6_3/mmc$	*C*14	$MgZn_2$
μ	47.6	*hR*13	$R\bar{3}m$	$D8_5$	Fe_7W_6
(Nb)	93.9 to 100	*cI*2	$Im\bar{3}m$	*A*2	W

H. Okamoto, *J. Phase Equilibria*, *16*(4), 369-370 (1995)

Figure A.5 Phase diagrams in B-Nb-Fe (Boron-Niobium-Iron) system [123].

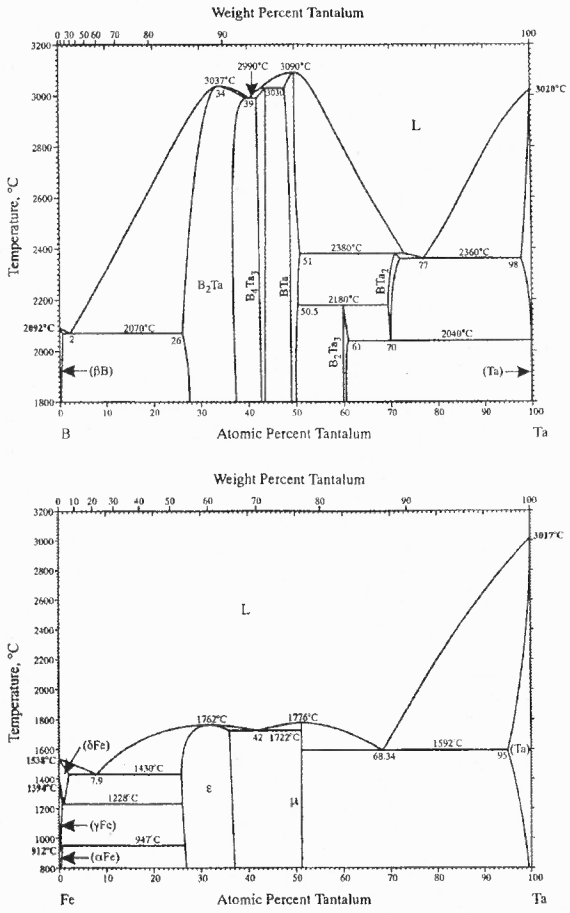

B-Ta

B-Ta

Phase	Composition, at.% Ta	Pearson symbol	Space group	Strukturbericht designation	Prototype
(βB)	0 to 1	*hR*108	$R\bar{3}m$	...	...
B_2Ta	26 to 39	*hP*3	*P6/mmm*	*C*32	AlB_2
B_3Ta_3	41 to 44	*oI*14	*Immm*	$D7_b$	Ta_3B_4
BTa	48 to 51	*oC*8	*Cmcm*	B_f	CrB
B_2Ta_3	60 to 61	*tP*10	*P4/mbm*	$D5_a$	Si_2U_3
BTa_2	69 to 72	*tI*12	*I4/mcm*	*C*16	Al_2Cu
(Ta)	98 to 100	*cI*2	$Im\bar{3}m$	*A*2	W

H. Okamoto, *J. Phase Equilibria*, *14*(3), 393-394 (1993)

Fe-Ta

Fe-Ta

Phase	Composition, at.% Ta	Pearson symbol	Space group	Strukturbericht designation	Prototype
(δFe)	0 to 2.5	*cI*2	$Im\bar{3}m$	*A*2	W
(γFe)	0 to 0.9	*cF*4	$Fm\bar{3}m$	*A*1	Cu
(αFe)	0 to 0.7	*cI*2	$Im\bar{3}m$	*A*2	W
ε	26 to 37	*hP*12	$P6_3/mmc$	*C*14	$MgZn_2$
μ	51	*hR*13	$R\bar{3}m$	$D8_5$	Fe_7W_6
(Ta)	95 to 100	*cI*2	$Im\bar{3}m$	*A*2	W

H. Okamoto, *J. Phase Equilibria*, *17*(1), 81-82 (1996)

Figure A.6 Phase diagrams in B-Ta-Fe (Boron-Tantalum-Iron) system [123].

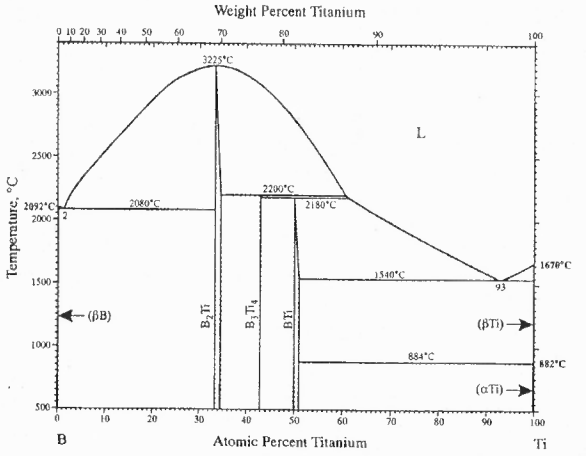

B-Ti

B-Ti

Phase	Composition, at.% Ti	Pearson symbol	Space group	Strukturbericht designation	Prototype
(βB)	0	*hR*108	$R\bar{3}m$	...	...
B_2Ti	33.3 to 34.4	*hP*3	*P6/mmm*	*C*32	AlB_2
B_4Ti_3	42.9	*oI*14	*Immm*	$D7_b$	Ta_3B_4
BTi	50 to 51	*oP*8	*Pnma*	*B*27	FeB
(βTi)	100	*cI*2	$Im\bar{3}m$	*A*2	W
(αTi)	100	*hP*2	$P6_3/mmc$	*A*3	Mg

J.L. Murray, P.K. Liao, and K.E. Spear, *Phase Diagrams of Binary Titanium Alloys*, J.L. Murray, ed., ASM International, Metals Park, OH, 33-38 (1987)

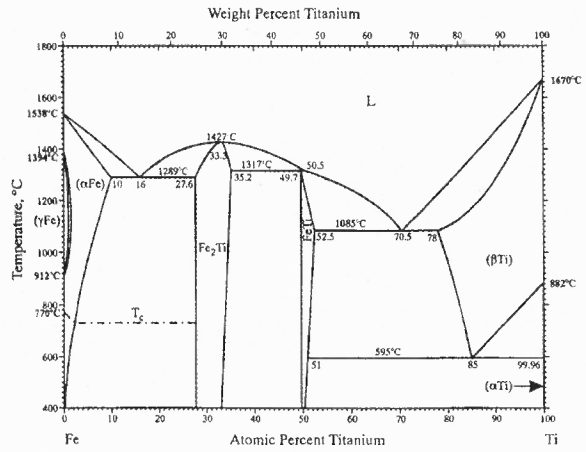

Fe-Ti

Fe-Ti

Phase	Composition, at.% Ti	Pearson symbol	Space group	Strukturbericht designation	Prototype
(αFe)	0 to 10	*cI*2	$Im\bar{3}m$	*A*2	W
(γFe)	0 to 0.8	*cF*4	$Fm\bar{3}m$	*A*1	Cu
Fe_2Ti	27.6 to 35.2	*hP*12	$P6_3/mmc$	*C*14	$MgZn_2$
FeTi	49.7 to 52.5	*cP*2	$Pm\bar{3}m$	*B*2	CsCl
(βTi)	78 to 100	*cI*2	$Im\bar{3}m$	*A*2	W
(αTi)	99.96 to 100	*hP*2	$P6_3/mmc$	*A*3	Mg

J.L. Murray, *Phase Diagrams of Binary Titanium Alloys*, ASM International, Metals Park, OH, 99-111 (1987)

see also
H. Okamoto, *J. Phase Equilibria*, *17*(4), 369 (1996)

Figure A.7 Phase diagrams in B-Ti-Fe (Boron-Titanium-Iron) system [123].

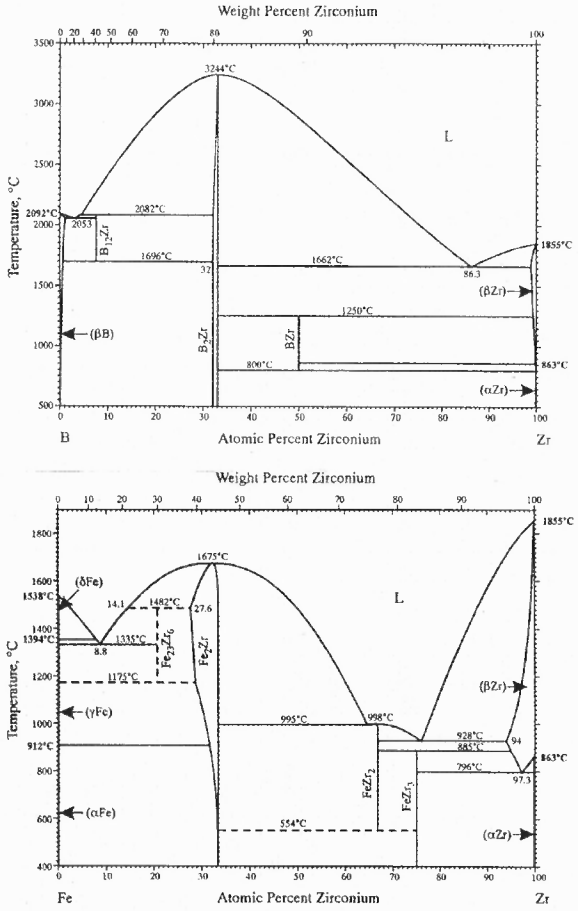

B-Zr

B-Zr

Phase	Composition, at.% Zr	Pearson symbol	Space group	Strukturbericht designation	Prototype
(βB)	0 to 1	*hR*108	$R\bar{3}m$	...	...
$B_{12}Zr$	7.6	*cF*52	$Fm\bar{3}m$	$D2_f$	UB_{12}
B_2Zr	32 to 33.3	*hP*3	*P6/mmm*	*C*32	AlB_2
BZr	50	*cF*8	$Fm\bar{3}m$	*B*1	NaCl
(βZr)	98.5 to 100	*cI*2	$Im\bar{3}m$	*A*2	W
(αZr)	100	*hP*2	$P6_3/mmc$	*A*3	Mg

H. Okamoto, *J. Phase Equilibria*, *14*(2), 261-262 (1993)

Fe-Zr

Fe-Zr

Phase	Composition, at.% Zr	Pearson symbol	Space group	Strukturbericht designation	Prototype
(δFe)	0	*cI*2	$Im\bar{3}m$	*A*2	W
(γFe)	0	*cF*4	$Fm\bar{3}m$	*A*1	Cu
(αFe)	0	*cI*2	$Im\bar{3}m$	*A*2	W
$Fe_{23}Zr_6$	20.7	*cF*116	$Fm\bar{3}m$	$D8_a$	$Mn_{23}Th_6$
Fe_2Zr	27.6 to 33.3	*cF*24	$Fd\bar{3}m$	*C*15	Cu_2Mg
$FeZr_2$	66.7	*tI*12	*I*4/*mcm*	*C*16	Al_2Cu
$FeZr_3$	75	*oC*16	*Cmcm*	$E1_a$	BRe_3
(βZr)	94 to 100	*cI*2	$Im\bar{3}m$	*A*2	W
(αZr)	100	*hP*2	$P6_3/mmc$	*A*3	Mg

H. Okamoto, *J. Phase Equilibria*, *18*(3), 316 (1997)

Figure A.8 Phase diagrams in B-Zr-Fe (Boron-Zirconium-Iron) system [123].

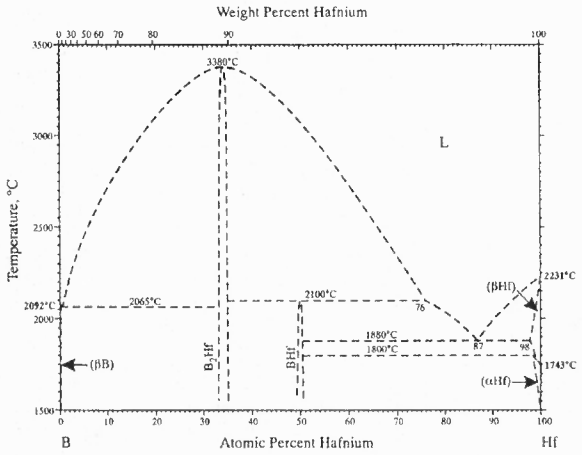

B-Hf

B-Hf

Phase	Composition, at.% Hf	Pearson symbol	Space group	Strukturbericht designation	Prototype
(βB)	0	*hR*108	$R\bar{3}m$	...	...
B_2Hf	33 to 35	*tI*12	*I*4/*mcm*	*C*16	Al_2Cu
BHf	49 to 51	*oP*8	*Pnma*	*B*27	FeB
(βHf)	98 to 100	*cI*2	$Im\bar{3}m$	*A*2	W
(αHf)	98 to 100	*hP*2	$P6_3/mmc$	*A*3	Mg

Binary Alloy Phase Diagrams, *2nd ed.*, T.B. Massalski, H. Okamoto, P.R. Subramanian, and L. Kacprzak, ed., ASM International, Materials Park, OH, 488-489 (1990)

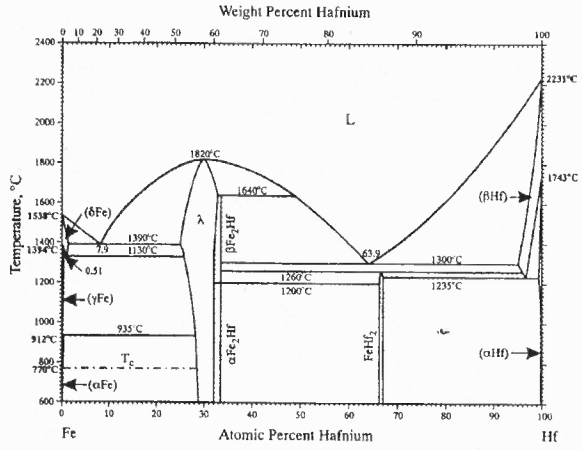

Fe-Hf

Fe-Hf

Phase	Composition, at.% Hf	Pearson symbol	Space group	Strukturbericht designation	Prototype
(δFe)	0 to 2	*cI*2	$Im\bar{3}m$	*A*2	W
(γFe)	0 to 0.51	*cF*4	$Fm\bar{3}m$	*A*1	Cu
(αFe)	0 to 0.22	*cI*2	$Im\bar{3}m$	*A*2	W
λ	25 to 33	*hP*12	$P6_3/mmc$	*C*14	$MgZn_2$
βFe_2Hf	33.3	*hP*24	$P6_3/mmc$	*C*36	$MgNi_2$
αFe_2Hf	33.3	*cF*24	$Fd\bar{3}m$	*C*15	Cu_2Mg
$FeHf_2$	65 to 67	*cF*96	$Fd\bar{3}m$	...	$NiTi_2$
(βHf)	? to 100	*cI*2	$Im\bar{3}m$	*A*2	W
(αHf)	? to 100	*hP*2	$P6_3/mmc$	*A*3	Mg

H. Okamoto, *Phase Diagrams of Binary Iron Alloys*, H. Okamoto, ed., ASM International, Materials Park, OH, 171-173 (1993)

Figure A.9 Phase diagrams in B-Hf-Fe (Boron-Hafnium-Iron) system [123].

APPENDIX B

PHASE PROPERTIES (CRYSTAL DATA)

The phase properties of all phases formed by boron and additional second element atoms in all nine experimental systems are depicted as follows.

Name and formula

Reference code:	04-007-6176
PDF index name:	Iron Boride
Empirical formula:	BFe
Chemical formula:	FeB

Crystallographic parameters

Crystal system:	Orthorhombic
Space group:	Pnma
Space group number:	62
a (Å):	5.4950
b (Å):	2.9467
c (Å):	4.0577
Alpha (°):	90.0000
Beta (°):	90.0000
Gamma (°):	90.0000
Volume of cell (10^6 pm^3):	65.70
Z:	4.00
RIR:	2.14

References

Primary reference:	*Calculated from LPF using POWD-12++*
Structure:	Kanaizuka T., *J. Solid State Chem.*, **41**, 195, (1982)

Structure

No.	Name	Element	X	Y	Z	Biso	sof	Wyck.
1	B1	B	0.03600	0.25000	0.11000	0.5000	1.0000	4c
2	FE1	Fe	0.18000	0.25000	0.62500	0.5000	1.0000	4c

Stick Pattern

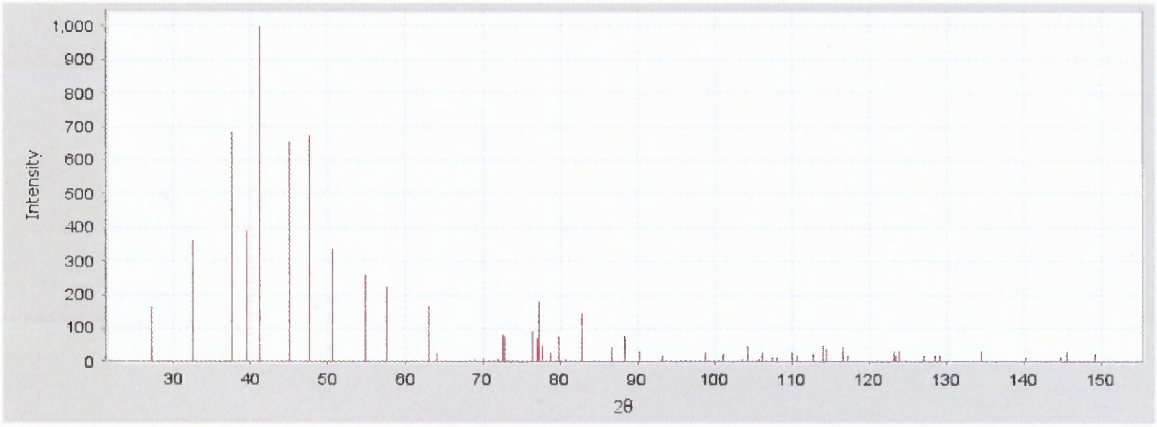

Figure B.1 The crystal data of FeB [124].

Name and formula

Reference code:	04-004-6913
PDF index name:	Iron Boride
Empirical formula:	BFe_2
Chemical formula:	Fe_2B

Crystallographic parameters

Crystal system:	Tetragonal
Space group:	I4/mcm
Space group number:	140
a (Å):	5.1000
b (Å):	5.1000
c (Å):	4.2400
Alpha (°):	90.0000
Beta (°):	90.0000
Gamma (°):	90.0000
Volume of cell (10^6 pm^3):	110.28
Z:	4.00
RIR:	6.36

References

Primary reference:	*Calculated from LPF using POWD-12++*
Structure:	Ganglberger E., Nowotny H., Benesovsky F., *Monatsh. Chem.*, **97**, 718, (1966)

Structure

No.	Name	Element	X	Y	Z	Biso	sof	Wyck
1	FE1	Fe	0.15810	0.65810	0.00000	0.5000	1.0000	8h
2	B1	B	0.00000	0.00000	0.25000	0.5000	1.0000	4a

Stick Pattern

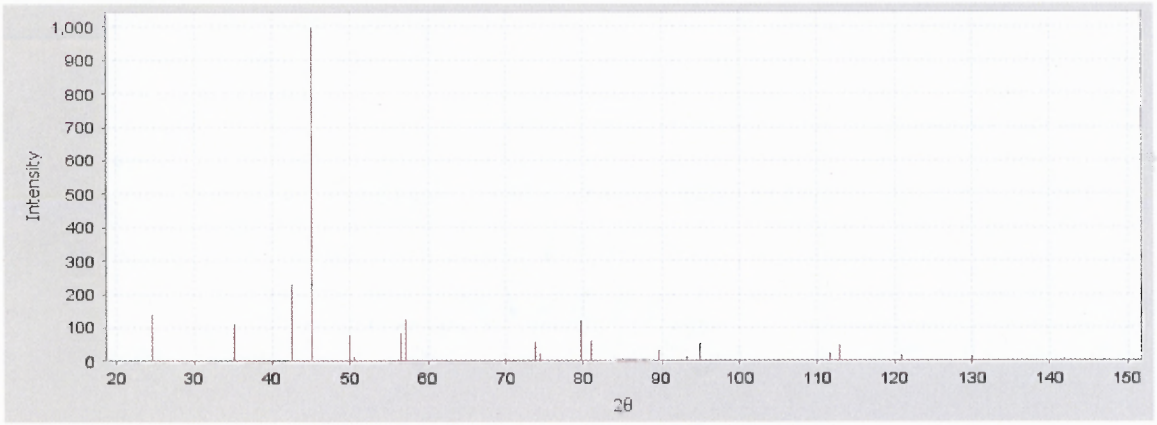

Figure B.2 The crystal data of Fe_2B [124].

Name and formula

Reference code:	04-003-6174
PDF index name:	Chromium Boride
Empirical formula:	BCr
Chemical formula:	CrB

Crystallographic parameters

Crystal system:	Orthorhombic
Space group:	Cmcm
Space group number:	63
a (Å):	2.9640
b (Å):	7.8580
c (Å):	2.9340
Alpha (°):	90.0000
Beta (°):	90.0000
Gamma (°):	90.0000
Volume of cell (10^6 pm^3):	68.34
Z:	4.00
RIR:	2.66

References

Primary reference:	*Calculated from LPF using POWD-12++*
Structure:	Telegus V.S., Kuz`ma Yu.B., Stefanishina T.K., *Soviet Powder Metall. and Met. Ceramics*, **8**, 133, (1969)

Structure

No.	Name	Element	X	Y	Z	Biso	sof	Wyck
1	B1	B	0.00000	0.10800	0.25000	0.5000	1.0000	4c
2	CR1	Cr	0.00000	0.36700	0.25000	0.5000	1.0000	4c

Stick Pattern

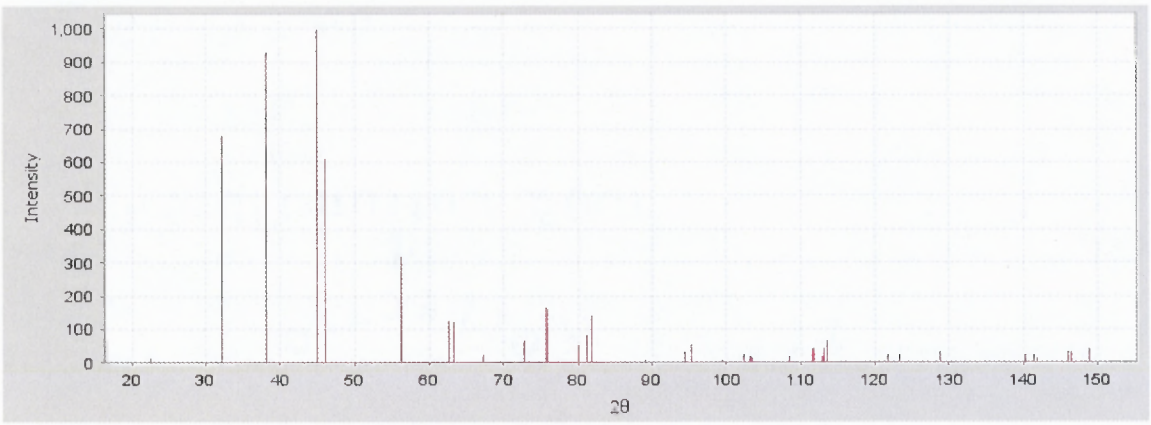

Figure B.3 The crystal data of CrB [124].

Name and formula

Reference code:	04-007-4811
PDF index name:	Chromium Boride
Empirical formula:	BCr_2
Chemical formula:	Cr_2B

Crystallographic parameters

Crystal system:	Orthorhombic
Space group:	Fddd
Space group number:	70
a (Å):	4.2498
b (Å):	7.4090
c (Å):	14.7118
Alpha (°):	90.0000
Beta (°):	90.0000
Gamma (°):	90.0000
Volume of cell (10^6 pm^3):	463.23
Z:	16.00
RIR:	2.32

References

Primary reference:	*Calculated from LPF using POWD-12++*
Structure:	Wong Ng W., McMurdie H.F., Paretzkin B., Zhang Y., Davis K.L., Hubbard C.R., Dragoo A.L., Stewart J.M., *Powder Diffraction*, **2**, 257, (1987)

Structure

No	Name	Element	X	Y	Z	Biso	sof	Wyck.
1	CR1	Cr	0.12500	0.12500	0.04150	0.5000	1.0000	16g
2	B1	B	0.12500	0.12500	0.49819	0.5000	1.0000	16g
3	CR2	Cr	0.12500	0.45860	0.12500	0.5000	1.0000	16f

Stick Pattern

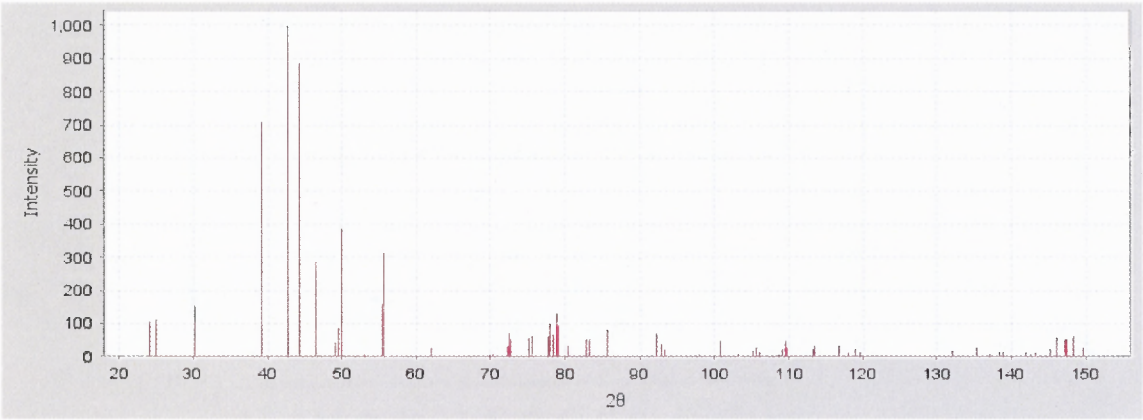

Figure B.4 The crystal data of Cr_2B [124].

Name and formula

Reference code:	04-003-5559
PDF index name:	Molybdenum Boride
Empirical formula:	BMo
Chemical formula:	MoB

Crystallographic parameters

Crystal system:	Tetragonal
Space group:	I41/amd
Space group number:	141
a (Å):	3.1100
b (Å):	3.1100
c (Å):	16.9700
Alpha (°):	90.0000
Beta (°):	90.0000
Gamma (°):	90.0000
Volume of cell (10^6 pm^3):	164.14
Z:	8.00
RIR:	4.97

References

Primary reference:	*Calculated from LPF using POWD-12++*
Structure:	Steinitz R., Binder I., Moskowitz D., *Trans. Am. Inst. Min. Metall. Pet. Eng.*, **194**, 983, (1952)

Structure

No.	Name	Element	X	Y	Z	Biso	sof	Wyck
1	B1	B	0.00000	0.25000	0.02300	0.5000	1.0000	8e
2	MO1	Mo	0.00000	0.25000	0.17900	0.5000	1.0000	8e

Stick Pattern

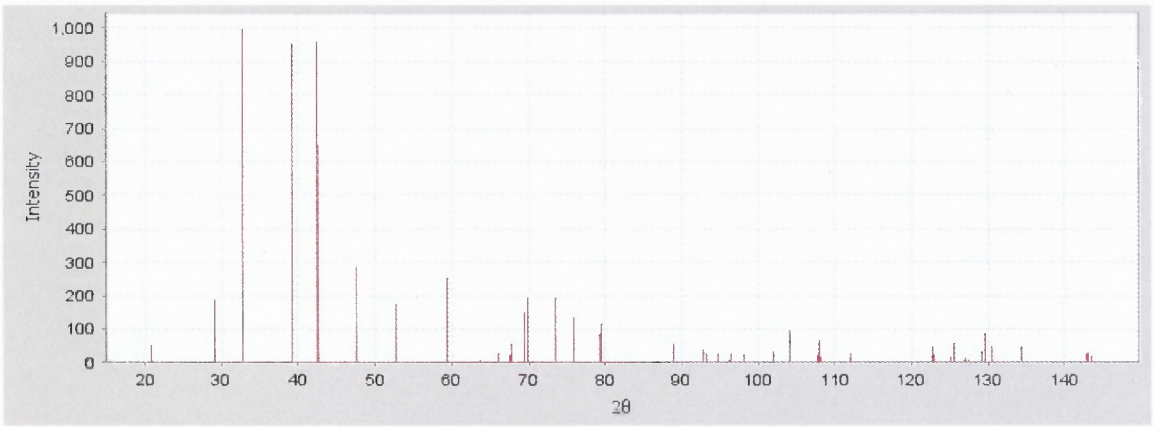

Figure B.5 The crystal data of MoB [124].

Name and formula

Reference code:	04-001-0963
PDF index name:	Tungsten Boride
Empirical formula:	BW_2
Chemical formula:	W_2B

Crystallographic parameters

Crystal system:	Tetragonal
Space group:	I4/mcm
Space group number:	140
a (Å):	5.5680
b (Å):	5.5680
c (Å):	4.7440
Alpha (°):	90.0000
Beta (°):	90.0000
Gamma (°):	90.0000
Volume of cell (10^6 pm^3):	147.08
Z:	4.00
RIR:	17.99

References

Primary reference:	*Calculated from LPF using POWD-12++*
Structure:	Havinga E.E., Damsma H., Hokkeling P., *J. Less-Common Met.*, **27**, 169, (1972)

Structure

No.	Name	Element	X	Y	Z	Biso	sof	Wyck.
1	W1	W	0.16920	0.66920	0.00000	0.5000	1.0000	8h
2	B1	B	0.00000	0.00000	0.25000	0.5000	1.0000	4a

Stick Pattern

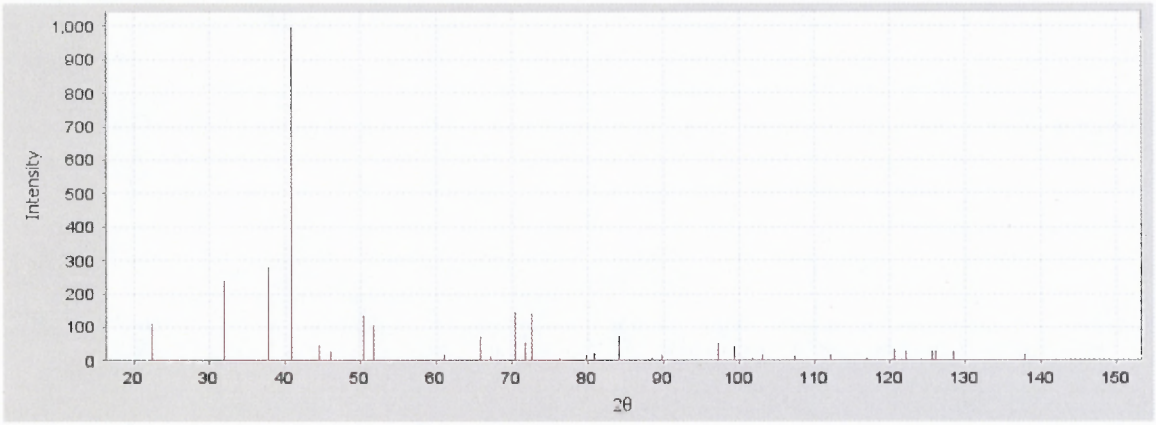

Figure B.6 The crystal data of W_2B [124].

Name and formula

Reference code: 04-006-2599

PDF index name:	Tungsten Iron
Empirical formula:	Fe_7W_6
Chemical formula:	W_6Fe_7

Crystallographic parameters

Crystal system:	Rhombohedral
Space group:	R-3m
Space group number:	166
a (Å):	4.7300
b (Å):	4.7300
c (Å):	25.8000
Alpha (°):	90.0000
Beta (°):	90.0000
Gamma (°):	120.0000
Volume of cell (10^6 pm^3):	499.89
Z:	3.00
RIR:	6.81

References

Primary reference:	*Calculated from LPF using POWD-12++*
Structure:	Smith C.S., *J. Appl. Phys.*, **12**, 817, (1941)

Structure

No.	Name	Element	X	Y	Z	Biso	sof	Wyck
1	FE1	Fe	0.50000	0.50000	0.09000	0.5000	1.0000	18h
2	W1	W	0.00000	0.00000	0.05200	0.5000	1.0000	6c
3	W2	W	0.00000	0.00000	0.15400	0.5000	1.0000	6c
4	W3	W	0.00000	0.00000	0.33333	0.5000	1.0000	6c
5	FE2	Fe	0.00000	0.00000	0.50000	0.5000	1.0000	3b

Stick Pattern

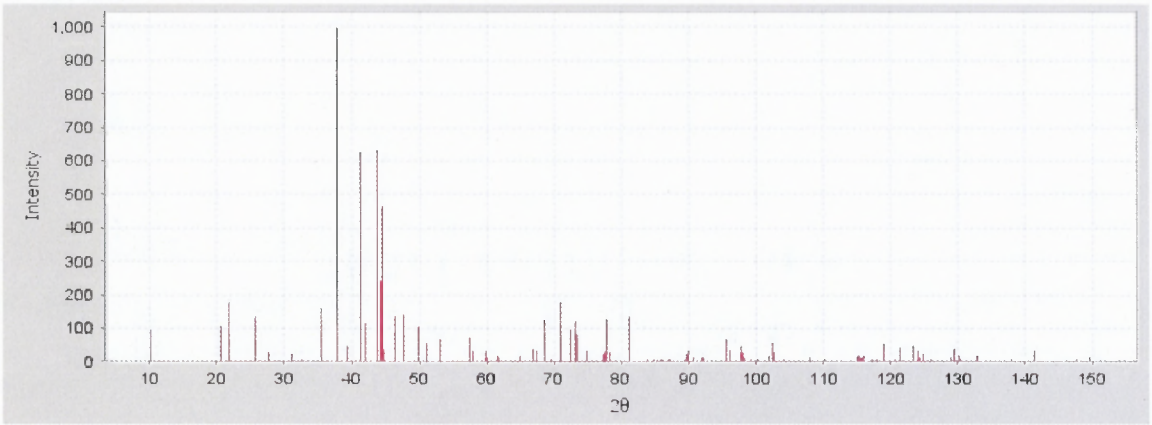

Figure B.7 The crystal data of W_6Fe_7 [124].

Name and formula

Reference code:	04-006-2101
PDF index name:	Niobium Carbide
Empirical formula:	CNb
Chemical formula:	NbC

Crystallographic parameters

Crystal system:	Cubic
Space group:	Fm-3m
Space group number:	225
a (Å):	4.4673
b (Å):	4.4673
c (Å):	4.4673
Alpha (°):	90.0000
Beta (°):	90.0000
Gamma (°):	90.0000
Volume of cell (10^6 pm^3):	89.15
Z:	4.00
RIR:	9.85

References

Primary reference:	*Calculated from LPF using POWD-12++*
Structure:	Shveikin G.P., Tskhai V.A., Mitrofanov B.V., *Inorg. Mater. (Engl. Transl.)*, **23**, 837, (1987)

Structure

No.	Name	Element	X	Y	Z	Biso	sof	Wyck.
1	NB1	Nb	0.00000	0.00000	0.00000	0.5000	1.0000	4a
2	C1	C	0.50000	0.50000	0.50000	0.5000	1.0000	4b

Stick Pattern

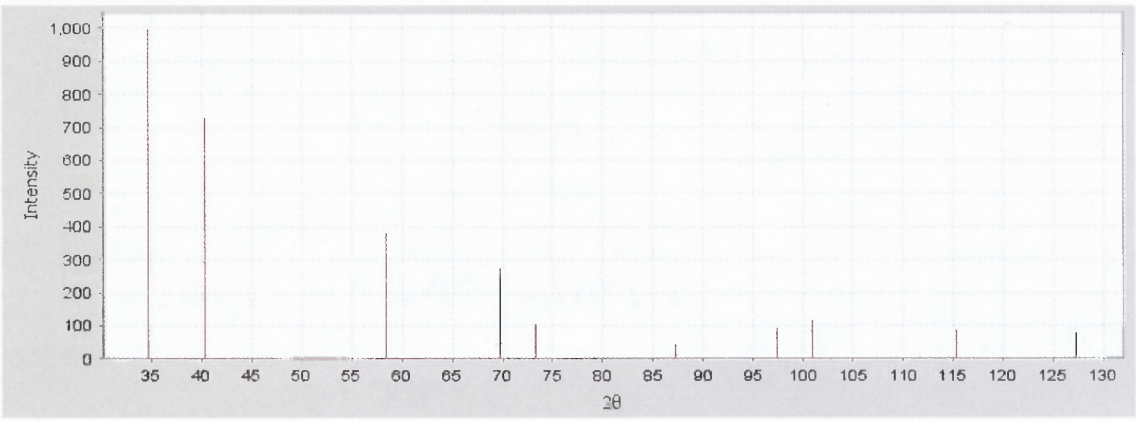

Figure B.8 The crystal data of NbC [124].

Name and formula

Reference code:	04-001-2980
PDF index name:	Tantalum Boride
Empirical formula:	B_2Ta_3
Chemical formula:	Ta_3B_2

Crystallographic parameters

Crystal system:	Tetragonal
Space group:	P4/mbm
Space group number:	127
a (Å):	6.1840
b (Å):	6.1840
c (Å):	3.2840
Alpha (°):	90.0000
Beta (°):	90.0000
Gamma (°):	90.0000
Volume of cell (10^6 pm^3):	125.59
Z:	2.00
RIR:	8.86

References

Primary reference:	*Calculated from LPF using POWD-12++*
Structure:	Rudy E., Benesovsky F., Toth L., *Z. Metallkd.*, **54**, 345, (1963)

Structure

No.	Name	Element	X	Y	Z	Biso	sof	Wyck.
1	TA1	Ta	0.18210	0.68210	0.50000	0.5000	1.0000	4h
2	B1	B	0.61590	0.11590	0.00000	0.5000	1.0000	4g
3	TA2	Ta	0.00000	0.00000	0.00000	0.5000	1.0000	2a

Stick Pattern

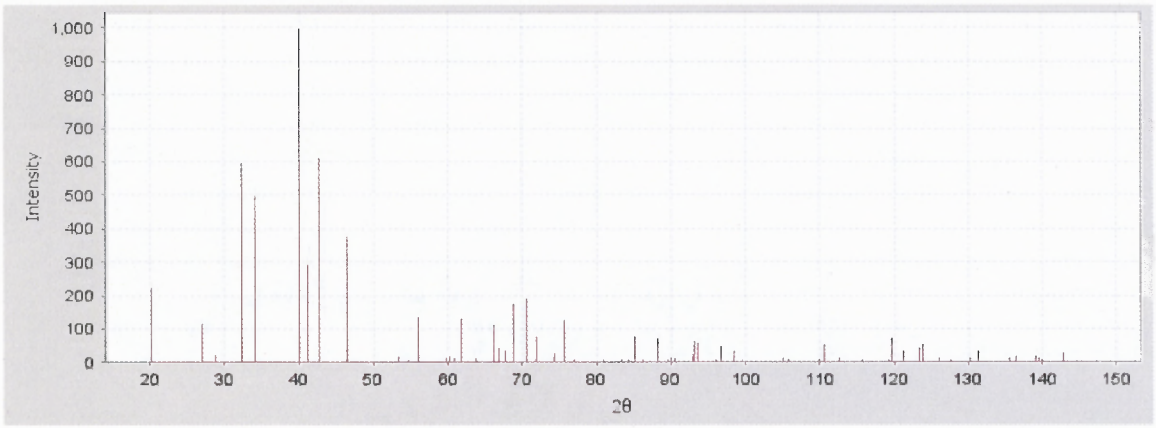

Figure B.9 The crystal data of Ta_3B_2 [124].

Name and formula

Reference code:	04-002-5180
PDF index name:	Titanium Boride
Empirical formula:	BTi
Chemical formula:	TiB

Crystallographic parameters

Crystal system:	Orthorhombic
Space group:	Pnma
Space group number:	62
a (Å):	6.1200
b (Å):	3.0600
c (Å):	4.5600
Alpha (°):	90.0000
Beta (°):	90.0000
Gamma (°):	90.0000
Volume of cell (10^6 pm^3):	85.40
Z:	4.00
RIR:	1.68

References

Primary reference:	*Calculated from LPF using POWD-12++*
Structure:	Fedorov T.F., Kuz`ma Yu.B., *Inorg. Mater. (Engl. Transl.)*, **3**, 1307, (1967)

Structure

No.	Name	Element	X	Y	Z	Biso	sof	Wyck.
1	B1	B	0.03600	0.25000	0.11000	0.5000	1.0000	4c
2	TI1	Ti	0.18000	0.25000	0.62500	0.5000	1.0000	4c

Stick Pattern

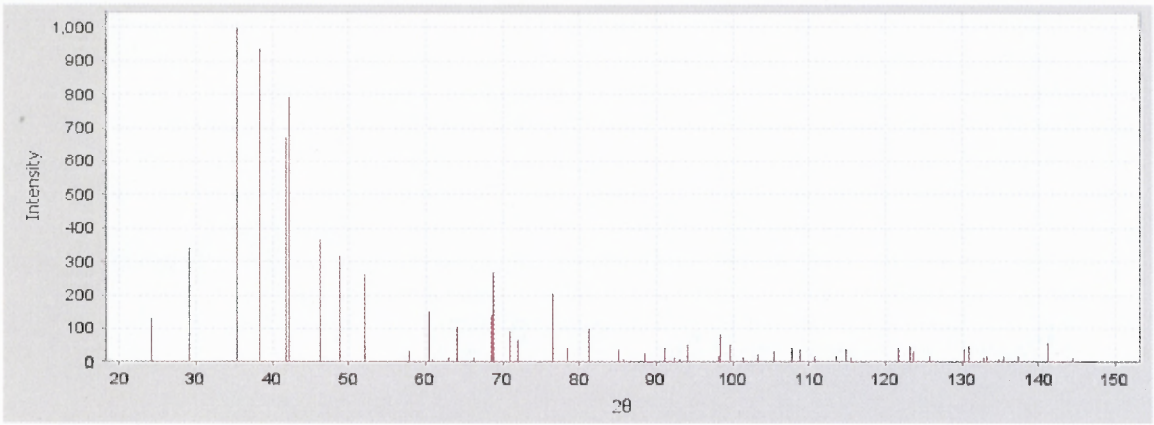

Figure B.10 The crystal data of TiB [124].

Name and formula

Reference code:	04-003-6142
PDF index name:	Titanium Carbide
Empirical formula:	CTi
Chemical formula:	TiC

Crystallographic parameters

Crystal system:	Cubic
Space group:	Fm-3m
Space group number:	225
a (Å):	4.3150
b (Å):	4.3150
c (Å):	4.3150
Alpha (°):	90.0000
Beta (°):	90.0000
Gamma (°):	90.0000
Volume of cell (10^6 pm^3):	80.34
Z:	4.00
RIR:	3.85

References

Primary reference:	*Calculated from LPF using POWD-12++*
Structure:	Eremenko V.N., Velikanova T.Y., *Soviet Powder Metall. and Met. Ceramics*, **2**, 347, (1963)

Structure

No.	Name	Element	X	Y	Z	Biso	sof	Wyck.
1	C1	C	0.00000	0.00000	0.00000	0.5000	1.0000	4a
2	TI1	Ti	0.50000	0.50000	0.50000	0.5000	1.0000	4b

Stick Pattern

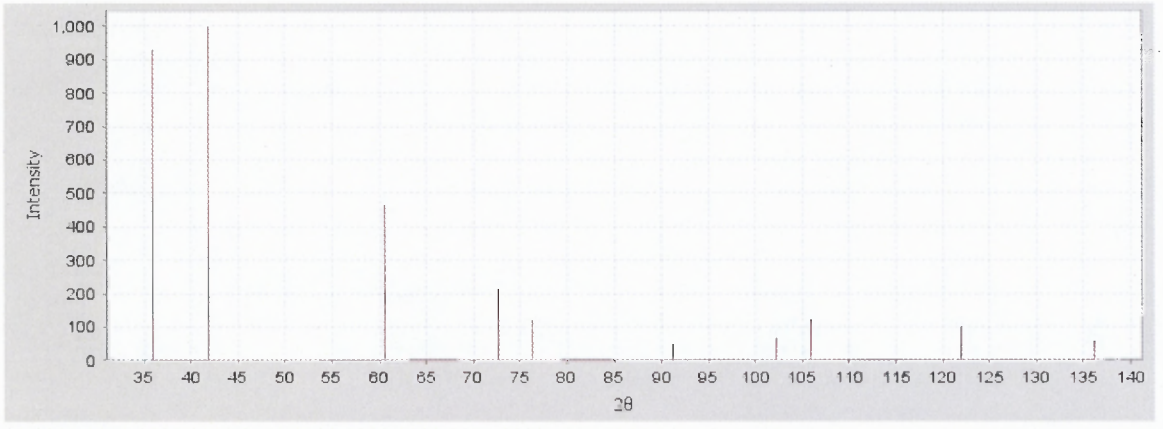

Figure B.11 The crystal data of TiC [124].

Name and formula

Reference code:	04-003-1470
PDF index name:	Titanium Boride
Empirical formula:	B_4Ti_3
Chemical formula:	Ti_3B_4

Crystallographic parameters

Crystal system:	Orthorhombic
Space group:	Immm
Space group number:	71
a (Å):	3.0420
b (Å):	3.2590
c (Å):	13.7300
Alpha (°):	90.0000
Beta (°):	90.0000
Gamma (°):	90.0000
Volume of cell (10^6 pm^3):	136.12
Z:	2.00
RIR:	1.96

References

Primary reference:	*Calculated from LPF using POWD-12++*
Structure:	Adsit N.R., *Trans. Met. Soc. AIME*, **236**, 804, (1966)

Structure

No.	Name	Element	X	Y	Z	Biso	sof	Wyck
1	TI1	Ti	0.50000	0.00000	0.18000	0.5000	1.0000	4j
2	B1	B	0.50000	0.00000	0.37500	0.5000	1.0000	4j
3	B2	B	0.00000	0.00000	0.44400	0.5000	1.0000	4i
4	TI2	Ti	0.00000	0.00000	0.00000	0.5000	1.0000	2a

Stick Pattern

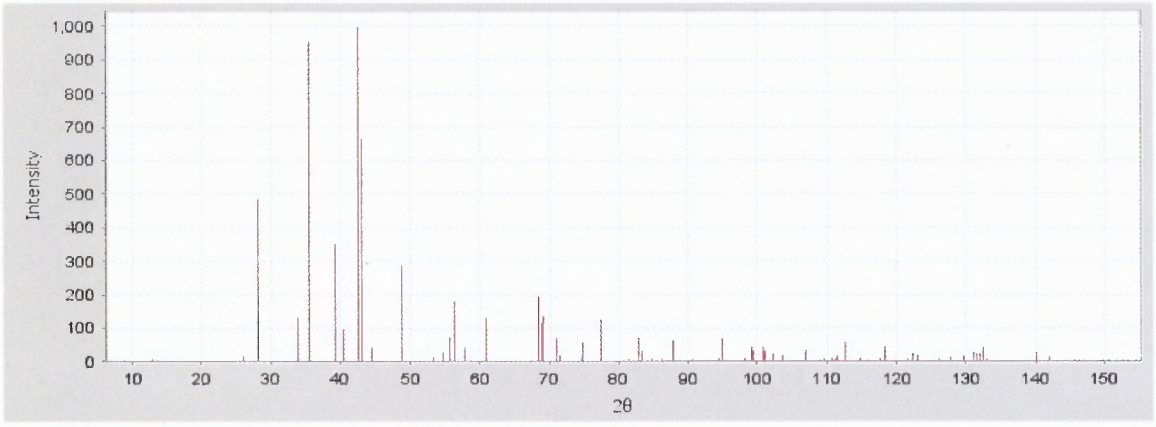

Figure B.12 The crystal data of Ti_3B_4 [124].

Name and formula

Reference code: 04-004-5938

PDF index name:	Titanium Boride
Empirical formula:	B_2Ti
Chemical formula:	TiB_2

Crystallographic parameters

Crystal system:	Hexagonal
Space group:	P6/mmm
Space group number:	191
a (Å):	3.0380
b (Å):	3.0380
c (Å):	3.2390
Alpha (°):	90.0000
Beta (°):	90.0000
Gamma (°):	120.0000
Measured density (g/cm^3):	4.34
Volume of cell (10^6 pm^3):	25.89
Z:	1.00
RIR:	3.88

References

Primary reference:	*Calculated from LPF using POWD-12++*
Structure:	Aivazov M.I., Domashnev I.A., *Inorg. Mater. (Engl. Transl.)*, 7, 1551, (1971)

Structure

No.	Name	Element	X	Y	Z	Biso	sof	Wyck.
1	TI1	Ti	0.00000	0.00000	0.00000	0.5000	1.0000	1a
2	B1	B	0.33333	0.66666	0.50000	0.5000	1.0000	2d

Stick Pattern

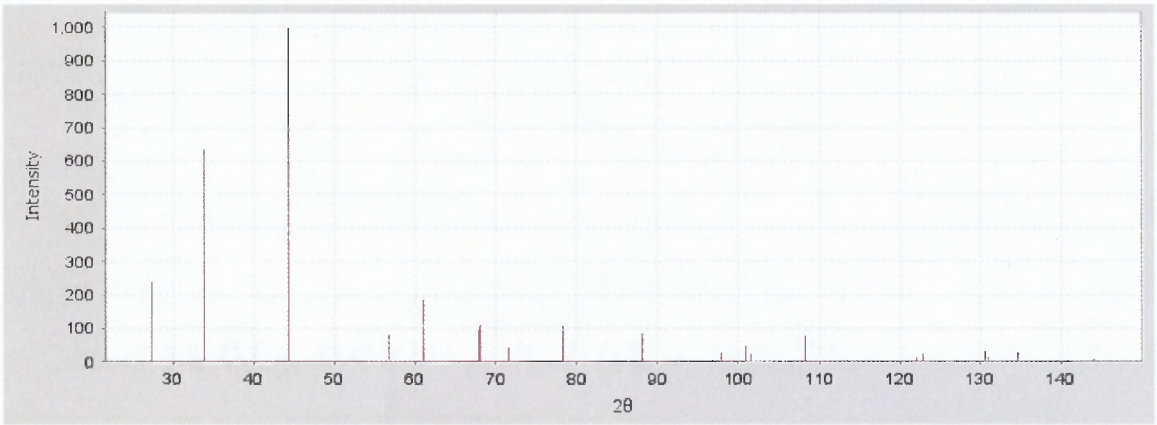

Figure B.13 The crystal data of TiB_2 [124].

Name and formula

Reference code:	04-004-7151
PDF index name:	Zirconium Boride
Empirical formula:	B_2Zr
Chemical formula:	ZrB_2

Crystallographic parameters

Crystal system:	Hexagonal
Space group:	P6/mmm
Space group number:	191
a (Å):	3.1670
b (Å):	3.1670
c (Å):	3.5300
Alpha (°):	90.0000
Beta (°):	90.0000
Gamma (°):	120.0000
Volume of cell (10^6 pm^3):	30.66
Z:	1.00
RIR:	8.09

References

Primary reference:	*Calculated from LPF using POWD-12++*
Structure:	Rudy E., Benesovsky F., *Monatsh. Chem.*, **92**, 415, (1961)

Structure

No.	Name	Element	X	Y	Z	Biso	sof	Wyck.
1	ZR1	Zr	0.00000	0.00000	0.00000	0.5000	1.0000	1a
2	B1	B	0.33333	0.66666	0.50000	0.5000	1.0000	2d

Stick Pattern

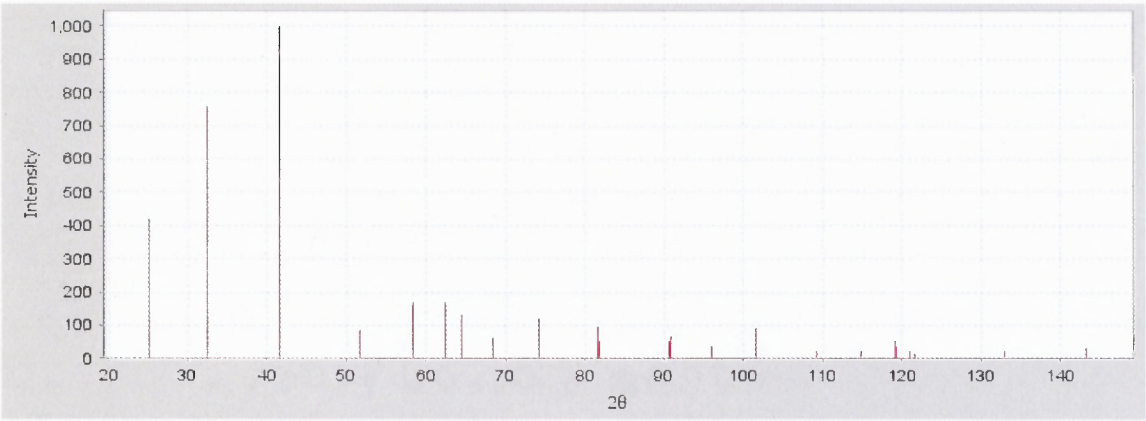

Figure B.14 The crystal data of ZrB_2 [124].

Name and formula

Reference code:	04-003-3765
PDF index name:	Zirconium Carbide
Empirical formula:	CZr
Chemical formula:	ZrC

Crystallographic parameters

Crystal system:	Cubic
Space group:	Fm-3m
Space group number:	225
a (Å):	4.6940
b (Å):	4.6940
c (Å):	4.6940
Alpha (°):	90.0000
Beta (°):	90.0000
Gamma (°):	90.0000
Volume of cell (10^6 pm^3):	103.43
Z:	4.00
RIR:	9.22

References

Primary reference:	*Calculated from LPF using POWD-12++*
Structure:	Duwez P., Odell F., *J. Electrochem. Soc.*, **97**, 299, (1950)

Structure

No.	Name	Element	X	Y	Z	Biso	sof	Wyck.
1	C1	C	0.00000	0.00000	0.00000	0.5000	1.0000	4a
2	ZR1	Zr	0.50000	0.50000	0.50000	0.5000	1.0000	4b

Stick Pattern

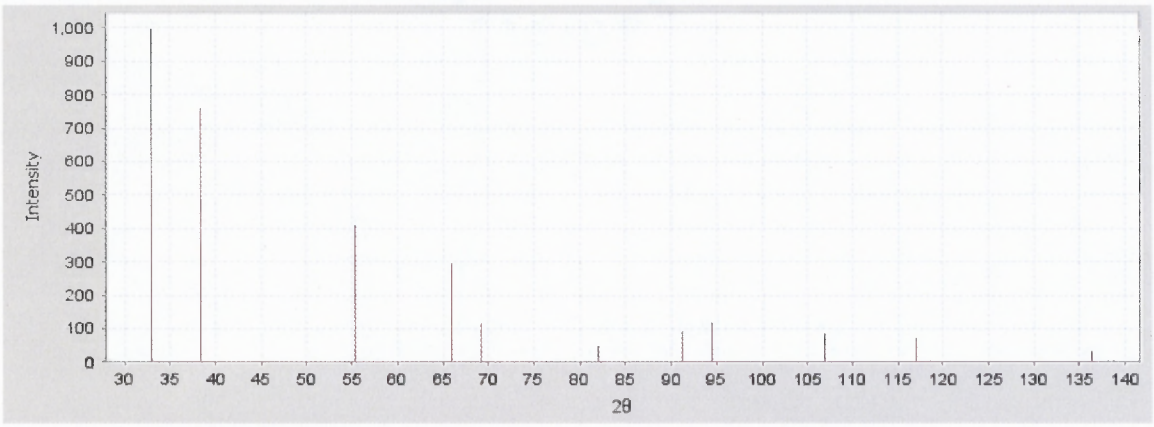

Figure B.15 The crystal data of ZrC [124].

Name and formula

Reference code:	04-003-6210
PDF index name:	Hafnium Carbide
Empirical formula:	CHf
Chemical formula:	HfC

Crystallographic parameters

Crystal system:	Cubic
Space group:	Fm-3m
Space group number:	225
a (Å):	4.6600
b (Å):	4.6600
c (Å):	4.6600
Alpha (°):	90.0000
Beta (°):	90.0000
Gamma (°):	90.0000
Volume of cell (10^6 pm^3):	101.19
Z:	4.00
RIR:	16.97

References

Primary reference:	*Calculated from LPF using POWD-12++*
Structure:	Denbnovetskaya E.N., *Soviet Powder Metall. and Met. Ceramics*, **6**, 194, (1967)

Structure

No.	Name	Element	X	Y	Z	Biso	sof	Wyck.
1	C1	C	0.00000	0.00000	0.00000	0.5000	1.0000	4a
2	HF1	Hf	0.50000	0.50000	0.50000	0.5000	1.0000	4b

Stick Pattern

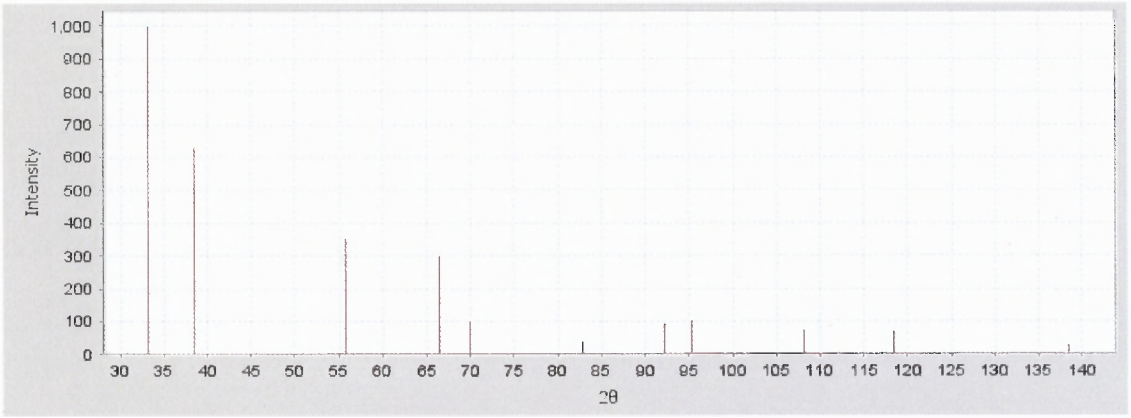

Figure B.16 The crystal data of HfC [124].

Name and formula

Reference code:	04-007-4812
PDF index name:	Hafnium Boride
Empirical formula:	B_2Hf
Chemical formula:	HfB_2

Crystallographic parameters

Crystal system:	Hexagonal
Space group:	P6/mmm
Space group number:	191
a (Å):	3.1425
b (Å):	3.1425
c (Å):	3.4760
Alpha (°):	90.0000
Beta (°):	90.0000
Gamma (°):	120.0000
Volume of cell (10^6 pm^3):	29.73
Z:	1.00
RIR:	13.15

References

Primary reference:	*Calculated from LPF using POWD-12++*
Structure:	Wong Ng W., McMurdie H.F., Paretzkin B., Zhang Y., Davis K.L., Hubbard C.R., Dragoo A.L., Stewart J.M., *Powder Diffraction*, **2**, 257, (1987)

Structure

No.	Name	Element	X	Y	Z	Biso	sof	Wyck.
1	HF1	Hf	0.00000	0.00000	0.00000	0.5000	1.0000	1a
2	B1	B	0.33333	0.66666	0.50000	0.5000	1.0000	2d

Stick Pattern

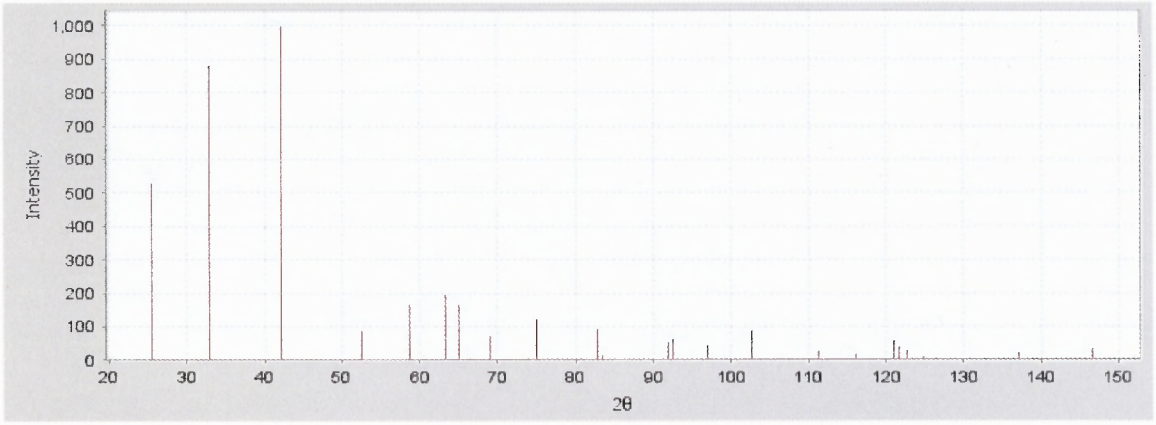

Figure B.17 The crystal data of HfB_2 [124].

REFERENCES

1. Davis, J. R. (2002). Boriding. Surface Hardening of Steels - Understanding the Basics. Ohio: ASM International, 213-226.

2. Stewart, K. (1997). Boronizing Protects Metals Against Wear. Advanced Material Processing, 155(3), 23-25.

3. Chatterjee-Fischer, R. (1989). Boriding and Diffusion Metallizing. Surface Modification Technologies. New York: Marcel Dekker, Inc., 567-609.

4. Dearnley, P. A., Bell, T. (1985). Engineering the surface with boron based materials. Surface Engineering, 1(3), 203-217.

5. Palombarini, G., Carbucicchio, M. (1984). On the morphology of thermo-chemically produced Fe_2B/Fe interfaces. Journal of Materials Science Letters, 3, 791-794.

6. Palombarini, G., Carbucicchio, M. (1987). Growth of boride coatings on iron. Journal of Materials Science Letters, 6, 415-416.

7. Sinha, A. K. (1991). Boriding (Boronizing). Heat Treatment Vol.4, ASM Handbook. Ohio: ASM International, 437-447.

8. Zlateva, R. S., Zakhariev, Z. T. (1993). Structure of boronizing layers on steels. Bulgarian Chemical Communication, 26(1), 82-89.

9. Skugorova, L. P., Shylkov, V. I., Netschaev, A. I. (1972). Apparatus and technology of gas borating. Metallovedenie i Termicheskaya Obrabotka Metallov, 5, 61-62.

10. Raveh A., Inspektor A., Carmi, U. & Avni R. (1983). Boronization of titanium and steels in a low pressure r.f. plasma. Thin Solid Films, 108, 39-45.

11. Hunger, H. J., Trute, G. (1994). Boronizing to Produce Wear-resistant Surface Layers. Heat Treatment of Metals, 2, 31-39.

12. Ozdemir, O., Metin Usta, M., Bindal, C., Ucisik, A. H. (2006). Hard iron boride (Fe2B) on 99.97wt% pure iron. Vacuum, 80, 1391–1395.

13. Asthana, P., Liang, H., Metin Usta, M., Ucisik, A. H. (2007). Wear and Surface Characterization of Boronized Pure Iron. Journal of Tribology, 129, 1-10.

14. Selçuka, B., Ipekb, R., Karamiş, M. B., Kuzucu, V. (2000). An investigation on surface properties of treated low carbon and alloyed steels (boriding and carburizing). Journal of Materials Processing Technology, 103, 310 – 317.

15. Selçuka, B., Ipekb, R., Karamiş, M. B. (2003). A study on friction and wear behavior of carburized, carbonitrided and borided AISI 1020 and 5115 steels. Journal of Materials Processing Technology, 141, 189–196.

16. Uslu, I., Comert, H., Ipek, M., Celebi, F.G., Ozdemir, O., Bindal C. (2007). A comparison of borides formed on AISI 1040 and AISI P20 steels. Materials and Design, 28, 1819–1826.

17. Soydan, Y., Köksal, S., Demirer, A., Çelik, V. (2008). Sliding Friction and Wear Behavior of Pack-Boronized AISI 1050, 4140, and 8620 Steels. Tribology Transactions, 51, 74-81.

18. Sen, S., Sen, U., Bindal, C. (2005). The growth kinetics of borides formed on boronized AISI 4140 Steel. Vacuum, 77, 195–202.

19. Sahin, S., Meric, C. (2002). Investigation of the effect of boronizing on cast irons. Materials Research Bulletin, 37, 971 – 979.

20. Meric, C., Sahin, S., Backir, B., Koksal, N.S. (2006). Investigation of the boronizing effect on the abrasive wear behavior in cast irons. Materials and Design, 27,751–757.

21. Sen, U., Sen, S., Yilmaz, F. (2004). An evaluation of some properties of borides deposited on boronized ductile iron. Journal of Materials Processing Technology, 148, 1–7.

22. Sen, U., Sen, S., Yilmaz, F. (2004). Effect of copper on boride layer of boronized ductile cast irons. Vacuum, 72, 199–204.

23. Campos-Silva, I., Ortiz-Domı´nguez, M., Keddam, M., Lo´pez-Perrusquia, N., Carmona-Vargas A., Elı´as-Espinosa, M. (2009). Kinetics of the formation of Fe_2B layers in gray cast iron: Effects of boron concentration and boride incubation time. Applied Surface Science, 255, 9290–9295.

24. Li, C., Shen, B., Li,G., Yang, C. (2008). Effect of boronizing temperature and time on microstructure and abrasion wear resistance of Cr12Mn2V2 high chromium cast iron. Surface and Coatings Technology, 202, 5882–5886.

25. Genel, K., Ozbek, I., Bindal, C. (2003). Kinetics of boriding of AISI W1 steel. Materials Science and Engineering A, 347, 311 – 314.

26. Ozbek, I., Bindal, C. (2002). Mechanical properties of boronized AISI W4 steel. Surface and Coatings Technology, 154, 14–20.

27. Genel, K. (2006). Boriding kinetics of H13 steel. Vacuum, 80,451–457.

28. Taktak, S. (2007). Some mechanical properties of borided AISI H13 and 304 steels. Materials and Design, 28, 1836–1843.

29. Kariofillis, G. K., Kiourtsidis, G. E., Tsipas, D.N. (2006). Corrosion behavior of borided AISI H13 hot work steel. Surface and Coatings Technology, 201, 19 – 24.

30. Min, Y.,Wu, X., Xu, L., Tang, W., Wallner, G., Liang, D., Fend, Y (2001). Influence of different surface treatment of H13 hot work die steel on its thermal fatigue behaviors. Journal of Shanghai University, 5(4), 326 – 330.

31. Ozdemir, O., Omar, M.A., Usta, M., Zeytin, S., Bindal, C., Ucisik, A.H. (2009). An investigation on boriding kinetics of AISI 316 stainless steel. Vacuum, 83, 175–179.

32. Brandstöter, J., Lengauer, W. (1997). Multiphase diffusion reaction of transition metal-boron systems. Journal of Alloys and Compounds, 262 – 263, 390 – 396.

33. Khor, K. A., Yu, L. G., Sundararajan, G. (2005). Formation of hard tungsten boride layer by spark plasma sintering boriding. Thin Solid Films, 478, 232–237.

34. Yu, L. G., Khor, K. A., Sundararajan, G. (2006). Boride layer growth kinetics during boriding of molybdenum by the Spark Plasma Sintering (SPS) technology. Surface and Coatings Technology, 201, 2849–2853.

35. Usta, M. (2005). The characterization of borided pure niobium. Surface and Coatings Technology, 194, 251– 255.

36. Usta, M. (2005). The characterization of borided pure tungsten. Surface and Coatings Technology, 194, 330– 334.

37. Ingole, S., Liang, H., Usta, M., Bindal, C., Ucisik, A.H. (2005). Multi-scale wear of a boride coating on tungsten. Wear, 259, 849–860.

38. Ribeiro, R., Ingole, S., Usta, M., Bindal, C., Ucisik, A.H., Liang H. (2006). Tribological characteristics of boronized niobium for biojoint applications. Vacuum, 80, 1341–1345.

39. Ribeiro, R., Ingole, S., Usta, M., Bindal, C., Ucisik, A.H., Liang H. (2007). Tribological investigation of tantalum boride coating under dry and simulated body fluid conditions. Wear, 262, 1380–1386.

40. Ribeiro, R., Ingole, S., Usta, M., Bindal, C., Ucisik, A.H., Liang H. (2006). A tribological comparison of pure and boronized chromium. Journal of Tribology, 128, 895 – 897.

41. Ueda, N., Mizukoshi, T., Demizu, K., Sone, T., Ikenaga, A., Kawamoto, M. (2000). Boriding of nickel by the powder-pack method. Surface and Coatings Technology, 126, 25 – 30.

42. Özbeka, I., Akbulut, H., Zeytin, S., Bindal, C., Ucisik, A. H. (2000). The characterization of borided 99.5% purity nickel. Surface and Coatings Technology, 126, 166-170.

43. Mu, D., Shen, B.-L., Yang, C., Zhao, X. (2009). Microstructure analysis of boronized pure nickel using boronizing powders with SiC as diluents. Vacuum, 83, 1481 – 1484.

44. Anthymidis, K. G., Zinoviadis, P., Roussos, D., Tsipas, D. N. (2002). Boriding of nickel in a fluidized bed reactor. Materials Research Bulletin, 37(3), 515 – 522.

45. Lou, D. C., Solberg, J. K., Akselsen, O. M., Dahl, N. (2009). Microstructure and property investigation of paste boronized pure nickel and Nimonic 90 superalloy. Materials Chemistry and Physics, 115, 239–244.

46. Torun, O. (2008). Boriding of nickel aluminide. Surface and Coatings Technology, 202, 3549 - 3554.

47. Kästner, P., Olfe, J., Rie, K.-T. (2001). Plasma-assisted boriding of pure titanium and TiAl6V4. Surface and Coatings Technology, 142 - 144, 248 – 252.

48. Anthymidis, K. G., Tsipas, D. N., Stergioudis, E. (2001). Boriding of titanium alloys in a fluidized bed reactor. Journal of Materials Science Letters, 20(22), 2067-2069.

49. Wank, A., Wielage, B., Podlesak, H., Matthes, K.-J., Kolbe, G. (2005). Protection of Ti6Al4V Surfaces by Laser Dispersion of Diborides. Journal of Thermal Spray Technology, 14(1), 134 – 140.

50. He, L., Zhang, X., Tong, C. (2006). Surface modification of pure titanium treated with B_4C at high temperature. Surface and Coatings Technology, 200, 3016–3020.

51. Çelikkan, H., Öztürk, M. K., Aydin, H., Aksu, M. L. (2007). Boriding titanium alloys at lower temperatures using electrochemical methods Thin Solid Films, 515, 5348–5352.

52. Atar, E., Kayali, E. S., Cimenoglu, H. (2008). Characteristics and wear performance of borided Ti6Al4V alloy. Surface and Coatings Technology, 202, 4583–4590.

53. Lee, C., Sanders, A., Tikekar, N., Ravi Chandran, K. S., (2008). Tribology of titanium boride-coated titanium balls against alumina ceramic: Wear, friction, and micromechanisms. Wear, 265, 375–386.

54. Budinski, K. (1988). Surface Engineering for Wear Resistance, Prentice-Hall, 303-345.

55. Pierson, H. O., Mullendore, A. W. (1981). The chemical vapor deposition of boron at low temperature. Thin Solid Films, 83(1), 87-91.

56. Wierzchoń, T., Michalski, J., Karpinski, T. (1983). Gas boronizing of steels. Mechanik, 56(8), 485-7.

57. Dearnley, P. A., Farrell, T., Bell, T. (1986). Developments in plasma boronizing. Journal of Materials Energy System, 8(2), 128-31.

58. Filep, E., Farkas, S., Kolozsvary, Z. (1988). Boron condensation from glow discharge. Surface Engineering, 4(2), 155-8.

59. Hunger, H. J., Trute, G., Lobig, G., Rathjen, D. (1997). Plasma-activated gas boronizing with boron trifluoride. HTM, Härt.-Tech Mitt., 52(1), 39-45.

60. Cabeo, E.R., Laudien, G., Biemer, S., Rie, K. -T., Hoppe, S. (1999). Plasma-assisted boriding of industrial components in a pulsed D.C. glow discharge. Surface and Coatings Technology, 116-119, 229-233.

61. Küper, A., Qiao, X., Stock, H. R., Mayr, P. (2000). A novel approach to gas boronizing. Surface and Coatings Technology, 130, 87-94.

62. Nam, K.-S., Lee, K.-H., Lee, D. Y., Song, Y.-S. (2005). Metal surface modification by plasma boronizing in a two temperature-stage process. Surface and Coatings Technology, 197, 51-5.

63. Lyakhovich, L. S., Isakov, S. A., Al'tshuler, S. A., Meshochkin, N. A. (1991). Glow-discharge boronizing from pastes. Zashchitnye Pokrytiya Na Metallakh, 25, 7-11.

64. Yoon, J. H., Jee, Y. K., Lee, S. Y. (1999). Plasma paste boronizing treatment of the stainless steel AISI 304. Surface and Coatings Technology, 112(1-3), 71-5.

65. Béjar, M. A., Henríquez, R. (2009). Surface hardening of steel by plasma-electrolysis boronizing. Materials and Design, 30, 1726–1728.

66. L. G. Yu, L. G., Khor, K. A., Sundararajan, G. (2002). Boriding of mild steel using the spark plasma sintering (SPS) technique. Surface and Coatings Technology, 157(2-3), 226-230.

67. Davis, J. A., Wilbur, P. J., Williamson, D. L., Wei, R., Vajo, J. J. (1998). Ion implantation boriding of iron and AISI M2 steel using a high-current density, low energy, broad-beam ion source. Surface and Coatings Technology, 103-104, 52-7.

68. Yan, P. X., Wei, Z. Q., Wen, X. L., Wu, Z. G., Xu, J. W., Liu, W. M., Tian, J. (2002). Post boronizing ion implantation of C45 steel. Applied Surface Science, 195(1-4), 74-9.

69. Dehlinger, A. S., Pierson, J. F., Roman, A., Bauer, Ph. (2003). Properties of iron boride films prepared by magnetron sputtering. Surface and Coatings Technology, 174 –175, 331–337.

70. Audronis, M., Kelly, P. J., Leyland, A., Matthews, A., (2006). Microstructure of direct current and pulse magnetron sputtered Cr–B coatings. Thin Solid Films. 515, 1511–1516.

71. Ignatenko, P. I., Terpii, D. N., Goncharov, A. A., (2003). Phase Composition of Films Deposited by ZrB_2 RF Magnetron Sputtering. Neorganicheskie Materialy. 39(5), 560–565.

72. Bourithis, L., Papaefthymiou, S., Papadimitriou, G. D., (2002). Plasma transferred arc boriding of a low carbon steel: microstructure and wear properties. Applied Surface Science, 2002(1-4), 203-218.

73. Junji Morimoto, J., Ozaki, T., Kubohori, T., Morimoto, S., Abe, N., Tsukamoto, M. (2009). Some properties of boronized layers on steels with direct diode laser. Vacuum, 83,185–189.

74. Rajput, D., Lansford, K., Costa, L., Hofmeister, W. (2009). Molybdenum-on-chromium dual coating on steel. Surface and Coatings Technology, 203, 1281–1287.

75. Anthymidisa, K.G., Maragoudakisa, N., Stergioudisb, G., Haidara, O., Tsipasa, D.N. (2003). A comparative study of boride coatings obtained by pack cementation method and by fluidized bed technology. Materials Letters, 57, 2399 - 2403.

76. Tsipas, D. N., Anthymidis, K. G., Flitris, Y. (2003). Deposition of hard and/or corrosion resistant, single and multi-element coatings on ferrous and nonferrous alloys in a fluidized bed reactor. Journal of Materials Processing Technology, 134(2), 145 – 152.

77. Balandin, Yu. A. (2004). Boronitriding of die steels in Fluidized bed. Metallovedenie i Termicheskaya Obrabotka Metallov, 46 (9 - 10), 25 – 27.

78. Balandin, Yu. A. (2005). Surface Hardening of Die Steels by Diffusion Boronizing, Borocopperizing, and Borochromizing in Fluidized Bed. Metallovedenie i Termicheskaya Obrabotka Metallov, 47(3 – 4), 27 – 30.

79. Galvanetto, E., Borgioli, F., Bacci, T., Pradelli, G. (2006). Wear behavior of iron boride coatings produced by VPS technique on carbon steels. Wear, 260, 825–831.

80. Kulka, M., Pertek, A., Klimek, L. (2006). The influence of carbon content in the borided Fe-alloys on the microstructure of iron borides. Materials Characterization, 56, 232–240.

81. Pertek, A., Kulka, M. (2003). Microstructure and properties of composite (B +C) diffusion layers on low-carbon steel. Journal of Materials Science, 38, 269 – 273.

82. Pertek, A., Kulka, M. (2003). Two-step treatment carburizing followed by boriding on medium-carbon steel. Surface and Coating Technology, 173, 309 – 314.

83. Pertek, A., Kulka, M. (2002). Characterization of complex (B + C) diffusion layers formed on chromium and nickel-based low-carbon steel. Applied Surface Science, 202, 252–260.

84. Kulka, M., Pertek, A. (2003). Characterization of complex (B+ C + N) diffusion layers formed on chromium and nickel-based low-carbon steel. Applied Surface Science, 218, 113–122.

85. Buijnsters, J. G., Shankar, P., Gopalakrishnan, P., van Enckevort, W. J. P., Schermer, J. J., Ramakrishnan, S. S., Ter Meulen, J. J. (2003). Diffusion-modified boride interlayers for chemical vapour deposition of low-residual-stress diamond films on steel substrates. Thin Solid Films, 426, 85–93.

86. Maragoudakis, N. E., Stergioudis, G., Omar, H., Pavlidou, E., Tsipas, D. N. (2002). Boron-nitriding of steel US 37-1. Materials Letter, 57, 949 – 952.

87. Yan, P. X., Su, Y. C. (1995). Metal surface modification by B-C-nitriding in a two-temperature-stage process. Materials Chemistry and Physics, 39, 304 – 308.

88. Petrova, R. S., Zakhariev, Z. T. (1993). Structure of boroaluminized layers on steels. Bulgarian Chemical Communications, 26(1), 82- 89.

89. Zakhariev, Z., Petrova, R. S. (1993). Gas phase reactions during simultaneous boronizing and aluminizing of steels. Journal of Alloys and Compounds, 196, 59 – 62.

90. Uzunov, N., Ivanov, R. (2004). Aluminothermic powder boriding of steels. Applied Surface Science, 225, 72 – 77.

91. Zakhariev, Z., Marinov, M., Penyashki, T., Tsokov, Pl. (2008). Simultaneous powdery boronaluminizing of steel stable in aluminum melts. Journal of Alloys and Compounds, 459, 501 – 503.

92. Maragoudakis, N. E., Stergioudis, G., Omar, H., Paulidou, H., Tsipas, D. N. (2002). Boron–aluminide coatings applied by pack cementation method on low-alloy steels. Materials Letters, 53, 406–410.

93. Tsipas, S. A., Omar, H., Perez, F. H., Tsipas, D. N. (2008). Boroaluminide coatings on ferritic–martensitic steel deposited by low-temperature pack cementation. Surface and Coatings Technology, 202, 3263–3271.

94. Chernega, S. M., Zaulichnyi, Ya. V., Karpets, M. V., Belous, M. V. (2000). Effect of chromium on the structure and properties of boride diffusion coating. Poroshkovaya Metallurgiya, 416(11 – 12), 88 – 93.

95. Lee, S. Y., Kim, G. S., Kim, B.-S. (2004). Mechanical properties of duplex layer formed on AISI 403 stainless steel by chromizing and boronizing treatment. Surface and Coating Technology, 177 – 178, 178 – 184.

96. Grachev, S. V., Mal'tseva, L. A., Mal'tseva, T. V.,Kolpakov, A. S., Dmitriev, M. Yu. (1999). Boronizing and borochromizing in a vibrofluidized bed. Metallovedenie i Termicheskaya Obrabotka Metallov, 41(11 – 12), 3 -6.

97. Balandin, Yu. A. (2005). Surface Hardening of Die Steels by Diffusion Boronizing, Borocopperizing, and Borochromizing in Fluidized Bed. Metallovedenie i Termicheskaya Obrabotka Metallov, 47(3 – 4), 27 – 30.

98. Bourithis, L., Papadimitriou, G. (2003). Boriding a plain carbon steel with the plasma transferred arc process using boron and chromium diboride powders: microstructure and wear properties. Materials Letters, 57, 1835 – 1839.

99. Ivanov, A. S., Karmanov, D. V., Vdovina, O. N. (1999). Surface saturation of low-carbon martensite steels with boron and copper. Metallovedenie i Termicheskaya Obrabotka Metallov, 41(5 - 6), 13 -16.

100. Sikorski, K., Wierzchon, T., Bielinski, P. (1998). X-ray microanalysis and properties if multicomponent plasma-borided layers on steels. Journal of Materials Science, 33, 811 -815.

101. Fillit, R., Mizera, J., Bielinski, P., Wierzchon, T. (1995). Determining the stress state in iron and iron-nickel boride layers produced under glow discharge conditions. Journal of Materials Science Letters, 14, 1633 -1634.

102. Balandin, Yu. A. (2006). Boron based complex wear-resistant coatings. Zashchita Metallov, 42(2), 150 - 153.

103. Sen, U., Pazarhoglu, S. S., Sen, S. (2008). Niobium boride coating on AISI M2 steel by boro-niobizing treatment. Materials Letters, 62, 2444 – 2446.

104. Carbucicchio, M. Casagrande, A., Palombarini, G. (1990). Competitive reactivity of iron towards boron and silicon in surface treatments with powder mixtures. Hyperfine Interactions, 57, (1769 – 1774).

105. Sambogna, G., Palombarini, G., Carbucicchio, M., Ciprian, R. (2008). Borosiliciding of Fe–Ni alloys and evaluation of their resistance to abrasive wear. Hyperfine Interactions, 187, 131–136.

106. Lou, D. C., Akselsen, O. M., Solberg, J. K., Onsoien, M. I., Berget, J., Dahl, N. (2006). Silicon-boronising of Nimonic 90 superalloy. Surface and Coatings Technology, 200(11), 3582-3589.

107. Gidikova, N. (2000). Vanadium boride coatings on steel. Materials Science and Engineering A, 278, 181 – 186.

108. Sen. S. (2005). The characteristics of vanadium boride coatings on AISI 8620 steel. Surface and Coatings Technology, 190, 1 – 6.

109. Bazhin, A. I., Goncharov, A. A., Petukhov V. V., Radjabov, T. D., Stupak, V. A., Konovalov, V.A. (2006). Magnetron sputtering of a vanadium-diboride target in Ar+N2 gaseous mixtures. Vacuum, 80, 918–922.

110. Mitterer, C, Komenda-Stallmaier, J., Losbichler, P., Schmölz, P., Werner, W. S. M., Störi, H. (1995). Sputter deposition decorative boride coatings. Vacuum, 46(11), 1281 – 1294.

111. Mitterer, C, Ott, H. -M., Komenda-Stallmaier, J., Schmölz, P., Werner, W. S. M., Störi, H. (1995). Sputter decorative hard coatings within the system LaB_6 – ZrB2. Journal of Alloys and Compounds, 239, 183 - 192.

112. Ürgen, M., Çakir, A. F., Eryilmaz, O. L., Mitterer, C. (1995). Corrosion of zirconium boride and zirconium boron nitride coated steels. Surface and Coatings Technology, 71, 60 – 66.

113. Xia, Y. –Q., Liu, W. -M., Yu, L. –G., Han, N., Xue, Q. –L. (2003). Investigation on the tribological properties of boron and lanthanum permeated mild steel. Materials Science and Engineering A, 354, 17 – 23.

114. Jayaraman, S., Gerbi, J. E., Yang, Y., Kim, D. Y., Chatterjee, A., Bellon, P., Girolami, G. S., Chevalier, J. P., Abelson, J. R. (2006). HfB_2 and Hf–B–N hard coatings by chemical vapor deposition. Surface and Coatings Technology, 200, 6629 – 6633.

115. Bel'skii, E. I., Sitkevich, M. V., Rogov, V. A., Kryukov, V. P. (1980). Chemicothermal treatment of dies. Metallovedenie i Termicheskaya Obrabotka Metallov, 6, 17 -19.

116. Kholin, A. S. (1999). Phase composition and crack resistance of alloy boride layers on steel. Metallovedenie i Termicheskaya Obrabotka Metalloy, 41(3-4), 159-161.

117. ASTM (2004). Standard test method for microindentation hardness of materials E384-99. Annual Book of ASTM Standards: Metals-Mechanical Testing; Elevated and Low-Temperature Tests: Metallography Vol.03.01. Pennsylvania: ASTM International.

118. Pyrus 1 TGA (2010). Pyris 1 TGA Thermogravimetric Analyzer. Perkin Elmer. Retrieved from http://las.perkinelmer.com/Catalog/ProductInfoPage.htm?ProductID=N5370742 , accessed May 3 2010.

119. Young, R. A. (1995). The Rietveld mehod (International Union of Crystallography Monographs on Crystallography 5). New York: Oxford University Press.

120. Pecharsky, V., Zavalij, P. (2005). Fundamentals of powder diffraction and structural characterization of materials. New York: Springer.

121. Glukhov, V. P. (1969). Boronizing steel. Institute of Material Physics, Academy of Sciences of the Ukrainian SSR, 278-283.

122. Suwattananont, N., Petrova, R. S. (2008). Oxidation kinetics of boronized low carbon steel AISI 1080. Oxidation Metals, 70, 307-315.

123. Okamoto, H. (2000). Desk handbook phase diagrams of binary alloys. Ohio:ASM International.

124. ICDD (2009). PDF-4+ Database. Pennsylvania: International centre for Diffraction Data.